List of Contributors

K. Schmidt-Rohr, *Department of Chemistry, Iowa State University, Ames, IA 50011, USA and* H. W. Spiess, *Max Planck Institut für Polymerforschung, Postfach 3148, 55021 Mainz, Germany*

Max A. Keniry, *Research School of Chemistry, The Australian National University, Canberra, ACT 0200, Australia* and John A. Carver, *Department of Chemistry, University of Wollongong, Wollongong, NSW 2522, Australia*

Cynthia L. Lean, Peter Russell and Carolyn E. Mountford, *Institute for Magnetic Resonance Research, P.O. Box 148, St Leonards, NSW 1590, Australia* and *Department of Magnetic Resonance in Medicine, University of Sydney, NSW 2006, Australia* and Ray L. Somorjai and Ian C. P. Smith, *Institute for Biodiagnostics, National Research Council of Canada, 435 Ellice Avenue, Winnipeg, Manitoba, R3B 1Y6, Canada*

A. Ted Watson, *Department of Chemical Engineering, Colorado State University, 100 Glover Building, Fort Collins, CO 80523-1370, USA,* Jeromy T. Hollenshead and Jinsoo Uh, *Department of Chemical Engineering, Texas A & M University, USA* and C. T. Philip Chang, *Engineering Imaging Laboratory, Texas A & M University, USA*

Y. R. Du and L. F. Shen, *State Key Laboratory of Magnetic Resonance and Atomic and Molecular Physics, Wuhan Institute of Physics and Mathematics, Chinese Academy of Sciences, Wuhan 430071, P.O. Box 71010, China* and S. Zhao, *Technical Institute of Physics and Chemistry, The Chinese Academy of Sciences, Beijing 100101, China*

Preface

Volume 48 of *Annual Reports on NMR Spectroscopy* contains sentient contributions relating to advances in various fields of NMR activity. It is a very great pleasure for me to have this opportunity to thank all of the reporters and the production staff at Academic Press (London) for their very considerable efforts devoted to the realization of this volume.

The first contribution relates to the Dynamics of Polymers from One- and Two-dimensional Solid State NMR Spectroscopy by K. Schmidt-Rohr and H. W. Spiess; this is followed by an account of the NMR Spectroscopy of Large Proteins by M. A. Keniry and J. A. Carver; next is an Accurate Diagnosis and Prognosis of Human Cancers by Proton MRS and a Three-stage Classification Strategy by C. L. Lean, R. L. Somorjai, I. C. P. Smith, P. Russell and C. E. Mountford; following this is an NMR Determination of Porous Media Property Distributions by A. T. Watson, J. T. Hollenshead, J. Uh and C. T. P. Chang; the final contribution is on NMR Studies of Micelles by Y. R. Du, S. Zhao and L. F. Shen.

Royal Society of Chemistry
Burlington House
London
UK

G. A. WEBB
March 2002

Dynamics of Polymers from One- and Two-dimensional Solid-state NMR Spectroscopy

KLAUS SCHMIDT-ROHR and HANS WOLFGANG SPIESS

Department of Chemistry, Iowa State University, Ames, IA 50011, USA, and Max-Planck-Institut für Polymerforschung, PO Box 3148, D-55021 Mainz, Germany

This report describes new magic-angle-spinning NMR techniques for quantifying dynamics in complex polymeric materials. Emphasis is placed on MAS techniques with recoupling of anisotropic interactions, such as dipolar couplings of protons or the chemical-shift anisotropy of ^{13}C, which makes these methods applicable at any spinning speed. Applications to glassy and semicrystalline polymers, dendrimer nanomaterials, protein gels, discotic liquid crystals, and polymer melts demonstrate the wide variety of organic materials that have become accessible to quantitative dynamics studies by NMR, mostly without isotopic labeling.

ANNUAL REPORTS ON NMR SPECTROSCOPY
VOLUME 48 ISBN 0-12-505448-3

1. INTRODUCTION

Solid-state NMR provides some of the most powerful techniques for elucidating details of segmental dynamics in solid materials and biomolecules.[1,2] Such dynamics have important effects on the mechanical properties of polymers,[3,4] activity of proteins,[2] stability of pharmaceuticals,[5] transport properties in zeolites,[6] and behavior of amorphous materials near the glass transition.[7] Relatively slow segmental reorientations, with rates of 0.1/s to 10000/s, can be observed and analyzed in detail in exchange NMR experiments, which detect changes in orientation-dependent NMR frequencies in real time.[1] Correlation-time[8–10] and reorientation-angle distributions,[1,11,12] orientational[1,13] and rate memory,[14,15] as well as the existence of dynamic heterogeneities,[14,16] can be characterized by multidimensional exchange NMR. Many of these techniques were reviewed in this series a few years ago.[17] A notable recent development has been the measurement of the size of dynamic heterogeneities above the glass transition temperature T_g in polymers and low-molar-mass glass formers. By combining reduced four-dimensional exchange NMR with spin diffusion in the central mixing time, 'domains' of slow-moving segments at $T_g + 10\,K$ were found to be 1–3 nm in diameter.[16,18]

The broadline exchange NMR techniques without magic-angle spinning provide some of the most detailed information available on the geometry of segmental rotations in disordered solids. However, their sensitivity and chemical-site resolution is limited. These shortcomings have been overcome by the recently introduced centerband-only detection of exchange (CODEX) NMR technique.[19,20] This enables the observation and characterization of slow segmental reorientations with the highest available ^{13}C NMR sensitivity and site resolution, in sideband-free magic-angle spinning spectra. In these experiments, the chemical-shift anisotropy serves as the probe of segmental orientation, since it is available without isotopic labeling. From short series of one-dimensional CODEX spectra, the correlation function and correlation time can be determined, and it can be established whether the motion is diffusive or whether it involves jumps between discrete sites. The fraction of segments rotating on the millisecond-to-second timescale can be determined accurately. In addition, motional amplitudes can be estimated, with relatively high sensitivity to small-angle motions. This information is obtained for each site with a resolved line in the sideband-free MAS spectrum. The ODESSA and time-reversed ODESSA exchange experiments,[21–23] though less versatile, can be described in the same framework, extending CODEX to short chemical-shift evolution times. This is particularly useful for aromatic and C=O signals with their large chemical-shift anisotropies.

In the applications shown, this review emphasizes results from the authors' groups. For instance, CODEX studies of glassy polymers provide, for the first time, quantitative information on the—often small—fractions of mobile

segments, and the effects of sidegroup size and temperature, e.g. in poly(alkyl methacrylates) with their COOR sidegroups.[24] They have also enabled the detection of slow reorientations in engineered protein materials.[25,26]

CODEX experiments can be applied at very high spinning speeds, at which undesirable dipolar spin exchange may be suppressed, so that it does not interfere with the detection of motions on the second timescale. An up to 10-fold slow-down of the ^{13}C spin diffusion has been demonstrated by CODEX at 28 kHz for unprotonated equivalent sites in several organic solids.[27]

Owing to the orientation dependence that it imparts to the NMR frequency, the chemical-shift anisotropy (CSA) has proven useful not only in studies of slow dynamics but also for characterizing segmental orientation distributions and fast segmental reorientations. While static powder patterns provide this CSA information in the most accessible form, site resolution by MAS is indispensable in all but the simplest unlabeled systems. The two requirements can be combined in two-dimensional (2D) separation experiments. Recently, a robust sequence, termed separation of undistorted powder-patterns by effortless recoupling (SUPER), was introduced that makes CSA measurements under standard MAS conditions routine.[28] It enables identification of functional groups and measurements of orientation distributions, segmental dynamics, and conformations.

Another important development in solid-state NMR employing fast MAS[29] concerns double quantum (DQ) NMR spectroscopy[30] of strongly dipolar coupled spins, such as ^{1}H–^{1}H, ^{1}H–^{13}C or ^{1}H–^{15}N. These techniques take advantage of the significant simplification of the multispin dipolar coupled network under fast MAS, where two-spin correlations predominate.[31] Comprehensive papers dealing with homonuclear and heteronuclear DQ NMR spectroscopy under fast MAS have recently been published.[32,33] Most of the applications reported so far have concentrated on elucidating the structures of supramolecular assemblies,[34,35] exploiting hydrogen bonds,[36,37] π–π interactions of aromatic moieties,[38,39] and chain organization on surfaces.[40] These studies have been reviewed in considerable detail elsewhere.[41]

DQ MAS NMR spectroscopy can, likewise, be used to study molecular dynamics, similar to the techniques introduced above. This will be demonstrated here by consideration of the axial rotation of discotics in columnar liquid crystalline phases,[38,42] and the restricted mobility of phenylene groups in shape-persistent polyphenylene dendrimers.[43,44] By extending DQ NMR to include the concept of 2D-exchange NMR, slow motions become accessible,[45] e.g. of polymer chains in the crystalline regions of semicrystalline polymers.[4,46] Moreover, exploiting the residual dipole–dipole couplings resulting from anisotropic rapid motion in polymer melts[47] and combining it with the theory of chain dynamics of polymers[48,49] allow us to infer structural information on the nanometer scale and study *translational* motions.[50]

2. CODEX FOR SLOW DYNAMICS

2.1. Principles of CODEX

Simply put, CODEX is a stimulated-echo exchange experiment under MAS conditions, with CSA recoupling and intensity referencing in the tradition of REDOR.[51] Figure 1(a) shows the CODEX pulse sequence. After cross-polarization (or single-pulse excitation), the magnetization evolves under the anisotropic chemical shift, recoupled by a series of 180° pulses spaced by $t_r/2$.[20,52] Then, one component of the magnetization is stored for the mixing time t_m, during which motion can occur. The mixing time is a multiple of the rotation period t_r, which is ensured by active rotor synchronization that uses the signal of the spinning-speed detector as a trigger. In successive transients, the phases of the 90° pulses which bracket the mixing time are changed together by 90°, so that both components, $\cos\Phi_1$ and $\sin\Phi_1$, of the magnetization are retained alternately, and the sum of two transients yields $\cos\Phi_1 + i\sin\Phi_1$. Thus, a stimulated echo forms at the end of the second recoupling period ($t_2 = t_1$). Its amplitude, which is reflected in the detected MAS peak intensity, is reduced by motion-induced changes in the CSA frequency during the long mixing period t_m.

In a simple CODEX experiment, the signal intensity $S(t_m,\delta Nt_r)$ is observed; here, the time Nt_r has been normalized by multiplication with the CSA parameter δ.[1] For quantitative analysis, a reference spectrum $S_0 = S(0,\delta Nt_r)$ is required

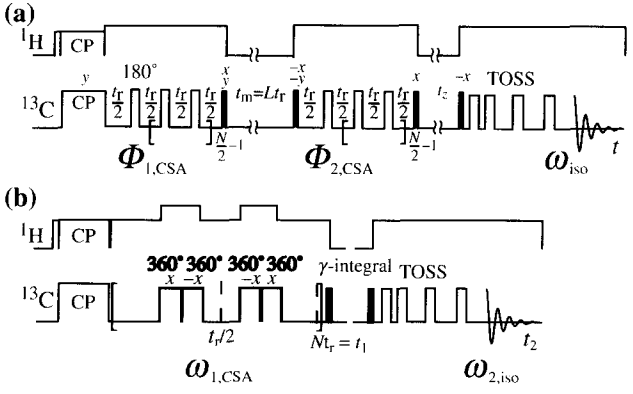

Fig. 1. (a) Basic CODEX pulse sequence[20] and its synchronization with the sample rotation. Ninety degree pulses are shown filled. The series of 180° pulses (short open boxes) during t_1 and t_2 recouple the anisotropic chemical shift, while removing the isotropic shift. The *xy*-8 phase sequence is used for the 180° pulse trains. The reference signal S_0 is obtained by interchanging t_m and t_z. (b) Pulse sequence of the SUPER NMR experiment. The increment of the evolution time t_1 is one rotation period t_r. Each of the two pulse blocks in a given rotation period consists of two 360° pulses. Details of the phase cycling scheme are described in ref. 28. TOSS, total suppression of sidebands by four 180° pulses[59] and the preceding 'γ-integral' over the rotor orientation.[20]

which has all the same relaxation factors but no motion during t_m. This is achieved by simply interchanging the durations of t_m and t_z (see Fig. 1(a)). Often, it is advantageous to subtract the CODEX spectrum $S = S(t_m, \delta N t_r)$ from the reference spectrum $S_0 = S(0, \delta N t_r)$, to obtain a pure-exchange CODEX spectrum $\Delta S = S_0 - S$. In this difference spectrum, the signals of non-exchanging components are removed from the spectrum. Figure 2 shows an example of this procedure for glassy poly(methyl methacrylate) (PMMA), measured near ambient temperature; it indicates that some of the sidegroups of this polymer are undergoing large-amplitude motions in the glassy state.[13,53] The pure-exchange approach can also serve as a useful 'filter' for the signals of slow-moving groups in a multicomponent system.

The normalized pure-exchange CODEX intensity

$$E(t_m, \delta N t_r) = \frac{\Delta S(t_m, \delta N t_r)}{S(0, \delta N t_r)} = \frac{S(0, \delta N t_r) - S(t_m, \delta N t_r)}{S(0, \delta N t_r)} \tag{1}$$

is plotted in Fig. 3(a) as a function of t_m for PMMA and two crystalline model compounds, dimethyl sulfone (DMS) and methylmalonic acid. For DMS, a single-exponential curve is obtained, while PMMA shows some non-exponentiality. Methylmalonic acid shows no exchange except for ^{13}C spin diffusion (see Section 3.2). In Fig. 3(b), exchange due to helical jumps in the crystallites of isotactic polypropylene[54,55] is shown.

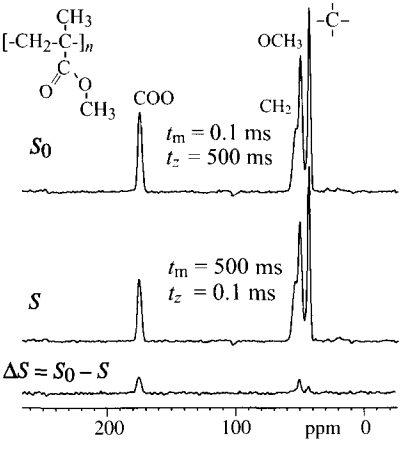

Fig. 2. (a) Full reference spectrum S_0, spectrum S after CODEX dephasing and pure-exchange CODEX spectrum $\Delta S = S_0 - S$ of unlabeled PMMA at 300 K, for $t_m = 500$ ms and $Nt_r = 800\,\mu s$. The intensity of ΔS is low, since only a minority of the sidegroups (35%) are undergoing flips. Reproduced from T. S. Bonagamba, F. Becker-Guedes, E. R. deAzevedo and K. Schmidt-Rohr. Slow ester sidegroup flips in glassy poly(alkyl methacrylate), characterized by centerband-only detection of exchange (CODEX) NMR, *Journal of Polymer Science*, Copyright © 2001 John Wiley & Sons. Reprinted by permission of John Wiley & Sons, Inc.

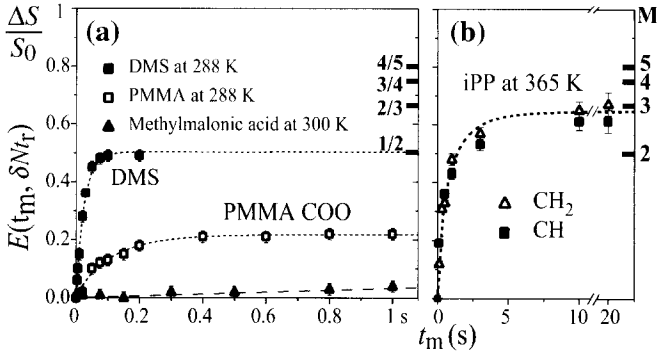

Fig. 3. Correlation functions of slow segmental motions obtained from the normalized pure-exchange CODEX intensities $\Delta S/S_0 = E(t_m, \delta Nt_r)$ as a function of t_m for: (a) COO groups in methylmalonic acid ($T = 300$ K, $\delta Nt_r = 7.6\pi$), COO groups in PMMA ($T = 288$ K, $\delta Nt_r = 8\pi$), and CH_3 groups in DMS ($T = 288$ K, $\delta Nt_r = 12.4\pi$); and (b) CH and CH_2 groups in iPP ($T = 365$ K; $\delta Nt_r = 3.6\pi$ and 8.5π, respectively). On the right, the expected final intensity values for M-site jumps are marked. Reprinted with permission from ref. 19. Copyright (2000) American Chemical Society.

2.2. CODEX analysis based on reorientation angle and difference tensor

Through variation of the duration Nt_r of the evolution under the recoupled CSA, the amplitude of the reorientations during t_m can be determined by CODEX NMR. The nuclear spins evolve for $N/2$ rotor periods with the phase Φ_1 before t_m, and for $N/2$ rotor periods with the corresponding phase Φ_2 after t_m. The normalized CODEX difference signal is therefore

$$\frac{\Delta S(t_m, \delta Nt_r)}{S(0, \delta Nt_r)} = 1 - \langle \cos(\Phi_2 - \Phi_1) \rangle = 1 - \left\langle \cos\left(N \int_0^{t_r/2} [\omega_2(t) - \omega_1(t)] dt\right) \right\rangle \quad (2)$$

The pointed brackets indicate the powder average, which also contains the effect of the correlation time τ_c and mixing time t_m. It can be shown that the dephasing is independent of the spinning speed and only depends on the total time Nt_r.[20] Owing to this ω_r independence, the CODEX pulse sequence works up to very high spinning speeds (see below).

In Eq. (2), the argument of the cosine function, which depends on δNt_r and the reorientation angles (α_R, β_R, γ_R), can be considered as the phase acquired within a time of $N/2t_r$ under the action of the chemical-shift difference tensor $\overleftrightarrow{\omega}^{\Delta} = (\overleftrightarrow{\omega}_2 - \overleftrightarrow{\omega}_1)$.[20] For uniaxial interactions, i.e. with $\eta = 0$, the principal values of the difference tensor are $\omega^{\Delta}{}_{22} = 0$, and the full-width anisotropy $|\omega^{\Delta}{}_{33} - \omega^{\Delta}{}_{11}|$ of ω^{Δ}, i.e. the range of possible frequency differences, is [20,56]

$$|\omega^{\Delta}{}_{33} - \omega^{\Delta}{}_{11}| = |(\omega_{33} - \omega_{11})\, 2 \sin\beta_R| \quad (3)$$

This represents a strong linear dependence on the reorientation angle for $\beta_R < 45°$, which permits relatively easy detection of small-angle motions.

Equation (3) applies in general, i.e. also for $\eta \neq 0$, to rotations by β_R around the ω_{22} principal axis, and with suitable permutations of labels to rotations around the other two principal axes.

Figure 4 shows simulated pure-exchange CODEX curves as a function of $\delta N t_r$ as a function of the sidegroup rotation angle α in PMMA. The rotation is taken to occur around the ω_{33} axis, which is the normal to the OCO ester plane and also close to the local chain axis. The predicted sensitivity to small-angle motions is clearly recognizable. The unitless variable $\delta N t_r$ shown at the top of Fig. 4(b) is particularly useful for distinguishing small- and large-amplitude motions for any CSA. The quantitative analysis of CODEX data requires knowledge of three principal values of the chemical-shift tensor, which can be obtained by the SUPER experiment described below.

In the case of a uniaxial NMR interaction, i.e. for $\eta = 0$, the information content of an exchange experiment at a given mixing time t_m can be summarized

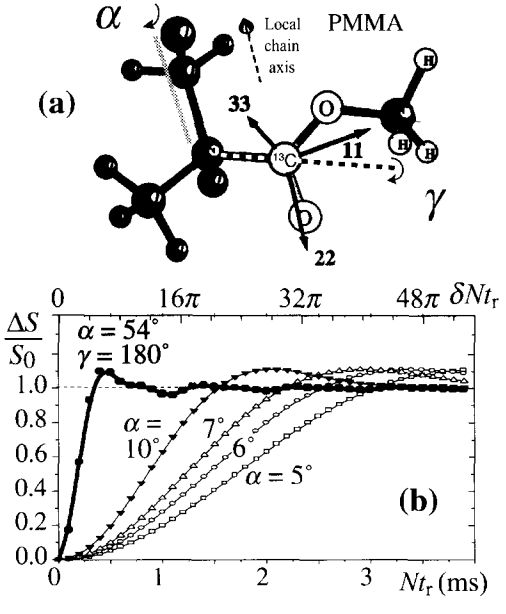

Fig. 4. (a) Rotation axes in the repeat unit of PMMA as considered in the simulations of CODEX curves. Rotations around the C–C bond connecting the sidegroup to the backbone are indicated by an angle γ. Rotations around the local chain axis, or equivalently the normal to the sidegroup plane, are characterized in terms of the angle α. (b) Simulations of motional-amplitude-dependent CODEX curves. Restricted rotations around the local chain axis, with $\alpha = 5°$, 6°, 7°, and 10°, produce a relatively slow rise of the normalized exchange intensity $\Delta S/S_0$ with the recoupling time $N t_r$. Large-amplitude flips of the sidegroup by $\gamma = 180°$ produce a much faster rise. Reproduced from T. J. Bonagamba, F. Becker-Guedes, E. R. deAzevedo and K. Schmidt-Rohr, *Journal of Polymer Science*, Copyright © 2001 John Wiley & Sons. Reprinted by permission of John Wiley & Sons, Inc.

in terms of the reorientation-angle distribution $R(\beta_R, t_m/\tau_c)$, i.e. the probability density of finding a reorientation angle β_R after a mixing time t_m.[1,10,12,57] Since the correlation time τ_c is the natural reference for t_m, only their ratio, t_m/τ_c, is relevant for the reorientation-angle distribution. The dephasing or pure-exchange intensity CODEX curves are simply $R(\beta_R, t_m/\tau_c)$-weighted superpositions of the CODEX curves $\varepsilon(\delta N t_r; \beta_R)$ for specific β_R values.[12,58]

On the basis of the characteristic evolution of the reorientation-angle distributions for pure jumps and diffusive motions with time t_m, CODEX NMR can distinguish these different types of processes.[1,10] For instance, symmetric N-site exchange is a common jump process, while isotropic rotational diffusion is the most important example of a diffusive reorientation. For many pure jump motions, the only change in the reorientation-angle distribution is the relative intensity of the reorientation-angle distribution at $\beta_R = 0$ and at $\beta_R \neq 0$. This holds for all two-site jumps, symmetric three-site jumps, random N-site jumps, and the isotropic random-jump model. As a result, the shape of the $E(\delta N t_r; t_m)$ curves, normalized by the long-Nt_r intensity $E(\infty; t_m)$ at the given t_m, does not change with t_m, (Fig. 5(a)). In contrast, all diffusive motions produce a characteristic change in the shape of $E(\delta N t_r)$ with increasing t_m. For short t_m, the curves rise quite slowly because only small reorientation angles have been reached, while an earlier and faster increase in $E(\delta N t_r)$ occurs at long t_m when larger reorientation angles have been attained. These features are clearly visible in Fig. 5(b), where uniaxial rotational diffusion has been simulated.

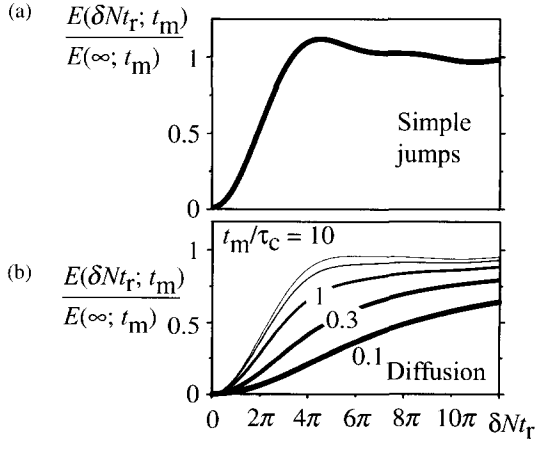

Fig. 5. Time evolutions of doubly normalized CODEX $E(\delta N t_r, t_m)/E(\infty, t_m)$ curves, showing clear differences between simple jumps and diffusive motion (for a uniaxial interaction, $\eta = 0$). As indicated at the top, the line thickness decreases with increasing t_m/τ_c (= 0.1, 0.3, 1.0, 3.0, and 10). (a) Two- or three-site jumps, with a 109° (or equivalently 71°) jump angle. The shape of the normalized curves is the same at all mixing times. (b) Uniaxial rotational diffusion on a cone with an apex angle of 141° (or equivalently $2 \times 109.5°$). Characteristically for diffusive motions, the shape of the curves changes with t_m.

2.3. Number of accessible orientations, and fraction of mobile segments

In complex systems such as amorphous polymers, broad distributions of correlation times and motional amplitudes often result in a complex exchange behavior. It is often a good approximation to analyze such situations in terms of a fraction f_m of significantly exchanging segments. A homogeneous system in which all equivalent segments are moving similarly, as is true for most crystals, has $f_m = 1$. Information about the fraction f_m and the number M of equivalent orientational sites accessible to the mobile segments is obtained from the long-time exchange intensity E_∞. Since a fraction $1/M$ of the mobile species will reside in the originally selected site, we have

$$E_\infty = E(t_m >> \tau_c, \delta N t_r >> 1) = f_m\,(1 - 1/M) \tag{4}$$

For $f_m = 1$, the minimum E_∞ is 1/2, obtained for $M = 2$. For diffusive reorientations of all segments, $M >> 1$ and $E_\infty \sim 1$. Also, if $E_\infty < 1/2$, as for the case of PMMA in Fig. 3(a), it must be concluded that $f_m < 1$, i.e. some segments do not participate in the slow motion. In fact, Eq. (4), with $M = 2$ and $M \to \infty$, yields $E_\infty < f_m \leq 2E_\infty$.

From E_∞ alone, f_m and M cannot be determined unambiguously. Fortunately, the number of sites M can be measured in a four-time CODEX experiment,[20] which is produced by concatenating two CODEX pulse sequences.

2.4. ODESSA and its relation to CODEX

The one-dimensional exchange spectroscopy by sideband alternation (ODESSA) and time-reversed ODESSA MAS exchange experiments[21–23] are closely related to the CODEX technique. The time-reversed (TR) ODESSA pulse sequence resembles that of CODEX in Fig. 1(a), but it has no 180° pulses, and the chemical-shift evolution times before and after t_m are just $t_r/2$. The mixing time is of duration $Lt_r + t_r/2$, so that the rotor echo ($Lt_r + t_r$ after the start of evolution) and the stimulated echo of the isotropic shifts coincide at the start of detection. Owing to these similarities, TR ODESSA can be regarded as CODEX with $N = 1$ rotation periods of CSA evolution. (Note that for regular CODEX, the minimum is $N = 2$, with 1 t_r before and 1 t_r after the mixing time.) Correspondingly, the intensity of the detected signal is modulated by $\cos[\Phi_2(t_r/2) - \Phi_1(t_r/2)]$. Thus, the ODESSA exchange intensity can be used to extend CODEX data to shorter CSA recoupling times. Particularly for large CSAs δ, this enables the acquisition of data at small $\delta N t_r$ while using moderate spinning rates <7 kHz ($t_r > 140\,\mu$s). Generally, ODESSA experiments need to be performed at sufficiently slow spinning rates so that significant sidebands are observable in the MAS spectrum.

Since the chemical-shift evolution cannot be varied easily over a wide range, ODESSA is used mostly to measure the t_m-dependence of the

exchange intensity. It does not provide much information about the motional amplitude, and even less on the fraction of mobile sites. An advantage of the ODESSA experiments is the reduced number of pulses, which, however, comes at the expense of a lower spinning rate and more loss of signal into sidebands.

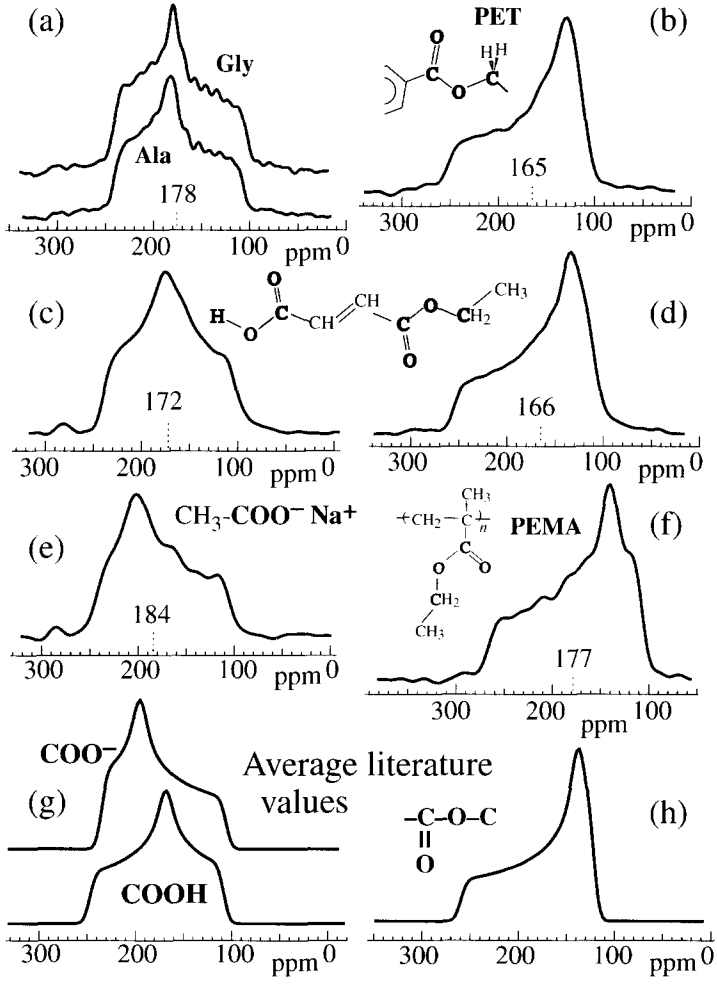

Fig. 6. COO powder spectra obtained as cross-sections from 2D SUPER of: (a) glycine and alanine (^{13}COO-labeled); (b) 10% ^{13}COO-labeled PET; (c, d) acid and ester site, respectively, of fumaric acid monoethyl ester; (e) sodium acetate; (f) 20% ^{13}COO-labeled PEMA ($\omega_{iso} = 177.6$ ppm). These spectra were taken at $\nu_r = 5$ kHz and scaling factor of 0.155, with weak ^{1}H decoupling power ($\gamma B_{1,H}/2\pi = 30$ kHz) during the ^{13}C pulses. (g, h) Simulated powder patterns obtained with the average principal values given in ref. 90 for (g) carboxylate and carboxylic acid groups and (h) ester groups. Adapted from ref. 28. Reproduced with permission of Academic Press.

2.5. Determination of chemical-shift parameters

For quantitative evaluation of CODEX or ODESSA dynamics measurements, the CSA of the sites investigated must be determined. A wide variety of methods with this goal have been proposed.[59–69] For CODEX and ODESSA experiments, a method using the same standard MAS equipment is desirable. A particularly robust technique that fulfills this requirement has recently been introduced.[28] It is derived from the technique of Tycko *et al.*,[61] but uses 360° instead of 180° pulses, as shown in Fig. 1(b). In combination with a suitable phase sequence, this makes the spectral patterns very insensitive to pulse-length errors and other imperfections. This method, termed separation of undistorted powder-patterns by effortless recoupling (SUPER), can be used at standard spinning speeds, between 2.5 and 5 kHz, and with standard radio-frequency power levels. With a CSA scaling factor of 0.155, accuracies of ±5, ±3 and ±1 ppm of the principal values can be achieved for protonated aromatic carbons, unprotonated sp^2-hybridized groups, and aliphatic sites, respectively. Examples of CSA-based assignment of COOC versus other COO or CON groups are shown in Fig. 6, while Fig. 7 demonstrates the deconvolution of the heavily overlapped CSA patterns of an aliphatic polymer.[28]

3. FAST MAGIC-ANGLE SPINNING

A particularly important recent advance in solid-state NMR is fast MAS with rotor frequencies $\omega_R > 2\pi \cdot 25$ kHz,[29] up to $2\pi \cdot 50$ kHz, as described by Samoson.[70] For most organic solids, the strongest ^1H–^1H dipole–dipole coupling, e.g. in CH_2 groups with a proton–proton distance of 0.18 nm, are of the order of $\omega_D \approx 2\pi \cdot 20.6$ kHz. Thus, the condition $\omega_R \geq \omega_D$ can be met even for the strongest dipole–dipole couplings. Since in most cases the remaining spins are further away, the corresponding remote couplings can effectively be 'spun out', and only the strongest couplings, originating from the shortest distances, are retained. This simple picture is indeed borne out in an elaborate theoretical treatment of multispin systems under fast MAS, combining Floquet theory and perturbation theory.[31] The higher-spin contributions are found to scale with increasing powers of the inverse rotor frequency and become less and less important at higher and higher ω_R.

3.1. Double-quantum NMR

Among fast MAS methods, homonuclear and heteronuclear DQ techniques have proven the most powerful and versatile. A detailed description of the principles of high-resolution DQ NMR spectroscopy of solids can be found in a previous review in this series.[17] Recent developments are covered in extended papers on

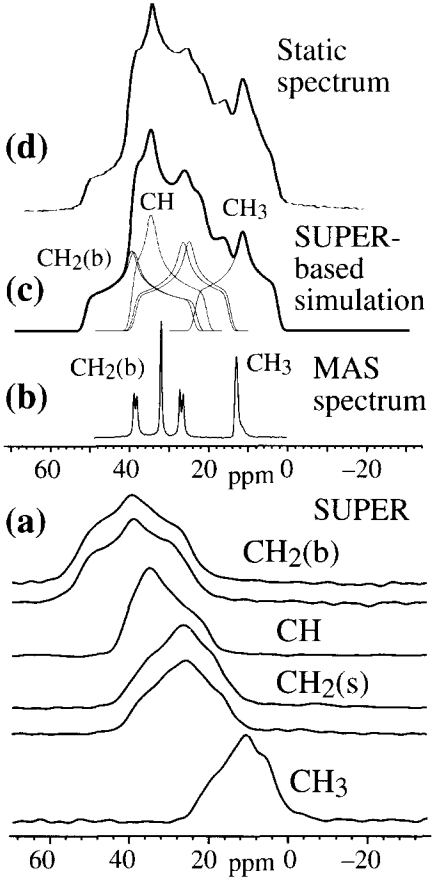

Fig. 7. ^{13}C spectra of iPB (form I). (a) SUPER cross-sections at the six peak maxima of the MAS spectrum in (b). The splittings of the CH_2 resonances in (b) have been attributed to packing effects.[91] (c) Simulation of the static powder pattern shown in (d), based on the experimental deconvolution in (a). The underlying six powder patterns are also shown; the CH_2 patterns were scaled up by a factor of two for clarity. Adapted from ref. 28. Reproduced with permission of Academic Press.

homonuclear[32] and heteronuclear[33] dipole–dipole couplings. In short, a double-quantum coherence (DQC) between two spins a and b coupled by a dipolar coupling D_{ab} is excited, which subsequently evolves during an incremented time period t_1 under the sum of the chemical shifts.[71] Then, the DQC is converted into observable single-quantum coherence (SQC), which is detected in the acquisition period t_2. During excitation and reconversion, the dipole–dipole interaction is recoupled. In the final 2D spectrum, centerbands occur at the sum frequency $\omega_a + \omega_b$ in the DQ dimension and can be detected at both frequencies ω_a and ω_b in the SQ dimension. Thus, such a pair of lines in the 2D NMR spectrum directly

maps the spatial proximity between spins a and b.[71] For short excitation times, the intensities of the DQ signals are proportional to D^2_{ab}. The dipole–dipole couplings may be estimated from DQ peak build-up curves,[72] which, for isolated spin pairs, such as doubly labeled ^{13}C–^{13}C, exhibit an oscillatory behavior.[51]

DQ *spinning sidebands* are generated by choosing a t_1 time increment well below τ_R so that the dipole–dipole Hamiltonian, being modulated by MAS due to its orientation dependence, differs at the beginning of excitation and reconversion.[73,74] The incomplete reconversion of the DQ coherence for $t_1 \neq kt_r$ results in a reduced signal for $t_1 \neq kt_r$, which is periodic with period t_r, and, after Fourier transformation, results in a sideband pattern. The stronger the dipolar coupling, or the larger the amplification of the dipolar coupling by a long recoupled DQ excitation time, the more spinning sidebands will be observed. In actual applications, the rotor frequency ω_R and the excitation time τ_{exc} will be chosen to generate up to third-order sidebands. This achieves sufficient signal-to-noise ratios, yet avoids multispin effects, which can be identified by the even-order sidebands that they generate.[75]

One way of studying molecular motions involves monitoring the reduction of dipole–dipole couplings probed by DQ spinning sidebands. The site selectivity is particularly high for heteronuclear DQ coherences. In Fig. 8, simulated sideband patterns are plotted for the C–H group, which is a sensitive probe of phenylene rotational motions, often met in practice. At low temperatures, one would expect

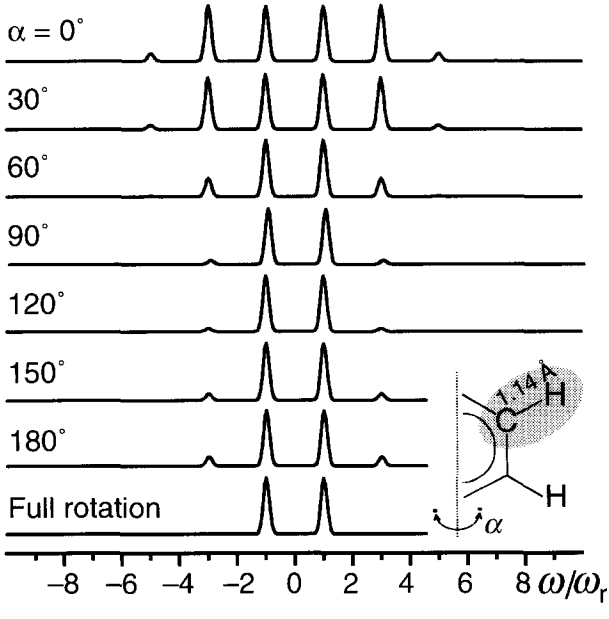

Fig. 8. Calculated heteronuclear DQ MAS NMR spinning sideband patterns for rotating phenylene groups and different flip angles α as indicated ($N_{rcpl}\, D_{IS}/\, \omega_R = 1.67$).

small-angle librations. With increasing temperatures, the angular excursions will increase until full rotation might be reached. The resulting motionally averaged dipolar couplings are readily calculated via the internet by use of our NMR-WEBLAB.[76] As shown in Fig. 8, the sideband patterns show a marked dependence of the flip angle α.

3.2. Dipolar spin exchange in CODEX and its slow-down under fast MAS

Fast MAS is also useful in suppressing ^{13}C spin diffusion (spin exchange) in CODEX experiments. These dipolar effects, which depend mostly on the ^{13}C–^{13}C couplings and are affected by the ^{1}H–^{13}C couplings, represent a usually undesirable competition to exchange by slow motions to be observed in CODEX.[77–80] For ^{13}C in natural abundance, it typically generates 4% exchange intensity within 0.5 s. Apart from isotopic dilution, the only known procedure for slowing down ^{13}C spin exchange between sites with similar isotropic chemical shifts is to increase the spinning speed. We have recently shown that for unprotonated sites, an increase of the spinning speed from 8 to 28 kHz does indeed

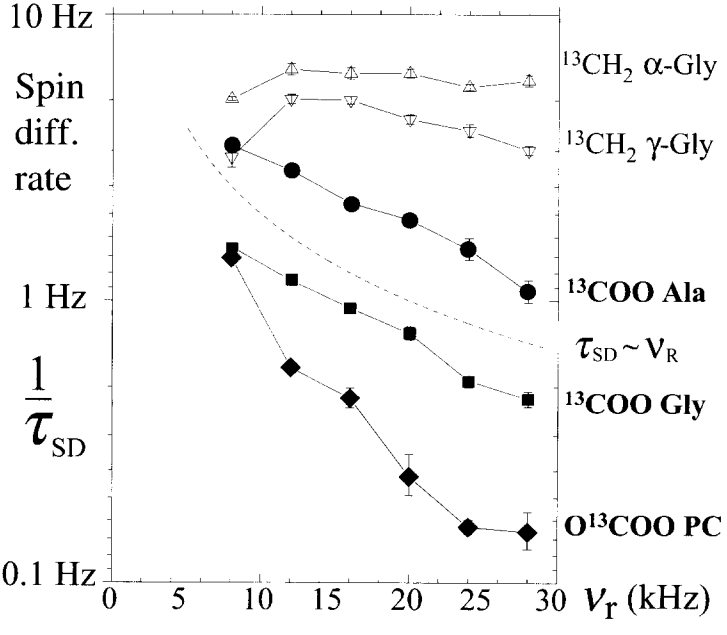

Fig. 9. Spin-exchange rates $1/\tau_{SD}$ versus MAS rotation frequency ν_R for five ^{13}C-enriched substances (four amino acids and polycarbonate, PC). The dashed line is the function $\tau_{SD} = 5 \times 10^{-5}\ \nu_R$. Adapted from ref. 27. Reproduced with permission of Academic Press.

decrease the spin exchange rate by a factor of 3–10 (Fig. 9).[27] This behavior can be explained semiquantitatively by the Maricq–Waugh analysis[81] of the behavior of dipolar-coupled spin pairs under MAS (dashed line in Fig. 9).[27] Thus, CODEX under fast MAS can significantly extend the range of correlation times accessible to exchange NMR measurements.

In ^{13}C-enriched proteins, deAzevedo *et al.*[25] have circumvented the ^{13}C spin-diffusion problem by performing a ^{15}N CODEX experiment followed by ^{15}N–^{13}C transfer and ^{13}C detection. The dipolar couplings between the ^{15}N nuclei, which are separated by three bonds and have smaller gyromagnetic ratios, are more than an order of magnitude reduced relative to those of ^{13}C in a uniformly labeled protein.

A second dipolar effect in CODEX is the relaxation-induced dipolar exchange due to dipolar couplings to heteronuclei,[82,83] in particular ^{14}N and ^{15}N, which undergo significant longitudinal relaxation during t_m. The relaxation removes a heteronuclear coherence term from the density operator and thus reduces the stimulated echo. This effect is described in detail in ref. 83.

4. SPECIFIC EXAMPLES

4.1. Dynamics in complex glassy polymers

So far, NMR studies of slow segmental motions of unlabeled polymers in the glassy state have been virtually impossible, due to sensitivity and line-overlap problems. CODEX and its non-spinning analog, 1D PUREX,[55] enable detailed, quantitative studies of these dynamics. The selective observation of exchanging sites in pure-exchange CODEX and 1D PUREX spectra leads to a great increase in resolution and in the dynamic range, which in turn reduces artefacts arising from the often dominant signals of immobile sites.

Examples of the detection of flipping sidegroups in PMMA by CODEX are shown in Figs 2 and 3. The characterization of the motion as a jump process between $M=2$ sites was confirmed in PMMA by 4-time CODEX.[20] Extending these experiments to a series of glassy poly(n-alkyl methacrylates) with COOR sidegroups of various sizes (Fig. 10), CODEX reflects flips and small-angle motions of the ester groups associated with the β-relaxation. The fraction of slowly flipping groups has been measured with 3% precision. In PMMA, only 34% of sidegroups flip, while the fraction is 31% in PEMA at 25°C. Even the large isobutylether and cyclohexylester sidegroups can flip in the glassy state, although the flipping fractions are reduced to 22% and ~10%, respectively (see Fig. 10).[24] Surprisingly, the fraction of flipping sidegroups was found to remain temperature-independent between 25°C and 80°C in PMMA with its small methylester sidegroup, while it

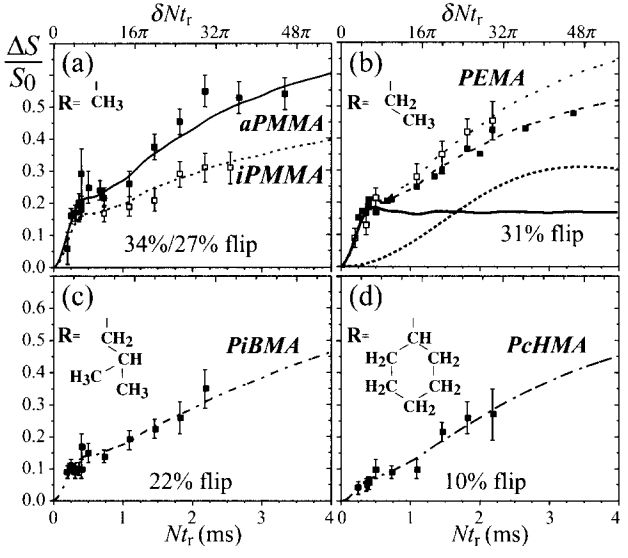

Fig. 10. Motional-amplitude-dependent CODEX curves, as a function of the recoupling time Nt_r. (a) Data for atactic PMMA (aPMMA) and isotactic PMMA (iPMMA). (b) PEMA, unlabeled (open symbols) and ^{13}COO-labeled (filled symbols) samples; (c) PiBMA. (d) PcHMA, with the initial rise arising due to ca. 9% of flipping sidegroups. The bimodal behavior observed in the curves is due to flips of some sidegroups, and small-angle motions of others (see Fig. 4). Adapted from T. J. Bonagamba, F. Becker-Guedes, E. R. deAzevedo and K. Schmidt-Rohr. Slow ester sidegroup flips in glassy poly(alkyl methacrylate)s characterized by centerband-only detection of exchange (CODEX) NMR, *Journal of Polymer Science*, Copyright © 2001 John Wiley & Sons. Reprinted by permission of John Wiley & Sons, Inc.

increases significantly with temperature in polymers with longer sidegroups (Fig. 11).[24]

4.2. Slow dynamics in peptides and proteins

In biological systems, knowledge of the three-dimensional molecular structure is important, but further insight into the segmental dynamics is also highly valuable. Segmental mobility and function in enzymes are thought to be particularly closely related. Owing to the large number of sites that may be distinguished in proteins, the sensitivity and site resolution of CODEX are indispensable for studies of slow motions. Hong and coworkers have introduced ^{13}C-detected ^{15}N CODEX for studies of slow motions in ^{13}C-labeled globular proteins.[25] In a triblock protein hydrogel, the experiments revealed large-amplitude reorientations of the α-helical segments that form the reversible cross-links.[26]

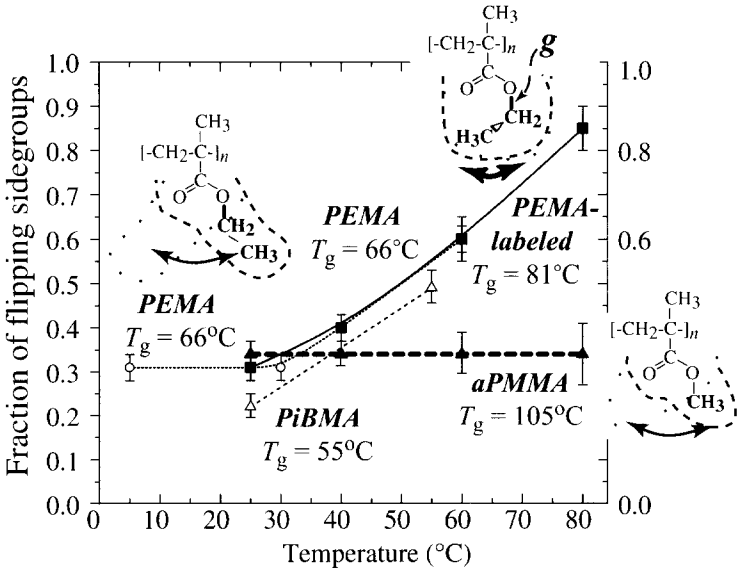

Fig. 11. Temperature dependence of the fraction of flipping sidegroups in aPMMA (solid triangles), two PEMA samples (open circles, commercial PEMA with $T_g = 66°C$; filled squares, ^{13}COO-labeled PEMA with $T_g = 81°C$), and in PiBMA (open triangles). Adapted from T. J. Bonagamba, F. Becker-Guedes, E. R. deAzevedo and K. Schmidt-Rohr. Slow ester sidegroup flips in glassy poly(alkyl methacrylate)s characterized by centerband-only detection of exchange (CODEX) NMR, *Journal of Polymer Science*, Copyright © 2001 John Wiley & Sons. Reprinted by permission of John Wiley & Sons, Inc.

4.3. Slow motions from double-quantum exchange NMR

As noted above, multidimensional exchange NMR spectroscopy provides unique information about the timescale as well as the geometry of slow molecular motions. Extending DQ NMR spectroscopy into that area, therefore, represented a special challenge. Recently, such a homonuclear DQ–DQ exchange experiment has been designed[45] by combining two DQ experiments, as depicted in Fig. 12(a). The dipole–dipole coupling between two distinct spins is used to generate a DQ coherence, and the orientation-dependent coupling is measured by means of the DQ MAS sideband pattern before and after a mixing time. In a reduced three-dimensional experiment, the two DQ sideband patterns are correlated, resulting in a DQ–DQ sideband pattern which is sensitive to the reorientation angle. By referencing the DQ–DQ time signal, the information content of the pattern is divided into the sidebands and the centerband, with the former reflecting only the moieties which have undergone a reorientation changing the dipole–dipole coupling, and the latter predominantly containing contributions from moieties which retained their dipole–dipole coupling because they remained in, or returned to, their initial positions. Hence, a single sideband

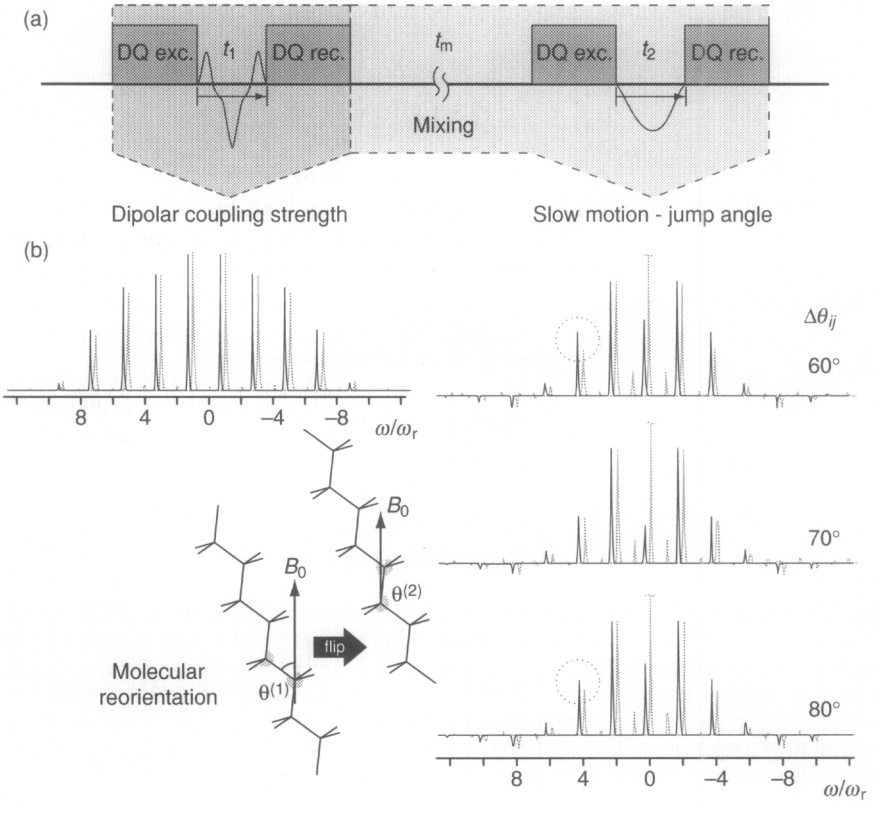

Fig. 12. (a) Schematic representation of DQ exchange experiments for elucidation of slow molecular dynamics.[45] (b) Calculated (black) and observed (gray) ^{13}C–^{13}C DQ MAS NMR sideband patterns of crystalline poly(ethylene) yielding the dipolar coupling strength and DQ–DQ exchange sideband patterns for different jump angles. For details, see ref. 45.

pattern provides access to the reorientation angle and the relative number of sites characteristic of the motional process. As a first example, Fig. 12 displays calculated (black) and experimental (gray) ^{13}C–^{13}C DQ MAS sideband patterns for the crystalline phase of doubly labeled poly(ethylene). The exchange spectra reflect the 180° flip motion due to the slow α-process of this material, yielding a C–C reorientation angle of 70°±5° in accord with 2D dipolar exchange NMR experiments on the same sample under static conditions.[46] One of the advantages of the MAS technique is its ability to probe the chain motion also in the non-crystalline regions, which is particularly important in view of the reviewed interest in the crystallization process of semicrystalline polymers[84] and the relation of the α-process to ultradrawability of such polymers.[4]

4.4. Phenylene motion in shape-persistent dendrimers

In a recent study of segmental motions in polyphenylene dendrimers[44] (Fig. 13(a)), DQ MAS and CODEX NMR were combined in an exemplary manner. The restricted phenylene dynamics in this new type of nanomaterial[43] are reflected in the DQ MAS sideband patterns from the aromatic CH signals, which are displayed in Fig. 14(a) as a function of both temperature and generation. An almost ideal sideband pattern for an isolated CH spin pair, being exclusively composed of odd-order sidebands, is observed in all three cases. Since the first-order sideband intensities are generally not reliable, due to the influence of remote protons,[33] the dipolar coupling constant was obtained from a fit of only the higher-order sidebands.

Simulations using the best-fit dipolar[73] coupling constant, and additionally taking fast motional averaging for different geometries into account, are shown

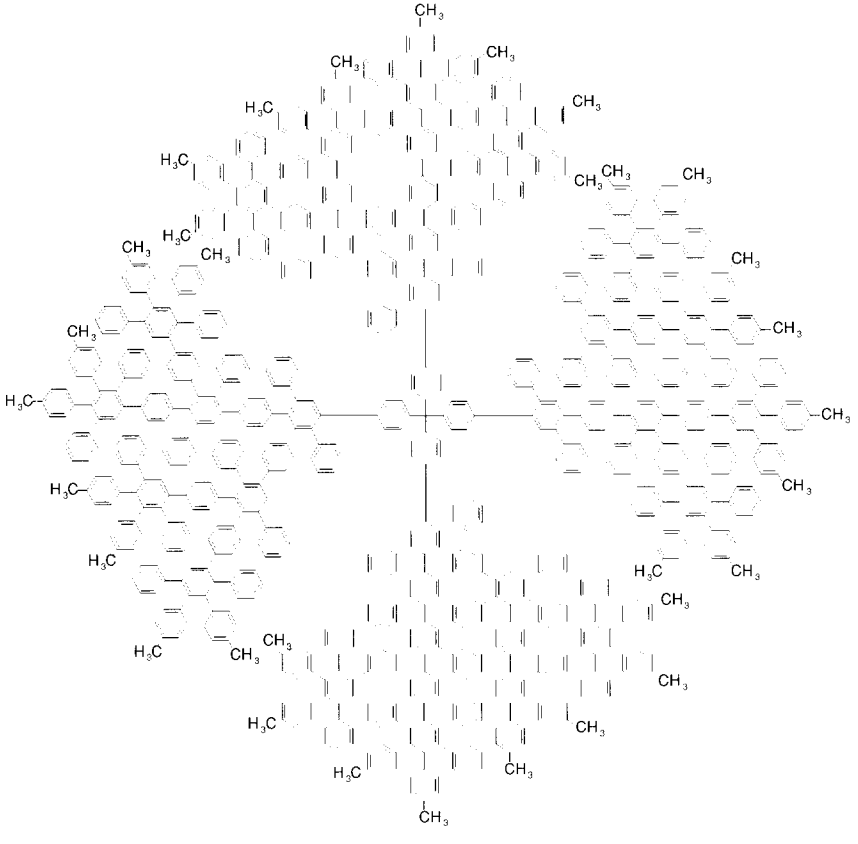

Fig. 13. Structure of a third-generation shape-persistent polyphenylene dendrimer[44] Td-$G_3(\text{-Me})_{32}$.

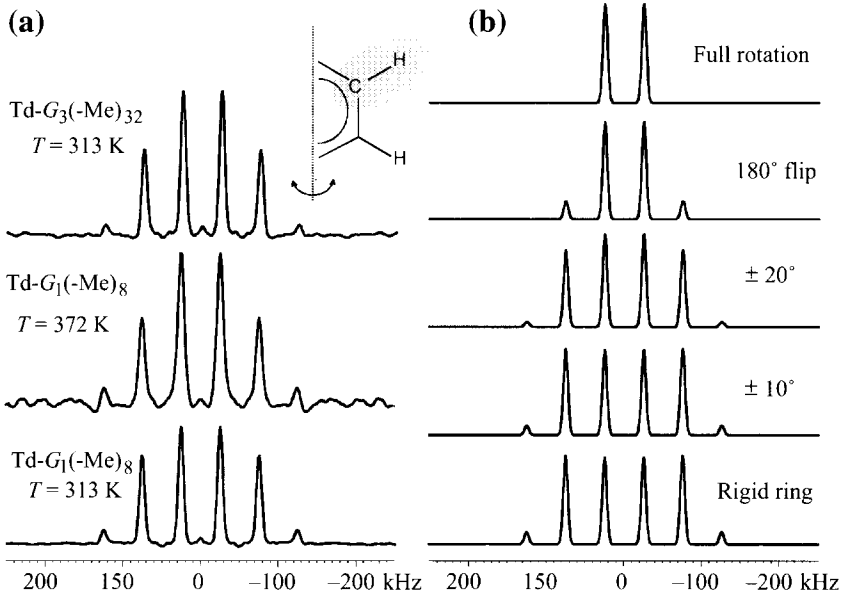

Fig. 14. (a) Solid-state ^{13}C spinning sideband patterns (sum projections) for the aromatic ternary CH in polyphenylene dendrimers, obtained at a spinning frequency of $\nu_R = 25$ kHz. The spectra were recorded for different temperatures and generations. (b) Corresponding simulated spectra, obtained by taking into account different models of phenyl ring reorientation processes on a microsecond-timescale. For details, see ref. 44.

in Fig. 14(b). Clearly, fast 180° flips and full rotations of individual phenyl rings can be ruled out, since they would lead to decreased higher-order sideband intensities. However, motional averaging due to small-angle fluctuations, Gaussian distributed with mean reorientation angles as indicated, does not lead to a strong effect. Thus, reorientations by as much as ±20° cannot be excluded. In summary, the dendritic systems are indeed mostly rigid on a microsecond-timescale, suggesting shape persistence on this timescale. The observed increased first-order sideband intensities, which increase further for higher temperature and higher dendrimer generation, might in part be attributed to a very small fraction of moieties undergoing fast larger-angle dynamics.

Slow motions in the same systems can be detected by CODEX NMR. Representative, pure-exchange intensities as a function of mixing time together with a corresponding reference spectrum are shown in Fig. 15(a). As indicated, the final intensities E_∞ differs significantly for the aromatic ternary ($E_\infty = 0.40$) and quaternary carbons ($E_\infty = 0.20$). This is in accord with the fact that, in the system studied, the fraction of mobile quaternary carbons, as obtained by simple counting, is only half that of the ternary ones; for details, see ref. 44. Assuming that all mono-substituted, terminal phenyl groups take part in the motional process, the observed plateau intensities can then be explained by reorientations

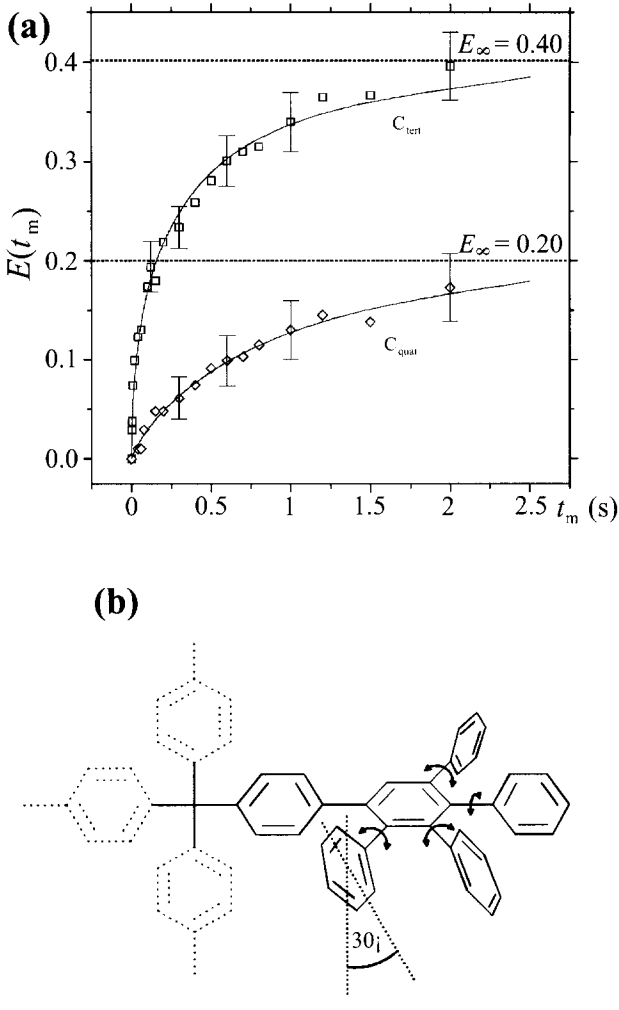

Fig. 15. (a) Normalized pure-exchange CODEX intensities $E(t_m)$ as a function of t_m for the aromatic ternary CH and the quaternary C_{quat} in Td-G_2(-Me)$_{16}$ dendrimer ($T = 363$ K). The fit curve for the ternary carbons is a stretched exponential $\exp[-(t_m/t_c)^\beta]$ with $\beta = 0.51$ and $t_c = 401$ ms. The dotted line indicates the final CODEX exchange intensities. (b) Motional model of the localized, cooperative dynamics in polyphenylene dendrimers, including two-site jumps of all phenyl substituents of a pentaphenyl benzene building block. As indicated by X-ray analysis and computer simulations, the peripheral aromatic rings are inclined by 30° with respect to an axis normal to the face of the central benzene ring. For details, see ref. 44.

between *two* distinct molecular positions or between two distributions of molecular positions.

As to the geometry of the reorientation process, it should be mentioned that the anisotropic chemical-shift tensor of the quaternary carbon atoms C_{quat} is

invariant under a π-flip, which corresponds to the motional process most commonly observed for *para*-substituted phenylene groups. Therefore, a reorientation of 180° would not cause any C_{quat} exchange intensity. The detected C_{quat} CODEX signal proves that the phenyl reorientation angle must differ from 180°. A smaller reorientation angle is then rationalized, realizing that the individual CH groups of the exo-phenyls cannot pass through the plane formed by the central ring as depicted in Fig. 15(b). A mean reorientation angle of about 60° is in accord with further CODEX and 2D static exchange data.[44]

4.5. Axial motion of discs in columnar liquid crystals

A particularly clearcut case of molecular dynamics results from the rotation of discs around the column axis in discotic liquid crystals.[42] This can be studied by both homo- and heteronuclear DQ spectroscopy, as shown by recent studies of hexa-peri-hexabenzocoronene (HBC) derivatives.[38,85] These systems are particularly interesting because of possible photovoltaic applications.[86] Figure 16 presents ^{1}H DQ MAS spinning sidebands of HBC-C_{12}, containing C_{12} alkyl chains, in (i) the crystalline and (ii) the liquid crystal (LC) phases.[38] The aromatic protons are grouped as well-separated pairs, and, thus, an analysis within the spin-pair approximation is appropriate. As is evident from the insets on the right of Fig. 16, the DQ spinning sideband patterns are very sensitive to the strength of

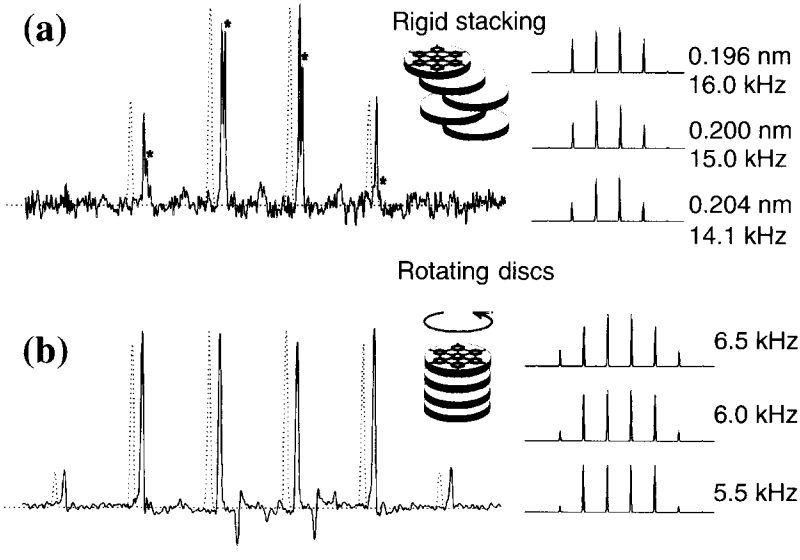

Fig. 16. ^{1}H–^{1}H DQ spinning sideband patterns of discotic HBC-C_{12} in the solid state (top) and in the columnar liquid crystalline phase (bottom), where the discs rotate around the column axis as indicated. For details, see ref. 38.

the dipolar coupling, which can be determined with high accuracy to yield values of (15±0.9) kHz and (6±0.5) kHz in the solid and the LC phases, respectively. The reduction factor due to the axial motion of the discs is thus 0.4, corresponding to an order parameter of 0.8, remembering that, for a completely regular column, the H–H vectors would be at right angles to the column axis and the reduction factor would be 0.5. The reduced order parameter indicates additional out-of-plane motion in addition to the axial rotation. By inserting phenylene rings between the core and the alkyl chains, this out-of-plane motion can be suppressed and the order parameter significantly enhanced. The ease with which this information is obtained with 10 mg of as-synthesized samples made it possible to report such findings together with the synthesis of these new materials.[85]

4.6. Chain order and translational motion in polymer melts

High-resolution DQ MAS NMR also offers new possibilities to probe dynamic processes involving considerably longer length scales. Figure 17 displays the ^{1}H DQ MAS NMR spectrum of 1,4-poly(butadiene) (PB) in the melt. The rapid segmental motion largely averages intra- and intermolecular dipole–dipole

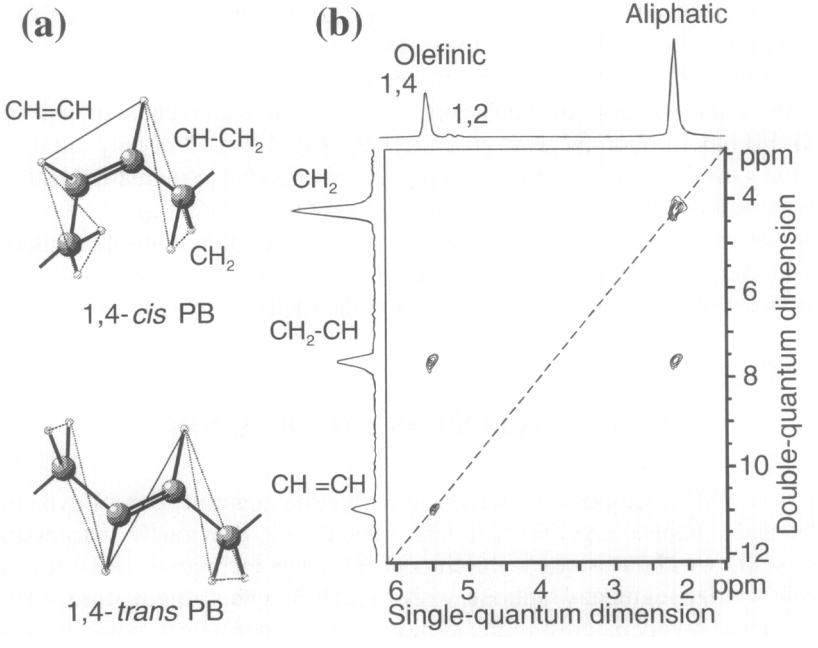

Fig. 17. (a) Spin-pair dipolar couplings in *cis* and *trans* polybutadiene (PB) units. (b) ^{1}H DQ MAS NMR spectrum (500 MHz) of a PB melt well above T_g. For details, see ref. 50.

couplings,[47] such that narrow lines result. Despite this, strong auto- and cross-DQ peaks are observed, from which residual dipole–dipole couplings between the different protons can be determined.[50] They result from the fact that the chain motion in an entangled melt is not completely isotropic on intermediate length scales and timescales. Numerous ways have been designed to probe the resulting dynamic order parameters by NMR.[47,87] ^{1}H DQ MAS NMR is the only method that can clearly distinguish *intra-* and *intergroup* couplings, and therefore determine order parameters for vectors directed *along* the chain, which were found to be considerably higher than anticipated.

In order to quantify our findings, the measured order parameters are analyzed in terms of the celebrated reptation model of chain motion, formulated by De Gennes[48] and Doi and Edwards.[49] As depicted in Fig. 18(a), the reptation model considers single chains subject to spatial restrictions due to entanglements, which are considered to act effectively like a tube through which the selected chain reptates. Four separate length scales and timescales are distinguished. In the different regimes, different scaling laws for the mean-square displacement of chain segment due to *translational* motion are predicted, which also show up in the correlation function $C_R(t)$ probed by the residual dipole–dipole couplings.[50,87] (Fig. 18(b)). Here, the crossover from regime II ($t^{-1/4}$) to regime III ($t^{-1/2}$) is most indicative of reptation. This crossover is indeed observed in polymer melts, as shown for PB in Fig. 18(c),[50] which forces us to conclude that the characteristic length scale for the residual dipole–dipole couplings is indeed the entanglement length as deduced from neutron scattering, i.e. nanometers.[88] Thus, DQ NMR emerges as a simple alternative for probing the chain organization of polymers. Further insight was provided through a recent study[89] where the effect of restricting the chain motion by anchoring one or both chain ends in polystyrene (PS)–PB block copolymers was investigated (Fig. 18(c)). Not only did the chain motion slow down, but the order parameters were found to increase drastically in these systems, where the polymer melt is confined to lamellae of a few tens of nanometers. These observations lead us to conclude that amorphous polymers are, in fact, structured in terms of nanodomains, which is also consistent with new views of polymer crystallization from the melt.[84]

5. CONCLUSIONS AND OUTLOOK

The new NMR methods reviewed here enable the quantification of dynamics in unlabeled complex organic materials, which were previously inaccessible to such studies without isotopic enrichment. The new techniques make it possible to characterize segmental motions, with correlation times ranging from $<10^{-6}$ s to 10 s, quantitatively in terms of the motional amplitude and geometry, the number of orientational sites accessible to the moving segments, and the fraction of mobile segments.

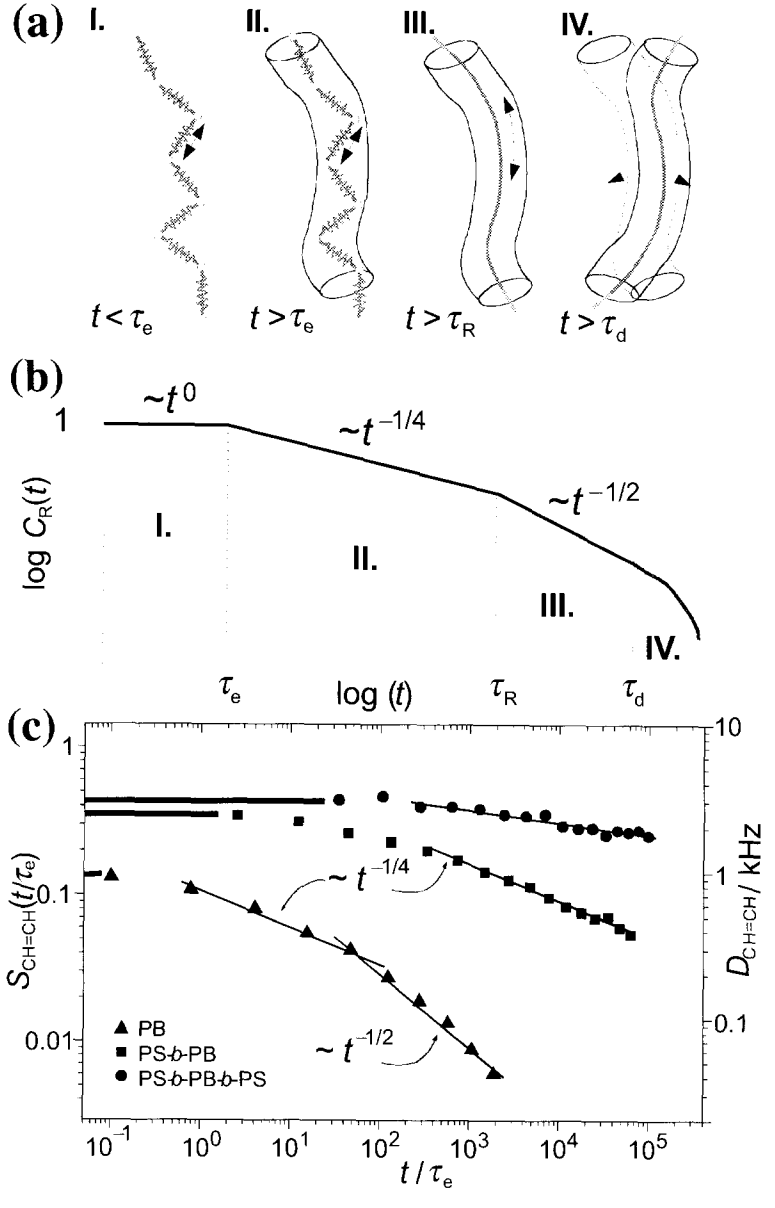

Fig. 18. (a) Illustration of the different dynamic regimes considered in the reptation model. (b) Scaling behavior of the correlation function $C_R(t)$ available through ^{1}H DQ MAS NMR in the different dynamic regimes shown in (a). (c) Experimental dipolar couplings for PB and polystyrene–PB diblock (PS–PB) and triblock (PS–PB–PS) copolymers. For details, see ref. 89.

This progress has been achieved by combining evolution under recoupled anisotropic interactions that probe segmental reorientations, with high-sensitivity MAS detection. Not only does MAS enhance the sensitivity, but it also greatly increases the site resolution, making assignments of motional effects to specific groups unambiguous. Owing to the use of recoupling rather than standard spinning sidebands, the methods discussed here have no upper limit in terms of the spinning speed; in fact, elimination of multispin dipolar couplings at high spinning speeds simplifies the spin systems greatly. This is particularly relevant for ^{1}H DQ experiments; for these, it is very favorable that the proton detection provides the sensitivity necessary for efficient work with the high-speed, small-volume rotors.

For slow motions, exchange NMR methods such as CODEX and the closely related time-reversed ODESSA method, as well as DQ exchange NMR, provide surprisingly high sensitivity to small-amplitude motions. This can be explained in terms of the chemical-shift difference tensor; such an analysis can also be applied to other stimulated-echo methods. Jumps and diffusive motions are directly distinguishable from the effect of mixing time on the recoupling-time dependence of their exchange intensity, which reflects the characteristic changes of the reorientation-angle distributions. The number of orientational sites accessible to the mobile segments and the fraction of mobile units are reflected in the long-time exchange intensity. Owing to the high sensitivity of CODEX and the slow-down of ^{13}C spin diffusion by fast MAS, the upper limit of the correlation range is an order of magnitude higher than in traditional 2D exchange NMR. Fast rotational motions of protonated segments are probed conveniently by C–H DQ sideband patterns, while in polymer melts, the strengths of specific residual proton–proton dipolar couplings are probed by homonuclear DQ spectroscopy.

Taken together, the new NMR methods enable studies of almost any dynamic process in polymers, and promise to contribute significantly to an improved understanding of the relations between chain motions and macroscopic—in particular mechanical—properties of polymer materials.

ACKNOWLEDGEMENTS

Most of the examples presented here were obtained by our research groups within the last three years. K. S. R. gratefully acknowledges productive collaborations with Eduardo R. de Azevedo, Fabio Becker-Guédes, Tito J. Bonagamba, and Weiguo Hu. H. W. S. would like to specifically thank his coworkers, Steven P. Brown, Thilo Dollase, Robert Graf, Andreas Heuer, Kay Saalwächter, Ingo Schnell, and Michael Wind. Last, but not least, the fruitful collaboration with Professor Klaus Müllen and his group is gratefully acknowledged.

REFERENCES

1. K. Schmidt-Rohr and H. W. Spiess, *Multidimensional Solid-State NMR and Polymers*, 1st edn, Academic Press, London, 1994.
2. A. G. Palmer, J. Williams and A. McDermott, *J. Phys. Chem.*, 1996, **100**, 13293.
3. T. M. Connor, B. E. Read and G. Williams, *J. Appl. Chem.*, 1964, **14**, 74.
4. W.-G. Hu and K. Schmidt-Rohr, *Acta Polymer.*, 1999, **50**, 271.
5. V. Andronis and G. Zografi, *Pharm. Res.*, 1998, **15**, 835.
6. D. E. Favre, D. J. Schaefer, S. M. Auerbach and B. F. Chmelka, *Phys. Rev. Lett.*, 1998, **81**, 5852.
7. G. B. McKenna, *Comp. Mater. Sci.*, 1995, **4**, 349.
8. H. W. Spiess, *J. Chem. Phys.*, 1980, **72**, 6755.
9. E. Roessler, *Chem. Phys. Lett.*, 1986, **128**, 330.
10. S. Wefing, S. Kaufmann and H. W. Spiess, *J. Chem. Phys.*, 1988, **89**, 1234.
11. C. Schmidt, S. Wefing, B. Blumich and H. W. Spiess, *Chem. Phys. Lett.*, 1986, **130**, 84.
12. S. Wefing and H. W. Spiess, *J. Chem. Phys.*, 1988, **89**, 1219.
13. K. Schmidt-Rohr, A. S. Kulik, H. W. Beckham, A. Ohlemacher, U. Pawelzik, C. Boeffel and H. W. Spiess, *Macromolecules*, 1994, **27**, 4733.
14. K. Schmidt-Rohr and H. W. Spiess, *Phys. Rev. Lett.*, 1991, **66**, 3020.
15. A. Heuer, M. Wilhelm, H. Zimmermann and H. W. Spiess, *Phys. Rev. Lett.*, 1995, **75**, 2851.
16. U. Tracht, M. Wilhelm, A. Heuer, H. Feng, K. Schmidt-Rohr and H. Spiess, *Phys. Rev. Lett.*, 1998, **81**, 2727.
17. H. W. Spiess, *Annu. Rep. NMR Spectr.*, 1997, **34**, 1.
18. S. A. Reinsberg, X. H. Qiu, M. Wilhelm, H. W. Spiess and M. D. Ediger, *J. Chem. Phys.*, 2001, **114**, 7299.
19. E. R. deAzevedo, W.-G. Hu, T. J. Bonagamba and K. Schmidt-Rohr, *J. Am. Chem. Soc.*, 1999, **121**, 8411.
20. E. R. deAzevedo, W.-G. Hu, T. J. Bonagamba and K. Schmidt-Rohr, *J. Chem. Phys.*, 2000, **112**, 8988.
21. V. Gerardy-Montouillout, C. Malveau, P. Tekely, Z. Olender and Z. Luz, *J. Magn. Reson.*, 1996, **123**, 7.
22. D. Reichert, H. Zimmermann, P. Tekely, R. Poupko and Z. Luz, *J. Magn. Reson.*, 1997, **125**, 245.
23. D. Reichert, G. Hempel, H. Zimmermann, P. Tekely, R. Poupko, Z. Luz, D. E. Favre and B. F. Chmelka, *Appl. Magn. Reson.*, 1999, **17**, 315.
24. T. J. Bonagamba, F. Becker-Guedes, E. R. deAzevedo and K. Schmidt-Rohr, *J. Polymer Sci. B: Phys. Ed.*, 2001, **39**, 2444.
25. E. R. deAzevedo, S. B. Kennedy and M. Hong, *Chem. Phys. Lett.*, 2000, **321**, 43.
26. S. B. Kennedy, E. R. deAzevedo, W. A. Petka, D. A. Tirrell, T. P. Russell and M. Hong, *Macromolecules*, 2001, **34**, 8675.
27. D. Reichert, T. J. Bonagamba and K. Schmidt-Rohr, *J. Magn. Reson.*, 2001, **151**, 129.
28. S.-F. Liu, J.-D. Mao and K. Schmidt-Rohr, *J. Magn. Reson.*, 2002, **155**, 15.
29. H. J. Jakobson, *Encyclopedia of Nuclear Magnetic Resonance*, Vol. 7, D. M. Grant and A. K. Harris (eds), Wiley, Chichester, 1996, 398.
30. M. Munowitz and A. Pines, *Adv. Chem. Phys.*, 1987, **66**, 1.
31. C. Filip, S. Hafner, I. Schnell, D. E. Demco, and H. W. Spiess, *J. Chem. Phys.*, 1999, **110**, 423.
32. I. Schnell and H. W. Spiess, *J. Magn. Reson.*, 2001, **151**, 153.
33. K. Saalwächter and H. W. Spiess, *J. Chem. Phys.*, 2001, **114**, 5707.
34. J. M. Lehn, *Supramolecular Chemistry*, Wiley-VCH, Weinheim, 1996.
35. J. L. Atwood, J. E. D. Davies, D. D. MacNiol and F. Vögtle, eds, *Comprehensive Supramolecular Chemistry*, Elsevier, Oxford, 1996.
36. I. Schnell, S. P. Brown, H. Y. Low, H. Ishida and H. W. Spiess, *J. Am. Chem. Soc.*, 1998, **120**, 11784.
37. S. P. Brown, X. X. Zhu, K. Saalwächter and H. W. Spiess, *J. Am. Chem. Soc.*, 2001, **123**, 4275.

38. S. P. Brown, I. Schnell, J. D. Brand, K. Müllen and H. W. Spiess, *J. Am. Chem. Soc.*, 1999, **121**, 6712.
39. S. P. Brown, T. Schaller, U. P. Seelbach, F. Koziol, C. Ochsenfeld, F.-G. Klärner and H. W. Spiess, *Angew. Chem. Int. Ed. Engl.*, 2001, **40**, 717.
40. L. N. J. Rodriguez, S. D. Paul, C. J. Barrett, L. Reven and H. W. Spiess, *Adv. Mater.*, 2000, **12**, 1934.
41. S. P. Brown and H. W. Spiess, *Chem. Rev.*, 2001, **101**, 4125.
42. D. Demus, J. W. Goodby, G. W. Gray, H. W. Spiess and V. Vill, eds, *Handbook of Liquid Crystals*, Wiley-VCH, Weinheim, 1998.
43. V. Percec, C. Ahn, G. Ungar, D. Yeardley, M. Möller and S. Sheiko, *Nature*, 1998, **319**, 161.
44. M. Wind, U.-M. Wiesler, K. Saalwächter, K. Müllen and H. W. Spiess, *Adv. Mater.*, 2001, **13**, 752.
45. I. Schnell, A. Watts and H. W. Spiess, *J. Magn. Reson.*, 2001, **149**, 90.
46. W.-G. Hu, C. Boeffel and K. Schmidt-Rohr, *Macromolecules*, 1999, **32**, 1611.
47. J. P. Cohen-Addad, *Progr. NMR Spectrosc.*, 1993, **25**, 1.
48. P. G. De Gennes, *J. Chem. Phys.*, 1971, **55**, 572.
49. M. Doi and S. F. Edwards, *The Theory of Polymer Dynamics*, Clarendon Press, Oxford, 1986.
50. R. Graf, A. Heuer and H. W. Spiess, *Phys. Rev. Lett.*, 1998, **80**, 5738.
51. T. Gullion and J. Schaefer, *J. Magn. Reson.*, 1989, **81**, 196.
52. T. Gullion and J. Schaefer, *Adv. Magn. Reson.*, 1989, **13**, 57.
53. S. C. Kuebler, D. J. Schaefer and C. Boeffel, *Macromolecules*, 1997, **30**, 6597.
54. A. Hagemeyer, K. Schmidt-Rohr and H. W. Spiess, *Adv. Magn. Reson.*, 1989, **13**, 85.
55. E. R. deAzevedo, T. J. Bonagamba and K. Schmidt-Rohr, *J. Magn. Reson.*, 2000, **142**, 86.
56. T. Terao, H. Miura and A. Saika, *J. Chem. Phys.*, 1986, **85**, 3816.
57. C. Schmidt, B. Blümich and H. W. Spiess, *J. Magn. Reson.*, 1988, **79**, 269.
58. F. Fujara, S. Wefing and W. F. Kuhs, *J. Chem. Phys.*, 1988, **88**, 6801.
59. W. T. Dixon, *J. Chem. Phys.*, 1982, **77**, 1800.
60. A. Bax, N. M. Szeverenyi and G. E. Maciel, *J. Magn. Reson.*, 1983, **51**, 400.
61. R. Tycko, G. Dabbagh and P. Mirau, *J. Magn. Reson.*, 1989, **85**, 265.
62. O. N. Antzutkin, S. C. Shekar and M. H. Levitt, *J. Magn. Reson. Ser. A*, 1995, **115**, 7.
63. D. W. Alderman, G. McGeorge, J. Z. Hu, R. J. Pugmire and D. M. Grant, *Mol. Phys.*, 1998, **95**, 1113.
64. H. Geen and G. Bodenhausen, *J. Chem. Phys.*, 1992, **97**, 2928.
65. J. Titman, S. Féaux de la Croix and H. W. Spiess, *J. Chem. Phys.*, 1993, **98**, 3816.
66. Z. H. Gan, D. M. Grant and R. R. Ernst, *Chem. Phys. Lett.*, 1996, **254**, 349.
67. J. D. Gross, P. R. Gross and R. G. Griffin, *J. Chem. Phys.*, 1998, **108**, 7286.
68. T. M. de Swiet, M. Tomaselli and A. Pines, *Chem. Phys. Lett.*, 1998, **285**, 59.
69. Y. Ishii and T. Terao, *J. Chem. Phys.*, 1998, **109**, 1366.
70. A. Samoson, in *Encyclopaedia of Nuclear Magnetic Resonance*, Vol. 9, D. M. Grant and R. K. Harris (eds), Wiley, Chichester, 2002.
71. A. Bax, R. Freeman, T. Frankiell and M. H. Levitt, *J. Magn. Reson.*, 1981, **43**, 478.
72. H. Geen, R. Graf, A. S. Heindrichs, B. S. Hickman, I. Schnell, H. W. Spiess and J. J. Titman, *J. Magn. Reson.*, 1999, **125**, 224.
73. J. Gottwald, R. Graf, D. E. Demco and H. W. Spiess, *Chem. Phys. Lett.*, 1995, **243**, 314.
74. R. Graf, D. E. Demco, J. Gottwald, S. Hafner and H. W. Spiess, *J. Chem. Phys.*, 1997, **106**, 885.
75. U. Friedrich, I. Schnell, S. P. Brown, A. Lupulescu, D. E. Demco and H. W. Spiess, *Mol. Phys.*, 1998, **95**, 1209.
76. V. Macho, L. Brombacher and H. W. Spiess, *Appl. Magn. Reson.*, 2001, **20**, 405.
77. C. E. Bronniman, N. M. Szeverenyi and G. E. Maciel, *J. Chem. Phys.*, 1983, **79**, 3694.
78. H. T. Edzes and J. P. C. Bernards, *J. Am. Chem. Soc.*, 1984, **106**, 1515.
79. D. L. VanderHart, *J. Magn. Reson.*, 1987, **72**, 13.
80. B. H. Meier, *Adv. Magn. Opt. Reson.*, 1994, **18**, 1.
81. M. M. Maricq and J. S. Waugh, *J. Chem. Phys.*, 1979, **70**, 3300.

82. J. R. Sachleben, V. Frydman and L. Frydman, *J. Am. Chem. Soc.*, 1996, **118**, 9786.
83. K. Saalwächter and K. Schmidt-Rohr, *J. Magn. Reson.*, 2000, **145**, 161.
84. G. Hauser, J. Schmidtke and G. Strobl, *Macromolecules*, 1998, **31**, 6250.
85. A. Fechtenkötter, K. Saalwächter, M. A. Harbison, K. Müllen and H. W. Spiess, *Angew. Chem. Int. Ed. Engl.*, 1999, **38**, 3039.
86. L. Schmidt-Mende, A. Fechtenkötter, K. Müllen, E. Moons, R. H. Friend and J. D. MacKenzie, *Science*, 2001, **293**, 1119.
87. R. C. Ball, P. T. Callaghan and E. T. Samulski, *J. Chem. Phys.*, 1997, **106**, 7352.
88. D. Richter, *Physica B.*, 2000, **22**, 276–278.
89. T. Dollase, R. Graf, A. Heuer and H. W. Spiess, *Macromolecules*, 2001, **33**, 298.
90. T. M. Duncan, *A Compilation of Chemical Shift Anisotropies*, Farragut, Chicago, 1990.
91. L. A. Belfiore, F. C. Schilling, A. E. Tonelli, A. J. Lovinger and F. A. Bovey, *Macromolecules*, 1984, **17**, 2561.

NMR Spectroscopy of Large Proteins

MAX A. KENIRY[1] and JOHN A. CARVER[2]

[1]*Research School of Chemistry, The Australian National University, Canberra, ACT 0200, Australia*
[2]*Department of Chemistry, University of Wollongong, Wollongong, NSW 2522, Australia*

Traditionally, the major obstacle to using NMR spectroscopy to gain meaningful structural information about proteins of mass greater than around 25 kDa has been the poor quality of spectra. In this chapter, we discuss inherent ways and recent advances in NMR methodology that can be used to circumvent or overcome the problem of poorly resolved spectra. For example, some large proteins have functionally significant regions of inherent flexibility that are observable by NMR spectroscopy. In the case of large proteins with intrinsic paramagnetic centres, e.g. haem proteins, significant structural information

ANNUAL REPORTS ON NMR SPECTROSCOPY
VOLUME 48 ISBN 0-12-505448-3

can be gleaned from the hyperfine shifts of resonances out of the diamagnetic envelope. Examples from both of these situations are presented. Advances in isotopic labelling are described which have increased the upper size limit of proteins to be studied by NMR. Transverse relaxation-optimized spectroscopy (TROSY) is a method that enables the acquisition of quality spectra for large proteins and therefore has the potential to revolutionize the study of these systems. Accordingly, the latest developments in the use of TROSY methods are reviewed. Recent advances are described in the use of partial alignment of proteins to determine residual dipolar couplings as additional input restraints for the structure determination of large proteins. Finally, the use of the latest software packages to assign NMR spectra and calculate and refine protein structures is discussed.

1. INTRODUCTION

Twenty-five years ago, in a review in this series, H. W. E. Rattle quoted a cynical observer who referred to biological NMR as 'the technique with the eternally rosy future'.[1] That rosy future is now upon us, brought about by great advances in instrumentation, technology and theory. It is doubtful that even the most optimistic reader in 1976 could have predicted that the full tertiary structure of proteins of size greater than 20 kDa could be solved by NMR techniques. Yet, the structure determination of proteins of molecular mass less than 20 kDa is becoming routine, and the full tertiary structure of a 44-kDa homotrimer,[2] the experimental model of a 51-kDa homodimer assembled from the NMR structures of the N- and C-terminal domains,[3] and the secondary structure of a 110-kDa protein,[4] have recently been reported. With the mapping of the human genome now complete, these advances in protein NMR technology will gain new importance as the direction of research focuses on the area of structural and functional genomics, e.g. the elucidation of the structure of the many proteins whose function is not known.

The great progress of protein NMR could not have been possible without the introduction of new and powerful techniques and the enhancement of older strategies. The most important of these developments include the following: (i) new techniques for incorporating stable isotopes into proteins; (ii) new and improved pulse sequences that increase the number and quality of restraints for the structure refinement process (TROSY and related techniques have been especially important in this respect, because of the improved resolution of resonances at very high magnetic fields); (iii) the construction of very high-field magnets and advances in probe design that have so dramatically improved sensitivity and resolution; (iv) the introduction of new technologies such as the partial alignment of proteins in bicelle and phage solutions and the use of long-neglected cross-correlation effects that have led to new classes of restraints for structure refinement; and (v) the increase in the number of atoms and restraints have required the development of better and more powerful software which, in

turn, has closely followed the explosive development of new computer hardware.

There are three major problems that beset the analysis of spectra of large proteins (i.e. ≥20 kDa in mass): increased linewidths due to more efficient transverse relaxation, spectral crowding due to large numbers of resonances, and poor signal-to-noise ratios. All these problems lead to fewer numbers of experimental restraints and less accurate structures. There have been several recent specialist articles that have reviewed strategies for overcoming these limitations, including approaches to labelling with stable isotopes,[5,6] new pulse sequences[7] and methods for obtaining additional restraints for the refinement process.[8–10] The intent of this chapter is to give an overview of all the major developments, with a focus on recent work.

2. HISTORICAL PERSPECTIVE

In 1976, at the time of Rattle's review, there was great emphasis on proteins with a large spectral dispersion created by the presence of paramagnetic ions or spin labels, in part because of the one-dimensional NMR techniques used and the low magnetic fields available at that time. There was a prevailing view that distance and orientation information from the chemical shifts and resonance line broadening induced by the paramagnetic metals or spin labels could be used to gain structural information in limited parts of the protein.[1] In fact, it has taken nearly 20 years for the full potential of the technique to be realized in the structure determination of a drug–DNA complex[11] and a number of proteins.[12–16] Towards the end of the 1970s, there were developments in two-dimensional NMR[17–19] and computational techniques such as distance geometry[20,21] and restrained molecular dynamics[22,23] which led to the structure determination of proteins up to 100 residues in size.

By the mid-1980s, despite the introduction of higher magnetic fields and further pulse sequence developments, the limitations of the homonuclear techniques were obvious. High protein concentrations, extensive overlap of ^{1}H resonances and the increase in linewidth of the resonances with protein size restricted the study of proteins greater than 10 kDa in mass to a handful of suitable candidates. New methods were developed to incorporate ^{15}N and ^{13}C isotope labels into proteins, and new pulse sequences were devised to separate the ^{1}H resonances into two, three and four dimensions according to the chemical shift of the directly bonded isotope label (for reviews see refs 24, 25 and 26). As well as providing more ^{1}H–^{1}H distance restraints, these new techniques permitted the introduction of new angular restraints from J coupling constants (for reviews see refs 27 and 28) and ^{13}C chemical shifts,[29] provided new methods for making stereospecific assignments (for a review see ref. 27) and overcame the major limitations of the through-space strategies for sequential assignment via nuclear Overhauser enhancements (NOEs) from homonuclear spectra by

making it possible to assign the backbone nuclei using through-bond correlations. The practical limit for these techniques for most fully protonated proteins is around 25 kDa in mass because of the decrease in sensitivity of many crucial NMR experiments caused by short transverse relaxation times.

In the past decade, there has been further progress towards pushing the boundaries of protein structure determination beyond this mass regime. Many of these new or improved technologies are reviewed below. They include improved techniques for fractional and complete deuteration of proteins, which ameliorates the fast ^{1}H–^{1}H dipolar spin relaxation in fully protonated proteins, advances in cell-free protein synthesis and segmental isotope labelling technologies, the exploitation of cross-correlation between the dipole–dipole (DD) interaction and chemical shift anisotropy (CSA) to narrow linewidths in multidimensional spectra, the introduction of new restraints from residual dipolar couplings, cross-correlation effects and paramagnetic interactions and advances in the automated assignment of heteronuclear protein spectra. In this chapter, we also discuss NMR applications that probe regions of internal flexibility in large proteins and applications that utilize intrinsic or extrinsic paramagnetic centres for protein structure determination.

3. ADVANCES IN ISOTOPE LABELLING TECHNIQUES

New developments in isotope labelling strategies for large proteins have recently been reviewed in excellent articles.[5,30,31] This section of the chapter is necessarily short, because we do not wish to traverse in detail these reviews but rather refer the reader to these articles for a more in-depth discussion of isotope labelling and assignment strategies.

Assignment strategies employing double labelling with ^{15}N and ^{13}C are limited to proteins with molecular masses below 25 kDa, because increasingly efficient relaxation pathways lead to lower sensitivity and resolution in high-molecular-weight proteins. TROSY experiments (see above) can, to some extent, overcome the resolution problem, but the efficient ^{1}H–^{1}H and ^{1}H–^{13}C dipolar relaxation in slowly tumbling, large proteins makes many of the standard three-dimensional (3D) and four-dimensional (4D) pulse sequences ineffective as relaxation times start to approach the length of delay times within these pulse sequences. Random uniform deuteration is a popular strategy for attenuating the ^{1}H–^{13}C and ^{1}H–^{1}H relaxation mechanisms, but at the expense of reducing the number of ^{1}H–^{1}H NOEs available for structure refinement. Of course, it is always possible to retrieve some of these ^{1}H–^{1}H NOEs by reinvestigating the fully protonated sample after the backbone assignments have been made with the deuterated protein, but this strategy is not viable for very large proteins (>30 kDa in mass). Several strategies have been devised to reintroduce a subset of protons into proteins with the aim of increasing the number of long-range NOEs crucial to improving the precision of the structure. Giesen *et al.*[32] have devised a cost-

effective means of introducing 50% $^{2}H,^{13}C,^{15}N$-labelled amino acids into proteins, and demonstrated the efficacy of the technique by obtaining residual dipolar couplings with high sensitivity and resolution. Kay and coworkers have devised a strategy where protonated methyl groups of leucine, valine and isoleucine are reintroduced into the protein by supplementing the deuterated media with [^{13}C] pyruvate[33] or [3-$^{2}H,^{13}C$]α-ketoisovalerate and [3,3-$^{2}H^{13}C$]α-ketobutyrate.[34] The selectivity of this strategy and the resolution of the methyl resonances are seen in the ^{1}H–^{13}C constant-time heteronuclear single quantum correlation (CT-HSQC) spectrum of maltose binding protein in Fig. 1. Methyl-methyl NOEs are then used in conjunction with backbone NOEs, dihedral angles and residual dipolar couplings to help fold the protein in the refinement process. The methyl region in large proteins is nevertheless very crowded, with extensive overlap of different types of methyl-containing amino acid residues. Atreya and

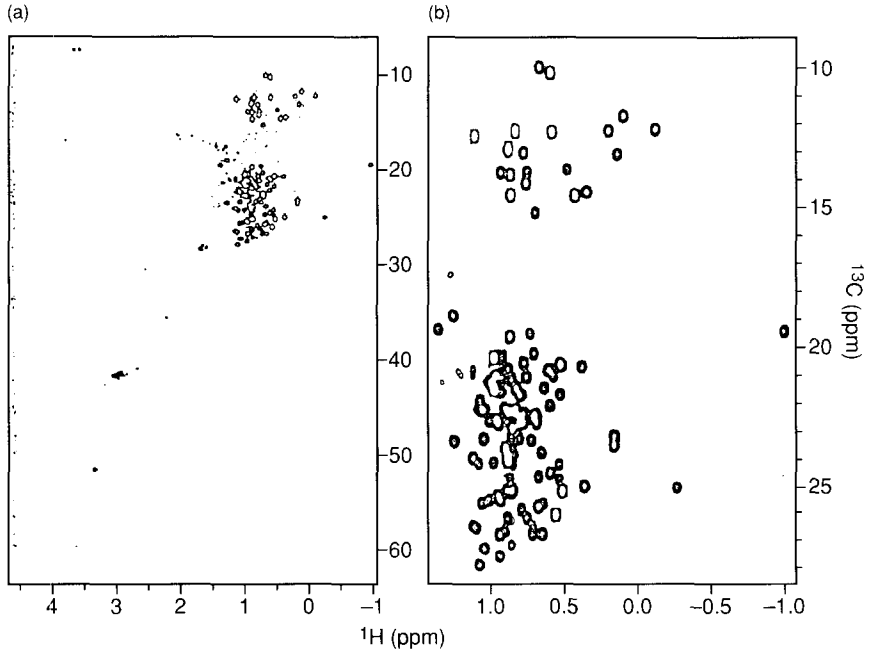

Fig. 1. ^{1}H–^{13}C CT-HSQC spectrum of a sample of 1.5 mM Val, Leu, Ile ($\delta 1$) methyl-protonated maltose-binding protein (MBP), 2 mM β-cyclodextrin, 20 mM sodium phosphate (pH 7.2), 3 mM NaN_3, 200 μM EDTA, 0. 1 mg/ml Pefabloc, 1 μg/μl pepstatin and 10% D_2O recorded at 37°C, on a Varian Unity+ 500-MHz spectrometer. Acquisition times of 28 and 64 ms were employed (t_1, t_2) along with a relaxation delay of 1.5 s, for a total measuring time of 3 h. (a) Aliphatic region of the ^{1}H–^{13}C correlation map of MBP, illustrating the selectivity of labelling. Small amounts of residual protonation are observed at the C_γ positions of a number of Pro/Arg residues, the C_β positions of Asp and Ser (aliased) residues, and the $C_\gamma 2$ methyl positions of Ile. In all cases, intensities of these cross-peaks are less than 10% of the methyl peaks. (b) Methyl region of the ^{1}H–^{13}C HSQC. Reproduced with permission from Kluwer Academic Publishers Goto *et al.*[34]

Chary[35] have shown that this region can be simplified by adding unlabelled amino acids to an otherwise ^{13}C-labelled medium. They further showed that this 'unlabelling' procedure can be used to assist in the stereospecific assignment of leucine and valine methyl groups. In a technique aimed at obtaining accurate methyl relaxation values, Ishima *et al.*[36] demonstrated that $^{13}CH_3$ methyl isotopomer contamination of $^{13}CD_2$ isotopomers could be substantially diminished by using media enriched in partially deuterated [3-^{13}C] pyruvic acid and partially deuterated [4-^{13}C] 2-ketobutyric acid. Most methyl groups are found in the hydrophobic core, so these procedures improve the quality of the structures,[37,38] but more information such as NOEs from aromatic amino acids and structural restraints from residual dipolar couplings are required for high-precision structures. Fesik and coworkers[39] have shown that inclusion of protonated phenylalanine and tyrosine in addition to protonated methyl groups substantially improves the quality of protein structures compared to the original strategy of Kay and coworkers.[33,34] There are other 'reverse isotope' strategies that are discussed at length by Goto and Kay.[5]

Other techniques are aimed at reducing the number of residues under investigation without reducing the size of the protein. One such method is labelling a protein made up of non-equivalent subunits, and then dissociating the subunits and reassembling the protein with only one of the subunits labelled with ^{13}C and ^{15}N. One such recent example of this strategy is the study of the α and β subunits of haemoglobin, where assignments of histidine and tryptophan residues were completed.[40] A parallel strategy can be followed in single-chain proteins by using chemical or trans-splicing techniques to ligate specific segments, labelled with stable isotopes, to unlabelled segments in large proteins.[5,41–45]

Most labelled proteins are grown in minimal medium supplemented with $^{15}NH_4Cl$, [^{13}C]glucose and D_2O. Sometimes, enriched algal or microbial hydrolysates are used as the isotope source. These strategies require large quantities of stable isotopes, and thus some effort has been expended on developing methods for labelling proteins that use the minimum amount of stable isotopes. Cai *et al.*[46] have demonstrated that growing the cell mass in unlabelled medium and then inducing protein expression in isotope-enriched minimal medium increases the amount of protein recovered without adversely affecting the incorporation rate of isotope label into the protein. Marley *et al.*[47] have improved on this procedure by growing to high cell density in unlabelled medium, and then exchanging into isotope-enriched minimal medium at higher cell density.

Another approach to inexpensive labelling of proteins is by means of cell-free protein synthesis.[48–50] These *in vitro* expression systems use a crude *Escherichia coli* fraction as a source of ribosomes and other factors necessary for the synthesis of proteins, T7 RNA polymerase for transcription, and dialysis to maintain levels of amino acids and nucleotides. In principle, the technology is capable of labelling proteins at specific sites without isotope scrambling and also of producing labelled proteins from small volumes of labelled medium.

Although much work needs to be done to improve the efficiency of the technique, it does show enormous potential for improving the efficiency and cost-effectiveness of isotope labelling for NMR experiments.

4. THE FLEXIBLE REGIONS OF LARGE PROTEINS

4.1. General

As discussed in Section 1, obtaining meaningful NMR spectra of proteins above a molecular mass of around 20 kDa is problematic for a variety of reasons, primarily because molecules of this mass tumble relatively slowly and have long correlation times. They therefore have short transverse relaxation times (T_2) and broad resonances result. By way of an example, using the Stokes–Einstein relationship, a spherical protein of 40 kDa in mass would have a correlation time, τ_c, of ~10^{-8} s and ^{1}H NMR linewidths around 50 Hz. However, in some proteins, due to local internal motions, not all amino acids will have the same correlation time as the overall protein. If this motion is enhanced compared to that for the overall protein, this region or regions will have shorter correlation time(s) than the bulk of the protein; that is, they will exhibit enhanced flexibility. If this flexibility is sufficiently rapid (i.e. τ_c values of 10^{-9} to 10^{-10} s), its motion can put it into the regime that gives rise to sufficiently narrow resonances (^{1}H linewidths of 5–20 Hz) to be observable by NMR spectroscopy.

Motion of a polypeptide implies that this region adopts a miscellany of conformational states and is therefore lacking in secondary structure. There is growing interest in these types of regions, with the realization that flexible regions in proteins are commonplace and are involved in a diversity of functional roles, e.g. in binding site recognition. Furthermore, it is becoming increasingly apparent that the partly folded or unfolded state is a common entity in proteins and that this state has functional and disease relevance, e.g. in the development of amyloid diseases such as Alzheimer's and Creutzfeldt–Jakob diseases.[51] Because these regions are mobile, even in the crystalline state, they are not resolved in electron density maps during X-ray crystal structure analysis. Thus, solution-phase NMR spectroscopy offers the only viable method to study flexible regions in proteins.

In this section, NMR spectroscopic characterization of flexible regions in large proteins is discussed. As is apparent from this discussion, flexibility in such proteins encompasses a diversity of proteins of varying function.

4.2. Applications

Urokinase or urokinase-type plasminogen activator is a multi-domain fibrolytic enzyme that activates plasminogen and is involved in tissue degradation, e.g. in

the breakdown of blood clots. It is a 46-kDa protein, which, *in vivo*, is significantly glycosylated, such that its mass is increased to around 54 kDa.[52–54] The protein is composed of three domains: an N-terminal epidermal growth factor (EGF) domain, a kringle domain, and a C-terminal serine protease domain. Despite its relatively large size, a well-resolved and dispersed ^{1}H NMR spectrum of urokinase was obtained. Some of the resonances in the spectrum were assigned, via 2D ^{1}H NMR techniques of the intact protein and proteolytically cleaved products, to, in the main, the kringle and protease domains. The implication from these experiments is that these two domains are structured but have extensive flexibility and motion, that is, the binding (EGF) and recognition (kringle) domains are relatively independent of the protease domain. A related protein, plasminogen, has similar NMR spectral properties to urokinase, in that its kringle domain is structured and has inherent mobility compared to the protease domain.[55]

Bushuev *et al.*[56] observed extensive flexibility in the dimeric L7/L12 protein from *E. coli* bacterial ribosomes (mass ~25 kDa). In this case, however, the protein has folded N- and C-terminal domains with an unstructured flexible linker in between, encompassing residues 37–50. The flexibility of this region of the protein is believed to be important for its function, to enable efficient interaction with other components of the ribosome machinery.

Ribonucleotide reductase consists of two different subunits, R1 and R2, that must be associated for enzymic activity. R1 and R2 have masses of around 180 and 90 kDa, respectively. 2D ^{1}H NMR spectroscopy of the R2 subunit revealed that it has a highly mobile and unstructured C-terminal extension encompassing the last 25 amino acids of the protein.[57] In the presence of the R1 subunit, however, this flexibility was lost, presumably because the extension facilitates the recognition and interaction between the two subunits. In agreement with the NMR results, mutagenesis studies showed that this C-terminal extension is crucially important in R1 and R2 interaction.[58]

Perham and coworkers undertook a series of NMR studies of large lipoic acid-containing enzymes and their fragments. For example, the *E. coli* pyruvate dehydrogenase multi-enzyme complex (mass $\sim 5 \times 10^6$ Da) has alanine–proline rich polypeptide regions of 20–30 amino acids in length that link the lipoyl and other domains in the dihydrolipoyl acetyltransferase component. NMR studies of the complex, and peptide fragments corresponding to these regions, revealed that the linkers are highly mobile in the enzyme complex, with ^{1}H resonance linewidths of ~10 Hz. This linker region is also partly structured.[59,60] The results of this work and work on enzymes that also have flexible linkers between their domains are well described in previous and recent reviews.[61,62] The latter review also describes NMR solution structure determination of the structures of various domains of these enzymes.

One of us (J.C.) has undertaken a systematic NMR study of eye lens crystallin proteins. Much of this work has been summarized in two recent review articles[63,64] and will not be repeated here. Suffice to say that the mammalian

crystallin proteins consist of three groups of proteins: α, β and γ. The β- and γ-crystallins are structurally related to each other. In humans, there are seven β-crystallin subunits and six γ-crystallin subunits. They are well-ordered proteins and are composed of two-domain subunits, with each subunit containing two β-sheet motifs. The β-crystallins are aggregates consisting of dimers through to octomers, encompassing a mass range from ~50 to 200 kDa, whereas the γ-crystallins are monomers of mass ~20 kDa. Crystal structures are available for representative members of the β- and γ-crystallins.[65] Apart from their different aggregation states, the significant difference between the two types of crystallins is the presence of terminal extensions from the domain core of the β-crystallins, which are not present, to any significant extent, in the γ-crystallins. In the bovine β-crystallins, the extensions vary in length from 11 amino acids (the C-terminal extension in βB2-crystallin) to 57 amino acids (the N-terminal extension in βB1-crystallin). The X-ray crystal structure of the major β-crystallin subunit, βB2, does not reveal electron density for the majority of the N- and C-terminal extensions, implying that these regions have conformational flexibility. Indeed, NMR studies of βB2-crystallin and other β-crystallin subunits[63] show that these regions give rise to well-resolved spectra, which can be assigned via conventional means. The extensions adopt little, if no, ordered structure and have great flexibility compared to the domain core of the β-crystallin subunits, which, themselves (as expected because of the size of these proteins), give rise to very few resolved resonances in the 1D and 2D ^{1}H NMR spectra.

The roles of the extensions in β-crystallin subunit structure and function are matters of debate. It would seem, however, that they are involved in regulating interactions between the β-crystallin subunits and their interactions with the α- and γ-crystallin subunits. As the concentration of proteins within the lens is very high, these interactions are of great importance in ensuring crystallin protein solubility and hence the maintenance of lens transparency. However, the specifics of which β-crystallin subunits interact with each other, and the role of the extensions in this process, are not known, and extensive NMR analysis is required to elucidate the hierarchy of subunit interactions. Furthermore, the extensions in the β-crystallin subunits undergo extensive post-translational modification, especially proteolysis, and these age-related changes alter the electrostatic interactions between the subunits.

By contrast, the six monomeric γ-crystallin subunits do not have long flexible regions at their termini. Five γ-crystallin subunits have a relatively conserved hydrophobic two-residue extension at their C-terminus (Phe–Tyr in γB-crystallin) that is readily observed in the ^{1}H NMR spectrum and is most likely involved in hydrophobic interactions with the other crystallin classes.[63,64] The γS-crystallin subunit lacks these two C-terminal residues but instead has a four-residue flexible extension at its N-terminus that does not interact with the other crystallin classes to the extent of the C-terminal region in the other γ-crystallin subunits.[63,64] As with the β-crystallin subunits, the functional roles of the γ-crystallin subunits and their short extensions in crystallin–crystallin interactions are not fully understood.

The major mammalian crystallin protein class is α-crystallin. α-Crystallin is not related to the β- or γ-crystallins, and its crystal structure is not known. It comprises two closely related subunits, A and B, each of mass around 20 kDa, but forms heterogeneous aggregates ranging from 300 to 1000 kDa. Despite its very large size, α-crystallin gives rise to a well-resolved ^{1}H NMR spectrum that originates from a 10–12 amino acid region of marked flexibility and no ordered structure at the C-termini of both subunits.[63,64] Figure 2 shows a HSQC spectrum of ^{15}N-labelled αB-crystallin in which the 12 cross-peaks arise from these H^N to H^α correlations of the C-terminal extension (T. M. Treweek and J. A. Carver, unpublished observations).

α-Crystallin is a member of the small heat-shock protein (sHSP) family of molecular chaperones. Chaperones form a class of proteins that interact with partly folded proteins to prevent their mutual (illicit) association, aggregation and potential precipitation. They are involved in a diversity of tasks including protein folding, trafficking and general stabilization. sHSPs fall into the latter class of molecular chaperones, and their expression is upregulated significantly under stress conditions, e.g. elevated temperature and infection, which lead to protein aggregation and precipitation. sHSPs are found in all organisms. Other

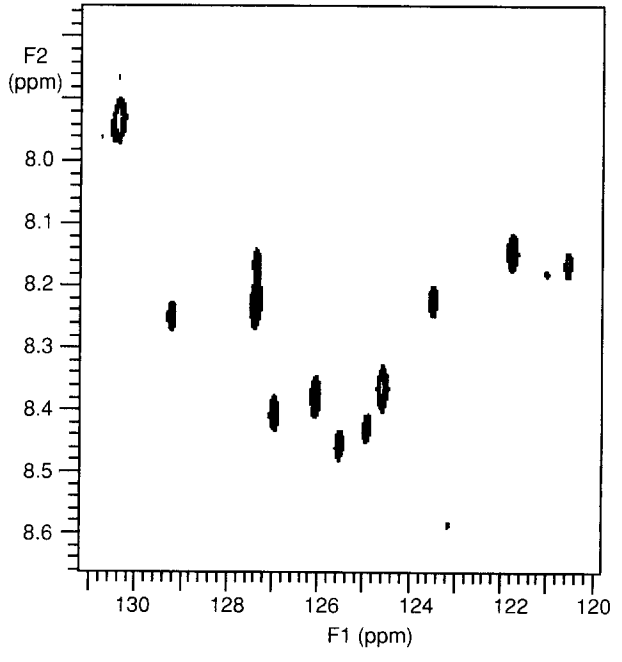

Fig. 2. ^{1}H–^{15}N HSQC spectrum of ^{15}N-labelled αB-crystallin (of total molecular mass ~650 kDa, 1 mM in 50 mM phosphate buffer, pH 7.2). Data were acquired at 25°C on a Varian INOVA-500 NMR spectrometer. Cross-peaks are observed for the highly mobile C-terminal extension encompassing the last 12 amino acids of the protein.

mammalian sHSPs also have C-terminal extensions of varying length and composition.[63,64] The common characteristic of these extensions is that they are relatively polar. It is proposed that this polarity imparts solubility to the relatively hydrophobic sHSPs and the complexes that they form with partly folded proteins under stress conditions.[63,64]

In addition to flexibility being present at the C-terminus of sHSPs, other molecular chaperones exhibit amino acid regions of marked flexibility. For example, *E. coli* GroES is the co-chaperone of the molecular chaperone GroEL, a large, cage-like, cylindrical structure that encases some partly structured proteins during protein synthesis to enable them to fold correctly. GroES forms a cap on both ends of the GroEL aggregate to cover its cavity. It is composed of seven identical subunits, each of mass ~10 kDa, arranged in a disk. ^{1}H NMR spectroscopy of the GroES aggregate reveals a highly mobile and surface-exposed loop, encompassing residues 17–32 of the protein, with a τ_c of ~1 ns.[66] Flexibility of the mobile loop is lost upon complex formation with GroEL, implying that this region is involved in the recognition between GroEL and GroES. The crystal structure of the GroES aggregate shows that the mobile loop is disordered but adopts a fixed conformation in the complex with GroEL.[67] The loop is proposed to be involved in regulating the interaction between the two proteins.

E. coli SecB is a molecular chaperone that is involved in mediating protein export across the inner membrane of the bacterium. SecB binds to newly synthesized proteins that are in a partly folded conformation and transports them to membrane-bound SecA prior to their translocation. In doing so, SecB prevents its bound proteins from aggregating or folding. The subunit mass of SecB is ~16 kDa, but it exists as a tetramer. 2D ^{1}H NMR spectroscopy of SecB enabled the localization of a highly flexible C-terminal extension encompassing the last 13 amino acids of the protein.[68] A mutant of SecB lacking this region still bound a partly structured protein, but, *in vivo*, this mutant was not capable of efficient protein export. It would seem, therefore, that the mobile C-terminal extension in SecB is involved in regulating the interaction between SecB and SecA, possibly by preventing them from associating too intimately.

Enhanced flexibility is also observed for large, relatively unstructured regions of some proteins. For example, the murine prion protein, *m*PrP(23–231), has a well-structured, mainly α-helical C-terminal region comprising the last 110 amino acids, while the remainder of the protein (98 amino acids) is unstructured.[69] Quantification of this difference was obtained via the measurement of heteronuclear ^{15}N{^{1}H} NOEs for the protein. In the unstructured N-terminal region, large negative NOEs were observed that were indicative of significant flexibility, i.e. arising from regions with τ_c values <1 ns. On the other hand, the structured C-terminal region had positive NOEs, implying τ_c values $\geq$ 1 ns, typical values for small globular proteins.[69] Thus, the motions of these two regions of *m*PrP(23–231) are essentially independent of each other. The conversion of this protein from α-helical to β-sheet in the C-terminal region is

accompanied by the formation of plaques (protein aggregates) in prion diseases such as Creutzfeldt–Jakob disease and scrapie. The presence of a large, unstructured N-terminal region in *m*PrP(23–231) may facilitate or regulate the transition between the two forms.

In a similar set of experiments, the structure and dynamics of the N-terminal domains of two yeast N-terminal transcriptional activation domains of the heat-shock factor (HSF) protein were investigated by NMR spectroscopy. HSFs regulate the transcription of HSPs when cells are exposed to stresses such as elevated temperature. Measurement of $^{15}N\{^1H\}$ NOEs for these domains when coupled to their adjacent, structured DNA-binding domains showed that they have negative values, i.e. in the regime expected for unstructured polypeptide regions.[70] In contrast, the DNA-binding domain resonances had positive $^{15}N\{^1H\}$ NOE values, as expected for a structured region. It is proposed that this unstructured activation domain acts as a 'lasso' to facilitate interaction with the various factors necessary to form the transcriptional complex.

As a variant of the studies discussed above, Lecroisey *et al.*[71] undertook an NMR study of the 11 amino acid C3 epitope from poliovirus VP1 following its insertion at eight different sites into maltose-binding protein (MBP) (mass ~41 kDa). The insertion of this epitope at the various sites did not cause significant structural changes to the protein so as to affect its ability to function normally and bind maltose. From ^1H NMR studies of these mutants, it was found that the epitope had significant conformational flexibility and that the mobility was maintained regardless of where it was placed into the protein.[71] Consistent with this mobility, the epitope adopted no ordered conformation in any of the mutants.

5. TRANSVERSE RELAXATION-OPTIMISED PULSE SEQUENCES

5.1. General

The exploitation of cross-correlation effects in high magnetic fields has introduced a new form of NMR spectroscopy called 'transverse relaxation-optimised spectroscopy' or TROSY. The cross-correlation of the optimised dipole-dipole (DD) and chemical shift anisotropy (CSA) relaxation mechanisms leads to differential transverse relaxation rates for the two components of the ^{15}N-^1H doublet in undecoupled spectra of ^{15}N-labelled proteins. For one component, DD and CSA relaxation constructively add to produce very efficient relaxation, leading to a broad line, whereas for the other component, the two relaxation mechanisms constructively interfere, leading to a narrow line when the two mechanisms are nearly equal. There is no optimum field where DD and CSA relaxation are equal for all amide bonds, because DD relaxation between the amide protons and other nearby protons differs for each residue.[72] Clearly, the overall effectiveness of TROSY is optimized when the non-exchangeable protons in the macromolecule

are fully or fractionally deuterated. In either case, the optimum benefits of the TROSY effect are seen at proton resonance frequencies in the range ~900–1100 MHz,[73] and substantial benefits can be observed as low as 600 MHz, which can be seen in a comparison of the ^{15}N-HSQC and TROSY spectra of the 30-kDa complex of the ^{15}N,^{13}C-labelled θ subunit and the unlabelled N-terminal domain ε(1–185) subunit of DNA polymerase III (Fig. 3).

TROSY uses phase cycling or pulsed-field gradient coherence selection to selectively cancel the broad lines of the ^{1}H–^{15}N multiplet, leaving only the narrowest component of the multiplet. Experimentally, the narrow line is preserved by not decoupling in F1 or F2 and by using phase cycling or pulsed-field gradient techniques to remove the broad components of the ^{1}H–^{15}N multiplet. A full mathematical treatment of the TROSY effect is beyond the scope of this chapter; the reader is referred to an excellent review by Pervushin[73] for an in-depth discussion of TROSY. Below, we discuss some of the applications of TROSY, except for its use in measuring J and dipolar coupling constants, which are discussed in Section 6.

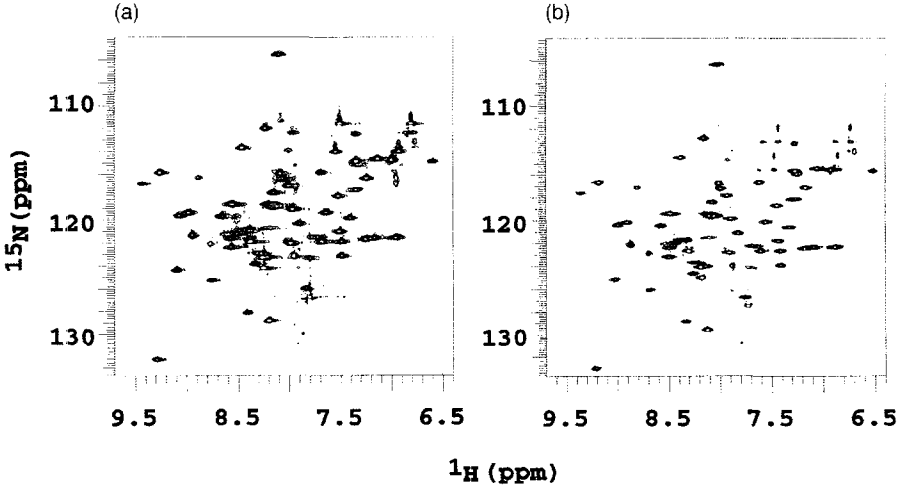

Fig. 3. A comparison of a ^{15}N-HSQC experiment (a) and a TROSY experiment (b) on the 30-kDa complex of the ^{15}N,^{13}C-θ subunit and the unlabelled N-terminal domain ε(1–185) subunit of DNA polymerase III. The spectra were recorded on a Varian INOVA 600 spectrometer operating at a ^{1}H frequency of 600 MHz. Spectra were acquired with 96 (t_1)×1024 (t_2) complex points and processed using VNMR software.

5.2. TROSY pulse sequences

5.2.1. Sensitivity enhancement and artefact elimination

There have been many enhancements of the original TROSY pulse sequence,[74] and even more applications that use TROSY as a building block in multi-

dimensional NMR experiments. Several sensitivity- and gradient-enhanced versions of TROSY soon appeared in the literature[75–78] following the first implementation of TROSY.[74] Pervushin *et al.*[78] introduced a single-transition to single-transition polarization transfer element (ST2-PT) into TROSY that afforded a $\sqrt{2}$ sensitivity enhancement over the original TROSY pulse sequence.[74] Rance *et al.*[77] identified the source of artefacts in TROSY spectra as relaxation-induced imbalance between the coherence transfer pathways utilized in the TROSY refocusing period. These artefacts can be suppressed by using a modified TROSY pulse sequence[79] or by shortening the second coherence transfer delay.[80] Further signal enhancement in TROSY experiments could be achieved by rotating water magnetization back to the equilibrium position prior to acquisition.[79] Similar schemes were used by Zhu *et al.*[81] to create sensitivity-enhanced and gradient-enhanced versions of TROSY with water flipback. Riek[82] has shown that judicious manipulation of the steady-state magnetization in the recycle delay can lead to sensitivity enhancements of some cross-peaks by up to 25%. Further efficiencies can be achieved in TROSY experiments by the simultaneous detection of ^{1}H–^{15}N, aromatic ^{1}H–^{13}C and side-chain $^{1}H_2$–^{15}N correlations in the same experiment.[83] The most obvious application of this strategy is in 3D and 4D NOESY (two-dimensional Overhauser exchange spectroscopy) experiments, which require several days of accumulation time.[83]

Rapid transverse relaxation within the INEPT (insensitive nuclei enhanced by polarization transfer) polarization transfer elements in TROSY becomes a limitation of the TROSY technique for very large proteins (>100 kDa). Riek *et al.*[84] have shown that a new experiment that combines INEPT with cross-correlated relaxation-induced polarization transfer (CRIPT) to produce a new experiment, CRINEPT, is optimum for proteins with correlation times in the range 50–300 ns. The CRINEPT experiment offers new possibilities for studying segmentally labelled fragments of proteins or nucleic acids within much larger macromolecular structures.

5.2.2. NOE experiments

The above-mentioned TROSY pulse elements have been included in a number of multidimensional pulse sequences, with interesting results. The obvious advantages are better resolution and greater sensitivity for larger proteins in high magnetic fields, but the suppression of diagonal peaks is also possible in TROSY-based pulse sequences. Several 2D and 3D NOESY experiments with TROSY elements have been described. Zhu *et al.*[85] and Meissner and Sørensen[86] have incorporated spin-state selective pulses into 2D and 3D TROSY-enhanced NOESY experiments, resulting in better resolution of cross-peaks in all dimensions and suppression of the diagonal in the amide region. However, lower sensitivity compared to normal NOESY-HSQC experiments was reported.[85] Xia *et al.*[87] have also constructed 3D and 4D TROSY versions of the $^{15}N/^{15}N$-separated HSQC-NOESY-HSQC experiment. Recently, a zero quantum 3D

TROSY–NOESY experiment was devised to optimize linewidths in three dimensions and to suppress diagonal peak resonances.[88]

5.2.3. Backbone assignments using TROSY

Both resolution and sensitivity are important considerations in developing pulse sequences for large proteins. Hence, much effort has been expended in incorporating TROSY elements into the most sensitive multidimensional experiments. A version of a constant-time 3D TROSY-HNCA, optimized for highly deuterated proteins, has been applied to the 110-kDa protein 7,8-dihydroneopterin (DHNA).[89] The experiment employs an ST2-PT pulse element to create the TROSY effect, and a constant-time carbon evolution time to prevent evolution of C^{α}–C^{β} homonuclear couplings. The dramatic improvement in resolution (Fig. 4) enabled most of the backbone of this very large protein to be traced with this experiment.[4] 3D TROSY-HN(CO)CA and 3D TROSY-HNCACB have also been developed by the same group[90] and applied with some success to DHNA.[4] Using a different approach, Meissner and Sørensen have developed 'sequential' HNCACB and CBCANH experiments.[91] The new experiments suppress coherence transfer between $^{13}C^{\alpha}$ and ^{15}N via the one-bond ^{15}N–$^{13}C^{\alpha}$ coupling, resulting in only sequential correlations being observed. A similar strategy was used to devise a 'sequential' TROSY-HNCA experiment. Permi and Annila[92] have used an alternative strategy in developing an MP-CT-HNCA experiment that distinguishes sequential from intraresidue cross-peaks in ^{13}C,^{15}N-labelled proteins. The intraresidue and sequential cross-peaks are distinguished from each other via the differing multiplet structure in the subspectra. These three experiments preclude the need to record HN(CO)CA or HN(CO)CACB experiments, which are not sensitive for very large proteins in high magnetic fields. Eletsky *et al.*[93] have proposed a new method of ^{1}H broadband decoupling in TROSY NMR suitable for partially deuterated or protonated proteins which retains the TROSY effect for ^{1}H–^{15}N cross-peaks but uniformly refocuses $^{1}J_{CH}$ scalar coupling. The technique was demonstrated in HNCA and HNCACB experiments on a 44-kDa partially deuterated protein. Incorporation of TROSY elements into 4D experiments also delivers increased resolution in the spectra of large proteins. Kay and coworkers[94] have developed a 4D $HNCO_{i-1}CA$ experiment that correlates intraresidue $^{1}H^{N}$,^{15}N,$^{13}C^{\alpha}$ chemical shifts with the $^{13}C'$ shift of the previous residue. The presence of a proline in an amino acid sequence frequently presents a barrier to the sequential assignment process. Löhr *et al.*[95] have devised two variants of an HN(CA)N experiment that correlate the backbone ^{1}H and ^{15}N chemical shifts with the ^{15}N chemical shifts of the preceding and following residues, thus providing a pathway for crossing the proline barrier. The two experiments utilize a TROSY detection scheme, sensitivity enhancement and gradient echo/antiecho coherence selection, and differ only in sensitivity and resolution in one of the nitrogen dimensions. The assignment of aromatic residues is a critical step towards obtaining high-quality structures, and

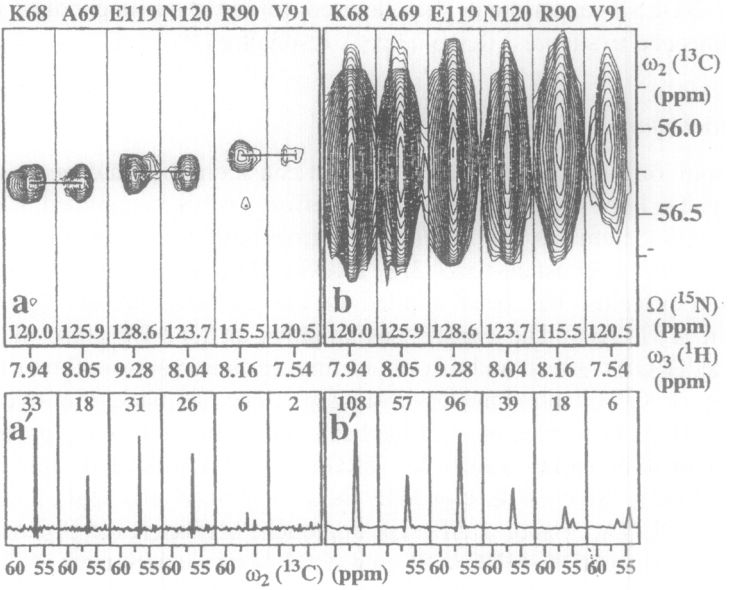

Fig. 4. Comparison of corresponding [ω_2(^{13}C),ω_3(^{1}H)] strips from HNCA spectra obtained with and without ^{13}C constant-time evolution: (a) [^{13}C]-ct-[^{15}N,^{1}H]-TROSY-HNCA recorded with the scheme of Fig. 1; (b) [^{15}N,^{1}H]-TROSY-HNCA.[225] The strips were taken at the ^{15}N chemical shifts indicated at the bottom, and are centred about the corresponding $^1H^N$ chemical shifts. At the top, the sequence-specific assignments are indicated by the one-letter amino acid symbol and the sequence number. In (a) the three sequential connectivities are indicated by horizontal lines. (a′) and (b′) show cross-sections along the ω_2(^{13}C) dimension through the centres of the strips in (a) and (b), respectively, where the chemical shift range from 52 to 62 ppm is plotted. The signal-to-noise ratios for the main peak in each cross-section are indicated at the top. Both spectra were recorded at 20°C with the same 0.5 mM sample of uniformly ^{2}H/^{13}C/^{15}N-labelled 7,8-dihydroneopterin aldolase from *Staphylococcus aureus*[226] in a mixed solvent of 95% H_2O/5% D_2O at pH 6.5, using a Bruker DRX-750 spectrometer equipped with four RF channels for generating the ^{1}H, ^{2}H, ^{13}C and ^{15}N RF pulses, a pulsed-field gradient unit, and a triple resonance probehead with an actively shielded z-gradient coil. When recording spectrum (b), the previous implementation of the [^{15}N,^{1}H]-TROSY-HNCA experiment[225] was modified so that ^{13}CO decoupling by Gaussian off-resonance pulses was replaced by 0.83-kHz off-resonance SEDUCE-1 decoupling,[227] and the RF pulses on the $^{13}C^{\alpha}$ channel were applied with a field strength of 20.83 kHz, exactly as described for [^{13}C]-ct-[^{15}N,^{1}H]-TROSY-HNCA in Fig. 1. The following parameter settings were used for (a): data size $42(t_1)\times128(t_2)\times1024(t_3)$ complex points; $t_{1max}(^{15}N)=17.4$, $t_{2max}(^{13}C^{\alpha})=25.6$, $t_{3max}(^1H)=75.6$ ms; spectral widths in ω_1(^{15}N), ω_2($^{13}C^{\alpha}$) and ω_3(^{1}H) 2400, 5000 and 13 550 Hz, respectively; 16 scans per increment were acquired, resulting in 4 days of measuring time. The data set was zero-filled to $128(t_1)\times256(t_2)\times2048(t_3)$ complex points. In (b) the same parameters were used, except for the following: data size in t_2 was 40 points, t_{2max} ($^{13}C^{\alpha}$) = 8 ms, 48 scans per increment were acquired in 4 days of measuring time, and zero-filling in t_2 was to 128 complex points. Prior to Fourier transformation, both data matrices were multiplied with a 75°-shifted sine bell window in the indirect dimensions and a 60°-shifted sine bell window in the acquisition dimension.[228] Data processing was performed using the program PROSA,[229] and for the data analysis the program XEASY[230] was used. Reproduced with permission from Kluwer Academic Publishers, Salzmann *et al.*[89]

the most useful experiment for assigning aromatic residues is HCCH-TOCSY. A major obstacle in HCCH experiments is the resolution of cross-peaks near the intense diagonal peaks. Meissner and Sørensen[96] have used a spin-state selective filter in the ^{13}C–^{13}C mixing sequence to suppress the diagonal peaks in a TROSY HCCH experiment.

5.2.4. Miscellaneous uses of TROSY

TROSY elements have been appended to pulse sequences designed to measure the dynamics of proteins or to identify the solvent-exposed amides. Zhu *et al.* have appended a TROSY sequence based on the ST2-PT sequence to standard T_1, T_2 and heteronuclear NOE sequences designed to probe the dynamics of amide nitrogens in ^{15}N-labelled proteins.[97] Loria *et al.* have developed a TROSY-CPMG pulse sequence designed to measure chemical exchange time constants in large proteins and demonstrate the effectiveness of the pulse sequence on a 54-kDa homodimeric protein.[98] Alternatively, it has been suggested that conformational exchange-induced transverse relaxation can be suppressed using the TROSY technique in certain circumstances.[99] The degree of transverse relaxation suppression is not dependent on the rate of exchange or on the relative population of the exchanging populations. The most favourable case is two-site exchange, but the suppression of exchange-induced relaxation deteriorates as the number of exchanging conformers increases. Significant improvement in the sensitivity of exchange-broadened cross-peaks is also possible by combining TROSY with INEPT polarization transfer elements containing the XY-16 pulse sequence.[100]

Pellecchia *et al.* have proposed the SEA-TROSY technique to identify solvent-exposed amide groups in ^{15}N-labelled proteins. Initially, all amide magnetization is eliminated with a ^{15}N filter, and then the magnetization of solvent-exposed amide protons is restored by exposure to water magnetization followed by detection of these amide protons by water flipback TROSY.[101] Figure 5 shows a comparison of a normal TROSY spectrum and an SEA-TROSY spectrum (50-ms mixing time) of a 30-kDa complex of ^{15}N,^{13}C-θ subunit and the unlabelled N-terminal domain ε(1–185) subunit of DNA polymerase III.

5.3. Applications of TROSY to large proteins

In a short period of time, there have been applications of TROSY to a number of diverse systems, demonstrating the great promise of this technique for extending the boundaries of NMR structure determination. New directions in the high-resolution NMR of membrane proteins are indicated by the structure determination of a 19-kDa transmembrane domain of the *E. coli* protein A in lipid micelles, revealing an eight-stranded β-barrel connected by tight turns.[102] TROSY-based dynamics experiments also revealed a gradient of flexibility

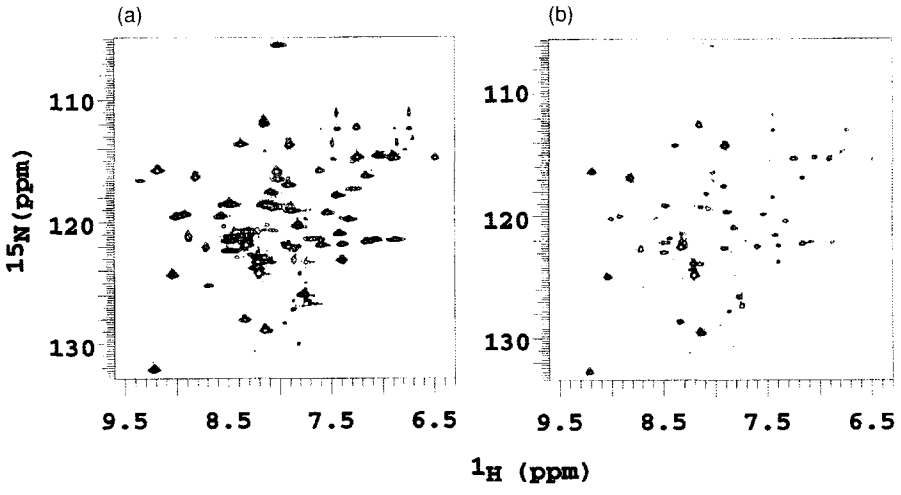

Fig. 5. TROSY spectrum (a) and SEA-TROSY spectrum (b) of the 30-kDa complex of ^{15}N,^{13}C-θ subunit and the unlabelled N-terminal domain ε(1–185) subunit of DNA polymerase III. The SEA-TROSY spectrum was recorded with the pulse sequence reported in Pellecchia *et al.*,[101] with a mixing time τ_m of 50 ms. The TROSY spectrum was recorded with the same pulse scheme minus the SEA-TROSY element. The spectra were recorded on a Varian INOVA 600 spectrometer operating at a ^{1}H frequency of 600 MHz. Spectra were acquired with 96 (t_1)×1024 (t_2) complex points and processed using VNMR software.

within protein A.[102] Ligand-induced conformational changes in a 41-kDa complex of maltotriose with MBP have been detected and used to determine the changes in the orientation of two domains of the protein.[103] The potential for application to protein–nucleic acid complexes was demonstrated by an investigation of the RNA-binding domains of nucleolin and an RNA stem-loop revealing a $\beta\alpha\beta\beta\alpha\beta$ protein fold and a flexible linker separating the RNA-binding domains of nucleolin.[104] The linker became ordered on binding to RNA, which interacts via the β-sheet of the protein.[104] The structure of a 38-kDa complex between two U1A proteins and an RNA regulatory region called the polyadenylation inhibition element (PIE) has been solved using TROSY NMR techniques.[105] A conformational change within the U1A protein on binding to PIE accounted for the cooperativity of binding to poly(A) polymerase.[105]

6. PARTIAL ALIGNMENT OF PROTEIN MOLECULES AND RESIDUAL DIPOLAR COUPLINGS

6.1. General

The classical techniques, which use distance and angular restraints derived respectively from ^{1}H–^{1}H NOE intensities and J-coupling constants as input

restraints for determining large protein structures, are limited in their effectiveness by the intrinsically local nature of these restraints. This limitation can be circumvented to some extent if there are large numbers of long-range ^{1}H–^{1}H NOEs, but there are many examples of large proteins where sufficient numbers of ^{1}H–^{1}H NOEs cannot be found. There is a need for truly global restraints to refine the structures of proteins and protein complexes (both with other proteins, and with nucleic acids) where there is a dearth of long-range ^{1}H–^{1}H NOEs. Over the past 5 years, there has been a considerable effort to utilize the orientation information of residual dipolar couplings in protein structure determination. The strategy is to restore the dipolar coupling to a level sufficient for accurate measurement but, at the same time, allow the protein to tumble rapidly enough to retain narrow resonance linewidths. Residual dipolar couplings are true global restraints, because they align internuclear vectors to a fixed molecular axis.

The partial alignment that is required to measure residual dipolar couplings can be generated by a strong magnetic field, in the case of molecules with large anisotropic magnetic susceptibilities,[106] or by utilizing the large anisotropic magnetic susceptibility of some paramagnetic ions if a binding site is available, or by introducing into the solution large macromolecules or macromolecular structures that can be aligned by the magnetic field.[107,108] The last technique is the most useful, because it is readily applicable to most systems, and the size of the residual dipolar coupling is tuneable, so that a measurable quantity without inducing too much dipolar broadening can be achieved. The size of the residual dipolar coupling, which is manifest in the spectrum as an induced splitting of the resonance lines,[109] is dependent on the degree of partial alignment, which is maintained at a modest level to ensure that the resonance linewidth remains narrow.

Residual dipolar couplings have been used to refine and improve structures of proteins where there is an ill-defined hydrophobic core,[37,110,111] to identify protein folds in proteins of unknown structure,[112,113] to properly orient the domains of multidomain proteins where there are few interdomain ^{1}H–^{1}H NOEs,[114–118] to orient the components of complexes where the orientation of those components is ill-defined,[119–122] and to obtain the conformation and orientation of ligands in the presence of large proteins.[120,121,123]

6.2. Theory

The residual dipolar coupling between two nuclei i and j, D^{ij}, can be expressed as

$$D^{ij} = \delta_0{}^{ij} A_a \{(3\cos^2\theta - 1) + (3/2)R(\sin^2\theta \cos 2\phi)\}$$

where A_a is the axial component of the molecular alignment tensor $\boldsymbol{A}$, and R is its rhombicity.[107] $\delta_0{}^{ij}$ comprises several constants, including the gyromagnetic ratios of i and j, the inverse cube of the distance between i and j, and the generalized order parameter describing fast angular fluctuations of the internuclear vector.

θ and ϕ are the polar angles that describe the orientation of the internuclear vector, *ij*, and the principal alignment frame.[107] The orientation of the alignment frame is defined relative to a fixed molecular frame by the Euler angles (α, β, γ). A_a and R can also be expressed in terms of the diagonal components of the alignment tensor.

The orientation of the *ij* internuclear vector can only be obtained once A_a and R are known. If the distribution of the *ij* internuclear vectors approximately covers all directions in space, then A_a and R can be calculated from the distribution of the experimental residual dipolar couplings.[124] The geometric part of the residual dipolar coupling can then be incorporated into simulated annealing protocols in the form of a penalty function.[124,125] There are several assumptions implicit in this approach, including the following. The distribution of residual dipolar couplings covers all directions in space (not necessarily true for α-helical proteins), and the whole molecule is sufficiently rigid to warrant a single alignment tensor. Warren and Moore[126] have developed a maximum-likelihood method that overcomes some of the problems implicit in the above approach in order to estimate A_a and R. The method also estimates errors in A_a and R, which can then be translated into errors for each individual residual dipolar coupling. The method has been shown to give reliable estimates of A_a and R for small anisotropic sets of residual dipolar couplings.[126]

In an alternative approach developed by Prestegard and coworkers,[114] residual dipolar couplings are formulated in terms of the five independent elements of a 3×3 symmetric and traceless order matrix. The five elements can be reformulated in terms of the three angles of the principal alignment axis (α,β,γ), the value of the principal order parameter (S_{zz}) and an asymmetry parameter ($\eta=(S_{xx}-S_{yy})/S_{zz}$). For a single rigid molecular fragment, all five of these elements can be derived from five or more independent measurements of D^{ij}. In practice, this amounts to creating and solving a set of linear equations relating the direction cosines of the internuclear vectors in the molecular frame to the experimental dipolar couplings. The set of equations can be solved by a simple grid search[127] or by singular value decomposition.[114]

There have been several variations on the above-mentioned strategies, aimed at overcoming some of the limitations of using residual dipolar couplings in the refinement of macromolecular structures. One of these limitations is related to the insensitivity of order parameters to axis inversion, making it difficult to accurately define the local and long-range geometry. This degeneracy can be lifted if two independent sets of residual dipolar couplings are measured in alignment media that produce non-coincident order tensors.[128,129] Ramirez and Bax[128] showed that the orientation of the alignment tensor may be altered by either adding an unstructured His-tag to the C-terminus of a protein, or by changing the sample pH, or by changing the net charge of the alignment medium. Alternatively, altering the ionic strength in aligned Pf1 phage molecules may be sufficient to yield linearly independent alignment tensors.[130] Prestegard and coworkers demonstrated that altering the orientation of the alignment tensor may

also resolve the problem of orientation degeneracy in the order tensor approach to refining molecular structures.[129]

Several groups have developed approaches that circumvent the need to determine the alignment tensor. One such method, developed by Griesinger and coworkers,[113,131] uses the residual dipolar couplings to calculate intervector projection angles. In this approach, the intervector angle restraints are introduced at the beginning of the refinement process instead of at the latter stages of structure refinement. Moltke and Grzesiek have introduced a non-linear least-squares method to calculate a penalty function from the residual dipolar coupling data without explicit knowledge of the alignment tensor.[132] Skrynnikov and Kay have used residual dipolar couplings to derive frame-independent, pairwise restraints to assess the quality of experimental structures.[133]

6.3. Techniques for partial alignment

There are a number of methods available for aligning molecules, including: (i) making use of the natural anisotropic magnetic susceptibility of the protein;[134] (ii) using paramagnetic ions that are naturally associated with[13,106,135–137] or synthetically attached to the protein;[128,138] (iii) using mechanical means such as trapping the protein between bicelles or phage molecules;[107,108,139,140] (iv) by dissolution in strained hydrated polyacrylamide gel;[141] or (v) by aligning molecules in electric fields.[142]

By far the most widely applicable method of alignment is by mechanical means. There is, however, no universal alignment medium. The choice of alignment medium is determined by the net charge of the solute, the pH, the temperature, and whether it is necessary to recover the labelled protein. Below, we discuss the properties of the different classes of alignment media.

Historically, the first alignment media used were bicelles, which are disk-like, nematic liquid crystals that have a time-averaged spatial alignment along the long axis in the presence of a magnetic field. Early versions of the bicelle-forming media suffered from instability at low pH[143] and alignment over a narrow temperature range.[107,143] The phase diagrams of some of these mixed phospholipid systems are also complex, depending on pH, salt concentration, and the relative concentrations of the bicelle components.[10] Hence, several bicelle systems have been introduced to cover a wide range of pH and temperature and overcome other problems such as association of the protein and the bicelle. The pH dependence of dimyristoyl-phosphatidylcholine (DMPC) and dihexanoyl-phosphatidylcholine (DHPC) caused by acid- or base-catalysed hydrolysis can be prevented by using the alkyl analogues of these lipids.[144] A mixture of 1,2-di-*O*-dodecyl-*sn*-glycero-3-phosphocholine (DIODPC) and 3-(chloramidopropyl)-dimethylammonio-2-hydroxyl-1-propane sulphonate (CHAPSO) is an appropriate bicelle system for work at low pH and is effective over a wide temperature range (10–50°C).[145] Similarly, a mixture of dilauroyl phosphatidylcholine (DLPC) and CHAPSO

works well over a wide temperature range (7–50°C).[146] Cetylpyridinium chloride/hexanol forms a stable liquid crystalline phase at high salt concentration,[147] but becomes unstable at high protein concentrations and is highly positively charged and hence may be unsuitable for negatively charged proteins.[148] Rückert and Otting have proposed a series of liquid crystalline media composed of n-alkyl-poly(ethyleneglycol)/n-alkyl mixtures that are uncharged, insensitive to pH, and suitable for use over a wide range of salt concentrations and temperature (0–40°C).[148] Sometimes, the addition of a small amount of a charged molecule can assist in improving the stability of the bicelle solutions. The positively charged hexadecyl(cetyl)trimethylammonium bromide (CTAB)[149] or the negatively charged sodium dodecylsulphate[149] have been used for this purpose, as well as changing the direction of the alignment tensor.[128,129] The pressure stability of the DMPC/DHPC/CTAB system has recently been investigated; the results suggest that residual dipolar couplings can be measured in proteins up to a pressure of 200 MPa.[150]

All of these bicelle systems present problems for recovery of the labelled protein. If recovery of the protein is important after the alignment experiments, then macromolecules such as filamentous phages,[139,151] fragments of purple membranes[152] or cellulose fibres[153] can be aligned in high magnetic fields. Filamentous phages tend to aggregate below pH 6, and at low phage concentrations the degree of alignment is dependent on the ionic strength.[10,148] Only one of these phage systems, Pf1, has been systematically characterized over a wide range of temperature and ionic strength.[130] Purple membrane fragments are suitable at low ionic strength but tend to aggregate and lose alignment properties above an ionic strength of 50 mM.[10] The cellulose fibre suspensions have many desirable qualities, such as stability under a variety of solution conditions, and possess a very low affinity for macromolecules.[153] Phage, purple membrane and cellulose fibres are all negatively charged, and some form of electrostatic interaction with the solute is to be expected; furthermore, this electrostatic interaction does have a role in the direction and degree of alignment of the solute.

6.4. Measuring residual dipolar couplings

Several strategies have been developed to measure residual dipolar couplings in ^{13}C-,^{15}N-labelled proteins. Residual dipolar couplings can be measured in the frequency domain of multidimensional spectra of ^{13}C- or ^{15}N-labelled proteins by not decoupling in either the direct or indirect dimension.[107,154] Alternatively, residual dipolar couplings can be measured from the *J*-modulation of the cross-peak intensity in multidimensional NMR experiments.[155,156] Frequency-based experiments are the simplest to implement but sometimes suffer because of the complexity of the spectrum created by twice the number of cross-peaks. This latter drawback may be overcome by simple editing techniques.[154,157–159] Intensity-based experiments are more prone to

systematic errors that must be taken into account in order to obtain accurate residual dipolar couplings.[160]

There are many variations of the basic experiments, with the purpose of overcoming some of the problems encountered in medium-to-large proteins, such as circumventing the extensive overlap caused by doubling the number of cross-peaks, or by decreasing the linewidth of the cross-peaks by using TROSY techniques or by measuring several different residual dipolar couplings simultaneously. The optimum strategy is dependent on the size of the protein, the transverse relaxation rates of the nuclei, the number of cross-peaks, and the size of the residual dipolar coupling to be measured, and the reader is referred to excellent reviews for a more detailed account.[10,161]

Several new methods have appeared recently; Lerche *et al.*[162] describe strategies and TROSY pulse sequences tailored to suit the size of the protein and the TROSY effect. Kontaxis *et al.*[163] describe similar strategies for measuring one-bond couplings in large proteins and demonstrate this technology with 2D TROSY, composite-pulse decoupled HSQC (cpd-HSQC) and modified HNCO pulse sequences. They showed that, for large proteins, residual dipolar couplings can be measured more accurately from a superposition of TROSY and cpd-HSQC experiments than by measuring the difference between the two components of the TROSY doublet where one of those components is broad. Permi and coworkers have devised several 2D and 3D experiments based on TROSY to extract backbone residual dipolar couplings from ^{15}N-HSQC spectra.[164–167] The pulse sequences of Permi *et al.*[164–167] employ spin-state selective filters, semi-constant time TROSY evolution, sensitivity enhancement, and gradient echo/antiecho selection. Concatenation of INEPT and TROSY to improve sensitivity, and accordion spectroscopy *J*-multiplication to scale up the coupling constants, have also been employed to measure residual dipolar couplings.[168] These experiments take advantage of the narrow lines of TROSY, the excellent spectral dispersion, and the favourable relaxation properties of amide protons and nitrogens. The 2D versions of these experiments will be of most use in large complexes where one of the components is labelled or where only part of a large protein is labelled. Chou *et al.* have demonstrated that a quantitative *J*-correlation experiment based on 3D TROSY-HNCO can be used to accurately measure $^{1}J_{C'N}$ splittings.[169] Alternatively, $^{3}J_{H^{N}H^{\alpha}}$ coupling constants have been measured in large proteins by a *J*-modulated TROSY.[170] The experiment employs a scaled *J*-modulation spin echo sequence and homonuclear H^{α} decoupling during acquisition to achieve excellent resolution of the doublets along the ^{15}N dimension. Successful strategies do not always rely on the manipulation of spins. Giesen *et al.* have shown that one-bond dipolar couplings, especially $D_{C^{\alpha}H^{\alpha}}$, can be obtained simply from standard HSQC spectra when only the backbone atoms are labelled by stable isotopes.[32] In the case of unstable proteins, it is essential to obtain as much data as possible in a short time period. De Alba *et al.* have devised modified HNCO and (HA)CA(CO)NH experiments that simultaneously measure $J_{C^{\alpha}C'}$, J_{NH} and $J_{C^{\alpha}H^{\alpha}}$, J_{NH} respectively.[171] Brutscher

has devised a novel *J*-mismatch compensated spin-state selective filter that is particularly effective in estimating very small residual dipolar coupling constants.[172] The new filter is demonstrated in modified HNCO experiments designed to measure ^{15}N–$^{13}C'$ and ^{1}HN–$^{13}C'$ coupling constants.

Most of the pulse sequences and strategies have been devised to extract coupling constants for the protein backbone, but there are some methods specifically derived for extracting residual dipolar couplings from side-chain atoms. Evenäs *et al.* have described two TROSY-based HN(CO)CA methods for obtaining $^{13}C^{\alpha}$–$^{13}C^{\beta}$ dipolar couplings.[117] In the first method, the $D_{C^{\alpha}C^{\beta}}$ dipolar couplings are recorded directly from the time modulation of the cross-peak intensities in a set of 2D ^{1}H–^{15}N correlated spectra. In the second method, the $D_{C^{\alpha}C^{\beta}}$ dipolar couplings are encoded in a frequency dimension. Quantitative *J*-correlated spectroscopy and TROSY have been combined in an experiment to simultaneously measure $^{3}J_{NC^{\gamma}}$ and $^{3}J_{C'C^{\gamma}}$ for the determination of the χ^{1} torsion angle.[173] The spectrum contains internal reference peaks and so there is no need to record a separate reference spectrum. Permi *et al.*[174] have devised pulse sequences for measuring $^{2}J_{HH}$ couplings for NH_2 and CH_2 groups in the side-chains of proteins. Bertini *et al.*[136] have measured $^{2}J_{HH}$ couplings in a Ca_2-calbindin protein that was aligned by substituting one of the calcium ions with a paramagnetic ion. Kontaxis and Bax[175] describe a simple editing procedure for extracting the residual dipolar couplings of methyl groups from ^{1}H–^{13}C HSQC spectra that have the simplicity of regular decoupled CT-HSQC.

Much of the early effort has focused on developing methods for one-bond D_{CH}, D_{CC}, D_{CN} and D_{NH} residual dipolar couplings, because the internuclear distance is fixed and only orientation information is available. ^{1}H–^{1}H dipolar couplings contain both distance and orientation information, but the determination of the sign of the residual dipolar coupling can be problematical, because the size of the residual dipolar coupling is of the same order as that of the ^{1}H–^{1}H *J* couplings. Several experiments have been described for extracting both the sign and the magnitude of ^{1}H–^{1}H dipolar couplings based on COSY or TOCSY experiments.[151,176–178] Peti and Griesinger[179] have proposed a method based on ECOSY, which uses the much larger ^{1}H–^{15}N splitting to detect the magnitude and sign of the residual ^{1}H–^{1}H dipolar coupling. The displacement of the components of the ^{1}H–^{15}N doublet due to the ^{1}H–^{1}H residual dipolar coupling in this experiment is shown in Fig. 6. Otting *et al.*[180] have described a modified version of J HH-TOCSY ('signed COSY'), designed to derive ^{1}H–^{1}H dipolar couplings in the presence of much larger J_{XH} couplings. Tian *et al.*[181] have demonstrated that the sign of the dipolar coupling can also be determined by variable angle sample spinning experiments. Small and unresolved ^{1}H–^{1}H dipolar couplings are best measured by intensity-based techniques. Tian *et al.*[182] have introduced a 3D ^{15}N-resolved CT-COSY experiment for measuring ^{1}H–^{1}H dipolar couplings, but the antiphase cross-peaks present problems for large proteins. Pellecchia *et al.*[183] have proposed a novel 3D experiment designed to measure the ^{1}H–^{1}H dipolar couplings from the intensity of in-phase cross-peak

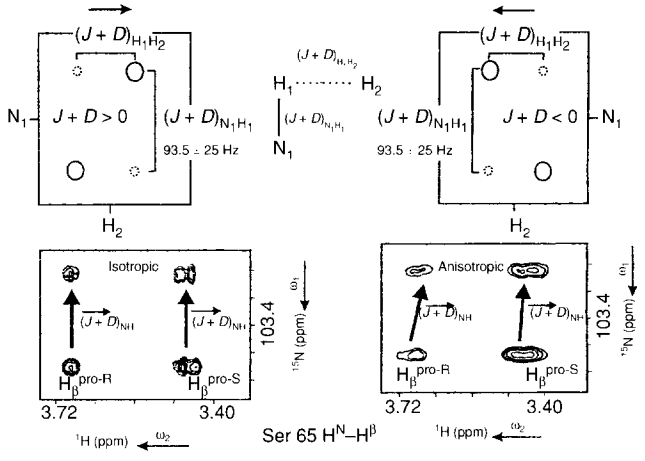

Fig. 6. Schematic cross-peak pattern for the J_{HH} NOESY. Owing to the defined sign of $J_1 + D_1$ (93.5 ± 25 Hz, provided that sufficiently weak alignment is used), the sign of the H,H dipolar coupling can be extracted. The dotted cross-peak contributions arise from the normally weak undesired coherence transfers. They cannot be avoided, since it is impossible to match Δ to all values of $J+D$. The dotted cross-peak contributions are also modulated by spinflips during the NOESY mixing time, as indicated in the text. Also two peaks out of the spectra of Ubiquitin are shown. They display the peaks of Ser 65 HN-H$^\beta$. In isotropic solution, the ^4J coupling is zero, but in anisotropic solution, a through-space dipolar coupling can be extracted. Reproduced with permission from the American Chemical Society. Peti and Griesinger.[179]

and diagonal peaks. Kaikkonen and Otting[184] have described a pulse sequence to derive ^{1}H–^{1}H residual dipolar coupling from methyl groups in proteins. The D_{HH} residual dipolar coupling is shown to be linearly related to the D_{CH} residual dipolar coupling and can thus be readily used for the structure refinement of proteins.

6.5. Applications

In a short period of time, residual dipolar couplings have found application in many structural problems, because they are easy to measure, they are not subject to spin diffusion, and they provide long-range orientation information. They have recently been applied to the determination of protein folds where few, if any, NOE or dihedral restraints are available.[13,37,112,185] Residual dipolar couplings are particularly useful for refining proteins that have domains where there is no well-defined hydrophobic core.[111] For example, the β-domain of the lysozyme has few long-range NOEs and is poorly determined by classical NOE-based refinement techniques. Inclusion of 209 residual dipolar couplings improved the quality of the structure, which also showed better agreement with

the X-ray structure.[111] Another application is to assist in the alignment of domains within proteins where there are few interdomain NOEs.[115,117] In one particularly good example of this application, Kay and coworkers[117] demonstrated that the two domains of the ligand-free form of MBP have the same relative orientation in the solution and crystalline states, but, in complex with β-cyclodextrin, the two domains of MBP vary by 11° between the solution and crystalline states.[116] Dosset *et al.*[186] have recently developed an interactive program module for aligning domains in multidomain proteins using residual dipolar couplings and have demonstrated its effectiveness using two model multidomain systems. The program requires the *xyz* coordinates of the domains of the structure and the residual dipolar couplings and their uncertainties, as well as an estimate of the order parameter. Ligand-induced conformational changes are readily identified by variations in the residual dipolar couplings.[116] The alignment of a ligand relative to a macromolecule is also possible using residual dipolar couplings.[121,122] Residual dipolar couplings have been particularly useful in the refinement of protein–nucleic acid complexes where the quality of the structure is compromised by a dearth of NOEs between the protein and the nucleic acid and the lack of long-range NOEs in the nucleic acid.[104,119]

Residual dipolar couplings have been used by Mittermaier and Kay[187] to probe the torsion angle dynamics of protein side-chains. Using the B1 domain of peptostreptococcal protein L, they show that the residual dipolar couplings can be used to distinguish static from mobile side-chains, and that the motions of most mobile side-chains can be adequately explained by rotamer-jump models.

7. PARAMAGNETIC IONS AND SPIN LABELS IN LARGE PROTEINS

7.1. General

The resonant chemical shift of an NMR-sensitive nucleus within, or near to, a paramagnetic molecule is shifted from its diamagnetic chemical shift by interactions with the unpaired electron. This shift is known as the hyperfine shift and may involve movements from its diamagnetic chemical shift of up to several hundred parts per million to either low or high field. In addition, the interactions between the unpaired electron and the nucleus can cause significant broadening of resonances. The amount of broadening is dependent on the electronic spin relaxation time of the unpaired electron (τ_s); that is, relatively long relaxing unpaired electrons cause large hyperfine shifts and broadened resonances. For example, Fe(III) is paramagnetic, and in the low-spin state ($S=1/2$) its τ_s is $\sim 2\times10^{-12}$ s, whereas in the high-spin state ($S=5/2$), τ_s is $\sim 1\times10^{-10}$ s.[188] Accordingly, NMR spectra of high-spin Fe(III)-containing molecules have a much larger chemical shift range and much broader resonances than those from the low-spin Fe(III) species.

Hyperfine shifts due to the presence of a paramagnetic centre can either be intrinsic to the protein, e.g. from the Fe(III) ion of a haem group, or extrinsic, e.g. from an added spin label. From the perspective of NMR spectroscopy of proteins, hyperfine shifts have advantages in that they shift resonances from the crowded diamagnetic envelope and therefore allow greatly enhanced resolution of these resonances and enable detailed structural probing of the environs of the paramagnetic centre. Accordingly, some of the earliest protein NMR studies that produced significant results, and showed the potential of the technique, arose from studies of haem proteins, particularly those with low-spin Fe(III) haem groups.[188]

In this section, recent NMR studies of large paramagnetic proteins will be presented. The determination of the solution structures of small paramagnetic proteins will not be discussed, as this has been well covered in recent reviews.[189,190] The use of paramagnetic spin labels to introduce selective broadening of resonances and to probe solvent-exposed regions of proteins will also be discussed.

7.2. Applications

7.2.1. Haem proteins

Haem oxygenase (HO) is a 265 amino acid protein that is responsible for haem catabolism; that is, it converts haem to biliverdin via oxygen-activated cleavage. La Mar and coworkers bound haemin to HO and monitored the effects on the ^{1}H NMR spectrum.[191,192] The spectra revealed that there are two haem orientations within the binding site,[191] which is proposed to have functional relevance. Furthermore, there is unusual spin density within the haem ring when bound to HO which was interpreted as arising from the electronic influence of HO, leading to electrophilic attack on the *α-meso* ring haem proton by a nearby acidic residue of HO. When high-spin Fe(III) haemin was bound to HO, resonances from nine aromatic residues were lost, due to the presence of the nearby paramagnetic iron, compared to the spectra acquired of the substrate-free protein.[192] These resonances were observed when low-spin, cyanide-inhibited haemin was bound to HO. From the 2D ^{1}H–^{1}H spectra, the axial and distal ligands for haem were assigned to His and Tyr residues respectively. Conclusions were also drawn about the arrangement of the haem group in the active site, in particular that the binding pocket is relatively open compared to globin and peroxidase haem proteins.

La Mar and coworkers have also undertaken detailed studies on the haem and near-haem residues in the low-spin Fe(III) cyano complex of the haemoglobin A (HbA) tetramer (mass ~65 kDa). A series of 2D experiments, including the use of sequence-specific methods, was used to assign these protons.[193] From these data, and a comparison of the experimental and theoretical dipolar chemical

shifts (calculated from the crystal structure of the diamagnetic Fe(II) CO complex of HbA), it was concluded that the CN ligand was complexed to the iron atom of the haem in a tilted orientation similar to that for the CO ligand when bound to HbA. In a more recent study, the hydrogen bonding interactions and orientations of the distal and proximal histidines were examined in close detail.[194] From this study, it was determined that these histidines were in a similar position to those of the crystal structure of the CO and O_2 complexes of HbA.

Horseradish peroxidase (HRP) is another relatively large haem-containing protein that has been investigated recently using NMR spectroscopy,[195,196] and often in the past (refs 11–29 in Asokan *et al.*[196]). HRP has a mass of 44 kDa and performs one-electron oxidation of aromatic substrates at the expense of H_2O_2. The resting state of HRP contains the iron atom of the haem in a high-spin ferric state, which leads to large hyperfine shifts of the haem and near-haem resonances. The recent NMR studies[195,196] used this state of HRP rather than the physiologically non-relevant CN-inhibited, low-spin derivative, which gives much better NMR spectra (e.g. ref. 197). From these former studies, many assignments were made of haem and near-haem resonances, and the structure of this region was compared between the solution and crystal states. It was concluded that the two structures were essentially indistinguishable, apart from the orientation of Phe68. The haem pocket is also tightly packed, as assessed by the relatively slow rate of rotation of proximal near-haem aromatic residues.[196] The distal His42 is one of the two key residues in the enzyme's mechanism of activation. NMR studies of the His42-to-alanine mutant revealed that a coordination number of five for the iron atom is retained in the mutant and that the structure of the haem pocket is essentially the same as in the wild-type protein.[196]

7.2.2. Non-haem, paramagnetic proteins

Iron superoxide dismutase (SOD) has 192 amino acids but exists as a dimer, giving an overall mass of ~42 kDa. The iron-containing protein converts O_2^- to O_2 and H_2O_2 via a two-step mechanism involving the conversion of Fe(III) to Fe(II) and back to Fe(III). In doing so, SOD minimizes cellular oxidative damage. The active-site iron atom is coordinated to two histidine residues and an aspartic acid residue equatorially, and has a histidine and a water molecule as axial ligands (in the Fe(II) state). In the Fe(III) state, the water is replaced by a hydroxide ion. The Fe(II) and Fe(III) forms are both paramagnetic. Vathyam *et al.*[198] labelled SOD with ^2H, ^{13}C and ^{15}N and acquired 3D NMR spectra of the Fe(II) and Fe(III) forms. As a result, they assigned all the observable backbone resonances arising from amino acids >14 Å from the iron atom. Small changes across the molecule were observed between the two oxidation states. In addition, the anion substrate binding site was localized to the highly conserved residue Tyr34. No assignment of the paramagnetically shifted resonances was attempted. Thus, the approach of Vathyam *et al.* was fundamentally different to

those described above with reference to NMR studies of paramagnetic proteins, in that their study focused on the diamagnetic resonances rather than the near-metal, paramagnetically shifted ones.

Sorkin and coworkers[199,200] have also undertaken NMR investigations of Fe(II) and Fe(III) SOD. The active-site Tyr34 is believed to have an important role in the mechanism of the protein and has a low pK value of 8.5 as determined by NMR spectroscopy and site-directed mutagenesis studies.[199,200] In their later publication,[199] they utilized specific amino acid isotopic labelling (substitution of ^2H for ^1H) at selective near-iron sites to make definitive assignments. For example, ^2H was introduced into various imidazole ring positions of histidine, and recombinant SOD was prepared with the side-chains of aspartic acid deuterated. Samples were also expressed and purified with histidine, aspartic acid and tyrosine protonated but the remainder of the protein deuterated. From the ^1H NMR spectra of these proteins, conclusive assignments were obtained for many of the iron ligand amino acids and for some nearby non-ligated amino acids in Fe(III) SOD. The assignments were significantly different to those based on model compounds of the Fe(III) SOD active site. Instead, the assignments for the axial histidine chemical shifts are similar to those for porphyrin-containing cytochrome *c*, implying similar electronic and chemical properties for iron ligation in both proteins.

Bondon and Mouro[201] used broadband ^1H decoupling of the diamagnetic envelope of resonances to improve the acquisition of ^1H 1D and 2D NMR spectra of paramagnetic proteins. As a result of the decoupling, the large signals from the diamagnetic envelope are reduced in intensity, giving much flatter baselines in the resultant spectra and improving the ability to observe very broad, hyperfine shifted NMR resonances. For example, the improvement in the NMR spectra of catalase, a tetrameric high-spin Fe(III) haem protein of ~230 kDa in mass, enabled the assignment of the broad, downfield resonance from the aromatic ring protons of the proximal iron ligand Tyr256. In spectra acquired without decoupling, this resonance was not observed, due to baseline distortion.

7.2.3. Paramagnetic spin labels as probes of protein structure

Spin labels have been used in NMR studies of proteins ever since the earliest structural work in the 1970s. For example, a variety of nitroxides have been bound to proteins and used to investigate the environs of the binding site of the spin label resulting from the specific broadening that arises due to enhanced relaxation of protons near to the spin label. A more general approach is to use spin labels dissolved in the solvent, which do not bind specifically to the protein, to enable the determination of solvent-exposed residues arising from their selective broadening in the NMR spectrum. Examples of both approaches will be presented.

Owing to the size of antibodies and their fragments, obtaining meaningful NMR spectra is difficult. Arata and coworkers[202,203] used deuterium-labelled

antibodies, e.g. at tyrosine and histidine residues, coupled with the binding to spin-labelled haptens, to identify binding site residues on the antibody. In a variation of this approach, Scherf *et al.*[204] bound a spin-labelled peptide antigen to the Fab fragment of the anti-cholera toxin peptide antibody (mass ~50 kDa) and recorded NOESY difference spectra. In this experiment, NOESY spectra are recorded in the absence and presence of the spin label, with the difference between the two arising from resonances in the vicinity of the binding site. The assignment of binding site residues was facilitated by the preparation of the Fab fragment selectively deuterated at various aromatic residues. From these data and derived restraints of the Fab fragment, a model was generated for the antibody-combining site.

NOESY and through-bond correlation 2D difference spectra were also used to investigate the environment of Asp61 in subunit *c* of the F_1F_0 ATP synthase complex.[205] Asp61 is believed to be the crucial residue in protonation–deprotonation during proton translocation across the membrane in the F_1F_0 ATP synthase complex. Within this structure, subunit *c* adopts a hairpin, dual helix-spanning transmembrane conformation. To undertake this study, a mutant of subunit *c* was prepared in which Ala67 was modified to a cysteine.[205] A spin label was subsequently attached to the sulphydryl group, and the NMR spectra were acquired on the reduced and oxidized mutant. Difference spectra gave rise to cross-peaks within ~15 Å of the spin label. As a result of the assignment of these resonances and the determination of distance restraints, a refined structure of the region near residue 67 was calculated. The structure showed that the two helices in subunit *c* are curved and offset by 30° from each other.

Paramagnetic spin labels have also been used to investigate the binding of a spin-labelled trinucleotide to a DNA-binding protein, M13 gene V.[206] A series of ^1H–^1H 2D difference spectra were analysed, and the secondary structure of the DNA-binding region of the protein was delineated. It was concluded that the binding region is localized on two β-loops, which are distributed over the two monomeric units of the gene V dimer.

Stremolysin 1 or matrix metalloproteinase 3 (MMP-3) is a zinc- or calcium-dependent protease which degrades components of the extracellular matrix. Its action is modulated by 1 : 1 complex formation with tissue inhibitors of metalloproteinases (TIMPs). A 126 amino acid fragment of TIMP, N-TIMP-1, retains its association with MMP-3. Arumugam *et al.*[207] undertook an NMR study of the complex of the ^{15}N,^{13}C-labelled catalytic domain of MMP-3 (MMP-3(ΔC)) with N-TIMP-1. MMP-3(ΔC) has 173 amino acids, and thus its complex with N-TIMP-1 has an overall mass of 33 kDa. Assignment of resonances in the free and complexed states enabled a mapping of the binding site for N-TIMP-1 on MMP-3(ΔC). In a novel approach, these results were compared with protection from NH resonance line broadening due to the presence of added paramagnetic Gd-EDTA afforded by the binding of N-TIMP-1 to MMP-3(ΔC). The protected regions are therefore relatively protected from solvent as a result of association between the two proteins. Conclusions were drawn about the alterations in the

active site of MMP-3 due to complexation. The results of the NMR study were consistent with those of the crystal structure of the complex between the two proteins.

Muscle contraction is regulated, to a significant extent, by the interaction of troponin (Tn) proteins: C, I and T. The interactions between Tn I and Tn C were studied by NMR using Tn C with a spin label attached to Cys84 and specifically ^{13}C-labelled at its 10 methionine residues.[208] From the known assignments of the methionine methyl cross-peaks in the HSQC spectrum of Tn C, and their absence from HSQC spectra in the presence of fragments of the bound Tn I, it was concluded that the linker between the two domains of Tn C is flexible, allowing association between the two domains in the presence of Tn I.

In another variant on the use of paramagnetic species to probe protein structure, Zhao *et al.*[209] determined the secondary structural features of Δ^{δ}-3-ketosteroid isomerase using 3D NMR techniques on the ^{15}N,^{13}C-labelled protein. This enzyme catalyses the conversion of Δ^{5}- to Δ^{4}-3-ketosteroids and is a homodimer of 125 amino acids per subunit. The NMR studies were undertaken on the steroid-bound protein. The amino acids near to the steroid were confirmed by binding a steroid incorporating a spin label and monitoring the disappearance from the ^{15}N–^{1}H HSQC spectrum of the cross-peaks associated with these residues.

The use of spin labels to induce general broadening of solvent-exposed resonances in the NMR spectra of proteins has been a focus of attention of several workers (reviewed in ref. 210). Studies have so far focused on well-characterized, small proteins, e.g. bovine pancreatic trypsin inhibitor,[211,212] whose X-ray crystal structures are available, and the correlations between solvent accessibilities determined by both methods have been good. In the latter study, spin label-induced attenuation of the nuclear Overhauser effects between the protein and its bound water molecules was determined. Conceivably, these techniques could be applied to proteins of larger size and those for which there is little detailed structural information available.

8. SOFTWARE ADVANCES

Despite all the advances in instrumentation and methodology, the complete assignment and structural determination of large proteins are still time-consuming processes. There is a need for software to improve the resolution of NMR data and to accelerate the assignment and structural refinement processes. Driscoll *et al.*[213] reviewed this area of research in 1999, and the reader is referred to this article for an in-depth discussion of software advances prior to 1999. We will briefly mention some of these techniques, because they are still relevant, but will discuss in more detail advances since that time.

Two programs, CNS (Crystallography and NMR system)[214] and DYANA (dynamics algorithm for NMR applications),[215] are widely used for refining

protein structures. CNS is a suite of programs designed for macromolecular structure determination by X-ray crystallography and NMR. CNS is a versatile program that has torsion-angle and Cartesian molecular dynamics and energy minimization capabilities and allows for a variety of input, including NOE-derived distances, *J*-coupling data, residual dipolar coupling data, diffusion anisotropy data, and hydrogen-bond restraints. DYANA performs simulated annealing by molecular dynamics in torsion-angle space and also allows for a variety of input restraints to assist in refining NMR structures. Modified versions of DYANA, PSEUDYANA[216] and PARADYANA[190] have been used to determine the structures of proteins containing paramagnetic centres via the incorporation of additional restraints from pseudocontact hyperfine shifts and residual dipolar couplings.

Spectral overlap, poor signal-to-noise ratio and the trend toward partial or full deuteration of large proteins reduce the number of long-range restraints available for structural refinement procedures. Hence, a number of groups have been working on procedures aimed at refining protein structures from sparse NMR data. Standley *et al.*[217] have introduced a new optimization procedure and an improved potential energy function to search for a global minimum of the protein fold in the presence of a limited set of long-range NOE data. The authors reported a substantial improvement in the root-mean-square deviation over standard distance geometry/molecular dynamics calculations for a test set of mixed α/β proteins. Bowers *et al.*[218] have used sparse NMR data to improve selection of a fragment basis set for an *ab initio* protein prediction method. The Rosetta method assembles fragments of known protein structures with sequence fragments similar to the target protein. The NMR data are used to improve the fragment selection strategy for the basis set. The method was tested on several proteins up to 152 residues in size.

The first step in any protein structure determination is to assign the backbone resonances. There have been several approaches to this problem over the years. The AUTOASSIGN program[219,220] employs data from a discrete set of triple resonance spectra and an expert system to determine the sequential assignment of backbone H^N, H^α, $^{13}C'$, $^{13}C^\alpha$ and ^{15}N resonances and side-chain $^{13}C^\beta$ resonances. Lukin *et al.*[221] have also devised a program that assigns the backbone and $^{13}C^\beta$ resonances of proteins from a series of 3D NMR experiments. The problem of chemical-shift degeneracy is overcome by collecting a large number of partly redundant NMR spectra from which assignments are made using a probabilistic Monte Carlo assignment algorithm.

One major problem in studying larger proteins is the large number of protein resonances and cross-peaks. Several approaches have been developed to handle this large amount of data and to assist in the assignment process. In the NOAH approach,[222] self-correcting distance geometry methods and structure-based filters are used to recognize correct distance restraints from a list containing both unambiguous and ambiguous distance restraints. The program iteratively cycles between structure calculations and automated spectral analysis in order to

optimize the number of correct restraints. The program, ARIA (Ambiguous Restraints for Iterative Assignment), developed by Nilges *et al.*,[223] relies on a complete list of proton assignments and a list of partially assigned NOEs to complete the assignment process by creating ambiguous NOEs for each cross-peak that satisfies a chemical-shift filter and a distance filter. A semi-automated approach similar to ARIA, called SANE (Structure Assisted NOE Evaluation), in which the user is involved in violation analysis at each round of structure analysis, was recently published by Duggan *et al.*[224] The procedure uses several filters (including chemical shift, distance, secondary structure, assignment and NOE contribution to the cross-peak intensity) to reduce the number of possible assignments. The SANE approach has been validated for a number of proteins, including some over 200 residues in size.

ACKNOWLEDGEMENTS

M.A.K. and J.A.C. would like to acknowledge the support of our research from the Institute of Advanced Studies, the Australian National University, the Australian Research Council, and the National Health and Medical Research Council of Australia.

REFERENCES

1. H. W. E. Rattle, *Annu. Rep. NMR Spectr.*, 1981, **11A**, 1.
2. M. Caffrey, M. Cai, J. Kaufman, S. J. Stahl, P. T. Wingfield, D. G. Covell, A. M. Gronenborn and G. M. Clore, *EMBO J.*, 1998, **17**, 4572.
3. E. Liepinsh, M. Baryshev, A. Shapiro, M. Ingelman-Sundberg, G. Otting and S. Mkrtchian, *Structure*, 2001, **9**, 457.
4. M. Salzmann, K. Pervushin, G. Wider, H. Senn and K. Wüthrich, *J. Am. Chem. Soc.*, 2000, **122**, 7543.
5. N. K. Goto and L. E. Kay, *Curr. Opin. Struct. Biol.*, 2000, **10**, 585.
6. D. Cowburn and T. W. Muir, *Methods Enzymol.*, 2001, **339**, 41.
7. R. Riek, K. Pervushin and K. Wüthrich, *Trends Biochem. Sci.*, 2000, **25**, 462.
8. J. H. Prestegard, *Nature Struct. Biol.*, 1998, **5 (suppl.)**, 517.
9. V. Dötsch and G. Wagner, *Curr. Opin. Struct. Biol.*, 1998, **8**, 619.
10. A. Bax, G. Kontaxis and N. Tjandra, *Methods Enzymol.*, 2001, **339**, 127.
11. K. Tu and M. Gochin, *J. Am. Chem. Soc.*, 1999, **121**, 9276.
12. F. Arnesano, L. Banci, I. Bertini, I. C. Felli and D. Koulougliotis, *Eur. J. Biochem.*, 1999, **260**, 347.
13. J. C. Hus, D. Marion and M. Blackledge, *J. Mol. Biol.*, 2000, **298**, 927.
14. M. Allegrozzi, I. Bertini, M. B. L. Janik, Y-M. Lee, G. Liu and C. Luchinat, *J. Am. Chem. Soc.*, 2000, **122**, 4154.
15. L. Banci, I. Bertini, A. Rosato and S. Scacchieri, *Eur. J. Biochem.*, 2000, **267**, 755.
16. F. Arnesano, L. Banci, I. Bertini, S. Ciofi-Baffoni, T. de Woodyear, C. M. Johnson and P. D. Barker, *Biochemistry*, 2000, **39**, 1499.
17. W. P. Aue, E. Bartholdi and R. R. Ernst, *J. Chem. Phys.*, 1976, **64**, 2229.
18. K. Wüthrich, in *NMR of Proteins and Nucleic Acids*, Wiley, New York, 1986.

19. K. Wüthrich, *Nature Struct. Biol.*, 2000, **7**, 188.
20. I. D. Kuntz, G. M. Crippen and P. A. Kollman, *Biopolymers*, 1979, **18**, 939.
21. T. F. Havel and K. Wüthrich, *Bull. Math. Biol.*, 1984, **46**, 673.
22. A. Brünger, in *XPLOR 3.1 A System for X-ray Crystallography and NMR*, Yale University Press, New Haven, 1992.
23. S. J. Weiner, P. A. Kollman, D. T. Nguyen and D. A. Case, *J. Comput. Chem.*, 1986, **7**, 230.
24. J. L. Markley, *Methods Enzymol.*, 1989, **176**, 12.
25. A. Bax, *Curr. Opin. Struct. Biol.*, 1994, **4**, 738.
26. G. M. Clore and A. M. Gronenborn, in *Biological Magnetic Resonance 16*, N. Rama Krishna and L. J. Berliner (eds), Kluwer, New York, 1998, p. 3.
27. G. W. Vuister, M. Tessari, Y. Karimi-Nejad and B. Whitehead, in *Biological Magnetic Resonance 16*, N. Rama Krishna and L. J. Berliner (eds), Kluwer, New York, 1998, p. 195.
28. C. Griesinger, M. Hennig, J. P. Marino, B. Reif, C. Richter and H. Schwalbe, in *Biological Magnetic Resonance 16*, N. Rama Krishna and L. J. Berliner (eds), Kluwer, New York, 1998, p. 259.
29. J. Kuszewski, J. Qin, A. M. Gronenborn and G. M. Clore, *J. Magn. Reson. Series B*, 1995, **106**, 92.
30. K. H. Gardner and L. E. Kay, in *Biological Magnetic Resonance 16*, N. Rama Krishna and L. J. Berliner (eds), Kluwer, New York, 1998, p. 27.
31. B. T. Farmer II and R. A. Venters, in *Biological Magnetic Resonance 16*, N. Rama Krishna and L. J. Berliner (eds), Kluwer, New York, 1998, p. 75.
32. A. W. Giesen, L. C. Bae, C. L. Barrett, J. A. Chyba, M. M. Chaykovsky, M. C. Cheng, J. H. Murray, E. J. Oliver, S. M. Sullivan, J. M. Brown, F. W. Dahlquist and S. W. Homans, *J. Biomol. NMR*, 2001, **19**, 255.
33. M. K. Rosen, K. H. Gardner, R. C. Willis, W. E. Parris, T. Pawson and L. E. Kay, *J. Mol. Biol.*, 1996, **263**, 627.
34. N. K. Goto, K. H. Gardner, G. A. Mueller, R. C. Willis and L. E. Kay, *J. Biomol. NMR*, 1999, **13**, 369.
35. H. S. Atreya and K. V. R. Chary, *J. Biomol. NMR*, 2001, **19**, 267.
36. R. Ishima, J. M. Louis and D. A. Torchia, *J. Biomol. NMR*, 2001, **21**, 167.
37. G. A. Mueller, W. Y. Choy, D. W. Yang, J. D. Forman-Kay, R. A. Venters and L. E. Kay, *J. Mol. Biol.*, 2000, **300**, 197.
38. G. Kelly, S. Prasannan, S. Daniell, K. Fleming, G. Frankel, G. Dougan, I. Connerton and S. Mathews, *Nature Struct. Biol.*, 1999, **6**, 313.
39. A. Medek, E. T. Olejniczak, R. P. Meadows and S. W. Fesik, *J. Biomol. NMR*, 2000, **18**, 229.
40. V. Simplaceanu, J. A. Lukin, T. Y. Fang, M. Zou, N. T. Ho and C. Ho, *Biophys. J.*, 2000, **79**, 1146.
41. T. Yamazaki, T. Otomo, N. Oda, Y. Kyogoku, K. Uegaki, N. Ito, Y. Ishino and H. Nakamura, *J. Am. Chem. Soc.*, 1998, **120**, 5591.
42. T. Otomo, N. Ito, Y. Kyogoku and T. Yamazaki, *Biochemistry*, 1999, **38**, 16040.
43. T. W. Muir, *Synlett.*, 2001, **6**, 733-740.
44. R. Xu, B. Ayers, D. Cowburn and T. W. Muir, *Proc. Natl. Acad. Sci. USA*, 1999, **96**, 388.
45. U. K. Blaschke, G. J. Cotton and T. W. Muir, *Tetrahedron*, 2000, **56**, 9461.
46. M. L. Cai, Y. Huang, K. Sakaguchi, G. M. Clore, A. M. Gronenborn and R. Craigie, *J. Biomol. NMR*, 1998, **11**, 97.
47. J. Marley, M. Lu and C. Bracken, *J. Biomol. NMR*, 2001, **20**, 71.
48. T. Yabuki, T. Kigawa, N. Dohmae, K. Takio, T. Terada, Y. Ito, E. D. Laue, J. A. Cooper, M. Kainosho and S. Yokoyama, *J. Biomol. NMR*, 1998, **11**, 295.
49. T. Kigawa, T. Yabuki, Y. Yoshida, M. Tsutsui, Y. Ito, T. Shibata and S. Yokoyama, *FEBS Lett.*, 1999, **442**, 15.
50. K. Madin, T. Sawasaki, T. Ogasawara and Y. Endo, *Proc. Natl. Acad. Sci. USA*, 2000, **97**, 559.
51. K. Wüthrich, *Nature Struct. Biol.*, 1998, **5**, 492.
52. U. K. Nowak, X. Li, A. J. Teuten, R. A. G. Smith and C. M. Dobson, *Biochemistry*, 1993, **32**, 298.

53. R. E. Oswald, M. J. Bogusky, M. Bamberger, R. A. G. Smith and C. M. Dobson, *Nature*, 1989, **337**, 579.
54. M. J. Bogusky, C. M. Dobson and R. A. G. Smith, *Biochemistry*, 1989, **28**, 6728.
55. A. J. Teuten, R. A. G. Smith and C. M. Dobson, *FEBS Lett.*, 1991, **278**, 17.
56. V. Bushuev, A. T. Gudkov, A. Liljas and N. F. Sepetov, *J. Biol. Chem.*, 1989, **264**, 4498.
57. P-O. Lycksell, R. Ingemarson, R. Davis, A. Gräslund and L. Thelander, *Biochemistry*, 1994, **33**, 2838.
58. D. Filatov, R. Ingemarson, A. Gräslund and L. Thelander, *J. Biol. Chem.*, 1992, **267**, 15816.
59. S. Radford, E. D. Laue, R. N. Perham, S. R. Martin and E. Appella, *J. Biol. Chem.*, 1989, **264**, 767.
60. J. D. Green, R. N. Perham, S. J. Ulrich and E. Appella, *J. Biol. Chem.*, 1992, **267**, 23484.
61. R. N. Perham, *Biochemistry*, 1991, **30**, 8501.
62. R. N. Perham, *Annu. Rev. Biochem.*, 2000, **69**, 961.
63. J. A. Carver, *Prog. Ret. Eye Res.*, 1999, **18**, 431.
64. J. A. Carver and R. A. Lindner, *Int. J. Biol. Macromol.*, 1998, **22**, 197.
65. C. Slingsby, B. Norledge, A. Simpson, O. A. Bateman, G. Wright, H. P. C. Driessen, P. F. Lindley, D. S. Moss and B. Bax, *Prog. Ret. Eye Res.*, 1997, **16**, 3.
66. S. J. Landry, J. Zeilstra-Ryalls, O. Fayet, C. Georgopoulos and L. M. Gierasch, *Nature*, 1993, **364**, 255.
67. J. F. Hunt, A. J. Weaver, S. J. Landry, L. Gierasch and J. Deisenhofer, *Nature*, 1996, **379**, 37.
68. T. L. Volkert, J. D. Baleja and C. A. Kumamoto, *Biochem. Biophys. Res. Commun.*, 1999, **264**, 949.
69. R. Riek, S. Hornemann, G. Wider, R. Glockshuber and K. Wüthrich, *FEBS Lett.*, 1997, **413**, 282.
70. H. S. Cho, C. W. Liu, F. F. Damberger, J. G. Pelton, H. C. M. Nelson and D. E. Wemmer, *Protein Sci.*, 1996, **5**, 262.
71. A. Lecroisey, P. Martineau, M. Hofnung and M. Delepierre, *J. Biol. Chem.*, 1997, **272**, 362.
72. G. Wider and K. Wüthrich, *Curr. Opin. Struct. Biol.*, 1999, **9**, 594.
73. K. Pervushin, *Q. Rev. Biophys.*, 2000, **33**, 161.
74. K. Pervushin, R. Riek, G. Wider and K. Wüthrich, *Proc. Natl. Acad. Sci. USA*, 1997, **94**, 12366.
75. M. Czisch and R. Boelens, *J. Magn. Reson.*, 1998, **134**, 158.
76. J. Weigelt, *J. Am. Chem. Soc.*, 1998, **120**, 10778.
77. M. Rance, J. P. Loria and A. G. Palmer III, *J. Magn. Reson.*, 1999, **136**, 92.
78. K. V. Pervushin, G. Wider and K. Wüthrich, *J. Biomol. NMR*, 1998, **12**, 345.
79. T. Schulte-Herbrüggen and O. W. Sørensen, *J. Magn. Reson.*, 2000, **144**, 123.
80. C. Kojima and M. Kainosho, *J. Magn. Reson.*, 2000, **143**, 417.
81. G. Zhu, X. M. Kong and K. H. Sze, *J. Biomol. NMR*, 1999, **13**, 77.
82. R. Riek, *J. Biomol. NMR*, 2001, **21**, 99.
83. K. Pervushin, D. Braun, C. Fernández and K. Wüthrich, *J. Biomol. NMR*, 2000, **17**, 195.
84. R. Riek, G. Wider, K. Pervushin and K. Wüthrich, *Proc. Natl. Acad. Sci. USA*, 1999, **96**, 4918.
85. G. Zhu, Y. L. Xia, K. H. Sze and X. Z. Yan, *J. Biomol. NMR*, 1999, **14**, 377.
86. A. Meissner and O. W. Sørensen, *J. Magn. Reson.*, 1999, **140**, 499.
87. Y. Xia, K. Sze and G. Zhu, *J. Biomol. NMR*, 2000, **18**, 261.
88. K. V. Pervushin, G. Wider, R. Riek and K. Wüthrich, *Proc. Natl. Acad. Sci. USA*, 1999, **96**, 9607.
89. M. Salzmann, K. Pervushin, G. Wider, H. Senn and K. Wüthrich, *J. Biomol. NMR*, 1999, **14**, 85.
90. M. Salzmann, G. Wider, K. Pervushin, H. Senn and K. Wüthrich, *J. Am. Chem. Soc.*, 1999, **121**, 844.
91. A. Meissner and O. W. Sørensen, *J. Magn. Reson.*, 2001, **151**, 328.
92. P. Permi and A. Annila, *J. Biomol. NMR*, 2001, **20**, 127.
93. A. Eletsky, A. Kienhöfer and K. Pervushin, *J. Biomol. NMR*, 2001, **20**, 177.
94. R. Konrat, D. W. Yang and L. E. Kay, *J. Biomol. NMR*, 1999, **15**, 309.
95. F. Löhr, S. Pfeiffer, Y. J. Lin, J. Hartleib, O. Klimmek and H. Rüterjans, *J. Biomol. NMR*, 2000, **18**, 337.
96. A. Meissner and O. W. Sørensen, *J. Magn. Reson.*, 2000, **144**, 171.

97. G. Zhu, Y. L. Xia, L. K. Nicholson and K. H. Sze, *J. Magn. Reson.*, 2000, **143**, 423.
98. J. P. Loria, M. Rance and A. G. Palmer III, *J. Biomol. NMR*, 1999, **15**, 151.
99. K. Pervushin, *J. Biomol. NMR*, 2001, **20**, 275.
100. K. Pervushin, V. Gallius and C. Ritter, *J. Biomol. NMR*, 2001, **21**, 161.
101. M. Pellecchia, D. Meininger, A. L. Shen, R. Jack, C. B. Kasper and D. S. Sem, *J. Am. Chem. Soc.*, 2001, **123**, 4633.
102. A. Arora, F. Abildgaard, J. H. Bushweller and L. K. Tamm, *Nat. Struct. Biol.*, 2001, **8**, 334.
103. J. Evenäs, V. Tugarinov, N. R. Skrynnikov, N. K. Goto, R. Muhandiram and L. E. Kay, *J. Mol. Biol.*, 2001, **309**, 961.
104. F. H. T. Allain, D. E. Gilbert, P. Bouvet and J. Feigon, *J. Mol. Biol.*, 2000, **303**, 227.
105. L. Varani, S. I. Gunderson, I. W. Mattaj, L. E. Kay, D. Neuhaus and G. Varani, *Nature Struct. Biol.*, 2000, **7**, 329.
106. J. R. Tolman, J. M. Flanagan, M. A. Kennedy and J. H. Prestegard, *Proc. Natl. Acad. Sci. USA*, 1995, **92**, 9279.
107. N. Tjandra and A. Bax, *Science*, 1997, **278**, 1111.
108. A. Bax and N. Tjandra, *J. Biomol. NMR*, 1997, **10**, 289.
109. A. A. Bothner-By, P. G. Domaille and C. Gayathri, *J. Am. Chem. Soc.*, 1981, **103**, 5602.
110. G. M. Clore, M. R. Starich, C. A. Bewley, M. L. Cai and J. Kuszewski, *J. Am. Chem. Soc.*, 1999, **121**, 6513.
111. H. Schwalbe, S. B. Grimshaw, A. Spencer, M. Buck, J. Boyd, C. M. Dobson, C. Redfield and L. J. Smith, *Protein Sci.*, 2001, **10**, 677.
112. A. Annila, H. Aitio, E. Thulin and T. Drakenberg, *J. Biomol. NMR*, 1999, **14**, 223.
113. J. Meiler, W. Peti and C. Griesinger, *J. Biomol. NMR*, 2000, **17**, 283.
114. J. A. Losonczi, M. Andrec, M. W. F. Fischer and J. H. Prestegard, *J. Magn. Reson.*, 1999, **138**, 334.
115. M. A. Markus, R. B. Gerstner, D. E. Draper and D. A. Torchia, *J. Mol. Biol.*, 1999, **292**, 375.
116. N. R. Skrynnikov, N. K. Goto, D. W. Yang, W. Y. Choy, J. R. Tolman, G. A. Mueller and L. E. Kay, *J. Mol. Biol.*, 2000, **295**, 1265.
117. J. Evenäs, A. Mittermaier, D. W. Yang and L. E. Kay, *J. Am. Chem. Soc.*, 2001, **123**, 2858.
118. G. A. Mueller, W. Y. Choy, N. R. Skrynnikov and L. E. Kay, *J. Biomol. NMR*, 2000, **18**, 183.
119. P. Bayer, L. Varani and G. Varani, *J. Biomol. NMR*, 1999, **14**, 149.
120. E. T. Olejniczak, R. P. Meadows, H. Wang, M. L. Cai, D. G. Nettesheim and S. W. Fesik, *J. Am. Chem. Soc.*, 1999, **121**, 9249.
121. P. J. Bolon, H. M. Al-Hashimi and J. H. Prestegard, *J. Mol. Biol.*, 1999, **293**, 107.
122. H. M. Al-Hashimi, A. Gorin, A. Majumdar and D. J. Patel, *J. Am. Chem. Soc.*, 2001, **123**, 3179.
123. B. W. Koenig, D. C. Mitchell, S. König, S. Grzesiek, B. J. Litman and A. Bax, *J. Biomol. NMR*, 2000, **16**, 121.
124. G. M. Clore, A. M. Gronenborn and A. Bax, *J. Magn. Reson.*, 1998, **133**, 216.
125. G. M. Clore, A. M. Gronenborn and N. Tjandra, *J. Magn. Reson.*, 1998, **131**, 159.
126. J. J. Warren and P. B. Moore, *J. Magn. Reson.*, 2001, **149**, 271.
127. C. R. Sanders and J. H. Prestegard, *J. Am. Chem. Soc.*, 1992, **114**, 7096.
128. B. E. Ramirez and A. Bax, *J. Am. Chem. Soc.*, 1998, **120**, 9106.
129. H. M. Al-Hashimi, H. Valafar, M. Terrell, E. R. Zartler, M. K. Eidsness and J. H. Prestegard, *J. Magn. Reson.*, 2000, **143**, 402.
130. M. Zweckstetter and A. Bax, *J. Biomol. NMR*, 2001, **20**, 365.
131. J. Meiler, N. Blomberg, M. Nilges and C. Griesinger, *J. Biomol. NMR*, 2000, **16**, 245.
132. S. Moltke and S. Grzesiek, *J. Biomol. NMR*, 1999, **15**, 77.
133. N. R. Skrynnikov and L. E. Kay, *J. Biomol. NMR*, 2000, **18**, 239.
134. N. Tjandra, J. G. Omichinski, A. M. Gronenborn, G. M. Clore and A. Bax, *Nature Struct. Biol.*, 1997, **4**, 732.
135. M. Schmiedeskamp, P. Rajagopal and R. E. Klevit, *Protein Sci.*, 1997, **6**, 1835.
136. I. Bertini, I. C. Felli and C. Luchinat, *J. Biomol. NMR*, 2000, **18**, 347.
137. I. Bertini, M. B. L. Janik, G. H. Liu, C. Luchinat and A. Rosato, *J. Magn. Reson.*, 2001, **148**, 23.

138. V. Gaponenko, A. Dvoretsky, C. Walsby, B. M. Hoffman and P. R. Rosevear, *Biochemistry*, 2000, **39**, 15217.
139. M. R. Hansen, L. Mueller and A. Pardi, *Nature Struct. Biol.*, 1998, **5**, 1065.
140. M. R. Hansen, P. Hanson and A. Pardi, *Methods Enzymol.*, 2000, **317**, 220.
141. Y. Ishii, M. A. Markus and R. Tycko, *J. Biomol. NMR*, 2001, **21**, 141.
142. S. A. Riley and M. P. Augustine, *J. Phys. Chem. A*, 2000, **104**, 3326.
143. M. Ottiger and A. Bax, *J. Biomol. NMR*, 1998, **12**, 361.
144. D. L. Jakeman, D. J. Mitchell, W. A. Shuttleworth and J. N. S. Evans, *J. Biomol. NMR*, 1998, **12**, 417.
145. S. Cavagnero, H. J. Dyson and P. E. Wright, *J. Biomol. NMR*, 1999, **13**, 387.
146. H. Wang, M. Eberstadt, E. T. Olejniczak, R. P. Meadows and S. W. Fesik, *J. Biomol. NMR*, 1998, **12**, 443.
147. R. S. Prosser, J. A. Losonczi and I. V. Shiyanovskaya, *J. Am. Chem. Soc.*, 1998, **120**, 11010.
148. M. Rückert and G. Otting, *J. Am. Chem. Soc.*, 2000, **122**, 7793.
149. J. A. Losonczi and J. H. Prestegard, *J. Biomol. NMR*, 1998, **12**, 447.
150. E. Brunner, M. R. Arnold, W. Kremer and H. R. Kalbitzer, *J. Biomol. NMR*, 2001, **21**, 173.
151. M. R. Hansen, M. Rance and A. Pardi, *J. Am. Chem. Soc.*, 1998, **120**, 11210.
152. B. W. Koenig, J. S. Hu, M. Ottiger, S. Bose, R. W. Hendler and A. Bax, *J. Am. Chem. Soc.*, 1999, **121**, 1385.
153. K. Fleming, D. Gray, S. Prasannan and S. Mathews, *J. Am. Chem. Soc.*, 2000, **122**, 5224.
154. M. Ottiger, F. Delaglio and A. Bax, *J. Magn. Reson.*, 1998, **131**, 373.
155. N. Tjandra and A. Bax, *J. Magn. Reson.*, 1997, **124**, 512.
156. M. Ottiger, F. Delaglio, J. L. Marquardt, N. Tjandra and A. Bax, *J. Magn. Reson.*, 1998, **134**, 365.
157. A. Ross, M. Czisch and T. A. Holak, *J. Magn. Reson. Ser. A*, 1996, **118**, 221.
158. A. Meissner, J. O. Duus and O. W. Sørensen, *J. Biomol. NMR*, 1997, **10**, 89.
159. A. Meissner, J. O. Duus and O. W. Sørensen, *J. Magn. Reson.*, 1997, **128**, 92.
160. J. R. Tolman and J. H. Prestegard, *J. Magn. Reson. Ser. B*, 1996, **112**, 245.
161. J. H. Prestegard, H. M. Al-Hashimi and J. R. Tolman, *Q. Rev. Biophys.*, 2000, **33**, 371.
162. M. H. Lerche, A. Meissner, F. M. Poulsen and O. W. Sørensen, *J. Magn. Reson.*, 1999, **140**, 259.
163. G. Kontaxis, G. M. Clore and A. Bax, *J. Magn. Reson.*, 2000, **143**, 184.
164. P. Permi, S. Heikkinen, I. Kilpeläinen and A. Annila, *J. Magn. Reson.*, 1999, **140**, 32.
165. P. Permi, T. Sorsa, I. Kilpeläinen and A. Annila, *J. Magn. Reson.*, 1999, **141**, 44.
166. P. Permi, P. R. Rosevear and A. Annila, *J. Biomol. NMR*, 2000, **17**, 43.
167. S. Heikkinen, P. Permi and I. Kilpeläinen, *J. Magn. Reson.*, 2001, **148**, 53.
168. M. Salzmann, G. Wider, K. Pervushin and K. Wüthrich, *J. Biomol. NMR*, 1999, **15**, 181.
169. J. J. Chou, F. Delaglio and A. Bax, *J. Biomol. NMR*, 2000, **18**, 101.
170. K. E. Kövér and G. Batta, *J. Magn. Reson.*, 2001, **151**, 60.
171. E. De Alba, M. Suzuki and N. Tjandra, *J. Biomol. NMR*, 2001, **19**, 63.
172. B. Brutscher, *J. Magn. Reson.*, 2001, **151**, 332.
173. F. Löhr and H. Rüterjans, *J. Magn. Reson.*, 2000, **146**, 126.
174. P. Permi, S. Heikkinen, I. Kilpeläinen and A. Annila, *J. Magn. Reson.*, 1999, **139**, 273.
175. G. Kontaxis and A. Bax, *J. Biomol. NMR*, 2001, **20**, 77.
176. M. L. Cai, H. Wang, E. T. Olejniczak, R. P. Meadows, A. H. Gunasekera, N. Xu and S. W. Fesik, *J. Magn. Reson.*, 1999, **139**, 451.
177. T. Carlomagno, W. Peti and C. Griesinger, *J. Biomol. NMR*, 2000, **17**, 99.
178. F. Tian, P. J. Bolon and J. H. Prestegard, *J. Am. Chem. Soc.*, 1999, **121**, 7712.
179. W. Peti and C. Griesinger, *J. Am. Chem. Soc.*, 2000, **122**, 3975.
180. G. Otting, M. Rückert, M. H. Levitt and A. Moshref, *J. Biomol. NMR*, 2000, **16**, 343.
181. F. Tian, J. A. Losonczi, M. W. F. Fischer and J. H. Prestegard, *J. Biomol. NMR*, 1999, **15**, 145.
182. F. Tian, C. A. Fowler, E. R. Zartler, F. A. Jenney Jr, M. W. Adams and J. H. Prestegard, *J. Biomol. NMR*, 2000, **18**, 23.
183. M. Pellecchia, C. W. Vander Kooi, K. Keliikuli and E. R. P. Zuiderweg, *J. Magn. Reson.*, 2000, **143**, 435.

184. A. Kaikkonen and G. Otting, *J. Am. Chem. Soc.*, 2001, **123**, 1770.
185. M. Andrec, P. C. Du and R. M. Levy, *J. Am. Chem. Soc.*, 2001, **123**, 1222.
186. P. Dosset, J. C. Hus, D. Marion and M. Blackledge, *J. Biomol. NMR*, 2001, **20**, 223.
187. A. Mittermaier and L. E. Kay, *J. Am. Chem. Soc.*, 2001, **123**, 6892.
188. K. Wüthrich, in *NMR in Biological Research: Peptides and Proteins*, North Holland, Amsterdam 1976.
189. I. Bertini, C. Luchinat and M. Piccioli, *Methods Enzymol.*, 2001, **339**, 314.
190. D. L. Turner, L. Brennan, S. G. Chamberlin, R. O. Louro and A. V. Xavier, *Eur. Biophys. J. Biophys. Lett.*, 1998, **27**, 367.
191. G. Hernández, A. Wilks, R. Paolesse, K. M. Smith, P. R. Ortiz de Montellano and G. N. La Mar, *Biochemistry*, 1994, **33**, 6631.
192. C. M. Gorst, A. Wilks, D. C. Yeh, P. R. Ortiz de Montellano and G. N. La Mar, *J. Am. Chem. Soc.*, 1998, **120**, 8875.
193. U. Kolczak, C. Han, L. A. Sylvia and G. N. La Mar, *J. Am. Chem. Soc.*, 1997, **119**, 12643.
194. G. N. La Mar, U. Kolczak, A. T. T. Tran and E. Y. T. Chien, *J. Am. Chem. Soc.*, 2001, **123**, 4266.
195. J. S. De Ropp, P. Mandal, S. L. Brauer and G. N. La Mar, *J. Am. Chem. Soc.*, 1997, **119**, 4732.
196. A. Asokan, J. S. De Ropp, S. L. Newmyer, P. R. Ortiz de Montellano and G. N. La Mar, *J. Am. Chem. Soc.*, 2001, **123**, 4243.
197. J. S. De Ropp, Z. G. Chen and G. N. La Mar, *Biochemistry*, 1995, **34**, 13477.
198. S. Vathyam, R. A. Byrd and A. F. Miller, *Magn. Reson. Chem.*, 2000, **38**, 536.
199. D. L. Sorkin and A. F. Miller, *J. Biomol. NMR*, 2000, **17**, 311.
200. D. L. Sorkin, D. K. Duong and A. F. Miller, *Biochemistry*, 1997, **36**, 8202.
201. A. Bondon and C. Mouro, *J. Magn. Reson.*, 1998, **134**, 154.
202. T. Nakayama, Y. Arata and I. Shimada, *Biochemistry*, 1993, **32**, 13961.
203. A. Odaka, J. I. Kim, H. Takahashi, I. Shimada and Y. Arata, *Biochemistry*, 1992, **31**, 10686.
204. T. Scherf, R. Hiller and J. Anglister, *FASEB J.*, 1995, **9**, 120.
205. M. E. Girvin and R. H. Fillingame, *Biochemistry*, 1995, **34**, 1635.
206. P. J. M. Folkers, J. P. M. van Duynhoven, H. T. M. Lieshout, B. J. M. Harmsen, J. H. Van Boom, G. I. Tesser, R. N. H. Konings and C. W. Hilbers, *Biochemistry*, 1993, **32**, 9407.
207. S. Arumugam, C. L. Hemme, N. Yoshida, K. Suzuki, H. Nagase, M. Bejanskii, B. Wu and S. R. Van Doren, *Biochemistry*, 1998, **37**, 9650.
208. Q. Kleerekoper, J. W. Howarth, X. Guo, R. J. Solaro and P. R. Rosevear, *Biochemistry*, 1995, **34**, 13343.
209. Q. J. Zhao, C. Abeygunawardana and A. S. Mildvan, *Biochemistry*, 1997, **36**, 3458.
210. M. Scarselli, G. Esposito, H. Molinari, L. Ragona, L. Zetta and N. Niccolai, *Trends Chem. Phys.*, 1996, **4**, 99.
211. H. Molinari, G. Esposito, L. Ragona, M. Pegna, N. Niccolai, R. M. Brunne, A. M. Lesk and L. Zetta, *Biophys. J.*, 1997, **73**, 382.
212. N. Niccolai, A. Ciutti, O. Spiga, M. Scarselli, A. Bernini, L. Bracci, D. Di Maro, C. Dalvit, H. Molinari, G. Esposito and P. A. Temussi, *J. Biol. Chem.*, 2001, **276**, 42455.
213. P. C. Driscoll, D. Esposito and M. Pfuhl, *Nucl. Magn. Reson.*, 1999, **29**, 340.
214. A. T. Brünger, P. D. Adams, G. M. Clore, W. L. DeLano, P. Gros, W. Grosse-Kunstleve, J-S. Jiang, J. Kuszewski, M. Nilges, N. S. Pannu, R. J. Read, L. M. Rice, T. Simonson and G. L. Warren, *Acta Cryst. D*, 1998, **D54**, 905.
215. P. Güntert, C. Mumenthaler and K. Wüthrich, *J. Mol. Biol.*, 1997, **273**, 283.
216. L. Bianci, I. Bertini, M. A. Cremonini, G. Gori Savellini, C. Luchinat, K. Wüthrich and P. Güntert, *J. Biomol. NMR*, 1998, **12**, 553.
217. D. M. Standley, V. A. Eyrich, A. K. Felts, R. A. Friesner and A. E. McDermott, *J. Mol. Biol.*, 1999, **285**, 1691.
218. P. M. Bowers, C. E. M. Strauss and D. Baker, *J. Biomol. NMR*, 2000, **18**, 311.
219. D. E. Zimmerman, C. A. Kulikowski, Y. P. Huang, W. Q. Feng, M. Tashiro, S. Shimotakahara, C. Y. Chien, R. Powers and G. T. Montelione, *J. Mol. Biol.*, 1997, **269**, 592.

220. D. E. Zimmerman, C. A. Kulikowski, L. L. Wang, B. A. Lyons and G. T. Montelione, *J. Biomol. NMR*, 1994, **3**, 241.
221. J. A. Lukin, A. P. Gove, S. N. Talukdar and C. Ho, *J. Biomol. NMR*, 1997, **9**, 151.
222. C. Mumenthaler and W. Braun, *J. Mol. Biol.*, 1995, **254**, 465.
223. M. Nilges, M. J. Macias, S. I. O'Donoghue and H. Oschkinat, *J. Mol. Biol.*, 1997, **269**, 408.
224. B. M. Duggan, G. B. Legge, H. J. Dyson and P. E. Wright, *J. Biomol. NMR*, 2001, **19**, 321.
225. M. Salzmann, K. Pervushin, G. Wider, H. Senn and K. Wüthrich, *Proc. Natl. Acad. Sci. USA*, 1998, **95**, 13585.
226. M. Hennig, A. D'Arcy, I. C. Hampele, M. G. P. Page, C. Oefner and G. E. Dale, *Nat. Struct. Biol.*, 1998, **5**, 537.
227. M. A. McCoy and L. Meuller, *J. Am. Chem. Soc.*, 1992, **114**, 2108.
228. A. DeMarco and K. Wüthrich, *J. Magn. Reson.*, 1976, **24**, 201.
229. P. Güntert, V. Dötsch, G. Wider and K. Wüthrich, *J. Biomol. NMR*, 1992, **2**, 619.
230. C. Bartels, T. Xia, M. Billeter, P. Güntert and K. Wüthrich. *J. Biomol. NMR*, 1995, **6**, 1.

Accurate Diagnosis and Prognosis of Human Cancers by Proton MRS and a Three-stage Classification Strategy

CYNTHIA L. LEAN,[1] RAY L. SOMORJAI,[2]
IAN C. P. SMITH,[2] PETER RUSSELL,[1] and
CAROLYN E. MOUNTFORD[1]

[1]*Institute for Magnetic Resonance Research, PO Box 148, St Leonards, NSW, 1590, Australia, and Department of Magnetic Resonance in Medicine, University of Sydney, NSW, 2006, Australia*
[2]*Institute for Biodiagnostics, National Research Council of Canada, 435 Ellice Avenue, Winnipeg, MB, R3B 1Y6, Canada*

ANNUAL REPORTS ON NMR SPECTROSCOPY
VOLUME 48 ISBN 0-12-505448-3

1. INTRODUCTION

Human biopsy material can be analysed by magnetic resonance spectroscopy (MRS), that may provide accurate diagnosis and, for some organs, prognosis of malignant disease. Consequently, improved patient management becomes feasible. The MRS method detects altered cellular chemistry that occurs before morphological changes are observed histologically, and thus can predict malignant potential even in the early stages of disease. In addition, information on prognostic variables that would currently require detailed, expensive and invasive techniques, such as sentinel node biopsy, is available from the primary lesion. The MR method is fast, accurate and robust, and will complement orthodox histopathology.

1.1. Limitations of histopathology

Histopathology has been the medical diagnostic gold standard for much of the 20th century, providing the diagnostic and prognostic parameters of human malignancy. Excellent though it is, histopathology has significant limitations. The principal limitation is the restricted range of morphological changes that tissues can express, each in a continuum, yet from which pathologists are expected to extract a sophisticated pattern specific for individual disease processes. These patterns overlap, are susceptible to subjective assessment, and may be altered by sampling error. The skill, experience and thoroughness of both surgeons and pathologists all play a part in ensuring the suitability of a given biopsy for assessment by histopathology and from which detailed diagnostic and prognostic clues are to be gleaned.

Patient assessment involves histological grading and clinicopathological staging. Staging of cancer determines the extent and spread of the disease. Since clinical presentation of patients does not usually reveal how long a neoplasm has been present, clinical staging is unable to distinguish between recent but aggressive primary tumours and older but more slowly growing ones. This is the role of histological grading. Grading attempts to establish the aggressiveness of

the tumour based on the degree of differentiation or anaplasia of tumour cells. Such a distinction is at best subjective and often inconclusive. Adequate staging of disease is an even greater problem. Histopathological assessment of lymph nodes for staging purposes is subject to observer and sampling errors due to the large volumes of tissue to be assessed and the time and resource constraints that prevent thorough and complete examination. A retrospective study[1] revealed that: 'Serial sectioning of lymph nodes judged to be disease-free after routine examination revealed micro-metastases in an additional 83 (9%) of 921 breast cancer subjects.'

Current histopathological procedures fall short of the 100% accuracy that we all strive for in medical diagnosis. This mandates the development of a new modality that would remove sampling errors and subjectivity (observer error). Improved methods should optimize diagnostic accuracy of established disease. An important advantage would be identification and measurement of prognostic variables prior to their becoming obvious histologically, i.e. the identification of true malignant potential of a lesion at an earlier, more readily treatable stage of development.

1.2. Cancer pathology determined by ^{1}H MRS on biopsy specimens

MRS reports on pools of chemicals in cells as they alter their function, be that physiological or pathological.[2] These changes are complicated and may involve a number of different biochemical pathways changing at one time. The MRS method reports only on pools of chemicals that are mobile and measurable on the MR timescale.[3] This restricts the information to pools of chemicals that change with disease processes[4–9] and ageing,[10] providing not only diagnosis of malignancy with accuracies that are equivalent to those achieved by histopathology,[11–20] but also information on prognosis[21] and malignant potential in early neoplastic disease states.

The clinical application of MRS to the management of cancer has, however, been slow to emerge and it has only in the last decade achieved the sensitivity and specificity necessary for use as a clinical method. Conventionally, MR spectra have been assessed visually, and peak height and/or integral ratios of preselected resonances have been used to analyse the data. This approach, termed in this review 'visual inspection', although accurate for many organs (approaching 100%),[13,15–18] makes use of a very small amount of the available information in each spectrum, and thus additional biological and diagnostic information is not utilized. Several groups have attempted to use more sophisticated methods to analyse MRS data[22–30] (Table 1). These studies, however, lack one or more of three important criteria: (i) analysis of MRS data against known clinical outcomes or careful and complete histopathological assessment of the entire biopsy specimen; (ii) patient cohorts of sufficient size to accommodate thorough statistical analysis; and/or

Table 1. Mathematical analysis of MRS data

Field of application	Number of samples	Preprocessing	Retention of spectral identity	Method of classification	Cross-validation	Aggregated classifiers	Reference
^{1}H, rat hepatoma, carcinosarcoma, fibrosarcoma, prolactinoma, induced mammary adenocarcinoma, normal liver, kidney, spleen	56	Digitized, normalized, PCA, cluster analysis	No	BP-NN			22
^{31}P, *in vivo*, rodent hepatoma, prolactinoma, fibrosarcoma, induced mammary tumours, normal liver, brain, muscle	58	Phasing, normalization, PCA on some, cluster analysis	Yes; PCA on some	BP-ANN	LOO		23
^{1}H, rat hepatoma, carcinosarcoma, fibrosarcoma, prolactinoma, normal liver, kidney, spleen	84	None	Yes	BP-NN			24
^{31}P, rat hepatoma, carcinosarcoma, prolactinoma, normal liver and brain	55	Phasing, normalization; wavelet transform on lipid metabolite peaks	Yes	LDA	LOO		25
^{1}H, *in vivo* human brain tumours	105	Zero-filling, application of Gaussian filter, averaged intensity for metabolites, normalized	Yes	LDA	LOO		26
^{1}H, *in vivo* human brain	61	HLSVD to remove water resonance; intensities relative to unsuppressed water resonance	Yes	BP-ANN	LOO		27
^{1}H, human glioma cell cultures	18			BP-NN	LOO		28
^{1}H, human brain tumour biopsies	118	Digitization, normalization, PCA, cluster analysis	Retained on some PCA on some	Competitive NN BP-NN	LOO		29
^{1}H, *in vivo* human brain	138	Zero filling, zero-order phase correction, baseline correction	Yes	ANN	K-fold		30

PCA, principal component analysis; NN, neural net; LOA, linear discriminant analysis; LOO, leave-one-out; HLSVD, filtering signals in the time domain; ANN, artificial neural networks.

(iii) robust and comprehensive methods of classification of the MR spectral data.

A series of clinical studies are now complete that fulfil the above criteria. The results demonstrate that ^{1}H MRS on biopsy material can diagnose or exclude malignancy with at least the accuracy of current aspiration or exfoliative cytological techniques used for thyroid, brain, ovary, prostate and breast and, in some cases, can greatly exceed this accuracy. In the case of sampling a primary breast cancer by fine needle aspiration biopsy (FNAB), the MRS method, combined with robust classification, can also provide prognostic information; specifically, it can predict the involvement of regional axillary lymph nodes and invasion of the peritumoral vasculature. This offers the potential for a paradigm shift in the management of breast cancer by eliminating the need for surgical removal of lymph nodes for staging of the disease (including the current and more conservative sentinel node identification and biopsy).

1.3. Robust data classification

MR spectra from cells and tissues can contain resonances from up to 60 different chemical species[6,7,31–36] that can all have altering MR parameters. It is this complex relationship that provides the detailed diagnostic and prognostic information. Advanced methods of data analysis are required to extract all available information reliably.

Multivariate methods of mathematical analysis are needed that are robust, non-subjective and make use of all spectral information. A summary of reports using multivariate methods for the analysis of biomedical MRS data is listed in Table 1. In these studies, however, the requirements for a large patient cohort, data preprocessing/reduction and/or validation of classifiers are not met.

It is essential for the clinical implementation of the MRS technology that high sensitivity and specificity are available reproducibly. This requirement was the driving force in the development of the statistical classification strategy (SCS)-based multivariate analysis methods that form the focus of this review. This review aims to summarize the clinical MRS studies reported to date that have included clinical outcomes and/or histopathological assessment of the entire biopsy specimen examined by MRS and where the data have been analysed in recognition of the criteria essential for robust data classification.

2. THREE-STAGE DATA CLASSIFICATION STRATEGY

The three-stage data classification strategy has been developed primarily during the MR and pathological assessment of the six separate organs summarized below. The stages were developed either as an improvement of the strategy *per*

se, or when further development was required due to the difficulty of the pathology of the disease process.

2.1. Introduction

The reliable, robust classification of diseases or disease states via biomedical spectroscopy requires special methodology that can handle complex data. In most cases, such data defy simple analyses that assume the presence of easily identified features ('markers') in the data set. In particular, the methodology must be able to handle data sets that contain relatively few spectra (in the 50s) but many attributes (data points) per spectrum (in the 1000s); ideally, it should also provide some measure of the degree of confidence in a given diagnosis.

A three-stage SCS was specifically developed at the Institute for Biodiagnostics (IBD), National Research Council Canada (NRC), to address these issues. The methodology has greatly enhanced the ability of researchers and clinicians to analyse spectroscopic data of biomedical origin, and has resulted in the development of highly accurate and reliable classifiers for a variety of clinical applications. These include diagnosis of astrocytomas,[37] classification of Alzheimer's disease[38,39] and various forms of arthritis,[40] determining grade and steroid receptor status of breast tumours,[41] and diagnosis of cancers of the prostate,[42] ovary,[43] colon,[44] oesophagus[45] and thyroid.[46] In addition, several classifiers have been developed to analyse the infrared (IR) spectra of blood serum[47,48] to distinguish between healthy subjects and patients with particular disease(s).

2.2. Limitations of commonly used classification methods

Biomedical spectroscopists have commonly used one of two methods to define diseases or disease states. The simplest approach attempts classification by determining peak ratios of compounds that are believed to be diagnostic on biochemical grounds. This classification approach lacks robustness, because it ignores most of the information in the data available for analysis. Furthermore, there is no statistically reliable way of assessing a class assignment's validity, especially on a new exemplar. In the multivariate classification context, visual inspection based on peak ratios corresponds to the overly optimistic resubstitution method, using all samples, and certain *a priori* selected peak ratios as the discriminating features.

Other attempts have focused on proof-of-concept aspects of classification, using standard supervised pattern recognition methods. Major deficiencies exist in this approach when attempting the classification of biomedical spectra, including the following.

2.2.1. *Inappropriate choice of feature space reduction methods*

Feature space reduction methods are mandatory for biomedical spectra, since spectra consist of a large number (N) of original features (intensities at N frequencies, typically $N = O(1000)$ ($O(N)$ means 'order of N'), and relatively few exemplars ($M = O(50)$). Most often, 'off-the-shelf', black box methods, such as principal component analysis (PCA), are chosen for feature reduction, without taking into account the methods' applicability or limitations. For example, for PCA, the first $K << N$ PCs are typically chosen as the new, reduced features. PCA is a linear method, which 'scrambles' the original features (frequencies), resulting in new combinations (Principal components PCs) that sequentially 'explain' the *variance* in the data. However, the inherent orthogonality constraints on the PCs produce undesirable mixing effects. Feature reduction by PCA falsely assumes that explaining most of the data variance will lead to maximal class discrimination. This is rarely the case. Because PCA is a global method (i.e. the PCs are linear combinations of *all* N original attributes), its first few PCs generally account for the gross aspects of the high-dimensional data, not their subtle differences. However, good discrimination generally requires identifying the latter. The first stage of the SCS method overcomes these and other limitations.

2.2.2. *Suboptimal and/or excessively complex classifiers*

Classifiers are most often created using all M samples (*resubstitution* method). This leads to overly optimistic classification results, with attendant poorer *generalizability*; that is, new samples, not used in developing the classifier, will be frequently misclassified. In principle, the method of *cross-validation* achieves more robust and reliable classification. However, the classical *leave-one-out* (LOO) version, which creates a classifier using M-1 of the M-sample data set and then assigns the excluded sample to the closest class (repeating this process for all M samples), does the classification of each sample with a (somewhat) different classifier. Although LOO produces an estimate of the misclassification error, for small M the variability among the M classifiers tends to be unacceptably large. A more serious failing is that the LOO process does not produce a single, optimal classifier.

Employing more sophisticated, complex classifiers, e.g. neural nets, is particularly dangerous, because when used as a black box, they can easily produce perfect classification of the training set ('overfitting'), while providing no generalization capability. The problem stems from using too many parameters for the fitting, which is particularly pernicious when the sample set size is small. The second stage of the SCS is designed to overcome many of these limitations.

2.2.3. *Lack of statistical confidence in class assignments*

For the majority of cases reported in the literature, class assignment is a categorical, yes–no proposition. This means that, more frequently than not, an

apparently good classification result is in fact effectively meaningless: unless *probabilities* of class assignment are explicitly given, the validity of a binary assignment lacks any measure of confidence (statistical significance). Computing (approximate) class assignment probabilities is easy; creating classifiers that produce statistically significant assignments for most samples is much more challenging. The third stage of the SCS approaches and solves this problem by using the outcome probabilities of several classifiers as new input attributes to an ultimate classifier.

2.3. The statistical classification strategy

The general SCS was designed specifically for MR and IR spectra of biofluids and tissue biopsies. The SCS evolved gradually. Its evolution is traced in more detail in the more specific discussions below. The current version of the strategy consists of three stages and is summarized in Fig. 1.

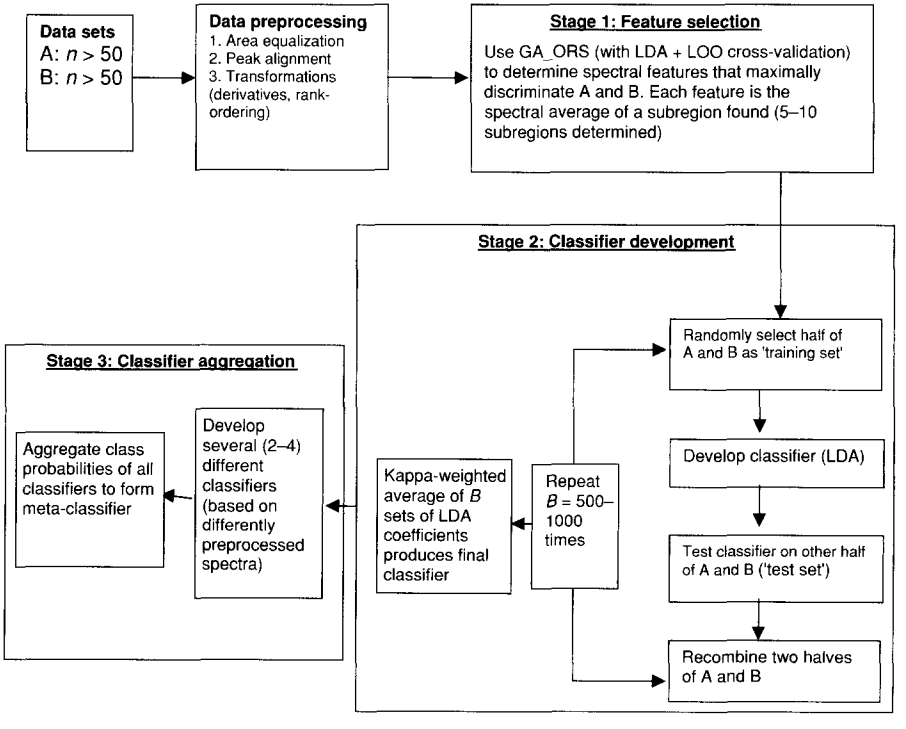

Fig. 1. Statistical classification strategy (SCS): a schematic road map of how the SCS method is developed for individual databases. GA_ORS, genetic algorithm based optimal region selection; LDA, linear discriminant analysis; LOO, leave-one-out (method of cross-validation); coeff, coefficients.

2.3.1. Stage 1: Data preprocessing and feature extraction

Prior to the actual feature extraction, a number of options are available and used to preprocess the spectra. The spectra are invariably converted to *magnitude* spectra (this avoids any subjectivity introduced by phasing procedures) and aligned on a reference peak. Other preprocessing may involve one or more of the following steps: the spectra are normalized to unit area; spectral derivatives are taken; spectral intensities are replaced by their *ranks*; some other nonlinear transformation, such as α-scaling,[49] is first applied to the spectra. Following such preprocessing, the most important aspect of the SCS is the feature extraction procedure that eliminates redundant information and/or noise. This methodology extracts discriminatory information from biomedical spectra while retaining spectral identity. A Genetic-Algorithm-based Optimal Region Selection algorithm (GA_ORS,[50,51]) is used. GA was chosen because it is a global minimizer, working on a string of 0s and 1s. For spectra, R_k consecutive 1s would correspond to the kth subregion of length R_k. The most relevant input into the algorithm is the maximum number K of features, i.e. distinct subregions required, the type of feature space-reducing operation/transformation (typically averaging) to be carried out, the population size, the number of generations, and a random seed.[51] The operations comprise the standard GA options: mutation and crossover. The algorithm then optimizes regions with respect to location and width. The K final discriminatory attributes are the *averages* (or some other predefined functions) of the intensities of these K subregions. The objective function that the GA_ORS algorithm optimizes has been devised to minimize simultaneously the misclassification error and the classification fuzziness, (i.e. increase class assignment probabilities). The present implementation of GA_ORS uses, at all GA stages of subregion processing, either a Linear Discriminant Analysis (LDA) classifier, or, for two-class problems, a robust regression variant, least trimmed squares, both with LOO cross-validation, to test how discriminatory are the current subregions. A few (at most 5–10) maximally discriminatory subregions in the spectra are identified, and the spectral averages of these subregions are the ultimate features used at the second stage.

For a limited number N of original features, exhaustive search (ES) for the best subset(s) is feasible. For larger N, we have developed a dynamic programming (DP)-based algorithm[51] that often produces near-optimal solutions, in feasible computer times.

2.3.2. Stage 2: Development of robust classifiers

Having obtained K most discriminatory subregion averages (the features), stage 2 consists of developing from these features a robust, reliable classifier. *Cross-validation* is the appropriate approach to deal with data sets with low numbers of samples (at least 50 samples per class are required for acceptable statistical significance). Inspired by *bootstrapping*, a modern statistical resampling

approach, the method randomly selects from each class half the samples (*training set*), creating a classifier (using the simple but reliable linear discriminant analysis (LDA), or its robust version, least trimmed squares). The other half of the samples (*test set*) is then used to assess the efficacy of this classifier. The training samples are then replaced (i.e. returned to the original pool) and the process is repeated, typically with $B = 500–1000$ repetitions. The optimized classifier coefficients for all B tries are saved. The *weighted average* of these B sets of coefficients produces the final classifier. The weights are Cohen's *measure of agreement*, κ, $\sim 0 \leq \kappa \leq 1$, with $\kappa = 1$ signifying perfect classification. κ is chance-corrected, that is, agreement due to chance is assessed and discounted. The B κ-values used for the weights are the ones obtained for the less optimistic *test sets*, *not* for the bootstrap training sets. Classifier outcome is reported as *class probability*. The way in which the final, single classifier is produced (as a κ_{test}-weighted average of B individual classifiers) is novel and has several advantages. Storage requirements are negligible, and new samples to be classified need be submitted only to a single classifier rather than to B separate ones. This means a B-fold speed-up in computation of the class probabilities. Furthermore, extensive experimentation showed that this single, κ-weighted classifier gives better classification results than would be obtained from the collection of B separate classifiers.

2.3.3. Stage 3: Classifier aggregation

In a clinical setting, classification robustness and reliability require that the class assignment of samples is statistically significant (high confidence). Thus, the class assignment probabilities need to be close to unity. For two-class classification, the confidence threshold has been set to 0.75, halfway between 0.5 (completely undecidable) and 1.0 (absolutely certain). (A sample's class assignment is termed *crisp* if its class probability is ≥ 0.75.) If the overall percentage crispness produced by a single classifier is low, or the accuracy is not satisfactory, a third stage of the SCS is activated. This aggregates the outputs (class probabilities) of several classifiers to form a new classifier. The consequence of aggregation is that classification accuracy and reliability are generally greater than for the best of the individual classifiers. Previous work has shown that classifier independence is not critical when consensus results are required. Thus, the third stage does not need to rely on widely different classifier methodologies (this is in contrast to the first attempt at classifier fusion[46]). Instead, LDA (least trimmed squares) is used as the only classifier type, but the spectra are prepared differently. To date, successful transformations prior to region selection have involved taking the first derivatives of the spectra and/or rank-ordering these first derivatives. The use of ranks has statistical advantages in that outlier influence is eliminated or diminished and the spectra do not need area normalization. Having produced L different two-class classifiers, each individual spectrum is submitted to all L classifiers, resulting in L different probabilities. These probabilities

constitute the new set of attributes to be used to develop the ultimate classifier, again using the bootstrap cross-validation method of stage 2. In practice, L is small, mostly only 2, and rarely greater than 4, and thus the ultimate classifier tends to be even more robust than the best of the L individual classifiers.

3. FOLLICULAR THYROID NEOPLASIA

Thyroid nodules are common, particularly in women, and are estimated as being clinically evident in up to 10% of the female population. While the vast majority (90–95%) of solitary thyroid nodules are benign,[52,53] the exclusion of malignancy in follicular thyroid nodules remains a significant problem in diagnosis, currently made on the excised organ obtained at a partial thyroidectomy. Preoperative FNAB cytology, although accurate in identifying papillary, medullary and anaplastic carcinoma, is unable to distinguish reliably malignant from benign follicular neoplasms, the latter being the commonly encountered nodules in these patients.

Follicular adenomas and follicular carcinomas are usually indistinguishable in radiological, cytopathological or clinical features, unless, of course, metastases are present. The distinction relies on detection of capsular or vascular invasion at the periphery of the carcinoma, and this, in turn, requires surgical excision—an expensive and not risk-free operation—and detailed pathological examination of the specimen.

Cytological examination of FNAB specimens taken from thyroid nodules has been one of the most significant advances in the investigation of thyroid disease in the past two decades. Unfortunately, the residual problem of the 'atypical follicular lesion' remains,[54] as noted above, and its resolution regularly requires surgery. MRS on the same FNAB specimen has been shown to be a technique that more accurately reflects the actual biology of follicular thyroid tumours, allowing a more definitive exclusion of the diagnosis of thyroid cancer and thus reducing the need for unnecessary surgery performed solely for diagnostic purposes.

3.1. Diagnosis of pathology by visual inspection of MR data

In a study of 53 patients with thyroid nodules, one-dimensional (1D) ^{1}H MRS distinguished normal thyroid tissue from proven carcinoma of all types with a sensitivity and specificity of 100% ($p < 0.0001$, Student t-test).[15] The basis of the discrimination was altered cellular chemistry reflected in the resonance intensity ratio at a chemical shift of 1.7 ppm (composite with major contribution from lysine) and the methyl groups at 0.9 ppm. The lipid spectral profile is much weaker in adenoma than carcinoma, showing the same trend previously observed for uterine cervix.[13]

Follicular thyroid neoplasms, not overtly malignant on current pathological criteria (see above), were found to span both the normal and malignant spectral patterns. The biological significance of the span of MR spectral ratios recorded for follicular lesions is unclear, although it would support the concept that there is a progression from benign to malignant that precedes any histological evidence of malignancy. While molecular genetic studies support this concept,[55] overlap between the two classes can arise due to biochemical and/or instrumental variation, which at this stage cannot be excluded.

Similar diagnostic information is obtainable from the MR spectra of as few as 10^6 thyroid cells, obtained from an FNAB.[17] In a study of FNAB and tissue specimens from 70 patients undergoing thyroidectomy for solitary or dominant thyroid nodules, a close correlation between fine needle MR spectra and tissue spectra for a range of benign and malignant neoplasms has been demonstrated.[17] The sensitivity or probability of correctly identifying thyroid cancer on the basis of MRS assessed on FNAB was 95%, although this result lacks robustness.

3.2. Development of computerized consensus diagnosis (CCD)

The application of classifier fusion, denoted *computerized consensus diagnosis* (CCD), to subsets of the above thyroid data allowed refinement of the discriminatory potential of spectral analysis.[46] The thyroid data were chosen for method development, since the database was of a reasonable size and it was known that thorough and accurate pathological assessment had been undertaken on all specimens. It was assumed in the study that no single multivariate classification technique would work equally well for all medical diagnostic problems. The strategy for improving classification reliability/robustness, therefore, was the cross-validated training of several independent classifiers of diverse conceptual and methodological origin on the same data and then combining the outcomes to form a *consensus diagnosis*. Classification methods, including LDA, a neural net-(NN) based method, and genetic programming (GP), were used on two spectral regions, and the median of six classification outcomes was chosen as the consensus. This procedure yielded 100% specificity and 100% sensitivity on the training sets, and 100% specificity and 98% sensitivity on samples of known malignancy in the test sets. The overall accuracy was 99% (Table 2). An important consequence of the study was that the reliability of any class allocation was quantitated (graded class membership, 0–100%) rather than being just a yes–no assignment.

One-dimensional MR spectra (Fig. 2) for 107 thyroid biopsies were analysed in this study, including 11 normal (N), 13 papillary carcinomas (PC), 4 other carcinomas (anaplastic, medullary), and 73 follicular adenomas, of which 10 were clinically manifest as follicular carcinoma (FC).[46]

Preprocessing of the data involved retaining only the 0.64–3.41 ppm region of the spectra and subdividing this region into lipid CH_2 and CH_3 peaks (LIP),

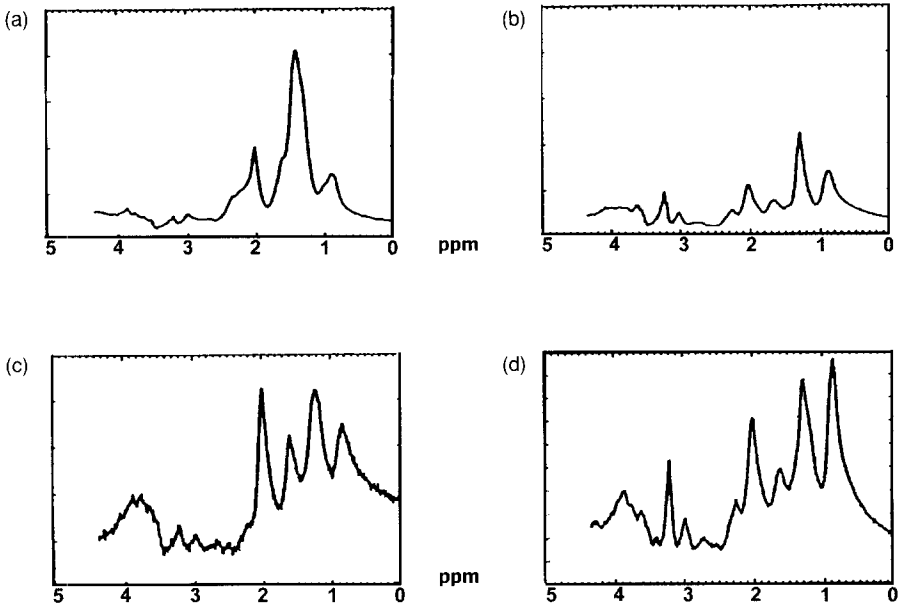

Fig. 2. Human thyroid biopsies. 1D ^{1}H MR spectra (8.5 T, 37°C) residual water suppressed by selective gated irradiation, sweep width 3957 Hz, using 8192 data points, 128 accumulations, and acquisition time of 1.14 s and relaxation delay of 2 s. (a) Normal thyroid tissue. (b) Known follicular carcinoma. (c) Thyroid follicular neoplasm predicted by MRS to be normal—confirmed by histopathology. (d) Thyroid follicular neoplasm predicted by MRS to be cancer and confirmed by histopathology—the presence of capsular invasion. Reprinted with permission from the National Research Council, Canada.

0.64–2.59 ppm, and choline-like peaks (CHO), 2.59–3.41 ppm. Spectra were normalized to the area of the choline region. Data compression was conducted via PCA, separately for the two subregions. For the final classification, the first 10 principal components (which accounted for 97% of the total variance of the data set) were retained.[46]

Data classification involved partitioning of data into a *training set* and a *test set*. Classifiers were optimized (trained) on the training set, and their reliability (and generalization power) tested on the test set. The LOO method was chosen for cross-validation to ensure minimum bias. It is an appropriate method when the samples per class in the training set are small. It was considered essential that the degree of 'fuzziness' be reported, so that samples too 'fuzzy' to be assigned reliably to any class could be removed and the remaining samples allocated more reliably. Detecting fuzziness in medical diagnosis is critical, since medical data are noisy and may be plagued by expert error. LDA,[56] NN[57] and GP[58] were applied separately to the CHO and LIP spectral regions, resulting in *six* different classifications for consensus diagnosis.

Table 2. Summary of MR data classification using a three-stage strategy.

Biopsy type (n)	Classification	Method[a]	Spectral regions (ppm)	Accuracy (%)	Reference
Thyroid ($n=107$)	Normal versus malignant	PCA CCD (LDA, NN, GP)	Spectral identity not retained	99.0	46
Brain ($n=206$)	Control versus malignant	PCA/ORS CCD (LDA, NN)	23/55 subregions	94.4	60
Astrocytoma ($n=91$)	High grade versus low grade	ORS SCS (LDA)	0.81–0.85, 1.71–1.75, 2.16–2.20, 2.46–2.50, 2.54–2.58, 3.02–3.06, 3.51–3.55[b]	95.7	37
Breast FNA ($n=140$)	Benign versus malignant	ORS_GA SCS (LDA)	**1:** 0.87–0.92; 1.20–1.25; 1.63–1.67; 1.79–1.82; 1.95–1.98; 2.85–2.87; 2.95–2.97; 3.19–3.33 **2:** 1.19–1.23; 1.32–1.38; 1.79–1.82; 1.96–2.00; 2.13–2.15; 2.70–2.76; 2.92–2.94; 2.97–2.99	96.1	83
	Lymph node involvement Yes/No		**1:** 0.43–0.51; 0.64–0.77; 1.10–1.20; 1.56–1.59 **2:** 0.44–0.51; 0.67–0.71; 1.13–1.19; 1.56–1.60; 1.86–1.96	95.0	83
	Vascular invasion Yes/No		**1:** 0.47–0.55; 0.57–0.62; 0.86–0.92; 1.00–1.03; 1.69–1.71; 1.99–2.05; 2.55–2.56; 2.63–2.72 **2:** 0.75–0.81; 0.90–0.94; 1.03–1.12; 1.21–1.24; 1.59–1.63; 2.00–2.04; 2.24–2.27; 2.70–2.74	91.9	83

Table 2. *continued.*

Biopsy type (n)	Classification	Method[a]	Spectral regions (ppm)	Accuracy (%)	Reference
Prostate ($n=87$)	Benign versus malignant	ORS_GA SCS (LDA)	3.46–3.52; 3.40–3.46; 2.50–2.56; 2.14–2.20; 1.84–1.90; 1.12–1.18	96.6	42
	Residual cancer after radiotherapy Yes/No		0.77–0.82; 0.94–1.00; 1.32–1.37; 1.59–1.71; 2.24–2.27; 3.19–3.28	91.4	71
Liver ($n=122$)	Normal versus HCC	ORS_GA SCS (LDA)	1.34–1.37; 2.28–2.33; 2.83–2.85	100	76
	Cirrhotic versus HCC		3.00–3.03; 3.56–3.60; 3.66–3.68	98.4	76
	Normal versus cirrhotic		1.52–1.57; 2.03–2.08; 3.63–3.67	92.1	76
Ovarian ($n=56$)	Normal versus cancer	ORS_GA SCS (LDA)	1.47, 1.68, 2.80, 2.97, 3.17, 3.34	98	43

[a] Preprocessing was an essential first step in all of the studies.
PCA, principle component analysis; CCD, computerised consensus diagnosis; LDA, linear discriminant analysis; NN, neural net; GP, genetic programming; ORS, optimal region selection; ORS_GA, optimal region selection using a genetic algorithm; SCS, statistical classification strategy; HCC, hepatocellular carcinoma.
[b] For magnitude spectra without α scaling.[37]

Three different training sets were used: 8 normals and 8 papillary carcinomas (8_8_PC); 8 normals and 8 follicular carcinomas (8_8_FC); and 9 normals and 16 carcinomas (9_16: 9 N+8 PC+8 FC). The *consensus* results on all three training sets yielded specificities and sensitivities of 100%. The test sets corresponding to each of the training sets all contained samples of known malignancy. Test sets were: 3 normals and 19 carcinomas (training sets 8_8_PC and 8_8_FC), and 2 normals and 11 carcinomas (training set 9_16). Follicular neoplasms of unknown malignancy ($n=63$) were also included in the test sets. For these samples, however, the consistency among the three sets of class assignments was low and this was attributed to the restricted number of samples in the training sets.[46]

The results of this study show that even the simplest consensus diagnosis gives better and more reliable prediction than any individual classification method would on its own. Emphasis is placed on careful and appropriate data preprocessing prior to classification. However, the PCA method chosen in this study does have a major drawback, in that the original spectral information is scrambled, since the discriminating PCs are linear combinations of the original data points. A method that retained spectral identity and hence biochemical origin of the class differences would be of greater benefit for an understanding of the biochemical manifestations of different disease states. The notion of 'classification undecidability' is also emphasized. Fuzzy predictions are reflections of real-life uncertainty and are to be expected in medical diagnosis. Undecidability, therefore, is a valuable classification outcome, as it encourages re-evaluation of both clinical diagnosis and experimental protocol.

In summary, this first report of a classification strategy specifically tailored to the classification of biomedical spectral data shows that reliable and robust classification must satisfy the following criteria: adequate data set size; proper data reduction; proper data classification (balanced training set with cross-validation, e.g. LOO); the use of several classifiers; and choice of appropriate consensus classification.

4. BIOPSIES FROM THE BRAIN

Compared with current modalities for identifying abnormalities of the brain, such as MRI and histopathology, which rely on morphological changes in the tissue, MRS accesses biochemical information.[59] While databases exist for neurospectroscopy *in vivo,* they suffer from a lack of confidence that the spectral data come from the same area that has given rise to the final tissue diagnosis.[26,27] Essential for the implementation of this MRS technology as a clinical tool is the ability to obtain diagnoses with high sensitivities and specificities reliably. In the study reported below, the biopsies were analysed by MRS and correlated with conventional histopathology on the same tissue sample.

4.1. The influence of preprocessing and CCD on classification accuracy

Integral to the development of the SCS was establishing the influence and advantages of (i) preprocessing of the data, and (ii) the use of CCD to combine classifiers generated using different methods (LDA or artificial neural nets) to obtain a meta-classifier superior to each of the individual classifiers. This was done in a study of the MR spectra of tissue specimens from meningiomas, astrocytomas and epilepsy.[60] The spectra were preprocessed by several methods. Each data set was partitioned into training and validation sets. Classification was carried out via LDA and NN, and their outcomes combined via CCD, and the results were compared with histopathological diagnosis of the MR specimens (Table 2).

Multiple surgical biopsies (0.02–0.1 g) were obtained during resections from brain tumours and from the active site and underlying white matter of patients with intractable epilepsies. Proton MR spectra were obtained on a Bruker AM 8.5 T spectrometer at 37°C. The data set consisted of the ^{1}H MR spectra of tissue specimens from meningiomas (M-95; 24 cases) and astrocytomas (A-74; 26 cases), and intractable epilepsy as the control (E-37; 8 cases).

Using all spectra, two data sets were established, one normalized (N) and the other unnormalized (U). Each of these data sets was then preprocessed in two ways: (i) spectral regions were subdivided into 55 equal subregions (R), and the 10 data points in each subregion averaged, reducing the 550-dimensional feature space to 55, while retaining spectral identity (useful for future understanding of the biochemical basis of clinical discrimination); (ii) PCA was used on the full 550-point spectral regions (the first 20 PCs accounted for 99.99% of the total variance in the data set) (P). Thus, four possible combinations (UP, UR, NP and NR) of the original data could be used to develop classifiers. Before classification, additional reduction of the feature space dimensionality of these four data sets was accomplished via an optimal region selector (ORS) algorithm.[50]

For data classification, the spectra were partitioned into training and validation (test) sets. The four differently preprocessed sets of ^{1}H MR brain spectra were subjected to two classification methods: LDA and a noise-augmented artificial neural net (NN). All classifier training was cross-validated via the LOO method. The two classifiers (LDA and NN) were used on three-class (E, M and A) data. CCD was then implemented based on stacked generalization.[61]

The average (LDA and NN) classification accuracies were 80.6%, 82.7%, 88.6% and 91.2% for UP, UR, NP and NR, respectively (Table 3).[60] The simple operation of spectral normalization (U $\rightarrow$ N) improved classification accuracy. The classification accuracy was further improved by replacing PC-based features with subregion-based features.

The CCD (LDA and NN) classification accuracies were 78.8%, 82.6%, 89.2% and 94.4% for UP, UR, NP and NR, respectively (Table 3). CCD increased the classification accuracy of the normalized sets only. The use of CCD also decreased the fraction of unclassifiable spectra.[60]

Table 3. Percentage classification accuracy for spectra as a function of preprocessing and CCD.

	UP (%F)	UR (%F)	NP (%F)	NR (%F)
LDA	79.1 (7.3)	83.7 (1.5)	89.0 (2.9)	93.7 (0.0)
NN	82.3 (9.7)	81.5 (16.0)	88.1 (6.3)	88.6 (1.9)
Average (LDA and NN)	80.6 (8.5)	82.7 (9.7)	88.6 (4.6)	91.2 (1.0)
CCD (LDA and NN)	78.8 (2.7)	82.6 (1.2)	89.2 (0.7)	94.4 (0.7)
CCD—average	−1.8 (−5.8)	−0.1 (−8.7)	0.6 (−3.9)	3.2 (−0.3)

Note: the percentage accuracy is based on crisp classification. %F refers to the percentage of the total number of spectra that were unclassifiable because of fuzziness.
LDA, linear discriminant analysis; NN, neural nets; P, principal component (PC-based); CCD, computerized consensus diagnosis; N, normalized; U, unnormalized; R, subregion-based; F, fuzzy.
Reprinted with permission from Somorjai *et al.*[60]

This study shows the essential role of preprocessing and data reduction and the importance of a robust classification strategy for obtaining reliable class assignments. Spectral normalization is beneficial, as is the use of subregion-based features as opposed to PC-based features. The use of subregion-based features has the added advantage of retaining spectral identity during data reduction. This allows the results to be interpreted in biochemically relevant terms, essential for elucidating the molecular basis of disease occurrence and progression. It is important to note that appropriate preprocessing of the spectra was found to be at least as important for accurate and reliable results as the use of CCD. Implementation of CCD was most effective in improving classification accuracy when the individual classifiers were accurate. In addition, CCD reduced the number of unclassifiable spectra, an outcome of extreme practical relevance.

4.2. Discrimination between low- and high-grade astrocytomas

Contemporary neurodiagnostic imaging, including MRI, is unreliable in grading astrocytomas (57% assignment accuracy) and is therefore not reliable enough for clinical decision-making. Nor is the technique objective or reliable. Patient management strategies, therefore, can only be carried out through histopathology of biopsies obtained during surgery.[62] A non-invasive method is needed that can differentiate reliably low- from high-grade astrocytomas before surgical intervention, and can predict the malignant potential of low-grade astrocytomas.

Multivariate analysis of ^{1}H MR spectra of brain tumour tissue has been shown to provide a high level of discrimination between low- and high-grade astrocytomas.[37] Such accuracy was achievable using two novel spectral preprocessing methods: α-scaling and an optimal attribute selector (Table 2).[49]

Multiple surgical biopsies (0.02–0.1 g) were obtained during resection from astrocytic brain tumours. ^{1}H MR spectra were obtained on a Bruker AM 8.5 T

spectrometer at 37°C. Typical spectra of biopsies of brain tumours classified as low grade and high grade are shown in Fig. 3. The data set consisted of the ^{1}H MR spectra of tissue specimens from patients with grade 1 and 2 astrocytomas (AL = 29; 11 cases), and grade 3 and 4 astrocytomas (AH = 62; 31 cases). Preprocessing of the spectra was performed in two ways to assess the need for phasing of spectra: (i) phasing by an objective algorithm and normalization to the total spectral area; (ii) normalized *magnitude* spectra (not phased). Preprocessing by α-scaling[37,49] was applied to the two data sets. This resulted in four final data sets: (i) magnitude/no scaling (MN); (ii) phased/no scaling (PN); (iii) magnitude/scaling (MS); (iv) phased/scaling (PS). For all four data sets, the final preprocessing step involved selection of optimal discriminatory regions using an ORS algorithm.[50] LDA, with LOO cross-validation, was used to optimize classification accuracy.

The classification accuracies of the four data sets were 95.7%, 89.1%, 95.7% and 91.3% for MN, PN, MS and PS, respectively (Table 4).[37] For all four data sets, the 45-sample training sets were classified 100% correctly and crisply.

The results from this study emphasize the importance of preprocessing the MR spectra. Robust and reliable classification of disease grades that are

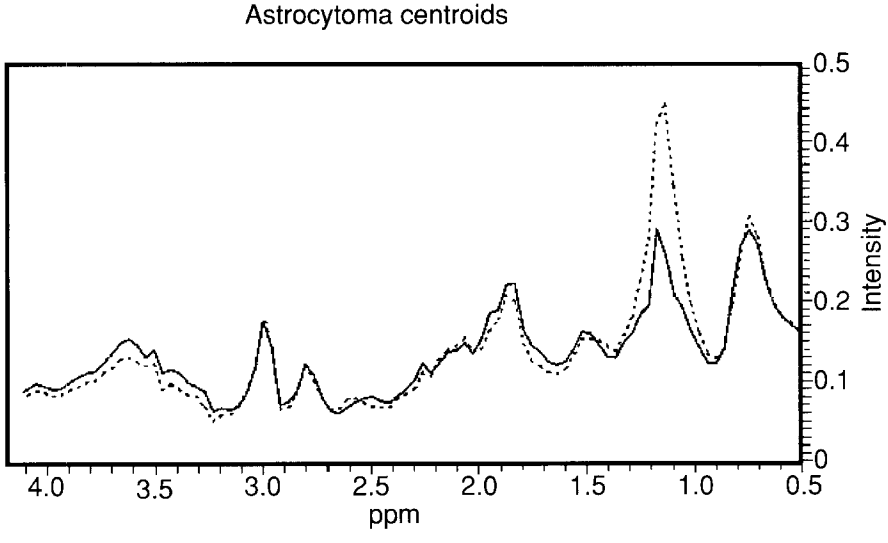

Fig. 3. Biopsies from brain tumours. Class-average magnitude ^{1}H spectra (8.5 T, 37°C) of biopsies of brain tumours classified as low grade (AL, solid line) and high grade (AH, dashed line). Spectra were acquired with 256–640 acquisitions, sweep width 5000 Hz, delay 2.41 s. Reprinted from R. L. Somorjai, B. Dolenko, A. E. Nikulin, P. Pizzi, G. Scarth, P. Zhilkin, W. Halliday, D. Fewer, N. Hill, I. Ross, M. West, I. C. P. Smith, S. M. Donnelly, A. C. Kuesel and K. M. Brière, Classification of ^{1}H MR spectra of human brain neoplasms: the influence of preprocessing and computerized consensus diagnosis on classification accuracy, *Journal of Magnetic Resonance Imaging*, Copyright © 1996.

Table 4. High- versus low-grade astrocytoma: classification accuracies, test sets.

Spectra	Scaling	Number of optimal subregions	Validation set classification accuracy (%)	
			Complete	Crisp
Magnitude	No	7	95.7	95.7
Phased	No	9	89.1	91.1
Magnitude	a	7	95.7	95.7
Phased	a	9	91.3	91.1

'Complete' is based on all samples, while 'Crisp' includes only those samples for which class assignment is >75%. For all four preprocessing examples, the training sets were classified to 100% accuracy.
Reproduced with permission from *Journal of Medicine and Biochemistry*.

clinically difficult to separate was achievable using only the relatively simple LDA classifier, providing that appropriate preprocessing was employed. Emphasizing this point, LDA-based classification using the full 100-attribute data set, but without α-scaling and/or optimal region selection, yielded only 57.8% accuracy for the magnitude spectra and 78.3% for the phased spectra.

This study also indicates that there is no need to phase MR spectra prior to classification: the magnitude spectra can be classified at least as well, and generally more accurately, without the inevitable subjectivity and consequent variability introduced by phasing. However, the ORS algorithm, by eliminating the majority of attributes, reduced the advantage gained by applying the α-scaling step.

The high degree of accuracy achieved in this study in the analysis of ^{1}H MR spectra of high- and low-grade astrocytomas suggests that significant attention should be focused on *in vivo* MRS studies of human brain tumours. A similar degree of success *in vivo* would yield a cost-effective, high-impact method for surgical planning.

5. OVARIAN CANCER

5.1. Clinical problem

Ovarian cancer is asymptomatic in its early stages and usually goes undetected until well advanced and difficult to treat. Screening for ovarian cancer has not yet been shown to be effective, partly for want of a preoperative technique to confirm or exclude malignancy in suspicious lesions that are identified by the screening process. *In vivo* MRS may offer such a method by early confirmation of ovarian cancers in high-risk women (i.e. with a family history of the disease) in whom screening would be warranted.

5.2. Pathology

Early studies with proton MRS successfully distinguished between normal/benign and malignant human ovarian tissue, with a sensitivity of 87% and a specificity of 91%,[8] using visual inspection of the MR data. Discrimination between the two groups was based on the peak height ratios of resonances at 3.0 ppm (creatine, phosphocreatine and lysine) 1.7 ppm (lysine, polyamines), and 1.7–1.3 ppm (lipid, lactate, fucose, threonine).[8]

A second, independent study repeated the visual inspection analysis and compared the sensitivities and specificities obtained using visual inspection and a precursor of the SCS analysis on the same data set.[43] Biopsy samples of post-menopausal ovaries, benign ovarian neoplasms and ovarian cancers (~0.5 g) were obtained during surgery. The histological types of these samples were normal (19), benign tumour (3), borderline tumour (3), serous carcinoma (13), endometroid carcinoma (17), mixed epithelial carcinoma (3), and small cell carcinoma (4). Proton MRS measurements were performed at 37°C at 8.5 T.[43]

Proton MR spectra from normal ovaries, benign and borderline tumours and ovarian cancers (Fig. 4) were initially analysed using the peak amplitude ratio method (visual inspection). Normal/benign samples could be distinguished from borderline and malignant samples with a sensitivity of 95% and a specificity of 86%. Excluding the benign samples, normal samples were distinguished from cancer samples with a sensitivity of 95%, a specificity of 89%, and an overall accuracy of 93%.

A precursor of the SCS-based multivariate analysis of the MRS data improved both the sensitivity and specificity of diagnosing malignancy compared to visual inspection analysis. Spectra were prepared for the analysis using an objective phasing algorithm and no baseline correction. Classification of normal and cancer specimens was undertaken using a training set composed of spectra from 12 normal and 22 cancer specimens, and a test set composed of 7 normal and 15 cancer specimens. Preprocessing using ORS_GA selected six attributes as maximally discriminating. The chemical shifts and the major metabolites contributing to the chosen spectral regions included 1.47 ppm, 1.68 ppm (lysine), 2.80 ppm, 2.97 ppm (creatine), 3.17 ppm (cholines) and 3.34 ppm (taurine). Using these six attributes, the method (using LDA) classified the data with high sensitivity and specificity (100% and 95%, respectively, averaged over the training and test sets). An overall accuracy of 98% was achieved. These results are summarized in Table 2.[43]

6. PROSTATE CANCER

Prostate cancer is the most common malignancy in men in North America and Australia. In Australia, prostate cancer is the second leading cause of death, with 10 000 new cases diagnosed each year,[63] whereas in the USA prostate cancer is

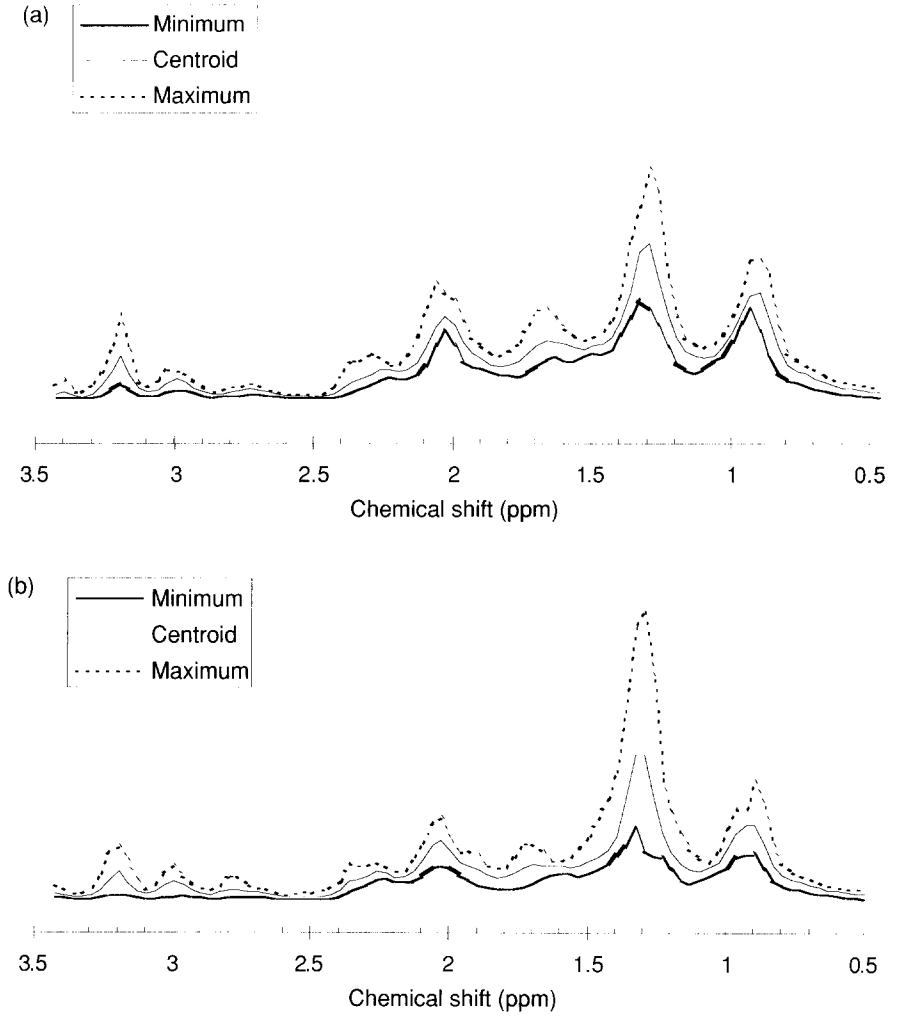

Fig. 4. Ovarian cancer. Mean and range of intensities observed in data-compressed ^{1}H MR spectra (8.5 T, 37°C) from: (a) normal ovaries, and (b) ovarian cancer specimens. Spectra were acquired with sweep width 5000 Hz, 640 accumulations, 4000 data points, and 2.41 s repetition rate; water was suppressed using selective gated irradiation. Reprinted with permission from Wallace *et al.*[43]

responsible for 31 500 deaths per year, with 198 000 new cases diagnosed every year.[64]

Treating prostate cancer in its early stage should be an effective means of achieving long-term survival. However, the non-invasive diagnostic tests currently available, i.e. digital rectal examination, transrectal ultrasound, and

measurements of PSA, are all relatively insensitive and are incapable of detecting small, well-differentiated cancers.[65] Furthermore, a major limitation in the management of the disease is the inability to distinguish early those cancers that will progress and become life-threatening from those that are clinically indolent. The search for a better diagnostic tool continues.

MRS has been applied *in vivo* by Kurhanewicz *et al.*[66,67] to provide biochemical and metabolic information from prostate tissue. The metabolic changes centred on citrate, creatine and choline as markers of disease, with a reported sensitivity and specificity of ca. 90% and ca. 83%, respectively. The use of these compounds as diagnostic markers was confirmed on extracts from biopsies, but only small sample sizes have been examined.[68,69] Kurhanewicz *et al.* have developed the *in vivo* method to a high degree of technical effectiveness, but still the method does not provide the specificity needed for optimal diagnostic clinical use.[66,67]

MRS analysis of excised tissue biopsies has an advantage over *in vivo* studies, by the ability to confirm the histology on the precise specimen examined by MRS. Studies are now completed,[70] which support the high degree of accuracy of the MRS method when complete and accurate histopathological information is used for data correlation.

6.1. Pathology

The first study where the SCS was applied to MRS analysis of prostate biopsies was undertaken at the IBD in Winnipeg.[42] Proton MRS (Bruker Instruments, 8.5 T were performed at 37°C on specimens of benign ($n=66$) and malignant ($n=21$) human prostate tissue specimens collected from transurethral resection of the prostate and radical prostatectomy from 50 patients. Typical spectra of malignant prostate tissue and benign prostate hyperplasia (BPH) are shown in Fig. 5.[42] The spectral data were subjected to visual inspection analysis and multivariate analysis, specifically LDA.

Spectra of human prostate tissue were dominated by signals from low-molecular-weight metabolites, such as choline-containing compounds (3.2 ppm), creatine (3.0 ppm), citric acid (2.5 ppm) glutamic acid (2.0 ppm), lysine (1.6 ppm), lactic acid (1.3 ppm), and amino acids (0.9 ppm), supporting the findings of Kurhanewizc *et al.*[66,67] The intensities of these various resonances were variable, and as a result the sensitivity and specificity for diagnosing malignancy obtained from the visual inspection analysis, i.e. peak height/area calculations, of the MR spectral data were low, at 81% and 80% respectively.[42]

The SCS was subsequently applied to the same data set to provide a robust method of classification based more on overall pattern recognition than on intensity ratios. Before commencing the multivariate analysis, the spectra were partitioned into a training set (33 BPH, 13 tumours) and a test set. Preprocessing of the data using ORS_GA (4) selected six optimally discriminatory regions,

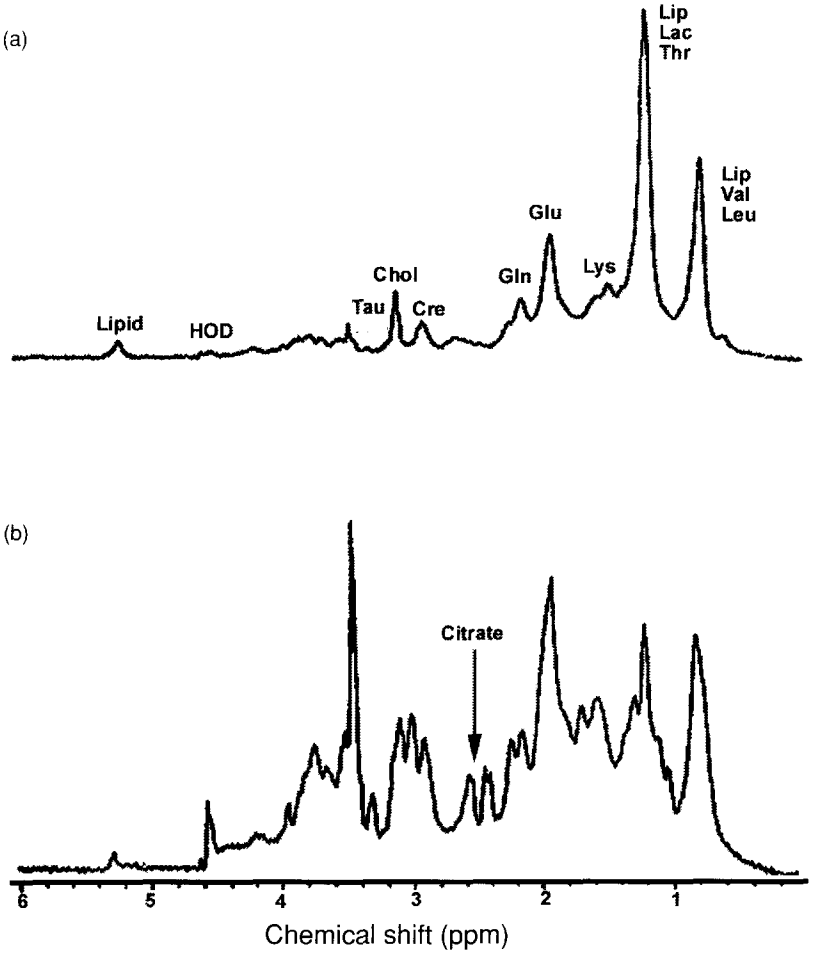

Fig. 5. Prostate biopsy. ^{1}H MR spectra (8.5 T, 37°C), of human prostate biopsy specimens: (a) cancer (Gleason's grade: 3+3); (b) benign prostatic hyperplasia (BPH). MR spectra were collected with presaturation of the water signal. Acquisition parameters included number of scans, 256 or 640, sweep width 5000 Hz, delay 2.41 s, and time domain data points 4K. Reprinted from *Cancer Research* with permission from the American Association for Cancer Research.

3.46–3.52, 3.40–3.46, 2.50–2.56, 2.14–2.20, 1.84–1.90 and 1.12–1.18 ppm. These include the resonances from taurine, citrate, and glutamate, supporting the findings of previous studies,[68,69] which report citrate as a possible marker for prostate cancer. Using the SCS, a sensitivity of 100% and a specificity of 95.5% were obtained for the diagnosis of malignancy, with an overall classification accuracy of 96.6% (Table 2). These values were remarkably higher than those obtained by visual inspection methods (81% and 80%, respectively).[42]

The findings of this study strongly indicated the superiority of sophisticated methods of data analysis for the diagnosis of malignancy from the MR spectra of prostate tissue. Proton MRS, combined with the SCS-based analysis, gives very high sensitivity and specificity and thus can be reliably used to distinguish between benign and malignant prostatic tissue. Consistent with the findings of studies, both *ex vivo* and *in vivo*, using conventional visual inspection data analysis, the SCS identifies citrate as a possible MRS marker for prostate cancer. Other regions of interest identified by the SCS-based analysis include the resonances due to taurine and glutamate.

6.2. Identification of recurrent malignancy after radiotherapy

Prostate carcinoma confined to the prostate gland can be definitively treated with radical radiation therapy. Accurate assessment of the success of tumour clearance after radiotherapy is of clinical importance to improve selection of patients for local treatment and to identify patients who would benefit from aggressive salvage therapy.[70] As such, there is a pressing need for a precise early measure of tumour response.

A recent MRS study undertook the task of comprehensively analysing a spectral data set of irradiated prostate tissue against early endpoints of local therapeutic effect and clinical outcome. The gold standard endpoint against which the MR spectra were calibrated was histopathologic diagnosis. Spectral metabolic changes in prostatic tissue after radiotherapy were described, and the MRS data, when combined with a multivariate SCS-based analysis, were able to identify residual viable tumour.[71]

Transrectal ultrasound-guided prostate biopsies ($n = 116$) from 35 patients were obtained 18–36 months after external beam radiotherapy and subjected to ^{1}H MRS (8.5 T, 37°C) followed by histopathology. Typical spectra of irradiated prostate tissue specimens positive and negative for malignancy are shown in Fig. 6.[71] For the spectral analysis, each magnitude spectrum was normalized. The 0.5–3.5 ppm region of each spectrum (450 data points) was selected to minimize the influence of spectral artefact created by suppression of the water peak at 4.6 ppm. Preprocessing consisted of the selection from the 450-point spectral region of six maximally discriminatory subregions (with ORS_GA), using cross-validation bootstrap methodology. The regions chosen were 0.77–0.82, 0.94–1.00, 1.32–1.37, 1.59–1.71, 2.24–2.27 and 3.19–3.28 ppm, and included resonances from choline, creatine, glutamine, and lipids (with the possible inclusion of lactic acid). Citrate, a discriminating resonance that was found at elevated levels in benign/normal prostates not exposed to radiation, was invisible in all spectra of postradiation biopsies, regardless of whether the biopsy was negative or positive for malignancy. The average values of the six maximally discriminating subregions served as the ultimate attributes. The ultimate classifier was determined as the *weighted average* of the classifier coefficients of

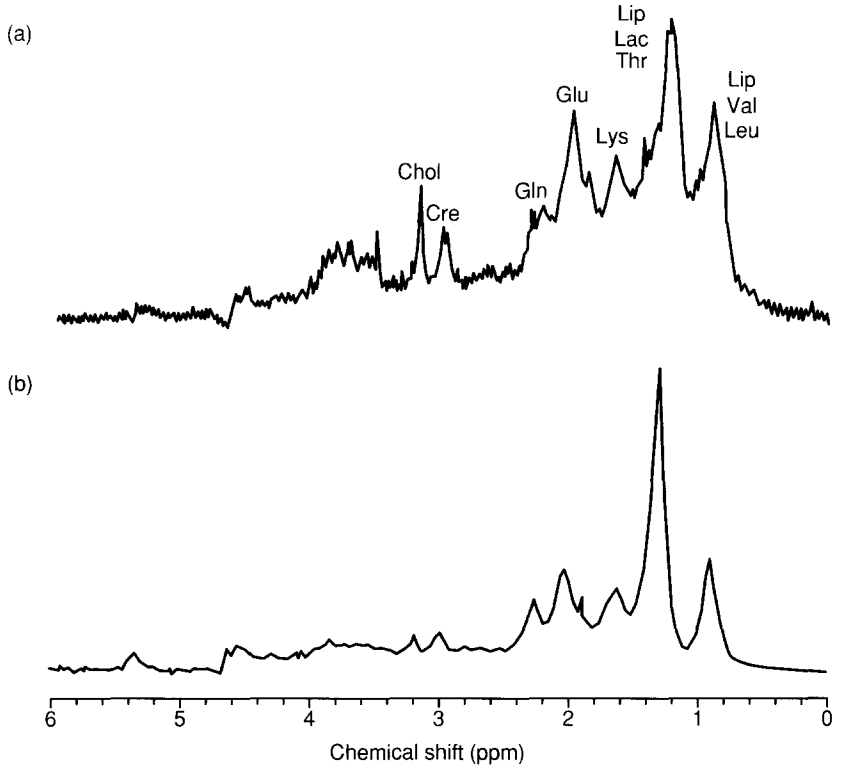

Fig. 6. Prostate biopsies following radiation therapy. ^{1}H MR spectra (8.5 T, 37°C), of irradiated prostate biopsy specimens: (a) positive for malignancy (time post-radiotherapy (XRT) 36 months, local failure); (b) negative for malignancy (time post XRT 20 months). MR spectra where collected with presaturation of the water signal using low-power continuous irradiation. Acquisition parameters include number of scans 640, sweep width 5000 Hz, delay 2.41 s and time domain data points 4K. Reprinted from *International Journal of Radiation Oncology, Biology and Physics*, **50**, C. Ménard, I. C. P. Smith, R. L. Somorjai, L. Leboldus, R. Patel, C. Littman, S. S. Robertson and T. Bezabeh, Magnetic resonance of the malignant prostate, p. 317, Copyright (2001), with permission from Elsevier Science.

the 1000 individual component classifiers. LDA was the choice for all classifiers, at all stages.

Using this methodology, the sensitivity and specificity of MRS in identifying a malignant biopsy were 88.9% and 92% respectively, with an overall classification accuracy of 91.4% (Table 2).[71] MRS has thus been shown to have promise in radiobiological imaging. Given the invasive nature, inherent sampling error and false-positive rate of transrectal ultrasound-guided biopsies, it would be desirable to seek with MR spectroscopy independent diagnostic or prognostic variables predictive of treatment failure.

6.3. Importance of correct pathological diagnosis for the SCS

In the Winnipeg study reviewed above,[42] standard pathology, reported as benign or malignant, was used to develop the SCS-based classifier for diagnosis of prostate malignancy. No prostate intraepithelial neoplasia (PIN), thought to be a preinvasive state in the development of prostate malignancy, was reported by the pathologists in this study, as is normal in that Province. Thus, the classifier was developed without PIN being accounted for, and using routine hospital sampling procedures.

A series of studies in Sydney is underway, attempting to identify markers of early disease using both visual inspection and the SCS method. Visual inspection of the MRS data indicated in 11% of cases that the routine histopathology was incorrect, due to incomplete examination of the tissue specimen. As a consequence, the pathology of these and another 15% of cases were reviewed blind. The tissues examined by MRS were serially sectioned, and sections every 100 μm were examined. The inaccuracy of routine hospital pathology procedures, where 5 μm sections at only two or three levels are examined, was highlighted.

The study showed that spectral profiles of tissue containing PIN, small focal areas (5% or less) of adenocarcinoma, and large areas (50% or more) of adenocarcinoma, were all different.[70] It is highly probable that the SCS could distinguish these three tissue subgroups, given the complete pathological assessment data, and thus be able to provide information on the presence and amount of premalignant and/or early malignant disease. This illustrates the importance of correct pathological diagnosis in the development of the SCS-based (or any other) classifiers to prevent tissue subsets of clinical importance being overlooked or included in another pathological category.

7. HEPATOCELLULAR CARCINOMA

7.1. Clinical problem

Hepatocellular carcinoma (HCC) is one of the most common internal malignancies worldwide.[72] It is the most frequent tumour in males[73] and the most common in Asia and Africa. The annual incidence in Western countries is 4 per 100 000.[73] HCC almost always occurs as a sequel to cirrhosis, and is increasingly prevalent because of the upsurge in cases of chronic hepatitis B and hepatitis C. HCC may form a large mass with or without satellite nodules, or may be multifocal and scattered throughout the liver. Nodules greater than 10 mm in diameter are likely to harbour HCC[74] and will be biopsied. Small nodules (less than 10 mm in diameter) may also contain HCC, but definitive diagnosis is difficult, since it is often not possible to distinguish HCC from tumour 'look-alikes' such as regenerative nodules.[75] A reliable and objective technique is required to unequivocally identify the pathology of smaller lesions.

7.2. Pathology

Proton MRS combined with SCS-based analysis has been used to distinguish normal liver tissue, cirrhotic liver and HCC with a high degree of accuracy. Liver tissue specimens from 54 patients undergoing either partial (hemi) or total hepatectomy were analysed by (1D) ^{1}H MRS at 8.5 T. Histologically, these specimens were confirmed as normal ($n=31$), cirrhotic ($n=59$), and HCC ($n=32$).[76]

Proton 1D MR spectra of HCC, cirrhotic liver and apparently healthy liver are shown in Fig. 7. Consistent differences between the MR spectra of

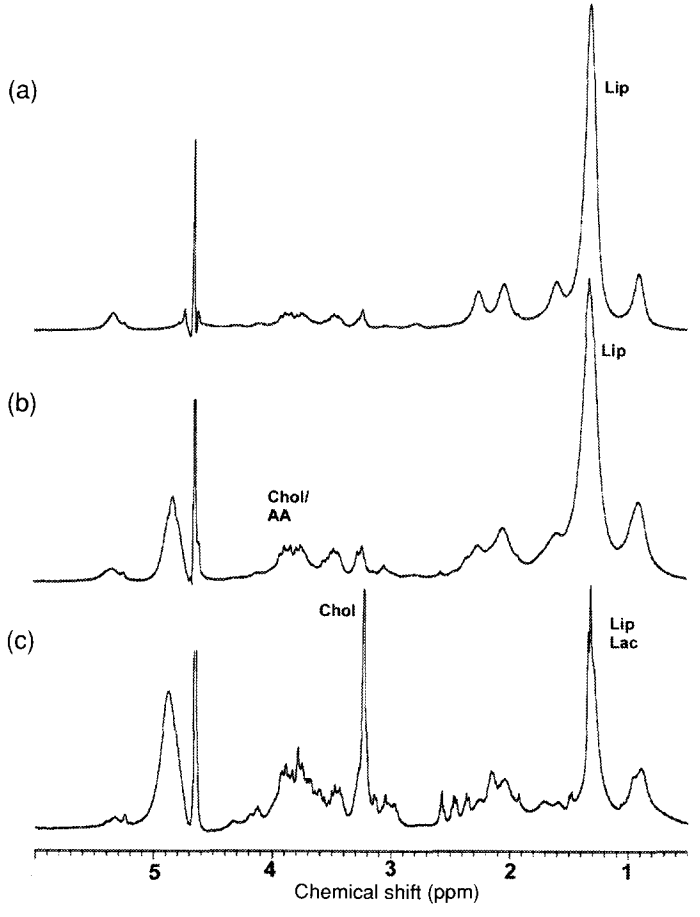

Fig. 7. Liver biopsies. ^{1}H MR spectra (8.5 T, 37°C) of liver biopsy specimens: (a) normal liver; (b) cirrhotic liver; and (c) hepatocellular carcinoma (HCC).[76] Data were collected with water suppression using selective gated irradiation, sweep width of 3600 Hz, 8K data points, 256 accumulations, repetition time of 2.3 s.

normal and cirrhotic liver compared to HCC include reduced amounts of lipids and carbohydrate residues and increased choline-containing compounds in HCC. The 3.2 : 3.0 ppm resonance ratio was above 4 for all HCC samples and below 3 for all cirrhotic and normal liver samples. No consistent and significant differences could be identified between MR spectra from apparently healthy and cirrhotic tissue using visual comparison of 1D and COrrelation SpectroscopY (COSY) MR spectra.

For the SCS-based analysis, magnitude spectra, consisting of 4096 data points over the spectral width of 10 ppm, were reduced to 1500 points between 0.35 and 4.00 ppm. The spectra were normalized to the total integral in this region. Rank-ordering (i.e. replacing the actual first derivative values by their positions in the sorted derivative list: the smallest derivative value would receive rank 1, the largest rank N, N being the number of derivative values) of the first derivative of MR spectra was used for the SCS analysis. The MR magnitude spectra were analysed by a GA-based ORS_GA to identify maximally discriminatory subregions in the spectra. The chosen regions were: normal versus HCC, 1.34–1.37, 2.28–2.33 and 2.83–2.85 ppm; cirrhotic versus HCC, 3.00–3.03, 3.56–3.60 and 3.66–3.68 ppm; normal versus cirrhotic, 1.52–1.57, 2.03–2.08 and 3.63–3.67 ppm. The averages of these subregions were the ultimate features for the second stage of the SCS, at which LDA-based pairwise classifiers were developed. These classifiers were made robust by bootstrap-based cross-validation, with the process repeated 1000 times. The ultimate classifier was the weighted output of the 1000 different bootstrap classifier coefficient sets.[76]

The SCS, applied to the MR spectra, distinguished between normal tissue and HCC with 100% sensitivity and specificity (i.e. 100% accurate). All spectra were crisply classified; that is, class probability was always larger than 75%. Using a separate classifier, cirrhotic liver tissue and HCC were distinguished with a sensitivity and specificity of 95.8% and 88.9%, respectively. The overall crispness was 84%. An overall accuracy of 98.4% was obtained when specimens classified as fuzzy were excluded. A third classifier was developed to distinguish normal from cirrhotic liver. These were distinguished with a sensitivity and specificity of 96.8% and 85.4%, respectively. The overall crispness of the data was, however, low at 79.7%. Here the SCS-based analysis misclassified one cirrhotic and four normal tissue samples, and 12 cirrhotic and four normal tissue samples were fuzzy (class probability less than 75%). When the fuzzy specimens were excluded, an overall accuracy of 92.1% was obtained. The spectral regions used in each of the classifiers and the classification accuracies are summarized in Table 2.

The SCS, applied to the MR spectra, has the potential to provide accurate identification of HCC in small biopsies and hence improved management of malignant liver disease. Such a method is of particular importance for the assessment of small, radiologically undetectable hepatocellular carcinomas in patients with cirrhosis, particularly those awaiting transplants.

8. BREAST CANCER

Breast cancer is the most common cancer affecting women in Western societies. In the past decade, the incidence has risen by 25% and the lifetime risk (from 0 to 74 years) for white women developing breast cancer is around 7–8%.[77] A combination of physical examination, mammography and fine needle aspiration cytology or needle core biopsy (triple assessment) is currently the most sensitive method for preoperative diagnosis of clinically and radiographically detected breast lesions.

While triple assessment has a high probability of detecting malignant lesions, its suboptimal specificity results in diagnostic uncertainty requiring open biopsy to exclude malignancy in many women. Physical examination has limitations, due to variation in breast consistency, the site and size of the lesion, and the presence of a diffuse versus discrete tumour. Screening mammography alone results in one benign lesion being biopsied for every malignant lesion detected,[78] yet 10–40% of palpable cancers are missed by this modality, especially in women under 50 years of age, in whom radiographically dense breast tissue may obscure changes associated with cancer.[79,80] FNAB has an overall sensitivity of 81–97%.[81] However, this includes atypical and suspicious diagnoses which are confirmed as malignant following open biopsy in only 50–80% of cases.[82]

8.1. Pathology

In a study of 218 biopsies of breast tissue, proton MRS distinguished benign from malignant breast lesions with a sensitivity and specificity of 95% and 96%, respectively, on FNAB by visual inspection of the spectral data (Fig. 8). The diagnosis was based on the resonance intensity ratio of choline-containing compounds at 3.27 ppm and creatine-containing compounds at 3.05 ppm.[19] The visual inspection method was, however, found to be limited, as it required the FNAB cellularity to be sufficient to generate spectra with a signal-to-noise ratio (2.8–3.5 ppm) greater than 10. In a clinical setting, aspirating sufficient cells to achieve a signal-to-noise ratio above 10 may not always be possible.

This limitation was overcome by using SCS-based analysis to assess the entire MR spectrum against clinicopathological criteria. In a second study, intra-operative FNAB were taken from 140 patients undergoing breast biopsy and analysed by proton MRS at 8.5 T.[83] Following visual inspection of the data and measurement of the ratio of choline and creatine, MR spectra were preprocessed using optimal region selection (ORS_GA).[51] Maximally discriminatory sub-regions included 0.87–0.92, 1.20–1.25, 1.63–1.67, 1.79–1.82, 1.95–1.98, 2.85–2.87, 2.95–2.97 and 3.19–3.33 ppm for the first derivatives of the spectra, and 1.19–1.23, 1.32–1.38, 1.79–1.82, 1.96–2.00, 2.13–2.15, 2.70–2.76, 2.92–2.94 and 2.97–2.99 ppm for rank-ordered spectra. Using LDA and bootstrap-based cross-validation, two separate classifiers, A (using the optimal regions from the first derivatives of the spectra) and B (using the optimal regions

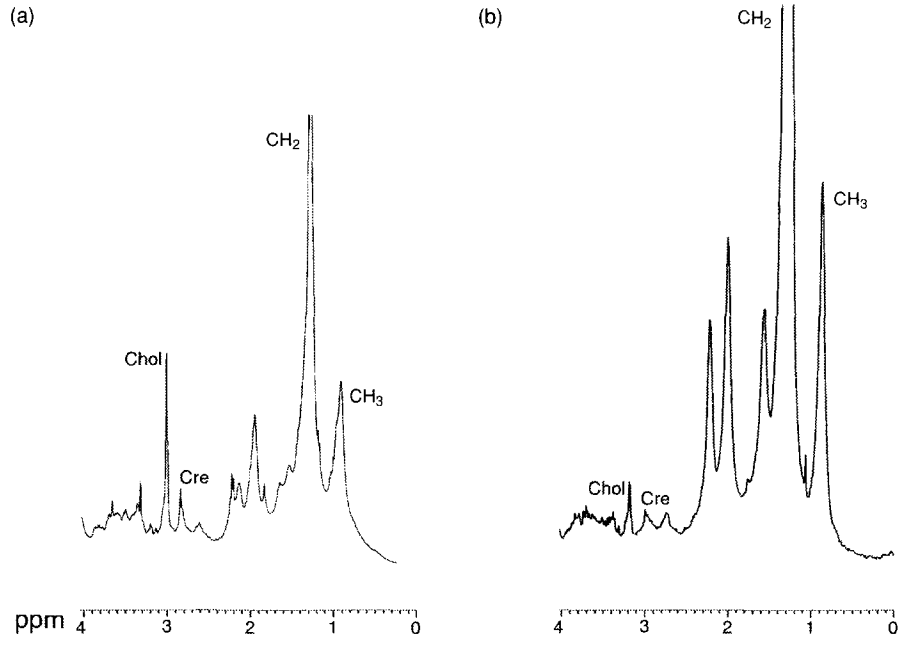

Fig. 8. Fine needle aspirates from the breast. ^{1}H MR spectra (8.5 T, 37°C) of breast fine needle aspiration biopsies (FNAB) with signal-to-noise ratio >10: (a) malignant; (b) benign. Spectra were acquired over a spectral width of 3597 Hz, 8192 data points, 256 accumulations and relaxation delay of 2 s. Reprinted with permission from Blackwell Scientific.

from the rank-ordered spectra), were developed. The final classifier was the Wolpert-combined A + B classifiers.[61]

Visual inspection methods distinguished benign and malignant pathologies with low sensitivity and specificity (85% and 83%, respectively). The use of the SCS greatly improved this outcome, distinguishing the two diagnostic subgroups for spectra from all FNAB, including those with low signal-to-noise ratio, with higher sensitivity and specificity (93% and 89% respectively; Table 2). That SCS could more reliably classify a greater proportion of spectra than could be assessed visually is testament to the robustness and greater generality of the computer-based approach. The specificity of the SCS-based diagnosis was further improved by presenting spectral data with high signal-to-noise ratio to the computer. Removing 31 spectra with poor signal-to-noise ratio increased the sensitivity and specificity to 94% and 98%, respectively.[83]

8.2. Disease prognosis

A major challenge in breast cancer is the need to identify and understand the factors that most affect a patient's prognosis. The best indicator of survival for

patients with early breast cancer is still regional lymph node status.[84,85] MRS combined with SCS-based analysis has been used to predict nodal involvement and vascular invasion in breast cancer patients from the cellular material derived solely from the primary tumour. In so doing, the SCS has been successful in developing classifiers based on patterns of complex information that were not visually obvious. This emphasizes the wealth of chemical information available in the MR spectrum that can be extracted with the appropriate statistical approach.

8.2.1. Lymph node involvement

MR spectra from 29 patients with breast cancer with nodal involvement and 32 without nodal involvement were subjected to SCS-based analysis.[83] Maximally discriminatory subregions were 0.43–0.51, 0.64–0.77, 1.10–1.20 and 1.56–1.59 ppm for the first derivatives of the spectra, and 0.44–0.51, 0.67–0.71, 1.13–1.19, 1.56–1.60 and 1.86–1.96 ppm for rank-ordered spectra. Using LDA and bootstrap-based cross-validation, two separate classifiers, A (using the optimal regions from the first derivatives of the spectra) and B (using the optimal regions from the rank ordered spectra), were developed. The final classifier was the Wolpert-combined A + B classifiers.[61]

The presence of lymph node metastases was predicted with a sensitivity of 97% and specificity of 94% (Table 2). The overall crispness of the data was 95.1%, that is, 3 of the total 61 samples were classified as fuzzy (class probability less than 75%). An overall 95.0% accuracy for the test was obtained when specimens classified as fuzzy were excluded.[83]

8.2.2. Vascular invasion

MR spectra from 33 patients with breast cancer with vascular invasion and 52 without were subjected to the SCS-based analysis. Maximally discriminatory subregions were 0.47–0.55, 0.57–0.62, 0.86–0.92, 1.00–1.03, 1.69–1.71, 1.99–2.05, 2.55–2.56 and 2.63–2.72 ppm for the first derivatives of the spectra, and 0.75–0.81, 0.90–0.94, 1.03–1.12, 1.21–1.24, 1.59–1.63, 2.00–2.04, 2.24–2.27 and 2.70–2.74 ppm for rank-ordered spectra. Using LDA and bootstrap-based cross-validation, two separate classifiers, A (using the optimal regions from the first derivatives of the spectra) and B (using the optimal regions from the rank-ordered spectra), were developed. The final classifier was the Wolpert-combined A + B classifiers.[61]

The presence of vascular invasion was predicted by the SCS with a sensitivity of 81.8% and specificity of 100% (Table 2). The overall crispness of the data was 94.1%; that is, 5 of the total of 85 samples were classified as fuzzy (class probability less than 75%). An overall 91.9% accuracy for the test set was obtained when specimens classified as fuzzy were excluded.[83]

8.3. Ductal carcinoma *in situ*

Ductal carcinoma *in situ* (DCIS) is by definition the pathological entity that immediately precedes invasive carcinoma of the breast. Assessment of DCIS to ascertain the malignant potential of the lesion and whether or not microinvasion is present is crucial to the successful management of early breast disease. MRS on FNAB has been shown to distinguish pure DCIS without comedonecrosis or microinvasion from DCIS specimens containing comedonecrosis or a few foci of microinvasion.[19] Pure DCIS was not, however, distinguished from benign lesions based on visual inspection analysis of the data, and this begs the question as to the precise malignant potential of so-called low- and intermediate-grade DCIS. SCS-based analysis of the MRS data from DCIS, by accessing all the available spectral information, will likely be able to make this distinction, as well as report on the malignant potential of the lesion. However, all classifiers, including those based on SCS, are only as accurate as the information from which they are developed, and for DCIS, which presents as a histological continuum, optimal histological assessment requires that the entire tissue specimen examined by MRS be assessed in sections taken every 100 μm.

The importance of thorough pathological assessment is shown in Fig. 9.[19] The top tissue section shows 'cancerization' of an adjacent lobule by DCIS with microinvasion (as confirmed by immunostaining for smooth muscle actin). In the bottom tissue section, taken 100 μm further through the tissue block, there is no evidence of invasion. This variability not only highlights the biological continuum through which invasive ductal carcinoma passes to reach clinical cancer, but the vagaries of histological sampling if accurate correlation is to be achieved with spectral findings.

9. FURTHER DEVELOPMENTS IN DATA ANALYSIS

9.1. Regression analysis/detection of outliers

Classification methods are designed to deal with well-defined classes. However, many diseases are characterized by an essentially continuous transition from healthy to the disease state. These types of problems are most appropriately dealt with by a *regression* approach. For two-class problems, classification by LDA and linear regression are equivalent. If the number of samples/class for the two classes is the same, then the two approaches are identical. The regression approach has the additional advantage that *robust* versions, which can detect the presence of *outliers*, can be readily implemented.

Outliers arise either because the exemplar to be classified is atypical of either class, or because it belongs to an entirely different one. In either case, it is important to make the identification, leading to additional tests. In a clinical

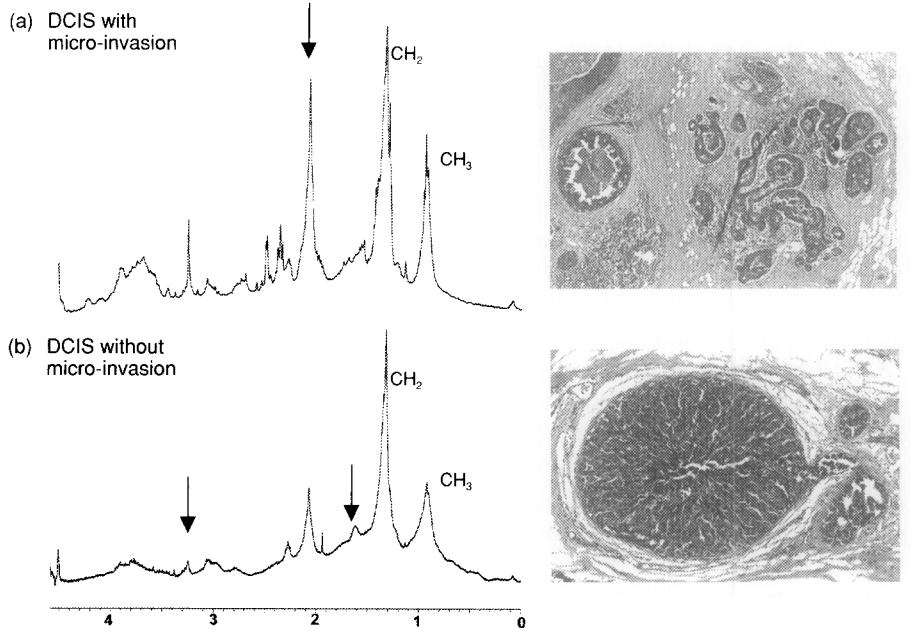

Fig. 9. Ductal carcinoma *in situ* of the breast. ^{1}H MR spectra (8.5 T, 37°C) of fine-needle biopsy specimens obtained from breast ductal carcinoma *in situ*: (a) with micro-invasion present; (b) without micro-invasion. Tissue sections of DCIS were taken 100 μm apart and are shown in: (a) with micro-invasion present; and (b) without micro-invasion. Spectra were acquired over a spectral width of 3597 Hz, 8192 data points, 256 accumulations, and relaxation delay of 2 s. Reprinted with permission from the *Journal of Women's Imaging*. Lippincott Williams & Wilkins © 2000.

context, identification of an outlier may indicate *multimorbidity*, or the presence of confounding medical conditions, or even of some other, unanticipated disease.

A preliminary example suggests the power and possibilities of the regression approach.[86] ^{1}H MRS (8.5 T) was performed on biopsy tissue obtained after radical prostatectomy. The 120 benign samples contained 5–60% stroma versus glandular tissue. In the 66 cancer samples, the amount of cancerous tissue ranged 1–70%, with 6 containing only 1–2%. The relative volumes of malignant glandular, benign glandular or stromal tissue were estimated by histopathology. At the ORS_GA stage, least trimmed squares (~10% outliers trimmed), one particular version of robust regression analysis (RA), on stromal versus glandular tissue, yielded, with five attributes, an average absolute error of 4.33% (for 60 spectra in the training set, TR) and 4.84% (for 60 spectra in the test set, TS). Removing the six largest outliers from each class decreased these average errors to 3.72% (TR) and 3.78% (TS). RA on cancerous versus benign tissue yielded, with six attributes, average errors of 6.63% (for 44 in TR) and 9.64% (for 22 in TS). Removing seven (5 + 2) outliers produced the improved 4.36%

(TR) and 6.95% (TS). Given the 'resolution' of the histopathology (not better than ± 5%), and the limited number of samples, these are very promising results.

9.2. Analysis of sparse data sets

Without a sufficient number of samples for analysis, the 'curse of data set sparsity' is, unfortunately, the clinical reality. To create robust classifiers, we have taken the approach (stage 1 of the SCS) of reducing the number of attributes to acceptable levels (1/5–1/10 of the number of samples). A complementary method would be to somehow augment the number of samples. This is easily visualized as a process of 'filling the gaps' in feature space between the existing samples. This would be possible in principle, if we knew the multivariate distributions of the classes. In practice, these are not known and not readily constructed. Instead, we have to rely on the existing, sparse data. A local, nearest-neighbour approach[87] could be used to produce 'surrogate' samples from the original data. The surrogate data set could be made arbitrarily large, and would serve as the training set. The original data would provide an 'independent' validation set. Preliminary experiments are promising.[88] Creating representative surrogate *spectral features* can be made more reliable by taking into account the inherent ordering of the spectral data points, i.e. features. In particular, surrogate *spectra* can be generated prior to feature selection, as has already been done for a different purpose.[89]

9.3. Nonlinear transformations of features

When using a linear method, such as LDA, the underlying assumption is that the two classes are linearly separable. This, of course, is generally not true. If linear separability is not possible, then with enough samples, the more powerful quadratic discriminant analysis (QDA) works better, because it allows the hypersurface that separates the classes to be curved (quadratic). Unfortunately, the clinical reality of small-sized data sets denies us this choice.

A possible remedy is applicable if the number of attributes is sufficiently small (≤10). Then the dimension of the attribute space can be simply augmented, e.g. by considering polynomial powers of the original attributes. As an example, a two-dimensional *linear* space, composed of x_1 and x_2, becomes five-dimensional (*quadratic*), by defining additional attributes $y_3 = x_1^2$, $y_4 = x_2^2$ and $y_5 = x_1 x_2$, in addition to the original y_1 ($\equiv x_1$) and y_2 ($\equiv x_2$). Then, a linear classifier, using the new attribute set $y_1, y_2, \ldots, y_5$, in this augmented feature space, will be able to separate the classes.

Another alternative for augmenting features in a low-dimensional feature space by nonlinear transformations is to create from the N starting features x_i all $N(N-1)$ possible feature *ratios* $y_k = x_i/x_j$, $k = 1, \ldots, N(N-1)$ ($i \neq j$, $i, j = 1, \ldots, N$). Including the N original features, there will be N^2 features in the augmented

feature space. From these, an optimal subset can be selected by the DP and/or ES approaches described in Section 2.3. The proposed procedure is to find first, by ORS_GA, N good discriminating features ($N \leq 10$), augment these by the ratio method, and use DP/ES to select the best subset. This approach puts on a firm statistical footing, and generalizes, the spectroscopists' peak-ratio method: The 'peaks' are the optimal subregions found, and all of their possible ratios are considered. We are currently exploring the possibilities of this approach (R. L. Somorjai, unpublished observations).

The above approaches encounter the 'curse of dimensionality' when the number N of original features is large: even for the simplest quadratic polynomial transformation, or for the ratio method, the number of transformed variables would be $O(N^2)$. However, a transformation we call the *α-scaling* method[49] could be applied to the original N features. This replaces each original spectral attribute f_k by $g_k = f_k \exp[-\alpha(f_k - \langle f_k \rangle)/\langle f_k \rangle]$, where $\langle f_k \rangle$ is the mean value of f_k over all spectra in the data set. Thus, there is no increase in the number of attributes. This method is expected to enhance differences between spectra of different classes, which should lead to better classification. The only parameter to be optimized is α, i.e. only a one-dimensional optimizer is needed. Furthermore, α could be optimized at the GA_ORS stage. However, mixed terms (e.g. $x_1 x_2$) cannot be accommodated with α-scaling.

10. CONCLUSIONS

MRS of human biopsy specimens has the potential to become the new gold standard for pathological and, in some organs, clinical characterization of human cancers. MRS can detect small populations of abnormal cells with high accuracy, and identify and subcategorize preinvasive states. In addition, MRS detects changes to cellular chemistry in human tissues prior to these changes being apparent under the light microscope and, hence, discernable by current methods. The development of a classifier for breast biopsy that determines both pathology and nodal involvement is a paradigm shift in the management of breast disease. It remains to be seen if such prognostic information is available in spectra from other organs such as prostate and oesophagus. This new methodology is of clinical importance in identifying the extent of abnormality in preinvasive states, particularly in patients with a predisposition to cancer. Accurate diagnosis and characterization of preinvasive states is at present a key missing link in the diagnostic chain, and would allow optimal management and minimal therapy for the many patients in whom cancer has not fully developed.

Integral to the ongoing success of MRS in the accurate and objective diagnosis of human disease states is the use of robust and comprehensive methods of analysing the spectral data. The three-stage SCS-based methodology, which is the focus of this chapter, has been specifically developed for this purpose. The method provides accurate and reliable classification of large amounts of bio-

medical spectral data, while ensuring that the complete content of the spectrum is considered, spectral identity is retained, and a degree of confidence in a given diagnosis is provided. Furthermore, the use of SCS allows the MRS method to be automated, a step which must precede the routine use of this technology by clinicians.

In order to realize the full potential of this new application, future clinical studies must include detailed pathological assessment of all tissue analysed by MRS. Importantly, if the MRS data are not compatible with the histological data, the entire tissue must be examined without knowledge of the MRS diagnosis, and the MRS data reviewed to ensure that the discrepancy is not due to sampling error. It must also be considered that the SCS, combined with MRS, can classify diseases or stages of disease that are clinically difficult to separate, and that histopathology may, in some cases, be an inadequate 'gold standard'. Being able to provide not only diagnostic but also prognostic information, the future applications of MRS combined with the SCS are many. It is important to note, however, that the methodology will provide accurate classifications only when correct and complete pathology is provided, and, due to the variability in data, sufficiently large numbers of subjects are included in the training of the classifiers.

11. GLOSSARY OF TERMS

Adenocarcinoma A form of cancer that involves cells from the lining of the walls of many different organs of the body.

Adenoma A benign epithelial tumour in which the cells form recognizable glandular structures or in which the cells are clearly derived from glandular epithelium.

Anaplasia Characteristics of a cell (structure and orientation) that make it identifiable as a cancer cell and malignant.

Carcinosarcoma A malignant neoplasm that contains elements of carcinoma and sarcoma so extensively intermixed as to indicate neoplasia of epithelial and mesenchymal tissue.

Cirrhosis Liver disease characterized pathologically by loss of the normal microscopic lobular architecture, with fibrosis and nodular regeneration.

Cytology The study of cells. Implies the use of light or electron microscopic methods for the study of morphology.

Fibrosarcoma Malignant tumour derived from connective tissue fibroblast.

Follicular Affecting the follicles.

Hepatoma Carcinoma derived from liver cells. A better term to use is hepatocarcinoma or hepatocellular carcinoma.

Histology The study of cells and tissue on the microscopic level.

Malignant	(oncology) Tending to become progressively worse and to result in death. Having the properties of anaplasia, invasion and metastasis, said of tumours.
Metastases	Cancer that started from cancer cells from another part of the body. For example: cancer that starts in the breast can spread to the lymph nodes and then be spread throughout the body.
Morphology	A study of the configuration or the structure of animals and plants.
Neoplasia	Literally new growth, usually refers to abnormal new growth and thus means the same as tumour, which may be benign or malignant.
Prognosis	A forecast as to the probable outcome of an attack or disease, the prospect as to recovery from a disease as indicated by the nature and symptoms of the case.
Prolactinoma	A pituitary gland tumour which secretes prolactin and can thus cause false symptoms of pregnancy.

ACKNOWLEDGEMENTS

The authors thank former and present staff, students and collaborators of the Institute for Magnetic Resonance Research, and the Informatics research team at the Institute for Biodiagnostics, particularly Brian Dolenko and Sasha Nikulin, involved in the research presented in this chapter, who have worked diligently towards developing magnetic resonance spectroscopy for routine use in the clinic. Particular thanks go to Peter Malycha, Martin Tattersall and Tom Reeve for their encouragement and support. We thank Raquel Baert for helping prepare Table 1, and Sinead Doran, Brooke O'Donnell and Deborah Edward for helping prepare the manuscript.

REFERENCES

1. A. M. Neville, R. Bettelheim, R. D. Gelber and A. Goldhirsch, *Lancet*, 1990, **336**, 759.
2. C. E. Mountford, C. L. Lean, W. B. Mackinnon and P. Russell (eds), *The Use of Proton MR in Cancer Pathology*, Academic Press, 1993.
3. C. E. Mountford, W. B. Mackinnon, M. Bloom, E. Burnell and I. C. P. Smith, *J. Biochem. Biophys. Meth.*, 1984, **9**, 323.
4. L. C. Wright, G. L. May, P. Gregory, M. Dyne, K. T. Holmes, P. G. Williams and C. E. Mountford, *J. Cell Biochem.*, 1988, **37**, 49.
5. K. T. Holmes, P. G. Williams, M. Bloom, M. Dyne, C. E. Mountford, N. King, M. Karaman, B. Ninham and R. Blanden, *Magn. Reson. Med. Biol.*, 1988, **1**, 75.
6. C. L. Lean, W. B. Mackinnon, E. J. Delikatny, R. H. Whitehead and C. E. Mountford, *Biochemistry*, 1992, **31**, 11095.
7. W. B. Mackinnon, L. I. Huschtscha, K. Dent, R. Hancock, C. Paraskeva and C. E. Mountford, *Int. J. Cancer*, 1994, **59**, 248.

8. W. B. Mackinnon, P. Russell, G. L. May and C. E. Mountford, *Int. J. Gynaecol. Cancer*, 1995, **5**, 211.
9. W. B. Mackinnon, L. Delbridge, P. Russell, C. L. Lean, G. L. May, S. T. Doran, S. Dowd and C. E. Mountford, *World J. Surg.*, 1996, **20**, 841.
10. A. Rutter, W. B. Mackinnon, L. I. Huschtscha and C. E. Mountford, *Exp. Gerontol.*, 1996, **31**, 669.
11. C. E. Mountford, E. J. Delikatny, M. Dyne, K. T. Holmes, W. B. Mackinnon, R. Ford, J. C. Hunter, I. D. Truskett and P. Russell, *Magn. Reson. Med.*, 1990, **13**, 324.
12. C. E. Mountford, J. K. Saunders, G. L. May, K. T. Holmes, P. G. Williams, R. M. Fox, M. H. Tattersall, J. R. Barr, P. Russell and I. C. P. Smith, *Lancet*, 1986, **1**, 651.
13. E. J. Delikatny, P. Russell, J. C. Hunter, R. Hancock, K. H. Atkinson, C. van Haaften-Day and C. E. Mountford, *Radiology*, 1993, **188**, 791.
14. C. L. Lean, R. C. Newland, D. A. Ende, E. L. Bokey, I. C. P. Smith and C. E. Mountford, *Magn. Reson. Med.*, 1993, **30**, 525.
15. P. Russell, C. L. Lean, L. Delbridge, G. L. May, S. Dowd and C. E. Mountford, *Am. J. Med.*, 1994, **96**, 383.
16. L. Delbridge, C. L. Lean, P. Russell, G. L. May, S. Roman, S. Dowd, T. S. Reeve and C. E. Mountford, *World J. Surg.*, 1994, **18**, 512.
17. C. L. Lean, L. Delbridge, P. Russell, G. L. May, W. B. Mackinnon, S. Roman, T. J. Fahey, 3rd, S. Dowd and C. E. Mountford, *J. Clin. Endocrinol. Metab.*, 1995, **80**, 1306.
18. P. A. Barry, C. Wadstrom, G. Falk, P. Shehan, P. Russell, C. L. Lean *et al.*, in *What is the Value of ^{1}H MRS in Detecting Early Malignant Changes?* (ed. R. Giuli), p. 1122, 1998.
19. W. B. Mackinnon, P. A. Barry, P. L. Malycha, D. J. Gillett, P. Russell, C. L. Lean, S. T. Doran, B. H. Barraclough, M. Bilous and C. E. Mountford, *Radiology*, 1997, **204**, 661.
20. C. E. Mountford, *Today's Life Science*, 1998, 22.
21. C. E. Mountford, C. L. Lean, R. Hancock, S. Dowd, W. B. Mackinnon, M. H. Tattersall and P. Russell, *Invasion Metastasis*, 1993, **13**, 57.
22. S. Howells, R. Maxwell, A. Peet and J. Griffiths, *Magn. Reson. Med.*, 1992, **28**, 214.
23. S. Howells, R. Maxwell, F.A. Howe *et al.*, *NMR Biomed.*, 1993, **6**, 237.
24. N. Branston, R. Maxwell and S. Howells, *J. Microcomp. Appl.*, 1993, **16**, 113.
25. A. Tate, S. Crabb, J. Griffiths *et al.*, *Anticancer Res.*, 1996, **16**, 1575.
26. M. Preul, Z. Caramanos, D. Collins *et al.*, *Nature Med.*, 1996, **2**, 323.
27. J.-P. Usenius, S. Tuohimetsa, P. Vainio *et al.*, *Neurochemistry*, 1996, **7**, 1597.
28. W. El-Deredy, S. Ashmore, N. Branston *et al.*, *Cancer Res.*, 1997, **57**, 4196.
29. R. Maxwell, I. Martinez-Perez, S. Cerdan *et al.*, *Magn. Reson. Med.*, 1998, **39**, 869.
30. H. Poptani, J. Kaartinen, R. Gupta *et al.*, *J. Cancer Res. Clin. Oncol.*, 1999, **125**, 343.
31. C. E. Mountford, S. T. Doran, C. L. Lean and P. Russell, *Biophys. Chem.*, 1997, **68**, 127.
32. K. J. Cross, K. T. Holmes, C. E. Mountford and P. E. Wright, *Biochemistry*, 1984, **23**, 5895.
33. L. C. Wright, M. Dyne, K. T. Holmes and C. E. Mountford, *Biochem. Biophys. Res. Commun.*, 1985, **133**, 539.
34. G. L. May, L. C. Wright, K. T. Holmes, P. G. Williams, I. C. P. Smith, P. E. Wright, R. M. Fox and C. E. Mountford, *J. Biol. Chem.*, 1986, **261**, 3048.
35. P. G. Williams, J. K. Saunders, M. Dyne, C. E. Mountford and K. T. Holmes, *Magn. Reson. Med.*, 1988, **7**, 463.
36. C. L. Lean, W. B. Mackinnon and C. E. Mountford, *Magn. Reson. Med.*, 1991, **20**, 306.
37. R. L. Somorjai, B. Dolenko, W. Halliday, D. Fowler, N. Hill, I. Ross, K. M. Brière and I. C. P. Smith, *J. Med. Biochem.*, 1999, **3**, pp. 17–24
38. N. Pizzi, L.-P. Choo, J. Mansfield, M. Jackson, W. Halliday, H. H. Mantsch and R. L. Somorjai, *Artificial Intelligence Med.*, 1995, **7**, 67.
39. L.-P. Choo, J. Mansfield, N. Pizzi, R. L. Somorjai, M. Jackson, W. Halliday and H. H. Mantsch, *Biospectroscopy*, 1995, **1**, 141.
40. H. Eysel, M. Jackson, A. E. Nikulin, R. L. Somorjai, G. Thomson and H. H. Mantsch, *Biospectroscopy*, 1997, **3**, 161.

41. M. Jackson, J. Mansfield, B. Dolenko, R. L. Somorjai, H. H. Mantsch and P. Watson, *Cancer Detect. Prevent.*, 1999, **23**, 245.
42. P. Hahn, I. C. P. Smith, L. Leboldus, C. Littman, R. L. Somorjai and T. Bezabeh, *Cancer Res.*, 1997, **57**, 3398.
43. J. C. Wallace, G. P. Raaphorst, R. L. Somorjai, C. E. Ng, M. Fung Kee Fung, M. Senterman and I. C. P. Smith, *Magn. Reson. Med.*, 1997, **38**, 569.
44. T. Bezabeh, I. C. P. Smith, E. Krupnik, R. L. Somorjai, D. G. Kitchen, C. N. Bernstein, N. M. Pettigrew, R. P. Bird, K. J. Lewin and K. M. Brière, *Anticancer Res.*, 1996, **16**, 1553.
45. S. T. Doran, G. Falk, R. L. Somorjai, C. L. Lean, U. Himmelreich, J. Philips, P. Russell, B. Dolenko, A. E. Nikulin and C. E. Mountford, Submitted,
46. R. L. Somorjai, A. E. Nikulin, N. Pizzi, D. Jackson, G. Scarth, B. Dolenko, H. Gordon, E. Russell, C. L. Lean, L. Delbridge, C. E. Mountford and I. C. P. Smith, *Magn. Reson. Med.*, 1995, **33**, 257.
47. G. Werner, J. Früh, F. Keller, H. Greger, R. L. Somorjai, B. Dolenko, M. Otto and D. Böcker, *Mid Infrared Spectroscopy as a Tool for Disease Pattern Recognition from Human Blood* (eds H. H. Mantsch and M. Jackson), p. 35, 1998.
48. W. Petrich, B. Dolenko, J. Früh, M. Ganz, H. Greger, S. Jacob, F. Keller, A. E. Nikulin, M. Otto, O. Quarder, R. L. Somorjai, A. Staib, G. Werner and H. Wielinger, *Appl. Optics*, 2000, **39**, 3372.
49. B. Dolenko and R. L. Somorjai, *Proceedings in Society of Magnetic Resonance, Third Scientific Meeting*, 19–25 August 1995, Abstract 1936.
50. A. E. Nikulin, K. M. Brière, L. Friesen, I. C. P. Smith and R. L. Somorjai, *Proceedings in Society of Magnetic Resonance, Third Scientific Meeting*, 19–25 August 1995, Abstract 1940.
51. A. E. Nikulin, B. Dolenko, T. Bezabeh and R. L. Somorjai, *NMR Biomed.*, 1998, **11**, 209.
52. E. Mazzaferri, *N Engl. J. Med.*, 1993, **328**, 553.
53. E. Mazzeferri, *Am, J. Med.*, 1992, **93**, 359.
54. V. A. LiVolsi, *Surgical Pathology of the Thyroid*, WB Saunders, Philadelphia, 1990, 173.
55. J. Fagin, K. Matsuo, A. Karmakar, D. Chen, S. Tang and H. Koeffler, *J. Clin. Invest.*, 1993, **91**, 179.
56. G. McLachlan, *Discriminant Analysis and Statistical Pattern Recognition*, John Wiley, New York, 1992.
57. J. Hertz, A. Krogh and R. Palmer, *Introduction to the Theory of Neural Computation*, Addison-Wesley Publishing Co., Redwood City, CA, 1991.
58. J. R. Koza, *Genetic Programming*, MIT Press, Cambridge, MA, 1992.
59. B. Ross and E. Danielsen, *Magnetic Resonance Spectroscopy: Diagnosis of Neurological Diseases*, Marcel Dekker, New York, 1999.
60. R. L. Somorjai, B. Dolenko, A. E. Nikulin, N. Pizzi, G. Scarth, P. Zhilkin, W. Halliday, D. Fewer, N. Hill, I. Ross, M. West, I. C. P. Smith, S. M. Donnelly, A. C. Kuesel and K. M. Brière, *J. Magn. Reson. Imaging*, 1996, **6**, 437.
61. D. Wolpert, *Neural Networks*, 1992, **5**, 241.
62. D. Kondziolka, L. D. Lunsford and A. J. Martinez, *J. Neurosurg.*, 1993, **79**, 533.
63. P. Swindle, S. McCredie, P. Russell, U. Himmelreich, M. Khadra, C. L. Lean and C. E. Mountford, Submitted.
64. American Cancer Society, *Cancer Facts and Figures*, 7, ACS, Atlanta, 1996.
65. M. B. Garnick, *Ann. Intern. Med.*, 1993, **118**, 804.
66. J. Kurhanewicz, D. B. Vigneron, H. Hricak, P. Narayan, P. R. Carroll and S. J. Nelson, *Radiology*, 1996, **198**, 795.
67. J. Kurhanewicz, D. B. Vigneron, H. Hricak, F. Parivar, S. J. Nelson, K. Shinohara and P. R. Carroll, *Radiology*, 1996, **200**, 489.
68. E. B. Cornel, G. A. Smits, G. O. Oosterhof, H. F. Karthaus, F. M. Deburyne, J. A. Schalken and A. Heerschap, *J. Urol.*, 1993, **150**, 2019.
69. M. E. Yacoe, G. Sommer and D. Peehl, *Magn. Reson. Med.*, 1991, **19**, 429.
70. S. McCredie, P. Swindle, C. L. Lean, S. Dowd, P. Russell and C. E. Mountford, *Proceedings in 7th Scientific Meeting International Society of Magnetic Resonance in Medicine*, 1999, Abstract 1508.

71. C. Ménard, I. C. P. Smith, R. L. Somorjai, L. Leboldus, R. Patel, C. Littman, S. J. Robertson and T. Bezabeh, *Int. J. Radiat. Oncol. Biol. Phys.*, 2001, **50**, 317.
72. R. G. Simonetti, C. Camma, F. Fiorello, F. Politi, G. D'Amico and L. Pagliaro, *Digest. Dis. Sci.*, 1991, **36**, 962.
73. C. Duvoux, *Ann. Chir.*, 1998, **52**, 511.
74. M. Sakamoto, S. Hirohashi and Y. Shimosato, *Human Pathol.*, 1991, **22**, 172.
75. Y. Nagato, F. Kondo, Y. Kondon, M. Ebara and M. Ohto, *Hepatology*, 1991, **14**, 473.
76. U. Himmelreich, R. Soper, R. L. Somorjai, B. Dolenko, D. Painter, C. L. Lean, C. E. Mountford and P. Russell, *Proceedings in International Society of Magnetic Resonance in Medicine—9th Scientific Meeting and Exhibition*, 2001, Abstract 268.
77. C. L. Lean, P. Russell and C. E. Mountford, *J. Women's Imag.*, 2000, **2**, 19.
78. S. Shapiro, W. Venet, P. Strax *et al.*, *J. Nat. Cancer Inst.*, 1982, **69**, 349.
79. National Program for the Early Detection of Breast Cancer Monitoring and Evaluation Reference Group, Commonwealth Department of Human Services and Health, *National Program for the Early Detection of Breast Cancer: Evaluation of Phase One 1 July 1991–30 June 1994*, Canberra, Australia, 1994.
80. G. Dodd, *Cancer*, 1977, **29**, 2796.
81. G. Hiller, M. Harney, S. Legg and S. Hart, *Aust. N.Z. J. Surg.*, 1987, **57**, 239.
82. D. Ingram, G. Sterrett, H. Sheiner and K. Shilkin, *Med. J. Aust.*, 1983, **2**, 170.
83. C. E. Mountford, R. L. Somorjai, P. L. Malycha, L. Gluch, C. L. Lean, P. Russell, B. H. Barraclough, D. J. Gillett, U. Himmelreich, B. Dolenko, A. E. Nikulin and I. C. P. Smith, *Br. J. Surg.*, 2001, **88**, 1234.
84. N. Weidner, *Curr. Opin. Obstet. Gynecol.*, 1995, **7**, 4.
85. B. Fisher, R. Ravdin, R. Ausman, N. Slack, G. Moore and R. Noer, *Ann. Surg.*, 1968, **168**, 337.
86. R. L. Somorjai, R. Bourne, A. E. Nikulin, B. Dolenko, P. Russell and C. E. Mountford, Classification and regression analyses of known mixtures of cancer and benign tissue in prostate biopsies, *Proceedings in International Society of Magnetic Resonance in Medicine*, 2002.
87. S. Raudys, *Statistical and Neural Classifiers: An integrated Approach to Design*, Springer, London, 2001.
88. R. L. Somorjai, A. Janeliunas, R. Baumgartner and S. Raudys, Submitted 2002,
89. P. Zhilkin and R. L. Somorjai, *Connection Science: Special Issue 'Combining Neural Nets'*, 1996, **8**, 427.

NMR Determination of Porous Media Property Distributions

A. TED WATSON[1], JEROMY T. HOLLENSHEAD[2*], JINSOO UH[2] and C. T. PHILIP CHANG[3†]

[1]*Department of Chemical Engineering, Colorado State University, USA,*
[2]*Department of Chemical Engineering, Texas A&M University, USA, and*
[3]*Engineering Imaging Laboratory, Texas A&M University, USA*

We use nuclear magnetic resonance (NMR) imaging to determine spatial distributions of properties used to describe flow in heterogeneous porous media. The methods are demonstrated on sandstone samples, which are characteristic of underground formations.

Static imaging experiments conducted on fluid-saturated samples are used to determine porosity distributions. Carr–Purcell–Meiboom-Gill (CPMG) imaging is used to evaluate the spin density. The local relaxation is modeled in order to estimate the intrinsic magnetization intensity, which is proportional to the amount of saturating fluid.

To determine permeability distributions, experiments are conducted whereby fluid is injected into saturated samples. A pulsed-field-gradient stimulated-echo technique is used to resolve the velocity field within the sample. An inverse problem is formulated and solved to determine the permeability distribution.

* Now with Sandia National Laboratories, Livermore, USA.
† Now with Millennium Technology Inc., Richmond, Canada.

ANNUAL REPORTS ON NMR SPECTROSCOPY
VOLUME 48 ISBN 0-12-505448-3

1. INTRODUCTION

The flow of fluids through permeable materials occurs throughout industry and nature. Many key industrial technologies rely on the flow of fluids through such structures; the use of filters for purification, membranes for gas separation, and porous catalyst supports for carrying out chemical reactions are just a few examples. The prevalence of this process is also seen within the human body itself, where many of the processes which sustain life depend on the flow of fluids through bone, organs, and other tissues throughout the body. Additionally, this same process is found on a considerably larger scale in the subsurface, where both water and petroleum products flow through soils and rocks to make up large systems of aquifers and petroleum reservoirs.

It is often desired to control processes which involve the flow of fluids through permeable materials. Important examples are improved recovery from petroleum reservoirs and remediation of polluted aquifers. We may also be interested in designing new porous materials, such as scaffolds for tissue engineering. A key element in accomplishing these things is a mathematical model of flow in the permeable media. This is normally done using volume-averaged equations. The volume-averaging method[1,2] is an extension of the well-known continuum description used to describe fluid flow. The continuum approach allows meaningful information describing the physical systems of interest to be determined by introducing various material properties, such as the viscosity and density, while avoiding specifying the exact interactions of individual molecules. Similarly, the volume-averaging approach allows meaningful information about systems to be determined by introducing a number of macroscopic properties which depend upon the media. This eliminates the need to specify the exact geometry of the solid–fluid interfaces.

The volume-averaged equations are developed by averaging the standard differential momentum, mass and energy balances over a local volume element. Although it is not necessary for the actual size of the averaging region to be specified, it is understood that it is large relative to some characteristic pore size, and small relative to the dimensions of the macroscopic sample of interest. The result of the averaging procedure is a set of equations that describes the transport of momentum, mass and energy through porous material. The equations include fluid states and macroscopic properties of the material. These media properties, which in general are smooth functions of position, represent macroscopic empiricisms which must be estimated using previously developed correlations or by solving a suitably posed inverse problem utilizing relevant experimental data.

The creeping flow of a single fluid phase through a stationary permeable media is the most basic physical situation of interest. In this case, the volume-averaged overall mass balance yields the equation of continuity:[3]

$$\frac{\partial(\phi\rho)}{\partial t} = -\nabla \cdot (\rho \mathbf{v}) + \psi \tag{1}$$

Here, the superficial velocity, $\mathbf{v}$, represents a fluid state, and the density, ρ, a fluid property which, for a compressible fluid, can be related to the pressure through an equation of state. The porosity, ϕ, which is defined as the void fraction within the media, is a macroscopic property of the porous material. Sources and/or sinks located within the physical system are represented using ψ. Volume averaging the differential momentum balance for the same physical situation yields Darcy's law:

$$\mathbf{v} = -\frac{k}{\mu}\,(\nabla p - \rho \mathbf{g}) \tag{2}$$

where the viscosity, μ, is a property of the fluid, the pressure, p, is a fluid state, and the acceleration of gravity is represented by $\mathbf{g}$. The permeability, k, is a macroscopic property of the porous material which indicates the relative ease with which fluid can flow through the material. Although permeability is derived to be a spatially varying second-order tensor, it is often assumed to be isotropic and represented as a scalar function of position.

The volume-averaged forms found in Eqs (1) and (2) are for the creeping flow of Newtonian fluids through a stationary porous material. For this case, the permeability and porosity are solely functions of the media structure. If certain aspects of the physical problem are changed, the functional dependence of the macroscopic properties in these equations may be different and modified forms of these equations may be appropriate. For example, it is well known that permeability may be a function of pressure for a gas in microporous structures. This dependence is due to a slip effect that becomes important when the molecular mean free path of the gas is on the order of a characteristic pore size of the material. Modifications may also be appropriate when inertial effects become important and for non-Newtonian fluids. For more complicated situations involving multiple fluid phases, additional macroscopic properties are required, and often their functional forms depend in part on the saturating fluids. In any case, the porosity and permeability play a crucial role in describing the flow of fluids through permeable material and are the most fundamental properties of such media.

The determination of the properties of a porous medium is accomplished experimentally, using samples which are considerably larger in size than the pore scale. When dealing with underground sedimentary formations, for example, the samples are typically an inch in diameter and a few inches in length. With conventional experiments, a single value is determined for each property which represents, at best, an average of the property within the sample. For example, the permeability is conventionally determined from data measured while flowing a single fluid phase at a constant rate through a saturated sample. Using an integrated form of Darcy's law based on assumption of a uniform value of permeability, measured values for the pressure drop and injection rate are used to calculate a single value of permeability. However, the permeability is a function of position, and it is believed that its value can vary significantly, even within a

small sample. Consequently, the value so obtained must be considered an 'apparent' value, as it is computed using an equation which does not strictly apply. The determination of the complete *distributions* of the properties is highly desirable. The key limitation has been the inability to adequately observe fluid states *within* the media itself. Standard experimental techniques are limited to examining fluid states only on or outside the boundaries of media samples.

The ability of NMR imaging to non-invasively probe fluid states within permeable media provides a unique opportunity to develop methodologies which can determine distributions of properties within such media. Once these methodologies are developed, further experimentation and analysis can lead to an improved understanding and description of complex processes which are affected by spatial variations in these basic properties.

A key factor in developing the methodologies needed to characterize heterogeneous porous media is the analysis of experimental NMR measurements to determine the desired properties. In this chapter, we describe progress in our research to develop reliable methods for determining spatially dependent porosity and permeability distributions within permeable media. In Section 2, we consider the determination of the porosity. We first describe the CPMG pulse imaging sequence in Section 2.1, and then describe a method for determining the intrinsic magnetization, which is proportional to the amount of fluid, from the measured data. The results for a few selected samples are shown in Section 2.4. The methodology for determining spatially variable absolute permeability distributions is put forth in Section 3. We first describe the pulsed-field-gradient experiments and explain the relationship between the NMR signal and the fluid velocity. Section 3.2 describes how we determine the permeability distribution from the experimentally observed velocities. The methodology is then demonstrated in Section 3.3.

2. POROSITY DISTRIBUTIONS

Porosity is a macroscopic property of porous materials that provides a measure of the local void fraction within a material. It is defined to be the ratio of the pore volume to total volume for some volume element whose characteristic length is much greater than the characteristic length of a single pore. For a media filled with p fluid phases, the porosity is expressed mathematically as

$$\phi \equiv \frac{1}{V} \sum_{i=1}^{p} V^{(i)} \tag{3}$$

where V refers to the volume over which the porosity is defined and $V^{(i)}$ represents the volume of fluid phase i. The calculated porosity value is typically assigned to the centroid of the volume element.

In order to calculate the porosity, it is necessary to determine the volume of void space within a known volume of porous material. The sensitivity of NMR

to active nuclei, such as the hydrogen in water molecules, allows the spatial discrimination of fluid amounts contained within porous materials. If the material is fully saturated so that all of the pores are completely filled with fluid, the intrinsic magnetization intensity will be proportional to the void fraction and may be used to calculate the porosity from Eq. (3).

The following sections detail our methodology for determining multi-dimensional porosity distributions using NMR. Section 2.1 describes the magnetic resonance imaging (MRI) pulse sequences used to spatially probe the sample and discusses the acquisition of the observed NMR signal. Because significant relaxation typically occurs before the signal is acquired, this experimentally observed magnetization may not be a good estimate of the intrinsic magnetization which is required to determine the amount of fluid within the media. This effect becomes increasingly important when observing media containing a large number of small pores or with relatively large surface relaxivity and is a consequence of the profound effect that the solid has on relaxation. In order to overcome this effect, we explicitly model the relaxation process occurring within the porous media to determine the intrinsic magnetization. This process is described in Section 2.2. An expression relating the intrinsic magnetization intensity to the local quantity of fluid within a porous media sample is then derived in Section 2.3 and used to determine the porosity distribution from Eq. (3).

2.1. Probing porous materials using NMR imaging

Previously, most work concerned with quantitative estimates of porosity using NMR have utilized the Hahn spin-echo imaging sequence at different echo times to obtain multiple image acquisitions.[4,5] However, one of the most effective ways of obtaining a series of relaxation images is by using the CPMG echo train[6] incorporated with a suitable imaging scheme. Since an entire series of relaxation-attenuated CPMG images is collected in one scan as a single spin-echo image, an obvious advantage of CPMG over the Hahn spin-echo is the shorter imaging time. Another advantage is that the CPMG technique allows for the acquisition of T_2 data, where the molecular diffusion time is controlled by an experimentally selected echo-spacing. By using a short echo-spacing, the diffusion attenuation rate is minimized and the interpretation of fitting parameters with suitable relaxation models is improved.

The CPMG pulse sequence is shown in Fig. 1. The initial 90° radio-frequency (RF) excitation pulse is followed by series of 180° RF pulses spaced to allow a train of echoes to be observed between the pulses. The echo amplitudes are attenuated due to relaxation effects, which are described in Section 2.2. Both the first 90° and subsequent 180° pulses are non-selective broadband pulses.

Spatial discrimination of the NMR signal is achieved by superimposing a linear magnetic field gradient, $\mathbf{G}$, on the static magnetic field, $\mathbf{B}_0$. Then the

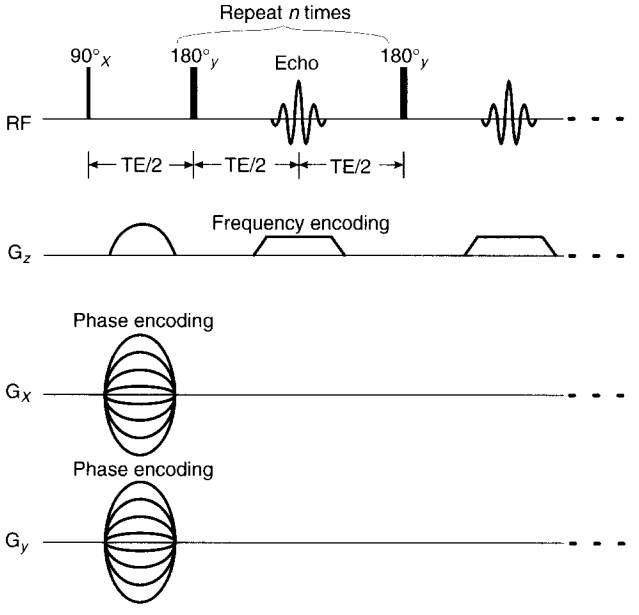

Fig. 1. Example of a three-dimensional CPMG pulse imaging sequence.

applied gradient field becomes a function of position $\mathbf{r}$ and proportional to the precessing frequency $\omega(\mathbf{r})$ of the nuclear moments with gyromagnetic ratio γ:

$$\omega(\mathbf{r}) = \gamma(\mathbf{B}_0 + \mathbf{G} \cdot \mathbf{r}) \tag{4}$$

The signal acquired from the imager in the rotating reference of frame is represented by[6]

$$S(\varphi) = \int I(\mathbf{r}) \exp\left(i\varphi\right)\mathrm{d}\mathbf{r} \tag{5}$$

where $I(\mathbf{r})$ is magnetic intensity at position $\mathbf{r}$. The phase of the signal, φ, depends on the duration of the time, t, for which the gradient field, $\mathbf{G}$, is applied:

$$\varphi(t) = \int_0^t \omega'(t')\mathrm{d}t' = \int_0^t \gamma\mathbf{G}(t') \cdot \mathbf{r}\mathrm{d}t' \tag{6}$$

where $\omega(t)$ is the precessing magnetic frequency in the rotating reference frame at on-resonance condition. For a stationary fluid, $\mathbf{r}$ is independent of time, and the signal, S, can be represented in $\mathbf{k}$-space:

$$S(\mathbf{k}) = \int I(\mathbf{r}) \exp\left(i\mathbf{k} \cdot \mathbf{r}\right)\mathrm{d}\mathbf{r} \tag{7}$$

with the following definition of $\mathbf{k}$:

$$\mathbf{k} = \gamma \int_0^t \mathbf{G}(t')\mathrm{d}t' \tag{8}$$

The observed NMR signal may be resolved in one, two or three spatial dimensions where the sample is assumed to be divided up into volume elements, called voxels. The signal S can be mapped out in $\mathbf{k}$ space by changing either duration (frequency encoding) or amplitude (phase encoding) of the applied gradient pulse. In addition to the RF pulse sequence, Fig. 1 also shows the gradient pulses associated with a three-dimensional CPMG pulse sequence. Here, frequency encoding is applied in the z-direction using the readout gradient, while phase encoding is applied in both the x and y directions by changing the magnitude of the gradient for each subsequent run. Through proper selection of the gradient pulses, the spatial discrimination of the magnetization intensity can be resolved to various degrees. The magnetization intensity, $I(\mathbf{r})$, is constructed from the observed signal $S(\mathbf{k})$ by an inverse Fourier transformation:

$$I(\mathbf{r}) = \int S(\mathbf{k}) \exp(-i\mathbf{k} \cdot \mathbf{r})\mathrm{d}\mathbf{k} \tag{9}$$

2.2. Quantification of the intrinsic magnetization intensity

The magnetization intensity $I(\mathbf{r})$ in Eq. (9) is acquired at each CPMG echo time, t_j, and expressed as a series of magnetization $M(t_j, \mathbf{r})$ for a fixed voxel located at $\mathbf{r}$. If a sufficiently long delay time T_R (e.g. $T_R > 5T_1$) is used, the echoes are attenuated only by transverse relaxation and, for a bulk fluid, the magnetization intensity is described by

$$M(t_j, \mathbf{r}) = m_0(\mathbf{r}) \exp\left(-\frac{t_j}{T_2}\right), j=1, \ldots, n \tag{10}$$

where $m_0(\mathbf{r})$ denotes the intrinsic magnetization intensity of the bulk fluid. On the other hand, heterogeneous porous media exhibit a distribution of relaxation times as local environments exhibit their own characteristic relaxation times. This situation can be represented formally as a collection of isolated pores whose relaxation is represented by the fast-exchange approximation.[7,8] Using a continuous distribution function to represent the relative amount of active nuclei corresponding to a given relaxation time, the observed magnetization intensity $M(t_j, \mathbf{r})$ is

$$M(t_j, \mathbf{r}) = \int_0^\infty m_0(\mathbf{r}, \tau) \exp\left(-\frac{t_j}{\tau}\right)\mathrm{d}\tau \tag{11}$$

The intrinsic magnetization of the voxel, $M_0(\mathbf{r})$, is found by evaluating Eq. (11) at $t_j = 0$:

$$M_0(\mathbf{r}) = \int_0^\infty m_0(\mathbf{r}, \tau)\mathrm{d}\tau \tag{12}$$

The goal, then, is to determine the distribution function $m_0(\mathbf{r}, \tau)$ for each voxel so that the intrinsic magnetization may be determined using Eq. (12). In what follows, the explicit dependence on position is dropped, with the understanding that the same analysis applies to each voxel throughout the sample. Equation (11) can be rewritten as a Fredholm integral equation of the first kind:

$$Y(t_j) = \int_0^\infty P(\tau)K(t_j, \tau)\mathrm{d}\tau + \varepsilon_j \tag{13}$$

The magnetization observed at time t_j constitutes the data, $Y(t_j) = M(t_j)$, and the kernel function, $K(t_j, \tau)$, is expressed as

$$K(t_j, \tau) = \exp\left(-\frac{t_j}{\tau}\right) \tag{14}$$

for transverse relaxation. The unknown relaxation distribution, $P(\tau)$, is a measure of intrinsic magnetization resulting from collections of nuclei relaxing with the same characteristic time, τ. For the relaxation analysis, the quantity of interest is the magnetization fraction $N(\tau)$, the amount of fluid relaxing at a given time τ over the total amount of fluid present. This quantity is interpreted as the volume fraction of relaxation times, and is obtained by normalizing $P(\tau)$:

$$N(\tau) = \frac{P(\tau)}{\int_0^\infty P(\tau)\mathrm{d}\tau} \tag{15}$$

The exact form of $P(\tau)$ is determined from nonparametric regression techniques.[9] These methods impose only a minimum structure on the distribution, in that it is only assumed that the unknown function possesses some degree of smoothness. The distribution function, $P(\tau)$, is a physical property and is expected to be well represented by a smooth, continuous function. Since every continuous function on a finite domain can be approximated arbitrarily accurately by a piecewise polynomial spline,[10] splines provide a good way to represent the unknown distribution function $P(\tau)$.[11] Splines are piecewise polynomials whose different polynomial segments have been joined together at knots in a way that ensures continuity properties. A spline of order m has $m-2$ continuous derivatives, providing the smoothest possible piecewise polynomial. B-spline basis functions provide a particularly good representation for splines. Then, the unknown distribution function is given by

$$P(\tau) = \sum_{j=1}^{n_s} c_j B_j^m(\tau, \mathbf{y}) \tag{16}$$

where $B_j^m(\tau, \mathbf{y})$ are B-spline basis functions, m is the order of the spline, and $\mathbf{y}$ represents the extended partition, the location of the knots. Once the partition is

chosen, the distribution is specified by the complete set of coefficients, c_j. The number of coefficients is given by the degrees of freedom n_s, the sum of the order and the number of interior knots. A sufficiently large dimension of the spline space n_s is used so that the estimation of the distribution function is largely uninfluenced by the number and position of knots.

We formulate a performance index based on least-squares or maximum-likelihood estimation principles:

$$J = \left[\mathbf{Y} - \mathbf{Y}^{\text{calc}}\right]^T \mathbf{W} \left[\mathbf{Y} - \mathbf{Y}^{\text{calc}}\right] + n\lambda \int_{\tau_{\min}}^{\tau_{\max}} \left[\frac{\mathrm{d}^2 P(\tau)}{\mathrm{d}\tau^2}\right]^2 \mathrm{d}\tau \tag{17}$$

The calculated values $\mathbf{Y}^{\text{calc}}$ are given by the evaluation of the integral in Eq. (13) using an estimate of the distribution function, $P(\tau)$. The weighting matrix $\mathbf{W}$ is chosen on the basis of maximum-likelihood principles;[12] in our work, we assume that the errors have mean zero and are identically distributed, so that $\mathbf{W}$ is the identity.

The first term in Eq. (17) represents the precision of the match of the calculated values to the measured data. The second term is the regularization term, which is used to stabilize the solution. While a number of different functional forms may be used, in the present case the regularization term takes the form of the second derivative operator, which acts to penalize a lack of smoothness and sharp changes in the estimated distribution function. This form of regularization is consistent with the representation of the unknown distribution as being relatively smooth. The regularization term is weighted relative to the first, data-fitting, term by a scalar, λ, the regularization parameter. Since the determined estimate of the relaxation distribution and subsequent value of the intrinsic magnetization depend upon the specification of this parameter, a good estimate for each voxel is essential.

The calculated values of the observed data are written in terms of the B-spline coefficients, $\mathbf{c}$:

$$\mathbf{Y}^{\text{calc}} = \mathbf{A}\mathbf{c} \tag{18}$$

where the components of $\mathbf{A}$ are given by

$$a_{i,j} = \int_{\tau_{\min}}^{\tau_{\max}} B_i^m(\tau, \mathbf{y}) K(t_j, \tau) \mathrm{d}\tau \tag{19}$$

The process of estimating the distribution corresponds to determining the coefficients that minimize the performance index:

$$\min_{\mathbf{c}} J = \| \mathbf{Y} - \mathbf{Y}^{\text{calc}} \|_W^2 + n\lambda \int_{\tau_{\min}}^{\tau_{\max}} \left[\frac{\mathrm{d}^2 P(\tau)}{\mathrm{d}\tau^2}\right]^2 \mathrm{d}\tau \tag{20}$$

$$= \| \mathbf{Y} - \mathbf{A}\mathbf{c} \|_W^2 + n\lambda \| \mathbf{M}\mathbf{c} \|^2 \tag{21}$$

The matrix $\mathbf{M}$ is determined by integrals of the products of the second derivatives of the B-spline basis functions used in the representation of the unknown distribution. This is a quadratic least-squares minimization problem.

Linear equality and inequality constraints

$$\Gamma \mathbf{c} \geq 0 \tag{22}$$

$$\mathcal{G}\mathbf{c} = 0 \tag{23}$$

are included to further stabilize the solution. Inequality constraints ensure that the estimated distribution is non-negative, while equality constraints are used to enforce the desired derivatives of the determined distribution $P(\tau)$ at the boundaries. For a specified value of the regularization parameter, there is a unique and global solution that minimizes Eq. (21) while satisfying Eqs (22) and (23). This solution is determined efficiently using a numerical least-squares solver capable of incorporating the equality and inequality constraints.[13,14]

In general, a regularization parameter should be chosen for each voxel. Since there may be thousands of voxels, the use of graphical or other methods requiring intervention is prohibitive. In the present work, an automatic, data-driven method is utilized to obtain a reliable estimate of the regularization parameter for each voxel. It is based on nonparametric statistical theory, which can incorporate a number of performance criteria, including unbiased prediction risk (UBPR),[9] cross-validation (CV),[15] and generalized cross-validation (GCV).[16]

Our analysis[17] indicates that the criteria often choose similar regularization parameters and the magnetization values calculated with the estimated relaxation distributions precisely match the observed magnetization data. In situations where different parameters are selected, the CV criterion consistently chooses the smallest parameter, which results in a high level of variability in the determined distribution. The UBPR criterion often chooses the highest regularization parameter, resulting in the smoothest relaxation distribution. Since each of the resulting relaxation distributions precisely fits the observed magnetization data, the UBPR criterion was chosen to be the most appropriate criterion for quantitative analysis of magnetic resonance images.

2.3. Determination of the porosity from the intrinsic magnetization

The amount of fluid corresponding to each imaged voxel is proportional to the intrinsic magnetization intensity determined for that voxel. The relationship between the mass of fluid, $\mathcal{M}$, and the magnitude of the intrinsic magnetization, M_0, is given as

$$M_0 = \xi \mathcal{M} \tag{24}$$

Here, the proportionality factor ξ is known as the specific magnetization intensity and depends on several experimental quantities such as the receiver gain, the

static magnetic field and, most importantly, the quality factor, Q, of the receiving coil.[18] This quality factor is a measure of the signal sensitivity in the receiving coil and is affected by changes of fluid states, particularly when aqueous ionic solutions, such as brine, are used. As a result, the Q value may change considerably during a flow experiment.[19]

The specific magnetization intensity, ξ, is determined by including a reference containing a known quantity of fluid in the receiver coil together with the sample to be studied.[20] During the imaging experiment, both the sample and reference experience the same receiver gain and quality factor Q, so that the value of ξ for both is the same throughout the experiment. The signals of the reference and the sample are separated on the basis of spatial location. Because the bulk fluid in the reference sample relaxes more slowly than the fluid contained within the porous media, it is necessary to first determine the intrinsic magnetization and then compare the intensities of the reference and sample to calculate ξ.

A second method for determining the specific magnetization intensity involves gravimetrically measuring the total mass of the fluid within the porous media sample and relating this to the NMR signal integrated over the entire sample using Eq. (24). To distinguish this approach from the previous one, we add subscripts 'r' and 's' to ξ, according to the manner in which the specific magnetization intensity is calculated: ξ_r for an independent reference sample, and ξ_s for self-reference.

Once the specific magnetization intensity is determined, Eq. (24) is used to relate the intrinsic magnetization to the mass of fluid within the porous media sample. Since we assume that the sample is fully saturated, this quantity is considered to be the pore space within the sample and is used in Eq. (3) to determine the porosity, ϕ_j, corresponding to voxel j:

$$\phi_j = \frac{M_{0j}}{\xi_{r/s}\, \rho_l\, V_j} \tag{25}$$

where ρ_l is the proton density of the observed fluid and V_j is voxel volume.

2.4. Results and discussion

The presented methodology is now demonstrated on a few different porous media samples. Each sample is laterally sealed using epoxy (Stycast 2651) and then mounted in a plexiglass core holder. The epoxy has very small T_2 values and does not contribute to the observed signal intensity. For each experiment, the samples are placed into a birdcage RF coil and then inserted into a GE 2-T CSI-II imager/spectrometer with a 31-cm magnet bore. The gradient coils used are self-shielded with a 15-cm bore and are capable of delivering a maximum of $\pm 20\,\mathrm{G\,cm^{-1}}$ in three perpendicular directions. A CPMG imaging pulse sequence is used to acquire a total of 54 images with an echo spacing of 3 ms. The image files are then processed to obtain relaxation data for each voxel within the image.

The quantitative method in Section 2.2 is used to determine the intrinsic magnetization intensity for each voxel. Cubic B-spline basis functions with a partition of 60 interior knots logarithmically spaced between 1×10^{-5} and 10 s are used to represent the relaxation distribution within each voxel. The optimal regularization parameter, λ, of each voxel is found within the range between 1×10^{-5} and 5×10^{-18} s by using the UBPR[9] criterion.

2.4.1. Determination of one-dimensional porosity distributions

Two different sandstone samples are used to demonstrate the methodology developed in Sections 2.1–2.3 in one spatial dimension. The first sample is a Bentheimer sandstone sample we have labeled KBE, which is saturated with oil. The second sample is a Brown sandstone sample, labeled MCD, that is saturated with water.

The Bentheimer sample is prepared to be parallelepiped with dimensions of 6.15 cm × 2.60 cm × 0.58 cm. When saturated under vacuum, 1.644 g of oil (Soltrol 130, Phillips Petroleum Co.) is absorbed, and a bulk porosity of 0.236 is determined gravimetrically. A reference sample containing 0.043 g of oil is placed with the sample when imaged. The field of view, which indicates the dimension of the observed image, is 10.00 cm in length. This length is divided into 128 voxels, which results in a voxel size of 0.078 cm × 2.60 cm × 0.58 cm.

Figure 2 shows a limited number of one-dimensional CPMG image profiles observed at selected echo times during the experiment. As the experiment

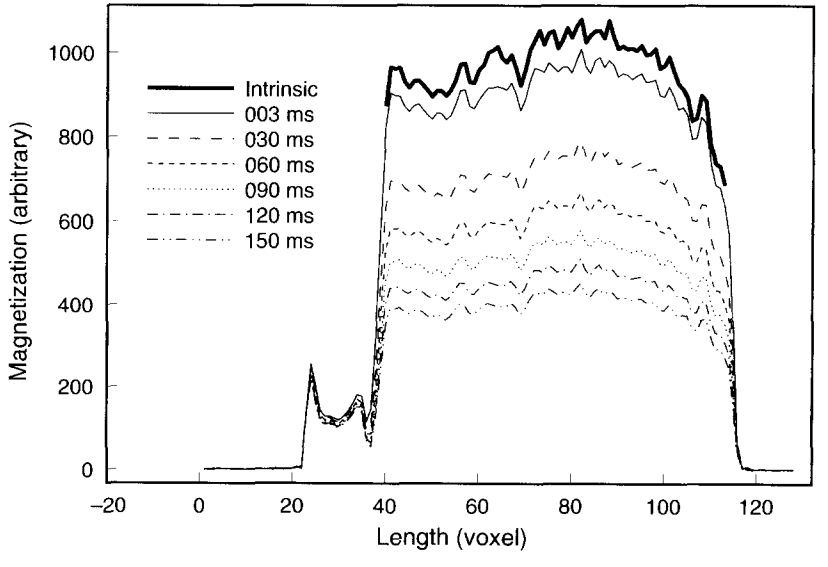

Fig. 2. One-dimensional CPMG images and the intrinsic magnetization for a Bentheimer sandstone sample (KBE).

proceeds, the profile images become attenuated, due to relaxation effects. The determined intrinsic magnetization is shown with a darkened line at the top of the plot. The peaks at the left edge of the sample come from the reference sample. The Bentheimer sample lies between voxel 40 and voxel 113, while the reference lies between voxel 24 and voxel 36. The relaxation data $\mathbf{Y}$ required in Eq. (21) are extracted from these successive images for each voxel.

It is helpful to investigate the relaxation behavior of one voxel to understand the relationship between the experimental signals and the estimated relaxation distribution. Figure 3 shows the relaxation behavior for voxel number 80. The data points in Fig. 3 indicate the experimental magnitude of magnetization of the fluid in the voxel with respect to the discrete echo times when the signal is detected from the imager. The predicted relaxation curve (solid line), calculated using Eq. (11), shows that the estimated relaxation distribution is consistent with the experimental data. Since the time axis is expressed in a log scale in Fig. 3, the intrinsic magnetization, where time is equal to 0, is represented by the negative asymptotic value of the solid line. The shape of the intrinsic magnetization image in Fig. 2 looks similar to the other images from relaxed echoes, but not exactly the same. This implies that the relaxation rates at each position can be different. The relaxation time, distribution of Eq. (15), for the 80th voxel, is plotted in Fig. 4 as $\tau N(\tau)$. This is done so that the area under any region of this semi-log

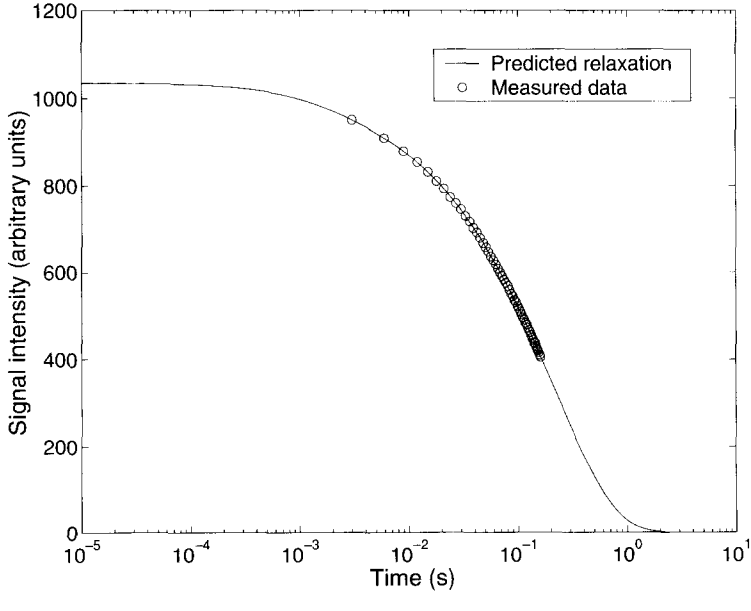

Fig. 3. Predicted and observed magnetization of the Bentheimer sandstone sample (voxel 80).

plot is proportional to the relative amount of fluid having the specified relaxation times. Figure 4 indicates that 64% of the nuclei relax with T_2 between 0.105 s and 0.520 s.

Figure 5 shows the determined one-dimensional porosity distribution for the sample using ξ_r. The porosity is plotted as a function of sample length. The

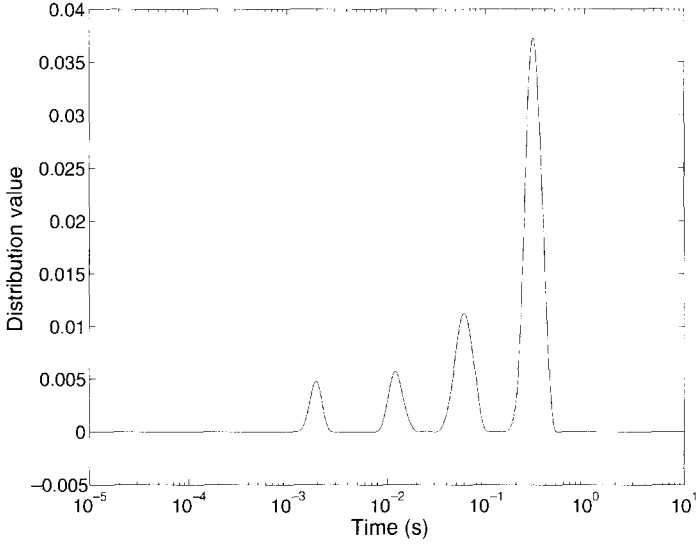

Fig. 4. Determined $N(\tau)$ distribution of the Bentheimer sandstone sample (voxel 80).

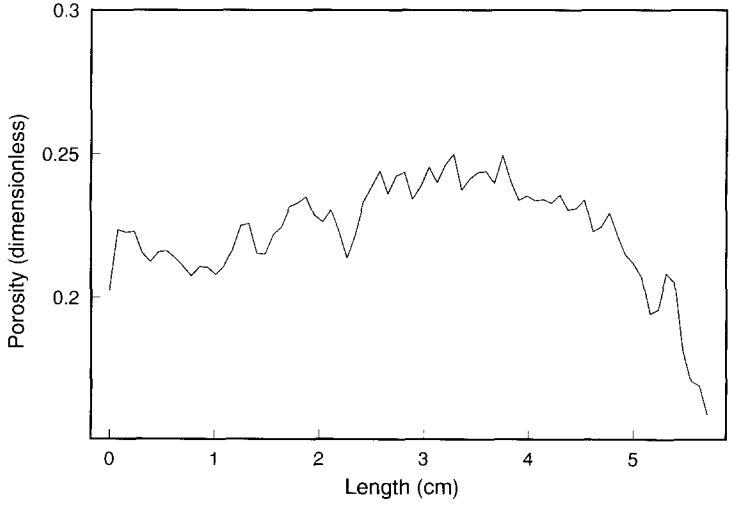

Fig. 5. One-dimensional porosity distribution for the Bentheimer sandstone sample (KBE), using ξ_r.

average of the one-dimensional porosities is 0.233, which is within 1.3% of the gravimetrically determined value 0.236.

The Brown sandstone sample has dimensions of 4.65 cm×2.40 cm×0.85 cm. The sample is saturated with a brine solution (3% NaCl and 0.03% NaN_3 by weight in distilled water) under vacuum. A bulk porosity of 0.219 is determined from the 2.08 g of brine solution absorbed, and 0.04 g of the fluid is included in the reference sample. A field of view of 10.00 cm is used again, which results in the same voxel sizes as that of KBE. The intrinsic magnetization determined in the MCD sample is shown in Fig. 6. The peak at the left edge indicates signal from the reference sample. The shape of the intrinsic magnetization is consistent with the images from attenuated magnetization.

The determined porosity of MCD sample using ξ_r is given in Fig. 7. The average value of one-dimensional porosities is 0.192, which is within 12.4% of the bulk value of 0.219.

2.4.2. Determination of two-dimensional porosity distributions

The developed methodology is now used to determine a two-dimensional porosity distribution on a Bentheimer sandstone sample (KBE) saturated with oil. The sample and reference used are the same as those for one-dimensional imaging in Section 2.4.1. A two-dimensional CPMG imaging sequence is applied with field of view of 10.00 cm×3.50 cm, which gives a voxel size of 0.078 cm×0.11 cm×0.58 cm. The porosity distribution of the two-dimensional

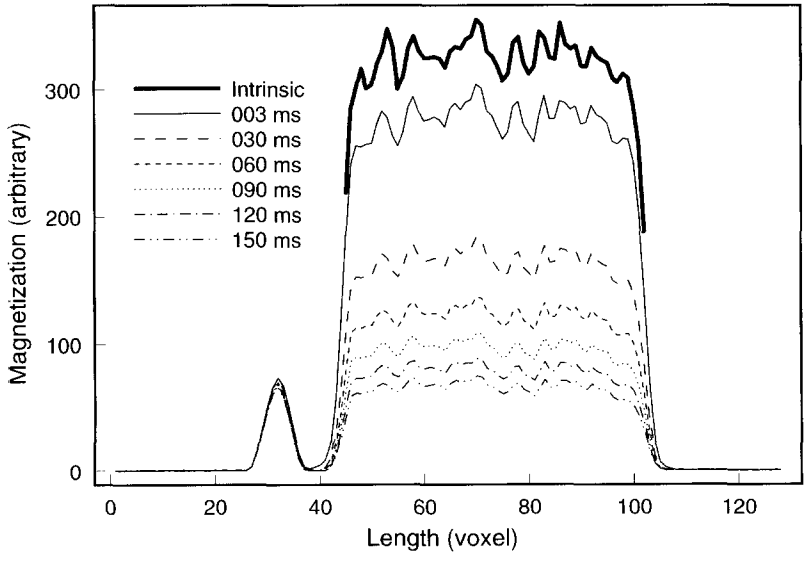

Fig. 6. One-dimensional CPMG images and the intrinsic magnetization for the Brown sandstone sample (MCD).

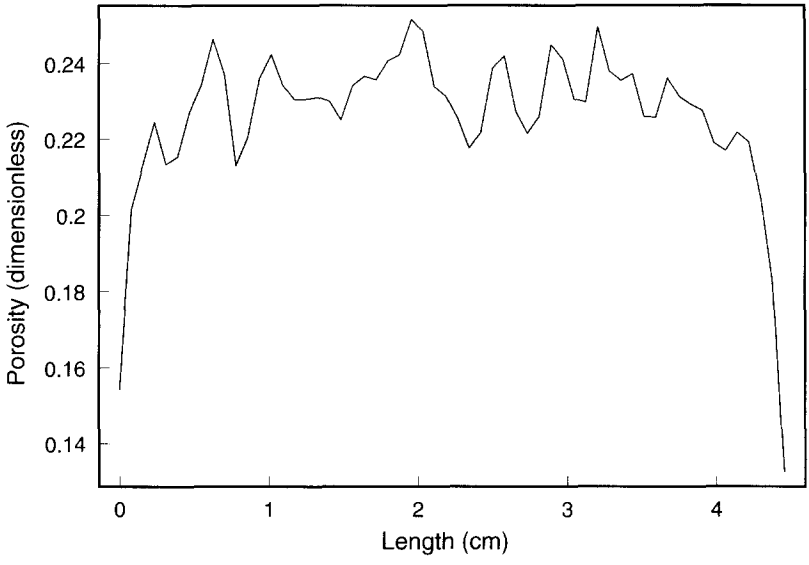

Fig. 7. One-dimensional porosity distribution for the Brown sandstone sample (MCD), using ξ_r.

experiment using ξ_r is represented on a gray scale in Fig. 8. The brighter areas indicate larger porosity. The large dark spot that appears near the right-hand side corner in Fig. 8 is consistent with the lower porosity corresponding to the right-hand side of the one-dimensional porosity graph (Fig. 5).

2.4.3. Determination of three-dimensional porosity distributions

The final demonstration of the developed methodology is to determine the three-dimensional porosity distribution of a porous media sample obtained from the subsurface. A cylindrically shaped rock sample was prepared, and is labeled MAG. The sample has a 2.54-cm diameter and is 3.90 cm in length. A bulk porosity of 0.284 was determined gravimetrically, with 5.61 g of brine solution being imbibed. The reference sample contained 0.217 g of water. The field of view was $10.0\,\text{cm} \times 3.0\,\text{cm} \times 3.0\,\text{cm}$, of which lengths are divided into $128 \times 8 \times 8$. This yields voxel sizes of $0.078\,\text{cm} \times 0.375\,\text{cm} \times 0.375\,\text{cm}$.

The three-dimensional porosity image of MAG sample is shown in Fig. 9. The porosity image is displayed as a series of two-dimensional images, each of which represents a plane of voxels sliced perpendicularly to the other direction. In Fig. 9, axial limits of the sample are apparent. The middle slices have more columns of voxels which are inside the sample than the others, due to the cylindrical shape of the sample. The white spots above the sample are attributed to the signal corresponding to the fluid in the reference. The resolution is poor because the voxel

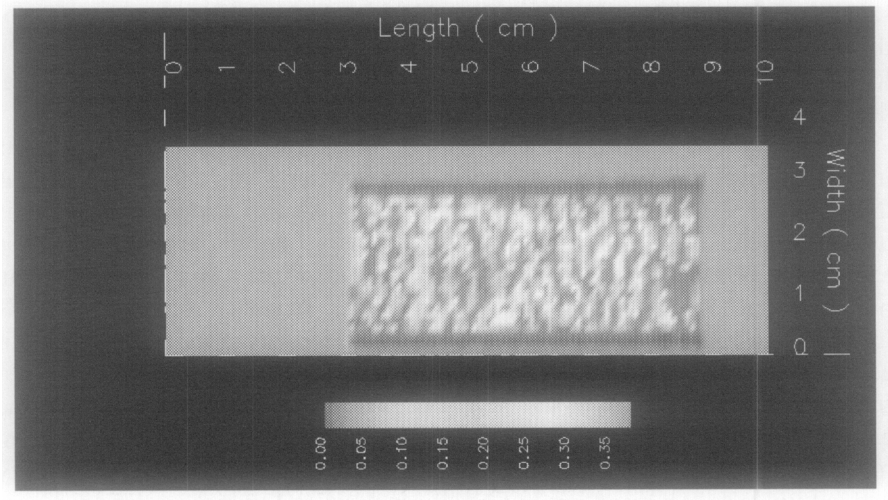

Fig. 8. Two-dimensional porosity distribution for the Bentheimer sample (KBE).

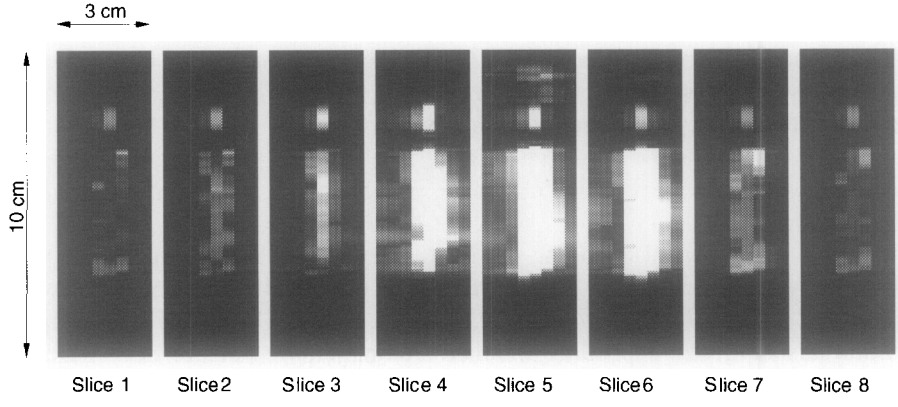

Fig. 9. Three-dimensional porosity image of a cylindrically shaped sample (MAG).

size is relatively large and the voxels at the edges of the sample include space outside the sample. In order to obtain higher resolution, it is necessary to increase the number of voxels.

The total scan time for the imaging experiment is given by the the product of one scan time, which includes pre-delay and CPMG echo trains, total number of phase encodings, and the number of acquisitions for signal averaging. In our work, the time required for one scan is about 5.2 s, with 5 s of delay time. Then the acquisition time, including repetitive scans of eight phase encoding gradients in the two transverse directions, is about 333 s. Assuming eight acquisitions for signal averaging, the total time required is up to 45 min. If we wish to have the

same resolution for the three-dimensional image of MAG (Fig. 9) as that of two-dimensional image of KBE (Fig. 8), then the imaging time would become much longer. However, this time may be sufficiently shortened by reducing the total delay time by adding spoiler gradients to the pulse sequence.

As the number of voxels in a sample is increased, the spatial resolution is increased, but the amount of signal corresponding to a single voxel is diminished.[21,22] Considering that the typical porosity of a porous medium is usually less than 30%, the magnitude of the signal from fluid in porous media is expected to be much smaller than that of bulk fluid. Thus, it is not easy to obtain higher signal-to-noise ratio (SNR) with higher spatial resolution in NMR imaging, because considerable time is required for increasing the number of acquisitions in order to get a desirable magnitude of signal. SNR may be increased by increasing the strength of the static magnetic field, $\mathbf{B}_0$, but this also has the effect of increasing the internal gradients within the sample (which arise from magnetic susceptibility variations[23]), which degrades the magnetic homogeneity and in turn leads to a broadening of NMR spectrum and spatial resolution.

For a sample with sufficiently narrow linewidth and strong magnetic field gradient, the image resolution Δr is determined by the voxel size, Δr_{voxel}

$$\Delta r = \Delta r_{\text{voxel}} \tag{26}$$

When imaging porous materials, the NMR linewidth tends to be broad and the image resolution is limited. If the linewidth of the sample within a voxel, Δf, is greater than $\gamma G \Delta r_{\text{voxel}}/2\pi$, the resolution is given by[5]:

$$\Delta r = \frac{2\pi \Delta f}{\gamma G} \tag{27}$$

where G is the spatial encoding gradient. Then the actual resolution becomes bigger than the voxel size, which results in overlapping of signals between adjacent voxels. The linewidths, Δf, of rock samples typically range up to thousands of hertz, depending on their components, structure and magnetic susceptibility. Equation 27 provides the limitation of imaging resolution attributed to the gradient strength and the linewidth of the sample. For an imaging of hydrogen nuclei ($\gamma = 2.675 \times 10^8\ \text{s}^{-1}\ \text{T}^{-1}$) using a maximum pulse gradient field of 20 G cm^{-1}, the resolution is limited to 1 mm if Δf of the sample is greater than 8500 Hz. With stronger gradients, better resolution can be achieved.

3. PERMEABILITY DISTRIBUTIONS

As discussed in Section 1, the absolute permeability is a constitutive macroscopic property which arises in the local volume-averaged momentum balance, which is Darcy's law (Eq. (2)). It is interesting that, while the porosity can be defined independently of the equation of continuity, the permeability is

essentially defined by Eq. (2)—that is, it represents the proportionality between the local volume-averaged velocity and gradient of the volume-averaged pressure. This means that the actual determination of permeability must be accomplished using that equation. This can be done by solving an inverse problem with an associated flowing experiment.

Our goal is to determine the permeability with millimeter resolution, approaching an intrinsic scale that corresponds to the minimum representative volume element. To do so, we first use NMR velocity-imaging experiments to determine the velocity distributions within a saturated porous medium undergoing a constant injection of water. Then, we solve an associated inverse problem to determine the permeability distribution.

The method to determine fluid velocities is described in Section 3.1. The inverse problem is described in Section 3.2, and demonstrated on data from a Bentheimer sandstone sample in Section 3.3.

3.1. Velocity imaging using NMR

The key challenge for the successful use of NMR velocity-imaging techniques to characterize fluid flow properties is the interpretation of the measured parameters. Different experimental strategies provide information about flow processes at different spatial and dynamic scales in porous media. In principle, the flow velocity can be probed either as a local quantity with an image resolution below the pore level,[24,25] or as a macroscopic flow property corresponding to local volume and temporal averages of fluid molecular displacements.[26] One must develop a suitable methodology to correctly determine the parameters that best describe the properties of interest.

There are two broad classes of imaging techniques useful for observing molecular translational motion using NMR: time-of-flight methods and phase-encoding methods.[6] In the time-of-flight methods, spatially selective excitation is used to tag spins with the result that the pixel brightness in an image is related to the velocity of the flowing spins passing through the selected slice. Here, a calibration step and *a priori* information about the flow field are required, since the image intensity is used to determine the velocity.[8] The second, phase-encoding approach, uses the magnetic gradient field to implement a phase shift on the nuclear spin while the fluid molecules are in motion. Although this method requires a longer imaging time, since both displacement encoding and spatial encoding are required, it has been considered a more reliable approach for precise quantification.[25]

3.1.1. Determination of molecular motion using phase shift

The use of phase shifts of nuclear magnetization to measure molecular motion has been investigated for decades,[27] and its application to the spatially resolved

measurement of flow velocity was first suggested by Moran.[28] However, its use in imaging velocities within porous materials has been limited to a few experimental studies which relied on models of porous media containing large pores[24,29,30] or to studies that reported a probability distribution of fluid velocities without spatial resolution.[31–33]

The phase shift method is based on the observation that nuclear spins moving in the presence of a magnetic field gradient exhibit a phase shift in the transverse magnetization. This phase shift can be associated with a displacement of fluid molecules in the direction of the pulsed-field gradient. Mathematically, if the nuclear spins have translational motion, the space vector $\mathbf{r}$ in Eq. (6) becomes dependent on time and can be expanded in terms of its initial state $\mathbf{r}(0)$ and time derivatives:[34]

$$\varphi(t) = \gamma \int_0^t \mathbf{G}(t') \cdot \mathbf{r}(t')\mathrm{d}t'$$

$$= \gamma \left[\mathbf{r}(0) \cdot \int_0^t \mathbf{G}(t')\mathrm{d}t' + \dot{\mathbf{r}}(0) \cdot \int_0^t \mathbf{G}(t')t'\mathrm{d}t' + \frac{1}{2}\, \ddot{\mathbf{r}}(0) \cdot \int_0^t \mathbf{G}(t')t'^2\, \mathrm{d}t' \ldots \right] \quad (28)$$

Here, the phase shift involves initial position $\mathbf{r}(0)$, velocity $\dot{\mathbf{r}}(0)$, and acceleration $\ddot{\mathbf{r}}(0)$ of the spin. Depending on the choice of the pulsed-field gradient $\mathbf{G}(t')$, the phase shift can be made sensitive to initial velocity or the acceleration.

An example of a velocity-encoding method is the bipolar-gradient method.[35] Here, two identical pulses are applied during the dephasing and rephasing periods of a spin-echo sequence. Since the two pulses are in opposite polarity with respect to the time domain, the phase shift $\varphi(t)$ in Eq. (28) is dominated by the velocity term, i.e. the first-order term of t' in the expansion.

The movement of the fluid within the porous media is irregular in time and space, as it is dispersed by the walls and throats of the structure. In order to obtain a well-defined molecular displacement, it is advantageous to use intense gradient pulses whose pulse widths are much shorter than the time interval between them.[26] If the pulse widths δ are short enough to assume that molecular displacement is negligible, Eq. (28) simplifies to

$$\varphi = \mathbf{q} \cdot \mathbf{r} \quad (29)$$

Here, $\mathbf{q}$ is defined as

$$\mathbf{q} = \gamma \int_{\text{pulse}} \mathbf{G}(t')\mathrm{d}t' \quad (30)$$

so that the exact value depends on the shape of the pulse profile used in the experiment; that is, for a rectangular pulse, q is $\gamma\delta G$, for a half-sine pulse, q is $2\gamma\delta G/\pi$, and for a rectangular pulse with finite ramp-up and ramp-down time, q is $\gamma(\delta + t_{\text{ramp}})G$.

Figure 10 shows the incorporation of the velocity-encoding field gradient pulses in a stimulated-echo imaging pulse sequence which was used in this work. A remarkable advantage of using the stimulated echo is that the relaxation

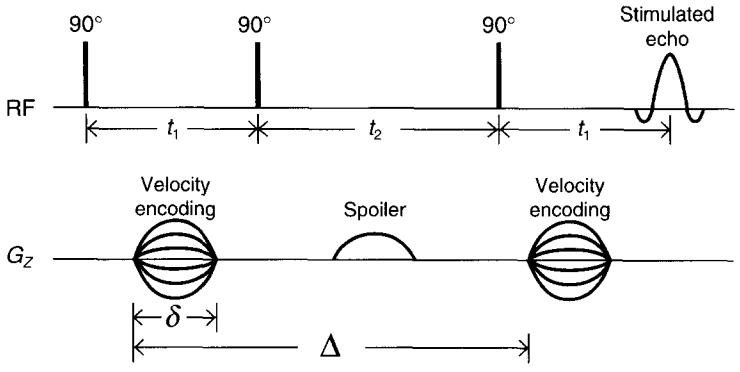

Fig. 10. The stimulated-echo pulse sequence used in this work for projection imaging of the z component of the velocity over the whole sample.

displays a T_1-like decay dependence instead of T_2 dependence during the interval between the last two 90° RF pulses. Since T_1 is usually much longer than T_2 for fluids in porous media, use of the stimulated-echo pulse sequence enables the measurement of longer displacements. The first 90° pulse imparts a phase shift $\mathbf{q} \cdot \mathbf{r}_0$ to a spin located at $\mathbf{r}_0$. This phase shift is inverted by the last two 90° pulses in the sequence, so that if a spin has moved to position $\mathbf{r}_0 + \mathbf{R}$ at the time of the second gradient pulse, the net phase shift for that particular spin is $\mathbf{q} \cdot \mathbf{R}$. In addition, spoiler gradient pulses are inserted to reduce the undesired signal in the transverse evolution periods. Fluid molecules are tracked during the time, Δ, between the velocity-encoding gradient pulses. The sequence is repeated using regularly spaced increments in the pulsed-gradient field to completely observe the sample in $\mathbf{q}$-space.

The total number of spins with displacement $\mathbf{R}$ during time Δ is mathematically described using a normalized distribution function $P'_\Delta(\mathbf{R})$ which satisfies

$$\int P'_\Delta(\mathbf{R})\, d\mathbf{R} = 1 \tag{31}$$

The observed signal $S(\mathbf{q})$ may then be written in terms of $P'_\Delta(\mathbf{R})$:

$$S(\mathbf{q}) = \int \rho P'_\Delta(\mathbf{R}) \exp(i\mathbf{q} \cdot \mathbf{R}) d\mathbf{R} \tag{32}$$

where ρ is spin density. By taking the inverse Fourier transform of the signal with respect to $\mathbf{q}$, the spin displacement distribution function is recovered:

$$P'_\Delta(\mathbf{R}) = \frac{1}{\rho} \int S(\mathbf{q}) \exp(-i\mathbf{q} \cdot \mathbf{R}) d\mathbf{q} \tag{33}$$

where $P'_\Delta(\mathbf{R})$ would represent the spin displacement distribution averaged over the total volume of the sample. Notice that Eq. (30) and Eq. (33) have analogies

with Eq. (8) and Eq. (9). In other words, signal S is mapped out in **q**-space for displacement distribution, whereas it is described in **k**-space for spin density distribution.

3.1.2. Extension of the phase shift method to provide spatial resolution

In order to obtain spatial resolution of the molecular translations within each voxel, it is necessary to combine the velocity-encoding gradient sequence shown in Section 3.1.1 with a standard imaging sequence such as frequency or phase encoding. The displacement distribution function, $P'_\Delta(\mathbf{R})$, must now be generalized to a spatial-displacement joint density function ς_Δ so that it describes the total number of spins located at **r** with displacement **R** during time Δ:[28]

$$\varsigma_\Delta(\mathbf{r}, \mathbf{R}) = \rho(\mathbf{r}) P'_\Delta(\mathbf{R}, \mathbf{r}) \tag{34}$$

where $P'_\Delta(\mathbf{R}, \mathbf{r})$ now depends on **r**.

The two-dimensional imaging pulse sequence used in this work is shown in Fig. 11. Here, the spatial information is phase-encoded in the x-direction and frequency-encoded in the z-direction.

The observed NMR signal is modulated by the two wave vectors: the first, **k**, is related to the spatial density of the spins, and the second, **q**, is related to a spatial displacement of spins:

$$S(\mathbf{k}, \mathbf{q}) = \iint \varsigma_\Delta(\mathbf{r}, \mathbf{R}) \exp(i\mathbf{k} \cdot \mathbf{r}) \exp(i\mathbf{q} \cdot \mathbf{R}) d\mathbf{r}\, d\mathbf{R} \tag{35}$$

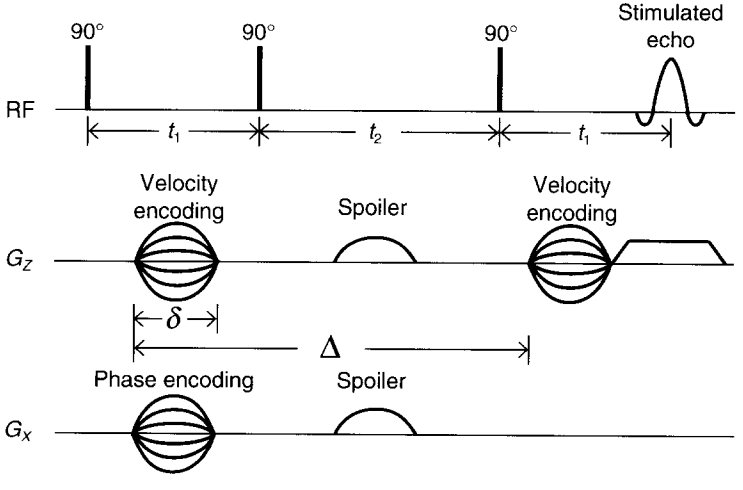

Fig. 11. The stimulated-echo pulse sequence used in this work for projection imaging in the x–z plane of the z-component of the velocity.

The joint density function for each voxel can be reconstructed by taking inverse Fourier transforms with respect to each of the wave vectors:

$$\varsigma_{\Delta}(\mathbf{r}, \mathbf{R}) = \iint S(\mathbf{k}, \mathbf{q}) \exp(-i\mathbf{k} \cdot \mathbf{r}) \exp(-i\mathbf{q} \cdot \mathbf{R}) d\mathbf{k}\, d\mathbf{q} \tag{36}$$

An example of a joint density function $\varsigma_{\Delta}(\mathbf{r}, \mathbf{R})$ is shown in Fig. 12. The sample is a Bentheimer sandstone in a rectangular parallelepiped shape 50 mm long extending in the z-direction, 25 mm wide along the x-direction, and 5 mm thick in the y-direction. The average volumetric flow rate of the water was 1.5 ml min^{-1} along the z-direction. The sample is located between the two spikes resulting from free water present in the end caps of the core holder.

The local mean velocity may be determined in terms of the phase shift by considering a voxel located at $\mathbf{r}$ position. By combining Eq. (34) with Eq. (35), the resulting expression for the signal is an obvious extension to the case found in Eq. (32), which is averaged over the given voxel:

$$S'(\mathbf{r}, q) = \rho(\mathbf{r}) \int_{-\infty}^{\infty} P'_{\Delta}(\mathbf{R}, \mathbf{r}) \exp(i\mathbf{q} \cdot \mathbf{R})\, d\mathbf{R} \tag{37}$$

If, for a particular direction (say the z-direction), the time average velocity of each spin in the direction of the gradient is defined as

$$\bar{v}_z = \frac{|\mathbf{R}|_z}{\Delta} = \frac{Z}{\Delta} \tag{38}$$

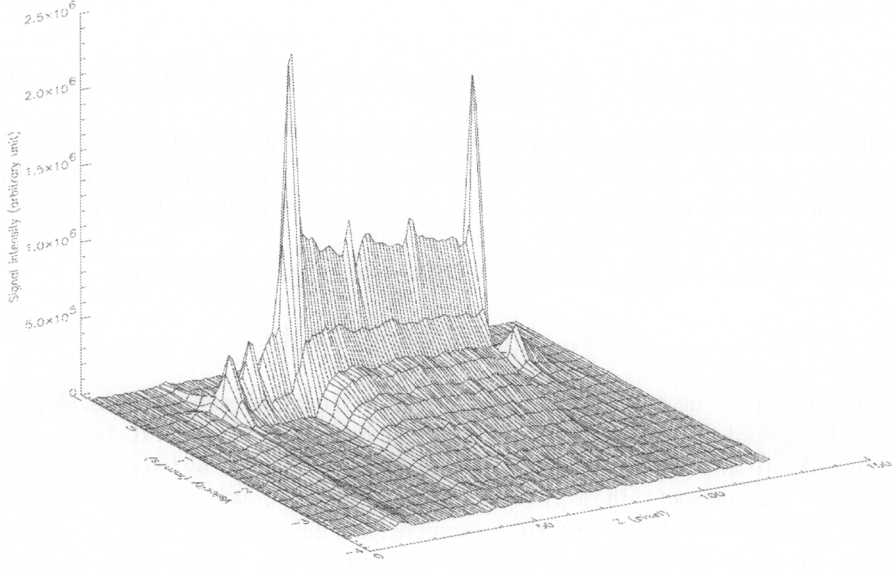

Fig. 12. The joint spin–velocity density function, $\rho(z)P_{\Delta}(\bar{v}_z, z)$, as a function of position z for water flow in the rectangular Bentheimer sandstone sample (voxel size is 0.94 mm).

where $Z = z(\Delta) - z(0)$ is the displacement in the z-direction, Eq. (37) may be expressed as

$$S'(\mathbf{r}, q) = \rho(\mathbf{r}) \int_{-\infty}^{\infty} P_{\Delta}(\bar{v}_z, \mathbf{r}) \exp(iq\bar{v}_z\Delta)\, \mathrm{d}\bar{v}_z \tag{39}$$

where $P_{\Delta}(\bar{v}_z, \mathbf{r})$ is the probability density of spins that are moving within the velocity range $\bar{v}_z$ and $\bar{v}_z + \mathrm{d}\bar{v}_z$. For an ensemble of molecules moving with a uniform velocity, the phase of $S'(\mathbf{r}, q)$ in Eq. (39) is expected to be proportional to $q\Delta$, which is equivalent to the first moment of the gradient, $\int t'G(t')\mathrm{d}t'$, provided that $\delta << \Delta$. In traditional velocity imaging approaches,[36] this proportionality is used to estimate the mean velocity. However, the linearity between phase shift and the average velocity is not satisfied unless the velocity field has a narrow distribution.[37] Thus, this method is not adequate for estimating the flow velocity field in porous media where a broad range of velocities may exist, since voxel sizes are typically much larger than the mean pore size.

In our work, the velocity distribution method is used, where the velocity distribution function $P_{\Delta}(\bar{v}, \mathbf{r})$ is estimated from the velocity imaging, and the average velocity at a voxel located at $\mathbf{r}$, $<\bar{v}>_{\mathbf{r}}$, is calculated. Consider the one-component (z-direction) velocity imaging in two-dimensional (z- and x-direction) space illustrated in Fig. 11. In this case, the velocity encoding is parallel to the frequency encoding. The signal intensity from the stimulated echo $S(k_z, k_x, q)$ is converted to the velocity distribution function $P_{\Delta}(\bar{v}_z, z, x)$ by combining Eq. (34) and Eq. (36):

$$P_{\Delta}(\bar{v}_z, z, x) = P'_{\Delta}(Z, z, x)$$

$$= \frac{1}{\rho(z, x)} \iiint S(k_z, k_x, q) \exp(-ik_z z) \exp(-ik_x x) \exp(-iqZ)\, \mathrm{d}k_z\, \mathrm{d}k_x\, \mathrm{d}q \tag{40}$$

If the porous medium is sufficiently homogeneous, the spin density $\rho(z, x)$ could be approximated as constant, but, for more precise measurement, $\rho(z, x)$ needs to be obtained from an independent spatial imaging experiment (as is described in Section 2) with the same sample.

The ensemble averaged velocity for each voxel is then evaluated by

$$<\bar{v}_z>_{(z,x)} = \int_{-\infty}^{\infty} \bar{v}_z\, P_{\Delta}(\bar{v}_z, z, x)\, \mathrm{d}\bar{v}_z \tag{41}$$

Figure 13 shows an example of $<\bar{v}_z>_{(z,x)}$ with respect to each voxel located at (z, x) for a fluid flowing through a Bentheimer sandstone sample, Fig 14.

In order to expand the velocity-encoding pulse sequence to two-component velocity measurement in a two-dimensional domain, we can superimpose another series of velocity-encoding gradients on the x-axis in Fig. 11, where phase-encoding is applied for spatial resolution. For steady-state flowing conditions, however, it may be faster and more convenient to use two different pulse sequences independently. After the data for the z-component velocity field

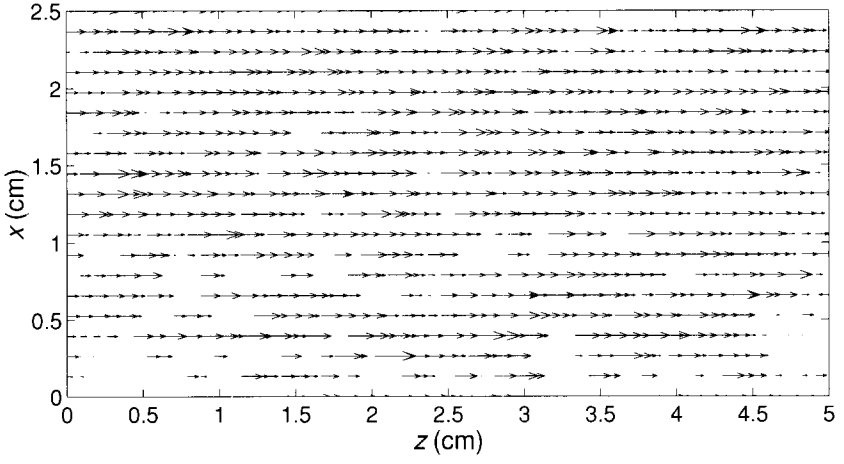

Fig. 13. One-component velocity distribution with the Bentheimer sandstone sample.

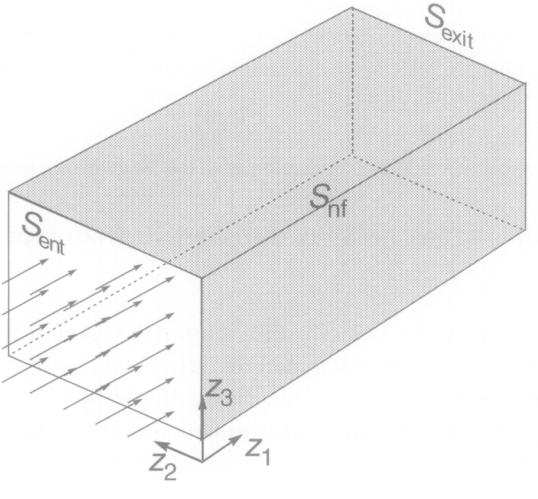

Fig. 14. Experimental flow domain for permeability estimation.

are obtained as described so far, another velocity-encoding pulse sequence which acquires only x-component velocity field data is applied. In this pulse sequence, the velocity-encoding gradient is supposed to be applied only along the x-axis, while the z-axis has only frequency encoding. Thus the velocity-encoding gradient is parallel to the spatial phase encoding in this case. The

procedure for evaluating the x-component velocity field is analogous to Eq. (40) and Eq. (41), and the ensemble averaged x-component velocity is given by

$$<\bar{v}_x>_{(z,x)} = \int_{-\infty}^{\infty} \bar{v}_x P_\Delta(\bar{v}_x, z, x)\, d\bar{v}_x \tag{42}$$

Equation (41) and Eq. (42) provide the two components of the velocity field respectively with respect to the voxel position (z, x). An example of the two-component velocity field is shown in Fig. 15.

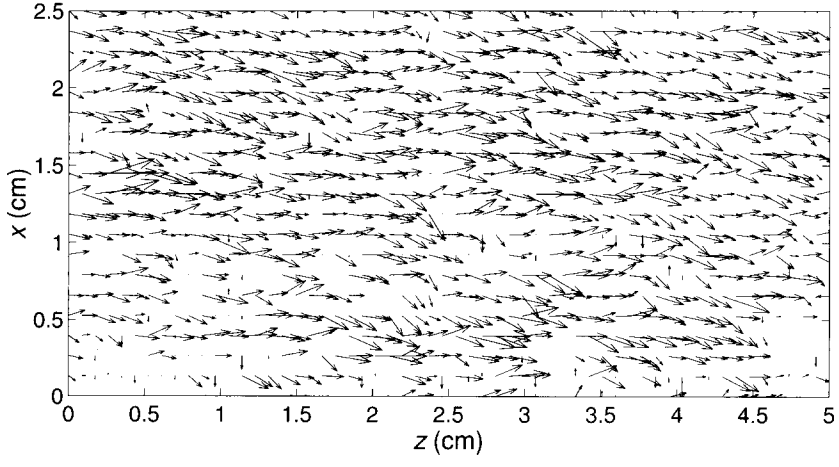

Fig. 15. Two-component velocity distribution with the Bentheimer sandstone sample.

3.2. Determination of permeability distributions from experimental velocities

Note that even though the velocity distribution is known, the corresponding permeability values cannot be computed directly from Darcy's law (Eq. 2), since the pressure gradient at locations within the medium is not known. Nevertheless, the permeability distribution can be determined as that function for which calculated velocity values corresponding to the mathematical model of the experiment most closely match those values actually obtained. In this section, we describe this inverse problem.

The experimental flow system is taken to be a rectangular parallelepiped of dimensions z_{1o}, z_{2o}, and z_{3o}, with a known porosity ϕ, which may vary with position. Figure 14 shows the key elements of the experimental domain. A fluid is introduced at the injection or entrance face S_{ent}, located at $z_1^* = 0$, at a constant flow rate that is assumed to be known. The fluid, on average, flows through the medium in the positive z_1 direction, although local heterogeneities in the sample will cause the velocity field to vary in both the z_2 and z_3 directions. No fluid is allowed to enter or leave the porous matrix through the sides, S_{nf}, and all of the fluid is even-

tually expelled out of the effluent or exit face S_{exit}, at $z_1^* = z_1^0$. Once the flow process has reached steady state, experimental measurements are gathered.

The absolute permeability is then determined by finding a property distribution that minimizes the discrepancy between the observed experimental data and those predicted through the solution of the equations describing flow. The problem is expressed formally as a minimization problem:

$$\min_{\mathbf{k}} J = J_{\text{expt}} + \lambda J_{\text{reg}} \tag{43}$$

The performance index J consists of two terms. The first, J_{expt}, is the data-fitting term, which measures the difference between experimentally observed and calculated values of the data. The second, J_{reg}, is a regularization term and is used to impose any *a priori* knowledge, such as smoothness constraints, on the functional form of permeability distribution obtained as a solution. These terms take the following forms:

$$\begin{aligned} J_{\text{expt}} &= \frac{1}{2} \sum_{n}^{N_V} \sum_{id}^{3} \int_V w_{z_{id},\, n} \left(v_{z_{id},\, n}^{\text{obs}} - v_{z_{id},\, n}^{\text{cal}}\right)^2 \hat{\delta}(V, V_n)\, \mathrm{d}V \\ &\quad + \sum_{n}^{N_P} \frac{1}{2} \int_V w_{P_n} \left(P_n^{\text{obs}} - P_n^{\text{cal}}\right)^2 \hat{\delta}(V, V_n)\, \mathrm{d}V \\ J_{\text{reg}} &= \sum_{id=1}^{3} \int_V \left(\frac{\mathrm{d}^2 k}{\mathrm{d}z_{id}^2}\right)^2 \mathrm{d}V \end{aligned} \tag{44}$$

The Kronecker delta function is defined as

$$\hat{\delta}(V, V_n) = \begin{cases} 1 & V = V_n \\ 0 & \text{otherwise} \end{cases} \qquad \text{or} \qquad \hat{\delta}(\mathbf{z}, \mathbf{z}_n) = \begin{cases} 1 & \mathbf{z} = \mathbf{z}_n \\ 0 & \text{otherwise} \end{cases}$$

where $\mathbf{z} \in V$ and $\mathbf{z}_n \in V_n$.

Here, $\mathbf{v}^{\text{obs}}$ and P^{obs} are observed experimental data, and $\mathbf{v}^{\text{cal}}$ and P^{cal} represent the corresponding calculated values from the numerical simulation. In the experimental data fit term, the differences between observed and calculated properties are individually weighted by $w_{z_{id},\, n}$ and w_n. These values depend on the relative accuracy of the experimental data, and are often taken to be the inverse of the variance of the errors in the experimental measurements. The regularization term is weighted relative to the data-fitting term by the regularization parameter, λ, which must be suitably determined.

The calculated values required to evaluate the performance index are determined from the solution of differential equations describing flow. Pressure and velocity values are obtained by solving the locally volume-averaged equation of continuity and differential momentum balance (Eqs (1) and (2)). For steady-state conditions, and incompressible flow, the equation of continuity becomes

$$\nabla \cdot \mathbf{v} = 0 \tag{45}$$

Our sample is thin, so that we take it to be uniform vertically. Then Darcy's equation is

$$\mathbf{v} = -\frac{k}{\mu} \nabla P \tag{46}$$

The forward problem involves numerically solving Eqs (45) and (46) along with appropriate boundary conditions. Boundary conditions associated with velocity field **v** correspond to no-flow conditions on the transverse sides.

The form of the other two boundary conditions associated with entering and exiting fluid conditions depends on the experimental design. In our work, the entering flow rate is controlled to be constant by a fluid-supply pump and the exiting flow is contacted by surroundings to have atmospheric pressure. The pressure and velocity fields are solved using finite differences.[17,38,39]

For simplicity, the porous medium is assumed to be isotropic and the permeability is interpreted to be a scalar function of position. Mathematically, the distribution is represented using normalized tensor product B-splines:[10,40]

$$k(\mathbf{z}) = \sum_{i}^{N_1} \sum_{j}^{N_2} \sum_{k}^{N_3} C_{i,j,k} B_i^{m_1}(z_1) B_i^{m_2}(z_2) B_i^{m_3}(z_3) \tag{47}$$

where m is the order of the B-spline, $B_i^{m_1}(z_1)$ is the ith B-spline basis function in the z_1th direction, and $C_{i,j,k}$ is the corresponding coefficient. The problem now involves determining the set of B-spline coefficients that minimizes Eq. (43), subject to Eqs (45) and (46) and the associated boundary conditions. This is accomplished using an implementation of the Broyden–Fletcher–Goldfarb–Shanno (BFGS) method.[41] The gradient of the performance index is computed using the method of adjoint states.[42,43]

3.3. Results and discussion

The methodology developed in Sections 3.1 and 3.2 is now demonstrated on Bentheimer sandstone. The sample is a rectangular parallelepiped shape having a length of 50 mm extending in the z-direction, width 25 mm along the x-direction, and thickness 5 mm in the y-direction. It was laterally sealed with epoxy (Stycast 2651) and mounted in plexiglass end-plates with O-rings and tube fittings. NMR velocity imaging was carried out using the proton resonance signal from brine (3% NaCl and 0.03% NaN_3 by weight in distilled water). An ISCO LC-5000 syringe pump established a stable brine flow through the sample, and the pressure drop between the inlet and outlet ports was monitored using a differential pressure transducer (Validyne Engineering). The measured total flow rate was 0.025 $cm^3\ s^{-1}$, and the pressure drop was 0.1 atm. The average permeability for the entire sample calculated from the integrated form of Darcy's law is 1.0 Darcy.

The imaging experiments were performed using the same imaging system described in section 2.4. A 4.4-cm i.d. birdcage RF resonator was used for both

RF transmission and reception of the NMR signal. For the stimulated pulse sequence, three hard pulses were used with the spin-warp sequence as discussed in Section 3.1. It is also necessary to obtain images corresponding to the porosity distribution as described in Section 2, in addition to the velocity images. This is because the images obtained in the velocity experiment are measures of the intrinsic velocity, the actual velocity of the fluid within the pore space. Darcy's law, however, is written in terms of the superficial velocity. The two velocities are simply related by the porosity:

$$v_s = \phi v_i \tag{48}$$

where v_s is the superficial Darcy velocity and v_i is the intrinsic velocity.

Two velocity-encoding pulse sequences were prepared for measuring two-component velocity fields in two-dimensional domains and applied successively at the same steady-state flowing condition. The two-component velocity field evaluated by Eq. (41) and Eq. (42) in Section 3.1 is shown in Fig. 15 for an image having a voxel size of 1.25 mm in the x (vertical) direction and 0.86 mm in the z (horizontal) direction. There are 58×20 uniformly spaced velocity measurements corresponding to the sample. The arrows indicate that the fluid is entering from the left-hand side and exiting on the right-hand side. Voxels containing very slow or stationary fluid are seen as dots instead of arrows, and it can be imagined that the permeability in these voxels will be smaller than in other voxels containing larger flows.

Figure 15 also shows that, due to heterogeneities in the porous medium, fluid velocities can vary significantly from one voxel to another. In order to observe such a wide distribution of velocities, it is necessary to have either a long observation time Δ or use a strong velocity-encoding gradient field. The longer the observation time, the more signal loss occurs due to relaxation effects, which is not practical for most porous media samples. Thus, the use of high gradient strength appears to be a better choice for porous media. If the magnitude of the velocity-encoding gradient is increased, a wider range of flow velocities can be detected at a shorter observation time with better resolution.

Using the methodology described in Section 3.2, the absolute permeability was estimated from the experimental velocity distribution observed previously. This distribution is shown as a three-dimensional plot in Fig. 16 and as a contour plot in Fig. 17. The three-dimensional plot shows that the permeability ranges from 0.1 to 3.5 Darcy, which may be compared to the determined apparent permeability of 1.0 Darcy. The contour graph is useful for understanding the permeability distribution in the two-dimensional domain where the experimental velocity field is measured. The brighter area indicates higher permeability in that region.

4. CONCLUSIONS

NMR imaging is an effective and novel probe that can provide useful information needed for characterizing properties of heterogeneous porous media. Its

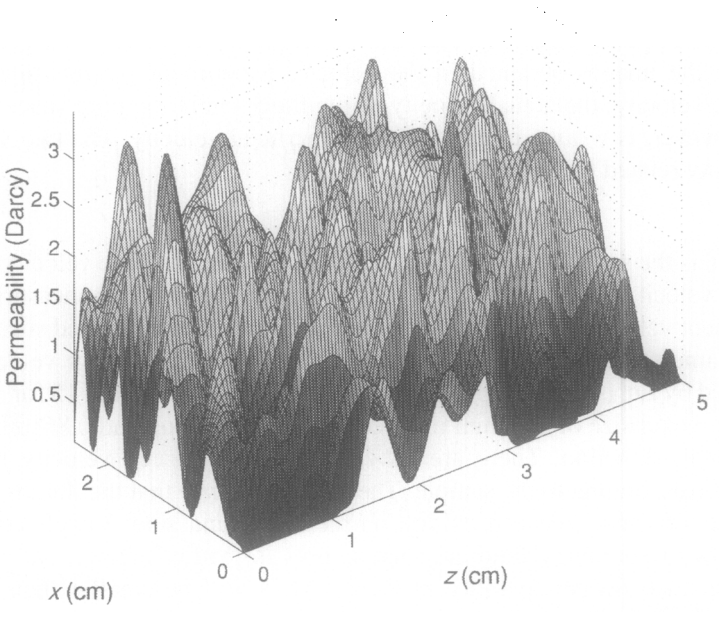

Fig. 16. Permeability estimate for the experimental velocity data—three-dimensional plot.

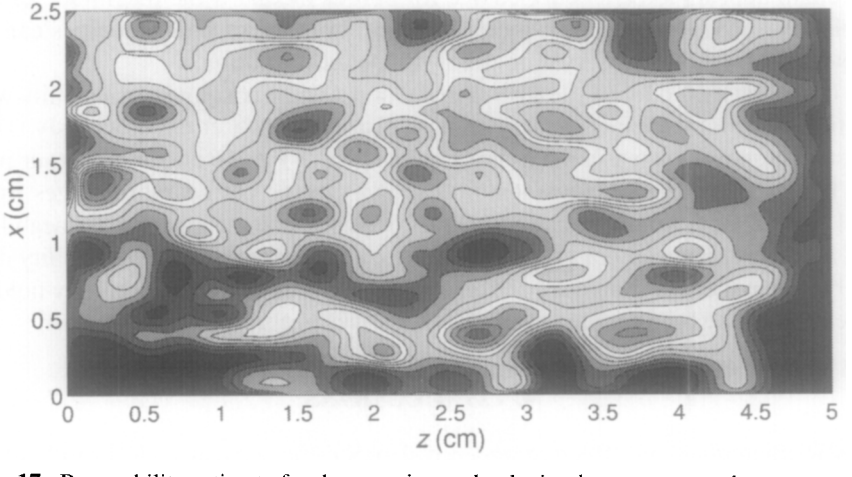

Fig. 17. Permeability estimate for the experimental velocity data—contour plot.

sensitivity to local fluid quantities and its ability to provide measures of macroscopic flow for use in associated inverse problems make it an effective tool for determining macroscopic storage and flow properties at finer scales than have previously been accomplished.

CPMG imaging experiments were used to resolve the porosity distribution. The relaxation response was modeled in each voxel to obtain accurate measures of the intrinsic magnetization, which was used to determine the porosity.

Pulsed-field-gradient stimulated-echo experiments were used to determine the velocity distribution during flowing experiments. An inverse problem was formulated and solved to determine estimates of the permeability distribution.

ACKNOWLEDGEMENT

We gratefully acknowledge funding from the US Department of Energy.

REFERENCES

1. J. C. Slattery. *Momentum, Energy, and Mass Transfer in Continua*. Krieger, New York, 1981.
2. S. Whitaker, *AIChE J.*, 1967, **13**, 420.
3. J. C. Slattery, *Advanced Transport Phenomena*, Cambridge University Press, New York, 1998.
4. S. Chen, F. Qin, K. H. Kim and A. T. Watson, *AIChE J.*, 1993, **39**, 925.
5. Songhua Chen, F. Qin and A. Ted Watson, *AIChE J.*, 1994, **40**, 1238.
6. P. T. Callaghan, *Principles of Nuclear Magnetic Resonance Microscopy*, Oxford University Press, New York, 1991.
7. K. R. Brownstein and C. E. Tarr, Spin-lattice relaxation in a system governed by diffusion, *J. Magn. Reson.*, 1997, **26**, 17.
8. A. T. Watson and C. T. P. Chang, *Prog. Nuclear Magn. Reson. Spectro.*, 1997, **31**, 343.
9. R. L. Eubank, *Nonparametric Regression and Spline Smoothing*, Marcel Dekker, New York, 1999.
10. L. L. Schumaker, *Spline Functions: Basic Theory*. John Wiley & Sons, New York, 1981.
11. H-K. Liaw, R. N. Kulkarni, S. Chen and A. T. Watson, *AIChE J.*, 1996, **42**, 538.
12. J. V. Beck and K. J. Arnold, *Parameter Estimation in Engineering and Science*. Wiley, New York, 1977.
13. R. N. Kulkarni and A. T. Watson, *AIChE J.*, 1997, **43**, 2137.
14. C. L. Lawson and R. J. Hanson, *Solving Least Squares Problems*, Prentice-Hall, Englewood Cliffs, NJ, 1974.
15. M. Stone. *J. R. Statist. Soc. Ser. B*, 1974, **36**, 111.
16. P. Craven and G. Wahba, *Numer. Math.*, 1979, **31**, 377.
17. J. T. Hollenshead, Nuclear magnetic resonance probes of heterogeneous porous media. PhD thesis, Texas A&M University, 2001.
18. A. Abragam, *The Principles of Nuclear Magnetism*, Oxford University Press, 1961.
19. D. I. Hoult and P. C. Lauterbur, *J. Magn. Reson.*, 1979, **24**, 425.
20. C. T. Chang, S. Mandava, A. T. Watson, S. Sarkar and C. M. Edwards, *Magn. Reson. Imaging*, 1993, **11**, 717.
21. P. Brunner and R. R. Ernst, *J. Magn. Reson.*, 1979, **33**, 83.
22. P. Mansfield and P. G. Morris, in *Advances in Magnetic Resonance, Supplement 2*. (ed. J. S. Waugh), Academic Press, New York, 1982.

23. C. T. Chang, A. T. Watson and C. M. Edwards, in *Methods in the Physics of Porous Media*, pp. 387–423, Academic Press, San Diego, 1999.
24. G. J. Nesbitt, T. W. Fens, J. S. van den Brink and N. Roberts, in *Magnetic Resonance Microscopy* (eds B. Blumich and W. Kuhn), p. 287, VCH, New York, 1992.
25. P. T. Callaghan and Y. Xia, *J. Magn. Reson.*, 1991, **91**, 326.
26. C. M. Edwards, C. T. Chang and S. Sarkar, in *The Society of Core Analysts Annual Technical Conference Preprints*, Paper No. 9310, 1993.
27. K. J. Packer, C. Rees and D. J. Tomlinson, *Adv. Molec. Relax. Processes*, 1972, **3**, 119.
28. P. R. Moran, *Magn. Reson. Imaging*, 1982, **1**, 197.
29. P. T. Callaghan, A. Coy, T. P. J. Halpin, D. MacGowan, K J. Packer and R. O. Zelaya, *J. Chem. Phys.*, 1992, **97**(1), 651.
30. Y. E. Kutsovsky, L. E. Scriven, H. T. Davis and B. E. Hammer, *Phys. Fluids*, 1996, **8**, 863.
31. L. Lebon, L. Oger, J. Leblond, J. P. Hulin, N. S. Martys and L. M. Schwartz, *Phys. Fluids*, 1996, **8**, 293.
32. K. J. Packer and J. J. Tessier, *Molec. Phys.*, 1996, **87**, 267.
33. J. J. Tessier, K. J. Packer, J. F. Thovert and P. M. Adler, *AIChE J.*, 1997, **43**, 1653.
34. B. Blumich, *NMR Imaging of Materials*, Oxford Science Publications, New York, 2000.
35. A. Caprihan, R. H. Griffey and E. Fukushima, *Magn. Reson. Med.*, 1990, **15**, 327.
36. A. Caprihan, S. A. Altobelli and E. Benitez-Read, *J. Magn. Reson.*, 1990, **90**, 71.
37. C. T. P. Chang and A. T. Watson, *AIChE J.*, 1999, **45**, 437–444.
38. K. Seto, J. T. Hollenshead, A. T. Watson, C. T. P. Chang and J. C. Slattery, *Transport Porous Media*, 2001, **42**, 351.
39. K. Seto, Miscible displacement simulation and permeability characterization in porous media, PhD thesis, Texas A&M University, 1999.
40. T. Lee, C. Kravaris and J. H. Seinfeld, *SPE Res. Eng.*, 1986, **1**, 521–534.
41. M. J. D. Powell, Report css 15, Technical report, AERE Harwell, 1975.
42. W. H. Chen, G. R. Gavalas, J. H. Seinfeld and M. L. Wasserman, *Soc. Pet. Eng. J.*, 1974, **257**, 593.
43. G. Chavent, M. Dupey and P. Lemonnier, *Soc. Pet. Eng. J.*, 1975, **15**, 74–86.

Nuclear Magnetic Resonance Studies of Micelles

Y. R. DU,[1] S. ZHAO[2] and L. F. SHEN[1]

[1]*State Key Laboratory of Magnetic Resonance and Atomic and Molecular Physics, Wuhan Institute of Physics and Mathematics, The Chinese Academy of Sciences, Wuhan 430071, P. R. China, and*
[2]*Technical Institute of Physics and Chemistry, The Chinese Academy of Sciences, Beijing 100101, P. R. China*

1. INTRODUCTION

A surface-active agent (or surfactant) is a substance that lowers the surface or interfacial tension of the medium in which it is dissolved. Surfactants have a characteristic molecular structure consisting of hydrophobic and hydrophilic groups. This is known as an amphipathic structure, and causes not only concentration of the surfactant at the surface and reduction of the surface tension of the solvent, but also orientation of the molecule at the surface with its hydrophilic group in the aqueous phase and its hydrophobic group oriented away

ANNUAL REPORTS ON NMR SPECTROSCOPY
VOLUME 48 ISBN 0-12-505448-3

from it. The abrupt change in physicochemical properties seen in aqueous solutions of surfactants with long hydrophobic chains when a specific concentration is exceeded is attributed to the formation of oriented colloidal aggregates. The narrow concentration range over which these changes occur has been called the critical micelle concentration (CMC), and the oriented molecular aggregates that are formed spontaneously above the CMC area are known as micelles.[1–6]

The role of micelles in practical systems derives from (i) their competition with monomers in adsorption processes, (ii) their use as a 'reservoir' of monomers, (iii) their ability to solubilize materials and affect their physical and chemical properties, and (iv) their usefulness as 'model' systems.

The usefulness of the micelle as a 'model' colloid for studying many problems of general interest in colloid science has been pointed out.[7] Micellar systems have proved to be very useful for studying the factors involved in hydrophobic and electrical interactions and for posing and answering many questions regarding the microenvironments encountered in interfacial systems of other kinds and membranes.[7–12] Various spectroscopic methods are particularly useful. The use of micelles as model systems for membranes or some aspects of enzymes has very important biological implications.[13–15]

Micellar media have been extensively used to affect rates of numerous organic and inorganic reactions.[16–21] Catalysis or inhibition of solubilized species involve many kinds of interactions and may vary with the nature of the surfactant. The kinetic studies performed so far in solutions of micelle-forming surfactants can be grouped into two categories: the first includes those cases in which a surfactant micelle acts only as a medium for the reaction, and the second includes reactions in which the surfactant participates directly either as a catalyst or as a substrate. This feature of surfactants determines their usefulness in practical processes.

Micelles play an important role in many industrial and technological processes. This mostly depends upon their ability to solubilize compounds which are not normally soluble in the solvent. Detergency is an example where micelles are quite important. In dry-cleaning, solubilization in reverse micelles plays a vital role in removing polar dirt from clothes. Micelles in non-aqueous media are used in motor oils to solubilize corrosive oxidation products and to prevent them from reacting with engine parts. Solubilized systems are used in many agricultural sprays and dyeing media. Micellar solutions have been found to be very effective in the removal of odor-causing molecules from factories and food-packaging plants. Micellar solubilization is important for 'deinking' in the paper industry; it is involved in photographic processes, and in microencapsulation via interfacial polymerization. It is also involved in the emulsion polymerization process, which involves the solubilization of the monomers in the micellar core.

Because of the energy crisis, there has been an increasing amount of work on applications of micellar solutions as injection fluids for enhanced oil recovery. The basic aim is to eliminate (reduce to less than 10^{-3} dyne cm^{-1}) the interfacial

tension between the injected and reservoir fluids, so that the remaining oil is mobilized and collected towards the oil wells. There are certain other requirements, which the micellar solutions should fulfill for these to be efficient in enhanced oil recovery. Micellar systems have been employed to facilitate the photochemical conversion of light energy into chemical energy.

Surfactant molecules are in dynamic equilibrium among three possible states (monomers adsorbed at the interface of the aqueous solution with a non-polar phase, monomers molecularly dispersed in the solution, and micellar aggregates formed when the CMC is reached). From various theoretical considerations, as well as experimental results, it can be said that micelles are dynamic structures whose stability is in the range of milliseconds to seconds.[22,23] Thus, in an aqueous surfactant solution, micelles break and reform at a fairly rapid rate, in the range of milliseconds.[24–26]

Equations (1) and (2)[23] show the two characteristic relaxation times, τ_1 and τ_2, associated with micellar solutions. The shorter relaxation time, τ_1, generally of the order of microseconds, relates to the exchange of surfactant monomers between the bulk solution and micelles, whereas the longer relaxation time, τ_2, generally of the order of milliseconds to seconds, relates to the dissolution of a micelle after several molecular exchanges.[27,28] It has been proposed that the lifetime of a micelle can be given by $n\tau_2$, where n is the aggregation number of a micelle.[29] Thus, the relaxation time τ_2 is proportional to the lifetime of a micelle. A large value of τ_2 represents a high stability of the micellar structure.

$$\text{Monomeric exchange } (\tau_1): \qquad A_n + A \leftrightarrow A_{n+1} \tag{1}$$

$$\text{Micellization–dissolution } (\tau_2): \qquad nA \leftrightarrow A_n \tag{2}$$

Ever Since McBain proposed the presence of molecular aggregates in soap solutions,[30] the structure of micellar aggregates has been a matter of discussion.[31] The details of micellar and mixed micellar (of different kinds of surfactants and of surfactant and polymers) structures have been intensely investigated over the years, and almost every technique devised by modern science, such as X-ray diffraction (XRD), nuclear magnetic resonance (NMR), electron spin resonance (ESR), small-angle neutron scattering (SANS), light scattering, fluorescence, calorimetry, chemical relaxation, ultrasonic relaxation and many other solution and spectroscopic techniques, have been applied.[32–34] NMR has played a more and more important role in the studies of micelles, with the continued development of new NMR techniques, especially at the end of the last century. Several reviews have appeared on the subject.[35–40]

2. SCOPE OF THE CHAPTER

This chapter will be concerned with the characterization of micellization processes, physical properties of micelles, the structure of self-aggregated

micelles, hydration and solubilization properties, and interactions between micelles and different kinds of surfactants, and those with biological compounds and polymers, by the existing NMR techniques at a molecular level. The multi-detection ability (^{1}H, ^{2}H, ^{13}C, ^{15}N, ^{17}O, ^{19}F, and ^{23}Na) is, of course, one unique characteristic of NMR. Early in the late 1960s, it was shown that ^{19}F chemical shifts are sensitive enough to characterize the micelle formation of fluorine-containing surfactants.[41,42] The CMCs of many fluorinated surfactants are obtained by following ^{19}F chemical-shift changes.[43,44] Characterization of micelle formation by chemical shifts of nuclei other than ^{19}F is mostly applicable for micelles of non-fluorinated amphiphiles. It is certain that monitoring chemical-shift changes as a function of the surfactant concentration is the simplest approach based on NMR. However, there are many other sophisticated NMR experimental methods conveniently available nowadays which can provide abundant information about the structure and dynamics of micelles, and interaction between surfactants, and between surfactants and polymers in their co-aggregates. These methods are NMR relaxation, self-diffusion coefficient, and, especially, multidimensional NMR measurements developed for the structural determination of complex organic compounds and biological macromolecules, such as proteins and nucleic acids. Two-dimensional (2D) nuclear Overhauser enhancement spectroscopy (NOESY) and 2D HOESY appear to be effective tools for elucidating the interactions between surfactant molecules of one kind or of different kinds, between water molecules and surfactants, and between surfactant and polymer molecules. It is worthwhile emphasizing that it is often difficult to draw definitive conclusions from the observed NMR data with the use of a single NMR method. A combination of several NMR methods is sometimes necessary. We do not attempt to cover all of the existing literature, but a number of studies will be selected to show which NMR methods are suitable for solving a given problem of interest.

3. STUDY OF THE MICELLIZATION PROCESS

The spontaneous formation of self-associated assemblies of small and medium-sized aggregates by surfactants is known as micellization. These micelles play important roles in drug delivery, enhanced oil recovery, detergency, catalysis in chemical reactions, biological membrane modeling, and cleaning processes. Therefore, the determination of the CMC, size, shape and aggregation number of the micelles is of prime importance. Also, a deep understanding of the structure of the micelles helps in their practical application. NMR spectroscopy has been used successfully in this respect. It is a versatile and powerful technique to investigate surfactant aggregates in solution. Parameters such as chemical shift, linewidth, and spin relaxation rate, and their variations with surfactant concentration, can give useful information about micellar properties and structures. The increased improvement of the method makes it possible to use new techniques to

obtain more information both on systems previously studied and on newly developed systems.

3.1. Critical micelle concentration and physical properties of micelles

The environment of the surfactant molecules undergoes a marked change when they associate together to form micelles. The chemical shifts of certain nuclei of the surfactant molecules in the micellar state will consequently become different from those in the molecular dispersed state. It is well known that the exchange between the molecules of the two states in the solution is fast, so the observed chemical shift is the weighted value of the two species according to the following expression:

$$\delta_{obs} = p\delta_{mic} + (1 - p)\,\delta_{mon} \tag{3}$$

where p is the fraction of surfactant molecules in the micellar state. A chemical-shift dependence on the concentration of the surfactant will be observed.

Owing to the 100% natural abundance, high sensitivity (0.83) and large dispersion of chemical shifts (100 to −300 ppm) monitoring the change in ^{19}F chemical shifts of fluorinated surfactants with their concentrations gives their CMC. ^{19}F NMR has been used to study the micelle formation of sodium salts of perfluorocaprylate in aqueous solution. The use of ^{19}F NMR is particularly helpful in this type of study, as the shifts of each of the separate groups of CF_3 and CF_2 may be distinguished. Their ^{19}F chemical shift–concentration curves consist of two separate lines, the intersections of which give the CMC.[41] All three resonance peaks (CF_3 and α- and β-CF_2) show remarkable turning points in the chemical shift–concentration curves at the same surfactant concentration, which resembles the CMC of heptafluorobutyric acid in aqueous solution.[42] The study of molecular aggregation of lithium perfluoro-octylsulfonate in aqueous solution at temperatures from 30°C to 250°C by ^{19}F NMR chemical shifts shows that the CMC increases moderately from 30°C to 100°C and becomes steep after 150°C is reached.[43] The CMCs of fluorine-labeled zwitterionic surfactants $CF_3(CH_2)_{11}N(CH_2)_2(CH_2)_nCO_2$-, where $n = 1$, 4, 5, and 7, over a 60°C temperature range were determined. It was found that replacing a terminal methyl group by a trifluoromethyl group does not dramatically change the micelle stability.[45]

For non-fluorinated surfactants, ^1H and ^{13}C nuclei are commonly used. Transformation of the shapes of sodium dodecylsulfate (SDS) micelles in aqueous solution was found by following the changes of the ^1H chemical shifts of CH_3 and α-CH_2 of SDS. A break at 8.0 mM from both the chemical shift versus SDS concentration curves corresponds to the first CMC, and breaks at 84 mM and 70 mM for protons of the methyl and α-CH_2 groups, respectively, correspond to the second CMC of SDS.[46] The CMCs of a series of polyfluorinated cationic surfactants, $C_nF_{2n+1}CONH(CH_2)_2N(CH_3)_3Br$, and their hydrocarbon analogs, were deduced by the change in proton chemical shift–concentration curves. The

CMCs of these polyfluorinated surfactants are of the order of 10^{-5} M.[47] Plots of the observed ^{1}H chemical shifts versus surfactant concentration of cetyl trimethyl ammonium chloride, cetyl pyridinium chloride, cetyl dimethyl phenyl ammonium chloride, cetyl dimethyl benzyl ammonium chloride, cetyl dimethyl-2-phenyl ethyl ammonium chloride, and cetyl dimethyl-3-phenyl propyl ammonium chloride, are sigmoidal and were fitted to a model based on the mass action. The ^{1}H chemical shift-based CMC values are in excellent agreement with those determined by the surface tension method.[48] The micellization processes of dodecyl trimethyl ammonium halides (chloride and bromide) studied by calorimetric titration show different behaviors at 298 K. However, these disappear at 313 K, while the results measured by the chemical shift versus surfactant concentration do not show this difference.[49] The CMC of 3-aminopropyl triethoxy silane in toluene is ca. 0.47 M, measured by ^{1}H and ^{13}C chemical shifts.[50] The CMC of optically active potassium *N*-n-dodecanoyl alaminate measured by ^{1}H and ^{13}C chemical shifts is lower (11–15 mM) in D_2O than that in a mixed solvent of 1,4-dioxane and D_2O (19 mM).[51] The ^{1}H chemical shift shows that the CMC of resorcinol-type calix[4] phosphoric esters having four alkyl side-chains, [4]Ar 5P-R-n, is insensitive to the length of the side-chains, *n*.[52] The CMC values of a family of surfactants, the sodium cyclohexyl alkanoates, with different lengths of the alkanoate side-chains, were obtained from ^{13}C chemical-shift measurements. The results show that these amphiphiles have high CMCs (0.12–1.02 M).[53]

The nucleus ^{31}P is useful in determining the micellization processes of phosphorus-containing surfactants. For the lithium ethyl (n-octyl) phosphate in D_2O, a critical micelle concentration was determined by ^{31}P NMR spectra.[54] Three CMCs were detected by the inflection points in the concentration-dependent slopes of the ^{31}P chemical shift of a soybean phosphatidylcholine in n-butanol. They are 7.5%, 35% and 63% w/w soybean phosphatidylcholine.[55]

Changes in ^{23}Na chemical shifts upon aggregation, although being one-tenth of that observed in shifting from water to ethanol, are consistent and, equally important, utilizable at concentrations as low as 10^{-5} M provided that enough accumulations are collected.[56]

As in the case of the concentration dependence of the chemical shift, the ^{1}H and ^{13}C band shapes of the surfactant resonance peaks are also concentration dependent. Analysis of ^{1}H NMR band shapes for large aggregates of a cetyl trimethyl ammonium bromide–water system results in a CMC of 1.0 mM; this is consistent with the value measured by other methods.[57] The ^{1}H NMR bands of alkyl trimethyl ammonium salicylate and hexadecyl pyridinium salicylate aqueous systems start to broaden at concentrations just above the CMC. The broadening continues up to a concentration above which the band shape is almost constant, as the concentration is further increased.[58] ^{13}C NMR linewidth analysis of sodium octanoate in aqueous solution gives reasonable estimated CMC values.[59]

The NMR self-diffusion coefficient measurements also provide a convenient tool for the study of the micellization process. They are based on the large

intrinsic difference in self-diffusion rates between monomeric and micellized surfactant molecules. The monomer lifetime in a typical micelle is short on the timescale of the self-diffusion measurement, so all of the self-diffusion coefficients become time averaged. Thus, the observed self-diffusion coefficient can be expressed analogously to the case of chemical shift. The CMC measured (2.6 mM) for the aggregation of sodium di-2-ethyl hexyl sulfosuccinate (Aerosol OT) is in good agreement with that measured by the surface tension method.[60] The NMR self-diffusion coefficient measurement method was widely used to measure the CMC values of various surfactants, such as tetraethylene n-octyl ether,[61] and branched alkyl glucosides,[62] the temperature dependence of the CMC of block copolymer systems containing anesthetics,[63] and the temperature and pH dependence of the CMC in sodium oleate aqueous solution.[64]

Besides the chemical-shift and band-shape NMR parameters, spin-lattice relaxation measurement is another approach for monitoring the micellization process. The chemical shift of a nucleus is influenced by its environment. Its spin-lattice relaxation time is affected by its local dynamics. Therefore, the spectral data may vary as a function of the concentration of the surfactant and should exhibit an inflection point when the micelles are formed, because the self-aggregation of the surfactant molecules induces a change in the chemical environment as well as the freedom of motion of the surfactant molecules. For several surfactants, the change in ^{1}H and ^{13}C chemical shifts with surfactant concentration is very slight, and hardly shows any significant inflection point that could be an indication of a micellization process, such as in the case of sodium cholate. However, the spin-lattice relaxation time (T_1) of sodium cholate varies with its concentration. At the CMC, the molecular correlation time increases substantially (due to the change from the molecularly dispersed to the self-associated form). A sharp decrease in T_1 at 16.0 mM is found, which is close to the CMC value obtained by the fluorescence method.[65] Variation of the spin-lattice and spin–spin relaxation times (T_1 and T_2) as a function of the surfactant concentration was also demonstrated for the well-known ionic and non-ionic surfactants, sodium dodecylsulfonate, cetyl trimethyl ammonium bromide and Triton X-100 (*p*-tert-octyl phenoxy-polyethoxy-ethanol). It was shown that the ratio T_2/T_1, which gives a measure of the degree of departure of the molecular motion from the extreme narrowing condition, gives sharper turning points on the concentration-dependence curve than the chemical-shift (Figs 1 and 2).[66] Paramagnetic relaxation by Gd^{3+}, Fe^{3+} and Mn^{2+} was also used to study the micellization process of SDS.[67]

The quadrupolar ^{2}H spin-lattice relaxation of specifically deuterated surfactants, such as the methyl deuterated n-alkyl phosphocholine surfactants, also shows a concentration dependence. The CMC of dodecyl phosphocholine was determined by exploiting the difference in the ^{2}H spin-lattice relaxation times of the monomers versus the micellar state.[68] Quadrupole splittings of ^{14}N were also used to characterize the micellization process of short-chain perfluoro-carboxylic acid salts.[69]

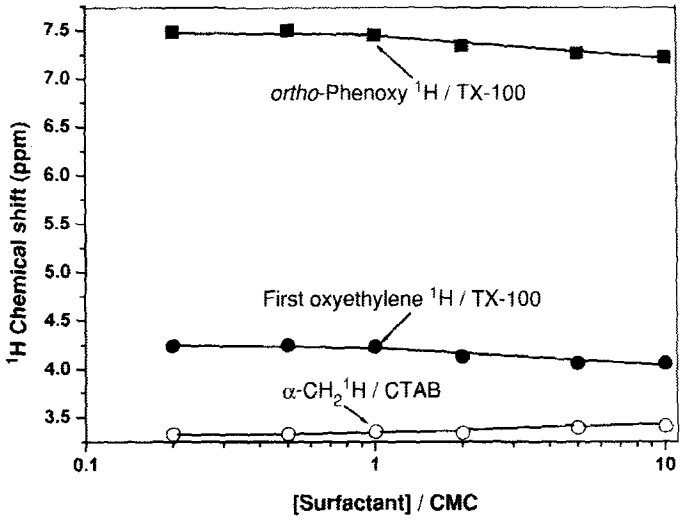

Fig. 1. ^{1}H chemical-shift dependence on the concentration of surfactants, Triton X-100 (TX-100) and cetyl trimethyl ammonium bromide (CTAB).

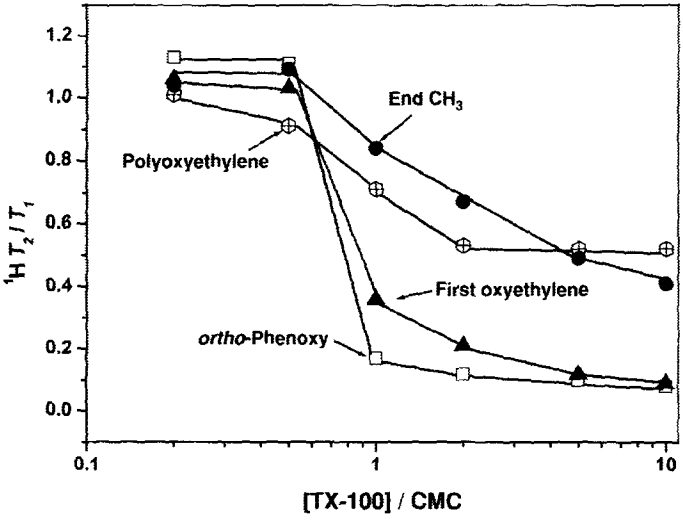

Fig. 2. T_2/T_1 ratio dependence on the concentration of surfactants.

It is well known that 2D NOESY is an effective method to study the three-dimensional (3D) structure of large molecules, such as proteins which have long motional correlation times.[70,71] Cross-dipolar interaction peaks in a NOESY spectrum rely on the cross-relaxation of the longitudinal magnetization during the mixing time. One can extract valuable information about intermolecular distances from the intensity of the NOESY cross-peaks. The appearance of

cross-peaks between protons attached to remote methylene carbon atoms of the surfactant molecules in a 2D NOESY map can be an indication of micellization, because cross-peaks appear in the 2D NOESY map only from proton pairs separated by less than 5 Å, while the distance between protons attached to remote carbon atoms on a hydrocarbon chain is far longer than this value. The 2D NOESY map of a dilute (0.5 CMC) Triton X-100 aqueous solution shows only cross-peaks between protons attached to the adjacent carbon atoms in the hydrocarbon chains (Fig. 3), while cross-peaks between protons of the remote

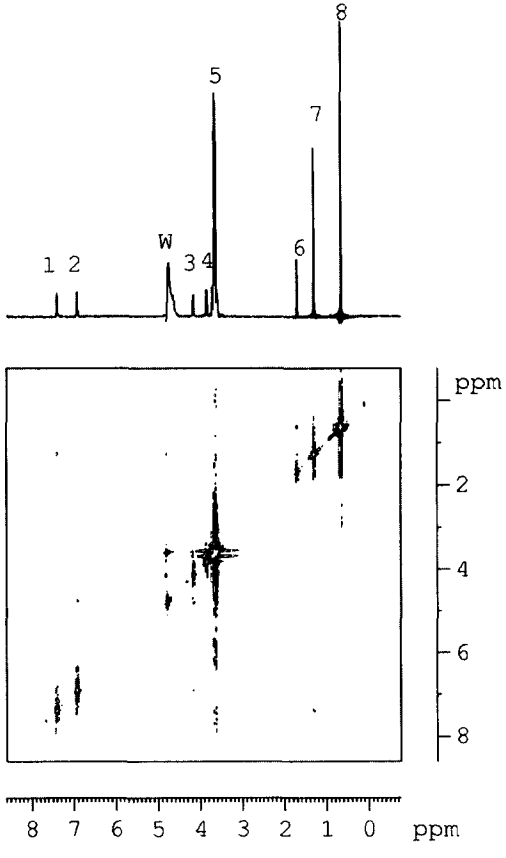

Fig. 3. 2D NOESYspectrum of Triton X-100 in aqueous solution at a concentration of 0.5 CMC with a mixing time of 500 ms, where 1 and 2 are the peaks of the aromatic protons of Triton X-100 ($(CH_3)_3CCH_2C(CH_3)_2C_6H_4OCH_2CH_2(OC_2H_4)_8OH$), 3 and 4 are the peaks of the protons on the first oxyethylene group next to the phenoxy ring, 5 is the overlapped peak of the protons on the polyoxyethylene chain, 6 is the peak of the methylene protons on the hydrophobic chain, 7 is the peak of the dimethyl protons attached to the carbon atom next to the phenoxy ring, and 8 is the peak of the trimethyl protons at the end of the hydrophobic chain. W is the peak of water protons. (Reprinted with permission from ref. 72, Copyright 2000 American Chemical Society.)

methylene groups exist in the 2D NOESY map of a concentrated (10 CMC) Triton X-100 aqueous solution (Fig. 4).[72]

The physical properties of the micelle, e.g. average aggregation number, shape and formation constant, can be deduced from the chemical-shift data from the mass action model.[48] Using the mass action law model for micelle formation, the

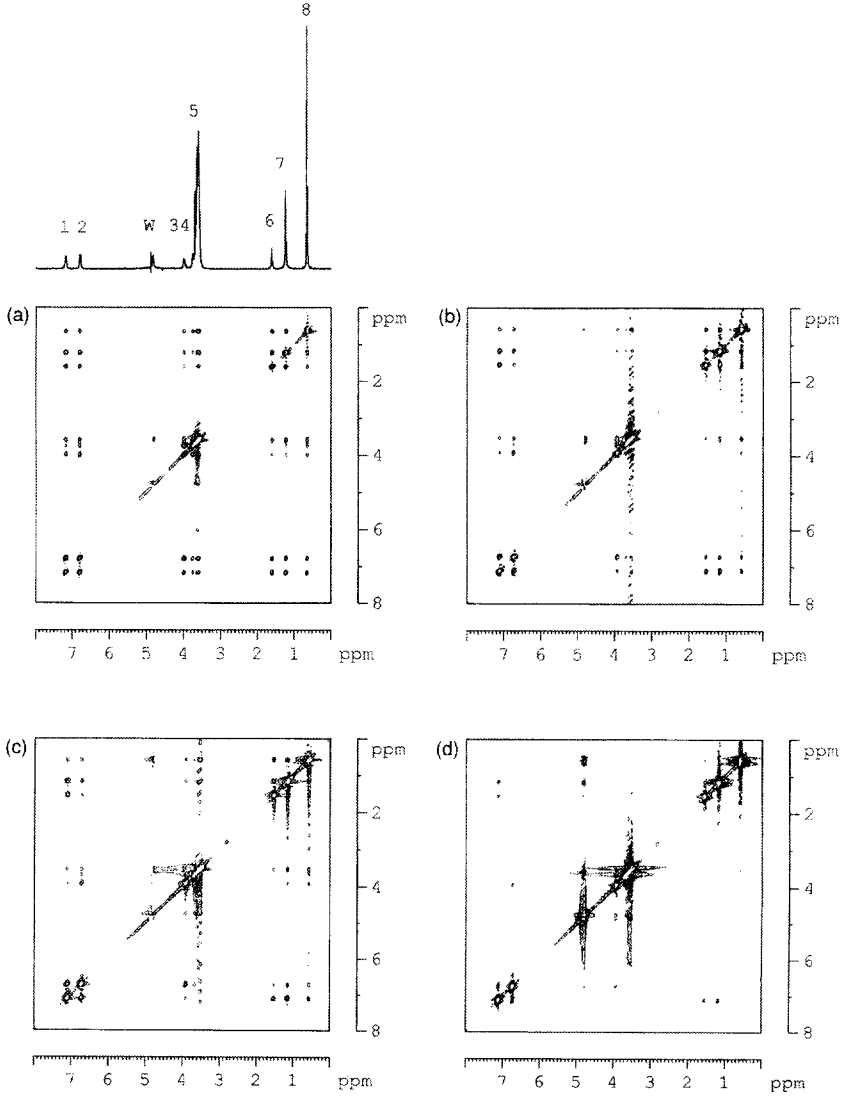

Fig. 4. 2D NOESY spectrum of Triton X-100 in aqueous solution at a concentration of 10 CMC with mixing times of (a) 500 ms, (b) 100 ms, (c) 50 ms, (d) 10 ms. Numbering of the peaks is the same as in Fig. 3. (Reprinted with permission from ref. 72, Copyright 2000 American Chemical Society.)

aggregation number was estimated by fitting the calculated ^{13}C chemical shifts of sodium hexanoate, octanoate and nonyl ammonium bromide as a function of the surfactant concentration to the experimental values.[73] Although the use of ^{13}C chemical shifts to obtain surfactant aggregation numbers from the application of the mass action model has been criticized as yielding low aggregation numbers for typical surfactants,[74] aggregation numbers estimated by this method for sodium cyclohexyl alkanoates with different lengths of the alkyl chain are in good agreement with those determined by viscosity measurements.[53] The aggregation number of lithium perfluoro-octylsulfonate in water decreases from 36 to 6.8 as the temperature rises from 30°C to 100°C, and then decreases slowly as the temperature increases further.[43]

The NMR self-diffusion coefficient measurement is an important method for estimating the size and shape of the micelles formed. It gives direct and easily interpretable information. The approach is based on the large intrinsic difference in self-diffusion rates between monomeric and micellized surfactant. The observed self-diffusion coefficient is the time average of the values of these two species. It can be expressed analogously to the case of the chemical shift. From the translational self-diffusion coefficient of the micelle, one can deduce the hydrodynamic radius using the Stokes–Einstein equation. It should be noted that, in estimating the hydrodynamic radii, the effect of intermicellar interactions must be taken into account. A series of studies on the size of micelles formed in aqueous solutions of non-ionic amphiphiles, polyethylene glycol alkyl ethers (C_xE_y), were performed by the use of NMR self-diffusion coefficient measurements. A coherent picture of the micelle size of $C_{12}E_6$ as a function of temperature is obtained.[75] The size of $C_{12}E_5$ micelles increases when the temperature approaches the cloud point, while no similar effect is shown for $C_{12}E_8$.[76] For the $C_{16}E_7$ aqueous system, it is found that, at low surfactant concentration, the self-diffusion coefficient decreases as the concentration increases, and at concentrations higher than 10% by weight, the self-diffusion coefficient versus log [surfactant] gives a positive slope of about 2/3.[77] The hydrodynamic radius decreases from 4.8 to 3.9 Å as the number of ethylene oxide groups increases from 3 to 5 in the C_6E_y molecule.[78] The errors caused by convection, arising from the variation of the temperature during measurement of a member of the oligo-oxylene alkyl ether groups, $C_{12}E_8$, makes the results less precise than those obtained by other methods.[79] Self-diffusion coefficient measurements of octadecylamide oligo(oxyethylene) ether, $C_{18}H_{37}CONH(CH_2CH_2O)_9H$, show that there are two kinds of micelles of different sizes: a small one of 20–30 Å in radius which is not concentration dependent, and a large one which is formed in dilute solution and grows quickly with the increase in concentration.[80] The hydrodynamic radii of polyethylene glycols, end-capped with short fluorocarbon tails, as deduced by self-diffusion coefficient measurements, are 25.6 and 17.6 Å for the fluorocarbon tails of eight and six carbon atoms, respectively. It is found that each C_8F_{17} micelle contains 30 end groups, and each C_6F_{13} micelle contains 20 end groups.[81] Self-diffusion coefficient data for *N,N*-dimethyl dodecyl amine oxide micelles in water are compatible with a broad distribution in micellar size at all the

amphiphile concentrations; however, in the presence of added dodecane, a narrow distribution results.[82] In the micellar composition range of sodium sulfonates, $CH_3(CH_2)_{n-1}SO_3Na$ ($n=5$–9, 11), in water trimethylsilane (TMS) was used to determine the micelle intra-diffusion coefficients, from which the micelle radii were obtained. Both the monomer surfactant and the micelle intra-diffusion coefficients show a sharp decrease above the CMC. These results are interpreted in terms of the obstruction effect due to the micelles.[83] The same phenomenon is observed for the alkyl trimethyl ammonium bromide surfactant systems.[84] The radius of a fatty acid-based heterogemini surfactant micelle was determined from the self-diffusion coefficient to be 40 Å.[85] The change in micelle size can also be monitored by spin–spin relaxation times,[86] field-dependent ^2H relaxation[87] and band-shape[61,88] measurements. Normally, micelles are spherical, with a radius equal to the length of the extended surfactant molecule. When the size of the micelles grows beyond this limit, it may cause a change in shape. Self-diffusion coefficient measurements with consideration of an obstructing effect may constitute a suitable approach to solve this problem.[89,90] It was found from this method that *N*,*N*-dimethyl dodecyl amine oxide forms spherical micelles with a narrow size distribution in the presence of dodecane and TMS,[82] and the shape of $C_{12}E_6$ is consistent with mono-dispersed spherical particles at 20–35°C.[75] Self-diffusion coefficient measurement of the surfactant molecules and water protons suggests that dodecyl tributyl ammonium bromide micelles are spherical at a concentration range of 0–80% volume.[91] Linewidths provide another NMR parameter which can be used for studying micellar shape. Combination of the self-diffusion coefficient and linewidth measurements shows that $C_{12}E_5$ micelles grow at low temperatures to form rods, while $C_{12}E_8$ micelles do not, and the methylene groups of $C_{12}E_8$ are less ordered than those of $C_{12}E_5$.[76] The proton linewidth of the alkyl chain protons of C_8E_4 is nearly constant between 25°C and 37°C, so any significant growth of individual micelles from spherical to elongated shape can be ruled out.[61] The shape of the aggregates of resorcinol-type calix [4] arene phosphoric esters having four side-chains is not globular, and the alkyl side-chains gather loosely in the aggregate.[52] The ^1H linewidth of calcium octyl sulfate reveals that the micelles are small and spherical over the entire range of existence of the micellar solutions, up to 40 wt% surfactant.[92] A field-dependent ^2H nuclear magnetic relaxation study of cetyl trimethyl ammonium bromide and SDS with the α-CH_2 deuterated showed that non-spherical aggregates, rod-shaped, are formed well below the second CMC for both systems.[87] The oblate micelle shape was excluded for cetyl trimethyl ammonium bromide, and the micelles were slightly elongated.[93]

3.2. Structure of micelles and dynamics

The microstructure of surfactant micelles was studied early in the 1960s using the ^1H spin-lattice relaxation times of hydrocarbon chain protons in a solution of sodium alkyl sulfates. The results indicate that when micelles are formed, the

relaxation rate of the CH_2 protons is remarkably increased, as their environment changes from D_2O to liquid hydrocarbon. The relaxation rate of the CH_2 protons in micelles suggests that part of the alkyl chains in the micelles are exposed to water, and that molecular motion in the micellar interior is more restricted than in a liquid hydrocarbon of the same chain length as the single ions making up the micelle. While the rotational and internal motions of alkyl chain compounds are much the same in aqueous and in non-aqueous solvents, the translational motion is more restricted in an aqueous solvent.[94] For the non-ionic surfactant, *p-tert*-octyl phenoxy (polyethoxy)$_n$ ethanols, where $n = 9$–10, 12–13, and 30, spin-lattice relaxation measurements of the protons reveal that the micelle interior is liquid-like and is not penetrated by solvent to any significant extent. The internal methyl and methylene groups of the hydrocarbon chain are actually in a non-polar environment in the micelle rather than in the bulk detergent. Contact with the solvent seems to begin in the region of the first ethoxy group following the phenyl group, and gradually increases toward the other end of the chain. The mobility of the segments increases in the same direction. Water molecules in the region between the polyethoxy chains appear to be partially immobilized.[95]

Chemical-shift changes of ^1H, ^{13}C ^{19}F and ^2H are often utilized in elucidating structures. The combination of ^1H and ^{19}F chemical-shift measurements of two homologous series of double-tailed hybrid surfactants containing a hydrocarbon chain and a fluorocarbon chain attached to the same hydrophilic group indicates that, when the hydrocarbon chain bears three or more carbon atoms, both the fluorocarbon and the hydrocarbon chains are incorporated inside the micelle.[96] A ^1H NMR study of alkyl benzene sulfonate isomers showed that aggregation induces conformational changes which depend on the position of the phenyl ring along the alkyl chain. The two protons on each methylene group attached to the methine group are magnetically non-equivalent below the CMC and become equivalent above the CMC. The changes in the chemical shifts of the terminal CH_3 indicate that the two chains experience dissimilar environments due to micellization; the shorter chain loops back towards the palisade area of the micelle, while the other occupies the central region of the micelle. The aromatic *meta*-protons show a large low-frequency shift on micellization, whereas the *ortho*-protons remain unshifted. Therefore, the water boundary in the micelles lies between the *ortho*- and *meta*-protons.[97] ^1H NMR experiments on pyrrole-containing cationic surfactants with various cations show that the pyrrole group remains confined in the micelle interior.[98] A multinuclear NMR investigation of sodium *N*-dodecanoyl-L-prolinate in CD_3OD and D_2O showed that the ratio of the two isomers is different in different solvents. Under micellar aggregation conditions, the presence of two isomers results in two signals for most of the nuclei. This indicates that the isomers micellize on the basis of a different stereochemical code in conformational domains that give two different ^1H and ^{13}C spectra.[99] ^1H and ^{13}C spectra provide discrimination of enantiomers by chiral micelles; the interaction of the aggregates with the solute can be very specific.[100] The ^{13}C chemical shifts of the C1, C2 and C3 atoms of sodium cyclododecylsulfate

show a low-frequency shift with the increase of surfactant concentration, while those of C4, C5, C6 and C7 shift to high frequency. Since a high-frequency shift is normally related to an increasing population of *trans* conformers, it can be inferred that surfactant micellization is accompanied by a change from the *gauche* to the *trans* conformation. The probability of *gauche* conformations at C1 to C3 is increased.[101] Most of the ^{13}C chemical shifts of a series of ionic surfactants (dodecyl pyridinium chloride, decyl trimethyl ammonium bromide, dodecyl trimethyl ammonium bromide, cetyl trimethyl ammonium bromide, SDS, and sodium octyl benzene sulfonate), especially the central carbons of the hydrocarbon chains, move to higher frequencies on adsorption on solid surfaces. In comparison with the micellar state of these surfactants, such changes correspond to the formation of surfactant aggregates on the solid surface. For most surfactants, these aggregates resemble the micellar state from a chain-conformational point of view.[102] Conformational changes of two series of gemini surfactants with rigid and flexible spacers, (phenylene dimethylene)-bis-(n-octyl ammonium)-dibromides, were studied by selective decoupling of ^{13}C and ^{1}H NMR spectra, below and above the CMC, in order to examine how the relative geometric disposition of the n-octyl chains affects the micellar behavior of the gemini molecules. Experimental results show that the introduction of rigid spacers into the gemini surfactants promotes the stabilization of the distance between the two hydrophilic groups, since the specific conformation of the spacer portion is preferentially stabilized upon micellization. For the two series with rigid and flexible spacers, the conformation of the two octyl chains tends to take up an all-*trans* conformation, implying that the two octyls play a significant role in micellar behavior.[103] Two anionic and a cationic gemini surfactants form small spherical rapidly tumbling micelles with narrow proton lines and little or no broadening, even at concentrations considerably above the CMC values.[56] Interesting results of the aggregation of the gemini chiral surfactant, (2*S*,3*S*)-2,3-dimethoxy-1,4-bis(*N*-hexadecyl-*N*,*N*-dimethyl ammonium)-butane dibromide, in various solvents have been observed by ^{1}H NMR spectra. In $CDCl_3$, the surfactant is present in dimeric assemblies and as reverse micelles, while in CD_3OD, the mass action law does not hold, despite the evidence that the surfactant is under aggregation conditions. It is scarcely soluble in D_2O. In the ^{1}H NMR spectrum, the signals relative to the tails and to one of the NCH_3 groups disappear, while the other head-group signals are well resolved, indicating the presence of large assemblies. This has been interpreted in terms of an aggregate conformation in which different environments are present.[104] The conformational behavior of aqueous micelles of sodium *N*-dodecanoyl-*N*-methyl-glycinate has been shown by ^{1}H and ^{13}C NMR studies. Paramagnetic relaxation data indicate that the micelles of surface polyfluorinated cationic surfactants, $C_nF_{2n+1}CONH(CH_2)_2N^+(CH_3)_3$, have a microstructure, with the fluoroalkyl chain extending straight into the bulk water phase.[47] NMR-induced shifts provide evidence for the chiral discrimination of fructo-oligosaccharides toward amino acid ester salts. The conformation of the saccharide drastically changes from a linear to a pseudo-ring structure with a given cation, such as a chiral organic

ammonium or an alkali metallic ion.[105] It is well known that the ^{1}H and ^{13}C spectra of amides may show two different signals for each of the nuclei when rotation about the amide bond is slow compared to the NMR timescale. The conformation of the two isomers of sodium *N*-dodecyl-*N*-methylglycinate exhibits this behavior. The CH_3 signal appears as two overlapping triplets in the range of micellar concentration. The population of each isomer detected indicates its dependence on aggregation but not on the rotation of the polar group.[106] Isotropic and anisotropic ^{31}P chemical-shift parameters, resonance line shapes and a combination of single-pulse and ^{1}H to ^{31}P cross-polarization spectra, by slow spinning ^{31}P magic-angle solid-state NMR, is effective in identifying and quantifying a variety of inorganic and organic phosphates, from the mobile and immobile inorganic hydroxyapatite-type phosphates to phosphates from κ-casein and the Ca^{2+}-binding phosphoserines from α-(S-1), α-(S-2) and β-casein.[107] Information about the structure of micelles may be obtained by other methods, such as ^{2}H relaxation of selectively deuterated surfactants,[108] and *in situ* NMR imaging using the NOE effect.[109]

A better picture of the relative arrangement of the surfactant molecular chain arrangement in the micelles can be obtained by the 2D NOESY experiment. A conformational change of the alkyl chain of sodium *cis*-7-dodecane-1-yl sulfate is observed upon micellization through the appearance of dipolar interactions between remote protons.[110] A 2D NOESY and relaxation study of the resorcinol-type calix [4] arenes, bearing four alkyl side-chains, suggests that the interaction between the alkyl side-chains in the micelles becomes weak. However, that between the resorcinol ring and the inner alkyl side group is increased with increasing alkyl side-chain length. This shows that the resorcinol protons and those of the side-chains are in close proximity.[111]

Distances between proton pairs of Triton X-100 in aqueous solutions below and above its CMC were calculated according to the intensity dependence on the 6th power of the distance between the proton pairs, r^6. No cross-peaks can be found between the hydrophilic and the remote hydrophobic protons on the 2D map of dilute solution below its CMC (Fig. 3), while significant cross-peaks between these protons exist for the micellar solution (Fig. 4). By comparing with the theoretical results calculated by HYPERCHEM, it was shown that the hydrophilic polyoxyethylene chains in the molecular dispersed state are extended, while in self-aggregation they become coiled, forming a layer thick in dimension and loose in structure surrounding the hydrophobic micellar core with a certain number of water molecules included.[72] Care should be taken in this experiment to ensure that a suitable mixing time is selected so that spin diffusion in the system is avoided and accurate results are obtained for proton distances.[112] Also, the combination with NMR relaxation measurements indicates the participation of the first oxyethylene group, which is next to the phenyl group, in the formation of the rigid surface layer of the hydrophobic micellar core.

The dynamics of surfactant molecules in micelles can also be studied by various NMR methods such as ^{1}H and ^{13}C chemical shift, band shape, relaxation

time, self-diffusion coefficient, 2D NOESY, and ^2H relaxation measurements.[113–129] ^1H NMR spectra of fluorocarbon hybride surfactants show some unusual characteristics. Within the micelle, the rotation of the fluorocarbon chain along the C–C bonds is restricted, causing the two fluorine nuclei in alternating CF_2 groups to have inequivalent chemical shifts. The exchange rate between the monomer and the micellar states is significantly lower than that for common ionic surfactants. The residence time of the CF_3 group in the micelle at the CMC ranges from 3×10^{-5} s for compounds with short chains to 7×10^{-4} s for those with longer chains. The residence time of the CH_3 group in the micelle increases with the total surfactant concentration. The average residence time of the CF_2 group in the micelle is about 3×10^{-5} s and is not very sensitive to changes in surfactant concentration.[114] Solvent spin–spin relaxation measurements indicate that the ethylene oxide segments in the adsorbed layers of $C_{12}E_6$ and $C_{12}E_{25}$ on hydrophilic surfaces have more conformational restrictions than those in polyethylene oxide layers, because of the association of the aliphatic tails.[115] It was found that the plot of the logarithm of the self-diffusion coefficient of $C_{16}E_7$, $C_{14}E_7$ and $C_{14}E_6$ versus logarithm of the concentration gives a straight line, whose slope is in good agreement with a theoretical prediction which takes into account the intermolecular migration of surfactant molecules.[124] Both the ^{14}N relaxation rates and self-diffusion coefficients of a 1 : 1 cetyl pyridinium chloride/sodium salicylate aqueous solution vary smoothly with the surfactant concentration, and, in particular, there is no discontinuity at the phase boundary between the micellar and the cubic phases. It is argued that this fact supports the notion that the microstructure in the micellar region is bi-continuous and resembles the structure in the cubic phase, albeit with no long-range order.[125] Multi-field ^2H spin-lattice and spin–spin relaxation measurements of a cetyl trimethyl ammonium chloride aqueous solution shows that the motion causing the frequency dependence in the NMR relaxation can be described with an exponential correlation function with a correlation time that increases with the size of the spherical micelle.[126] Anisotropic rotational correlation times of salicylate anions in cetyl trimethyl ammonium bromide containing thread-like micelles studied by field-dependent spin-lattice relaxation are found to be in good agreement with those estimated from fluorescence anisotropy measurements.[129]

3.3. Counterion binding

The spatial distribution and dynamics of counterions close to charged micelles are of general interest. In particular, replacing one negatively charged counterion by another is often accompanied by large ion-specific changes in the various micellar properties, as has been known for a long time. The counterion effect on micellization can be elucidated by ^2H and ^{13}C NMR spectra,[130] and that on the aggregation number by ^{35}Cl and ^{14}N linewidth changes.[131] A series of studies are related to the counterion binding by ^1H,[132–136] ^{13}C,[136–138] and ^{19}F,[137,139] chemical-

shift changes and aromatic-induced shift changes,[140] band-shape analysis,[141] self-diffusion coefficient measurements,[138,139,141–145] and field-dependent ^{35}Cl[146] and ^{81}Br relaxation studies.[147] ^{1}H chemical-shift data allow inferences to be drawn about the penetration of aromatic counterions into the head group region of cationic micelles[132,135] and the fractions of micellar-bound organic anion to be measured.[133] More direct information on counterion binding can be obtained from the ROESY experiment[136] and the NMR spectra of the counterions, ^{133}Cs, and the ^{19}F atom of the α-CF_2 group.[137]

3.4. Interaction of water with micelles

The state of the interface between surfactant aggregates and the solvent, which is most often water, has been extensively studied. The interaction between the micellar surface and water has great importance for the properties of surfactant micelles. Early in the 1960s and at the beginning of the 1970s, the behavior of water in solutions of sodium alkyl sulfates was monitored by ^{1}H NMR chemical-shift and spin-lattice relaxation measurements.[148,149] It was found that water does not penetrate into the non-ionic micelles formed by alkyl polyethylene glycol.[150,151] Later, measurements based on the quadrupole relaxation of the water nucleus, ^{17}O,[152–154] and self-diffusion coefficients were used to study the hydration of micellar surfaces.[90,155] Both methods are based on the fact that the measured NMR parameters are population averages of water in the interface and the bulk-phase regions, and the exchange of the two states is fast on the NMR timescale. It is difficult to separate the dynamic and the population information. The use of heteronuclear cross-relaxation between water protons and nuclei of surfactant atoms seems to be promising.[156–160] The average location of water, with respect to octanoate and decanoate polar heads, in a micelle was obtained directly from heteronuclear cross-polarization from water protons to non-protonated carbonyl nuclei of the surfactant. The water–surfactant polar head distance was found to be around 3–4 Å.[159] Because of the large chemical-shift dispersion range, 100% natural abundance, and the large magnetogyric ratio of ^{19}F, ^{1}H–^{19}F cross-relaxation studies between water protons and surfactant fluorines are potentially helpful in estimating the degree of hydration of amphiphile micelles. A small and positive cross-relaxation rate shows that the water residence time in the head group region of a fluoro-surfactant is short. The distance between water protons and the first CF_2 segment is small, indicating strong water penetration to the depth of the first segment of the alkyl chain.[160]

3.5. Reverse micelles

Micelles of amphiphatic surfactant molecules in non-polar solvents have the reverse structure when compared with micelles in aqueous solvents. The polar

heads are packed together to form a central core surrounded by the hydrocarbon tails immersed in the non-polar solvent. The presence of trace amounts of water is considered to be a prerequisite for the formation of reverse micelles. The stability of the reverse micelles is dependent on the nature of the solvent. Most of the NMR studies of reverse micelles have been devoted to the properties of AOT, bis(2-ethyl hexyl)sulfosuccinate, aggregates.[161–166] The dynamic structure of AOT in reverse micelles has been studied by ^{13}C spin-lattice relaxation, and ^{13}C $\{^1H\}$ NOE of the individual carbon atoms of each 2-ethyl hexyl chain of AOT; NOESY and ROESY have been used to investigate the spatial proximity of the 2-ethyl hexyl chains.[162] The magnitude of the difference in ^1H chemical shifts shows that AOT interacts more strongly with 1,2-ethanediol than with water in n-heptane.[163] The ^1H NMR chemical shift of solubilized H_2O–D_2O mixtures has been measured as a function of the deuterium content of the aqueous nanodroplet. These data were used to calculate the so-called 'fractionation factor' of the aggregate-solubilized water, the value of which was found to be unity. This shows that, although different from bulk water, the aggregate-solubilized water does not seem to coexist in layers of different degrees of structure.[165] The effect of the electrolytes NaCl, $NaNO_3$, $MgCl_2$, and $AlCl_3$ on the water solubilized by AOT micelles was examined by ^1H NMR. Two types of water were found, water bound directly to the ionic head groups of the surfactant, and water interacting with the hydrated head groups in swollen micelles through hydrogen bonds.[166] ^1H NMR investigations of the chemical shifts of the surfactants dodecyl ammonium propionate, dodecyl ammonium benzoate and dodecyl ammonium butyrate, as a function of the concentration of 2,3,4,6-tetramethyl-α-D-glucose in benzene and cyclohexane, provide information about strong interactions between the hydrophilic groups of the micellar surfactants and the 2,3,4,6-tetramethyl-α-D-glucose molecules solubilized in the core of the reverse micelle.[167] An inversed micelle-like structure in which the hydrophobic ethyl groups form a sheath largely restricting access to the hydrophilic Mg-6(Et_2NCO_2) has been characterized by ^1H and ^{13}C NMR spectroscopy. It was shown that the helical structure is maintained in solution. The intramolecular dynamics of this compound, relating to motions of the ethyl group, are substantially hindered in solution. This is the result of a combination of hindered rotation about the carbamato C–N bond and efficient packing of the ethyl groups around the micelle core.[168] The sphere–rod–sphere transition of polymer-like reversed micelles formed in a soybean–water–perdeutrated cyclohexane system has been demonstrated by the measurement of the NMR self-diffusion coefficient of water as a function of concentration.[169] The interaction between dipyridamole and the cationic surfactant cetyl trimethyl ammonium chloride was studied by proton chemical-shift and spin-lattice relaxation data. The results showed that dipyridamole incorporates into the polar region of the reverse micelles of cetyl trimethyl ammonium chloride in chloroform, influencing the packing and dynamics of the surfactant head groups. In contrast, in aqueous cetyl trimethyl ammonium chloride micelles, the

preferential location of pyridamole is inside the non-polar micelle core, and the binding constant is two orders of magnitude above that for the reverse micelle.[170]

4. SOLUBILIZATION

The capacity of aqueous surfactant aggregates to incorporate solutes is the reason for the widespread use of such systems in industrial, biological, pharmaceutical and synthetic chemical applications. Owing to the variety of applications, the investigation of the solubilization properties of surfactants has attracted the interest of many researchers for a long time. Knowledge on the nature of solubilization and the chemical and physical properties of the solute is of fundamental importance.

Solubilization of alcohols in anionic and cationic micelles has been studied by NMR self-diffusion coefficient, multi-field ^{2}H and ^{13}C relaxation, and paramagnetic relaxation measurements.[171–174] Solubilization equilibria for a homologous series of alcohols in SDS micelles in D_2O solution at 25°C were determined from the self-diffusion coefficient.[171] The data on the self-diffusion coefficient show that the addition of propanol to SDS caused an increase in the self-diffusion coefficient of SDS, and a decrease in that of propanol. This corresponds to a change in micellar shape from ellipsoidal to small spherical aggregates. Addition of butanol causes a change in micellar shape from ellipsoidal to worm-like. Addition of pentanol causes decreases in the self-diffusion coefficients of both the surfactant and the alcohol. This gives information about the solubilization of pentanol in the SDS micelles.[172] Analysis of the ^{2}H and ^{13}C multi-field relaxation data shows that the addition of alcohols and oils decreases the degree of aggregation.[173] The partition coefficients of two isomeric alcohols, 1,2- and 1,6-hexanediols, in SDS and dodecyl trimethyl ammonium bromide micellar aqueous solutions have been determined by paramagnetic relaxation.[174] Solubilization of pentanol and decanol in sodium octanoate,[175] and the alkyl chain order in the sodium *p*-octyl-benzenesulfonate—short-chain alcohol—water systems, were determined by ^{13}C and ^{1}H NMR spectroscopy.[176] The 2D NOESY technique was found to provide deeper insight in terms of the solubilization of molecules in the interior of micelles. Significant positive cross-peaks between protons of the SDS micelle and those of the solubilizates (1-butanol and benzene) as well as between the protons of benzene and dodecyl trimethyl ammonium bromide micelle protons were observed in the 2D NOESY map. This correlates well with the expected results.[177]

Information concerning solubilization of hydrocarbons in ionic surfactant micelles was obtained from ^{2}H NMR relaxation and ^{1}H NMR paramagnetic relaxation measurements. The location of the hydrocarbons (benzene naphthalene, triphenylene cyclohexane, cyclododecane and *tert*-butylcyclohexane) in micelles

of alkyl trimethyl ammonium bromides and alkyl pyridinium halides was investigated by determining the aromatic ring current-induced ^1H chemical shift along the surfactant alkyl chain and by comparing the spin-lattice relaxation enhancement of the hydrocarbons and the surfactant alkyl chain, induced by Mn^{2+} on the micellar surface. It was shown that the unsaturated hydrocarbons reside near the polar head groups of the cationic surfactant micelles, but are evenly distributed in the micellar core of the anionic micelles, and the saturated hydrocarbons reside in the interior of the micellar core.[178] Field-dependent ^2H relaxation measurements show that solubilization of cyclohexane, cyclo-octane, cyclodecane, *trans*-decaline, n-hexane, 2,3-dimethyl butane and adamantane in small amounts causes the cetyl trimethyl ammonium bromide micelles to grow. Further addition causes a decrease in aggregation size. n-Octane, n-decane and n-dodecane cause a decrease in micellar size even in small amounts. Owing to the presence of solubilizate, the rod-like micelles grow in the axial direction at a constant radius, while the decrease in size at higher solubilizate content occurs as a shortening of the rods accompanied by an increase in radius.[179]

Solubilization of aromatic compounds in cationic micelles has been intensively studied.[93,180–187] The aromatic solubilizates, benzene and bromobenzene, are localized to a large extent in the cetyl pyridinium chloride micelle–water interface, as shown by the change in ^1H chemical shift.[180] The predominating solubilization mechanism for benzene, *N,N*-dimethylaniline and nitrobenzene involves adsorption at the micelle–water interface, whereas isopropyl benzene and cyclohexane are preferentially solubilized in the hydrocarbon part of the micelle.[181] The medium effects of water, n-hexane, acetonitrile and dimethylsulfoxide on the ^1H chemical shift of benzene solubilized in sodium decanoate, and poly-oxyethylene lauryl ether micelles have been observed.[182] Solubilization sites of a series of aromatic optical probes, acridine, 1-methylindole, and benzophenon, in cationic cetyl trimethyl ammonium bromide, anionic SDS, and non-ionic Brij-58 surfactant micelles by chemical shifts show that the solubilizates are preferentially positioned in the polar-head region of these micelles. Hence these probes sense and monitor not the micellar interior but the head-group–water interface.[183] Shape changes of the cationic micelles upon solubilization of aromatic compounds and counterions have been studied by ^2H field-dependent relaxation,[93] ^1H spin-lattice relaxation,[184] and ^1H, ^{13}C and ^{14}N chemical-shift variations,[185] respectively. Field-dependent ^2H NMR relaxation of cetyl trimethyl ammonium bromide deuterated at the α-carbons suggests that the micelles are slightly elongated even before benzene addition, and become longer and more poly-dispersed after the addition. Above a particular amount of benzene addition, the surfactant relaxation data suggest no further elongation but radial growth, while the benzene relaxation shows that a large proportion of the benzene is residing in the interior region with near-bulk characteristics.[93] ^1H spin-lattice relaxation studies show that 2,6-di-*tert*-butyl-4-methylphenol and 2-*tert*-butyl-4-methoxyl phenol in cetyl trimethyl ammonium bromide and chloride micelles enhance the counterion binding to the micelles.

Although they do not induce shape changes of the chloride micelles, they do increase the concentration of the bromide ion at which a shape change is known to occur in the absence of any additives. The low-frequency shift is most significant for the protons near the polar heads, which suggests that the solubilizates are located in the head-group region.[184] According to the relaxation time values of cetyl trimethyl ammonium salts of different anions—bromide, chloride, nitrate, methylsulfonate, and sulfate—a conclusion has been drawn that a small reduction in the size of the micelles occurs due to the addition of benzene to the various micelles. At low concentrations of benzene, it displaces the water molecules which are closer to the first portion of the surfactant aliphatic chain; once this location has been saturated, the aromatic solute displaces the deeper water, as shown by the change in chemical shift in the ^{1}H NMR spectra.[185] The study of solubilization of organic perfume molecules with different degrees of hydrophilic and hydrophobic characters in SDS micelles by ^{1}H chemical-shift changes shows that the addition of phenolic compounds (phenol, 4-methylphenol, 4-allyl-2-methoxyphenol, anisole, 4-methylanisole, and 4-propenylanisole) causes the unresolved methylene protons of SDS to split into a broad doublet with uneven intensities depending on the concentration of the substrate.[186] ^{1}H chemical-shift experiments on aromatic carboxylic acids incorporated in cationic micelles show that the aromatic carboxylate ions are near the micellar surface, with the aromatic ring between adjacent quaternary ammonium head groups, while the non-dissociated carboxylic acids penetrate more deeply into the micelle. The association of aliphatic carboxylate ions, with cetyl trimethyl ammonium bromide micelles, increases with their chain length.[187] 2D NOESY NMR experiments result in more direct evidence about the solubilization sites at a molecular level. In an aromatic solubilizate–cholate system of bile salts, intra- and intermolecular interactions have been detected.[188] The ability of micellar solutions to incorporate solubilized material is one of the fundamentally important properties of micelles and provides a basis for the widespread use of surfactants and micellar solutions. NMR studies of solubilization have primarily focused on elucidating the nature of the interactions between the solute and the micelles, or on the location of the solubilized species, as mentioned above. The solubilities of benzene in cetyl and dodecyl trimethyl ammonium bromides were measured by following the peak intensities.[189] The NMR paramagnetic relaxation method, using the 3-carboxypropyl anion as the relaxation agent for anionic micelles, has been developed as an alternative procedure for the determination of the distribution coefficients of solubilizates in micellar systems,[190] solubilization equilibria for anionic micelles,[191] and solubilization and aggregation numbers in micellar mixtures of anionic and cationic surfactants with solubilized tetraethylene glycol and tetraethylene glycol dimethylether.[192] The use of paramagnetic relaxation in the solubilization systems (1-methyl-4,4-bipyridinium reporter ion in SDS and TEMPO and TEMPOL in dipyridamole) provides location information.[193,194] The ^{1}H aromatic ring current effect was utilized in the study of solubilization of aromatic

compounds (benzene, naphthalene, acridine, and pyrene) in aggregates of poly(maleic acid-co-butyl ether) and dodecyl trimethyl ammonium bromide. The aromatic molecules are primarily solubilized near the head groups of dodecyl trimethyl ammonium bromide in the aggregates of dodecyl trimethyl ammonium bromide and polymaleic acid-co-butyl vinyl ether. Very small ring current-induced ^1H chemical shifts on the polymer alkyl side-chains are observed upon solubilization of the aromatic molecules, indicating that the polymer side-chain is probably not close to the head groups of the surfactants.[195] This aromatic ring current effect has also been used in the study of the adsorption of a metal-chelating agent at a micelle–water interface to determine the site of solubilization of the free ligand 7-(4-ethyl-1-methyl)-8-hydroxyquinoline and its metal complex in the host $C_{12}E_8$ micelles. At the core–water interface, the metal complex favors the more hydrophobic region of the micelles.[196] ^1H chemical shift–concentration plots of a series of synthetic amphiphiles, which have rigid planar structures with one polar face and one non-polar face, show that they are proportional up to a very high concentration, indicating the presence of intermolecular interactions. The changes in chemical shift with increasing concentration are gradual, which indicates that these aggregation processes do not correspond to the classical models of micelle formation. The results show that the azo dye orange OT does not solubilize in these micelles when no side-chains are attached to the rigid planar structure.[197] The association of guest molecules in aggregates of a modified cyclodextrin has been investigated for four different sparingly water-soluble molecules and an anionic surfactant, SDS. The binding and spatial proximities have been determined for these different guests by NMR (NOE pumping). Three pulsed magnetic field gradient NMR sequences were used in addition to the normal proton sequences. The standard bipolar pulse stimulated-echo experiment was used in order to evaluate the type of interaction that occurs between the micelles and the guest molecules.[198] NMR studies of the solubilization of relatively hydrophobic organic compounds (chloroform, chlorobenzene, methyl cyclohexane, benzene, toluene cyclohexane, and hexane) by the core of poly(methyl methacrylate)-block-poly(arylic acid) micelles show that the core-captured amount of the solubilizate, and its solubilization rate, chiefly depend on its interaction with poly(methyl methacrylate).[199] ^{13}C NMR was used to obtain the absolute number average molar mass and overall composition on the solubilization of alkyl cyanobiphenyls in aqueous solutions of a di-block copolymer of propylene oxide and ethylene oxide.[200]

5. INTERACTIONS OF MICELLES

The study of structures and properties of mixed micelles formed from different types of surfactants and surfactants with biological compounds and with polymers, by various methods, is a topic of intense research.

5.1. Interactions between micelles of different types of surfactants and organic compounds

Mixtures of surfactants, rather than individual surfactants, are widely used in many applications. In some cases, the commercial surfactants are mixtures of surface-active agents, due to the non-homogeneity of the raw materials. Specially mixed surfactant systems exhibit better properties than those obtainable from any of the individual surfactants. Although this behavior of the mixing systems has been utilized extensively, the mechanism of this synergism remains unclear. Therefore, interactions between the mixed surfactants are of fundamental interest. In ideal situations, the surfactant head groups do not interact significantly, and mixed micellization is driven by the hydrophobic interaction of alkyl chains of the surfactants. This approach is valid in handling binary nonionic and binary ionic surfactants.

^{1}H chemical-shift changes on co-micellization of linear alkyl benzenesulfonate and oleate show that the α-CH_2 protons of oleate are shielded due to the ring current of the aromatic group of the linear alkyl benzenesulfonate, while no change occurs in the linear alkyl benzenesulfonate spectrum due to co-micellization, although upon self-aggregation of the linear alkyl benzenesulfonate the *meta*-protons show a shift of 0.25 ppm to low frequency, and the *ortho*-protons remain unchanged.[201] ^{13}C NMR experiments show that sodium linear alkyl sulfonate co-micellizes with sodium laurate at concentrations close to the CMC of the two surfactants. In the mixed micelles, the oleate molecules loop back and adopt a bent conformation.[202] Binary mixtures of fluorocarbon–hydrocarbon surface-active agents have been examined by a combination of ^{1}H and ^{19}F NMR spectroscopy over a range of fluorocarbon–hydrocarbon ratios. From the chemical-shift data of ammonium perfloro-octanoate and ammonium decanoate, it has been possible to elucidate the micelle composition as a function of total surface-active agent concentration. The experimental results show that the mixing of hydrocarbon and fluorocarbon is non-ideal and unfavored.[203] A similar approach has been used in the study of counterion effects on the micellar structures formed by tetraethyl ammonium and lithium perfluoro-octylsulfonates.[204]

Interactions between oppositely charged micelles in aqueous solutions spontaneously form vesicles. The self-diffusion coefficient of water and ^{2}H relaxation of ^{2}H-labeled dodecyl trimethyl ammonium chloride of the dodecyl trimethyl ammonium chloride–sodium dodecyl benzenesulfonate systems show that in these mixtures there is limited growth of the micelles with changes in composition. The vesicles abruptly begin to form at a characteristic mixing ratio of the two surfactants. The transition is continuous.[205] Transformation from micelle to vesicle in dodecyl trimethyl ammonium chloride–sodium perfluorononanoate aqueous solution has been studied by self-diffusion coefficient measurements, and it was found that at a concentration of 35 wt% with a molar ratio of 1 : 1, the self-diffusion coefficient of the mixed micelles is far smaller than that of the two individual micelles.[206] The characteristics of mixed surfactant

systems of sodium perfluoro-octanoate with non-ionic (*N*-triethoxylate heptanyl amide), zwitterionic (3-dodecyl dimethyl ammonio-1-propanesulfonate), and cationic (octyl trimethyl ammonium bromide) hydrocarbon surfactants have been followed by ^{1}H and ^{19}F chemical-shift changes. In the perfluoro-octanoate–*N*-triethoxylate heptanyl amide and the perfluoro-octanoate–3-dodecyl dimethyl ammonio-1-propanesulfonate systems, only one type of mixed micelle was formed, with a non-ideal large negative deviation, while in the perfluoro-octanoate–octyl trimethyl ammonium bromide system, the CMC was tremendously reduced upon mixing. The results suggest that the mixed surfactants coagulate to form large aggregates.[207]

Mixed micelles of non-ionic ($C_{12}E_5$, $C_{12}E_8$)–anionic (SDS) and cationic (dodecyl trimethyl ammonium chloride) surfactants have been studied by self-diffusion coefficient and ^{1}H relaxation measurements.[208,209] The results show a good correlation between the self-diffusion coefficient and the linewidth measurements. A minimum of the self-diffusion coefficient versus mole fraction of $C_{12}E_5$ curve occurs at a concentration of 20% of SDS; after that, the self-diffusion coefficient increases. The appearance of the minimum was attributed to repulsion between micelles and an increase in the self-diffusion coefficient corresponding to a decrease in micellar size. The observed decrease in the self-diffusion coefficient as one starts to replace the non-ionic by ionic groups is mainly due to an increase in micelle–micelle repulsion. Hence, a diffusion mechanism in which monomers can be exchanged between different aggregates is partly inhibited. The increase in self-diffusion coefficient occurring at higher fractions of ionic surfactant is shown to be due to a decrease in micellar size. Small additions of ionic surfactant dramatically increase the cloud point temperature, but negligibly affect the observed self-diffusion coefficient.[208] The phase separation model of micellization and the regular solution approximation have been used to explain the non-ideal behavior of the mixing of the cationic cetyl trimethyl ammonium bromide with a series of non-ionic surfactants with different poly-oxyethylene chain lengths. The molecular interaction parameter β of these systems exhibits negative values. The longer the poly-oxyethylene chain, the smaller the β value. This shows that the interaction is stronger, and hence the mixed micelles are more stable between cetyl trimethyl ammonium bromide and the non-ionic surfactant with longer hydrophilic chains than that with shorter hydrophilic chains. With the increase in the mole fraction of cetyl trimethyl ammonium bromide, the β value increases and the mixed micelles become less stable, due to the repulsion of the head groups of cetyl trimethyl ammonium bromide. ^{1}H NMR chemical-shift measurements show changes in the positions of the characteristic peaks due to various functional groups in mixed systems of cetyl trimethyl ammonium bromide with Brij-30 and Brij-35, respectively. The peak position of the trimethyl groups as well as that of the poly-oxyethylene groups show considerable low-frequency shifts as a function of the mole fraction of cetyl trimethyl ammonium bromide. In all cases, the micellar structures are loosened by the mutual coulombic repulsions of the ionic

head groups. As to the structure and relative arrangement of the chains in the mixed micelles, the following conclusions were drawn from the chemical-shift change experimental data: (i) the hydrophilic groups of cetyl trimethyl ammonium bromide are extended so that they can also interact with the oxyethylene units remote from the hydrocarbon chains; and (ii) the oxyethylene units are not only restricted to the polar phase, but some of them are extended into the hydrocarbon phase of the micelle.[210] Mixed micellization of non-ionic (Triton X-100 and Tween-40) and anionic surfactants (sodium decyl sulfate, dodecyl sulfate and tetradecylsulfates) has been studied by the paramagnetic-induced ^1H relaxation of water. The results show that the relaxation time of water decreases due to the formation of mixed micelles. The sulfate counterion cannot bind to the mixed micelle at a ratio of anionic to non-ionic equal to 1 : 2, probably due to the blocking effect of the poly-oxyethylene chains.[211] A detailed analysis of the self-diffusion coefficient data has been made for the micellization of anionic (SDS) and non-ionic ($C_{10}E_5$ and lauryl amidopropyl betain) surfactants. The composition of the mixed micelles is evaluated by using the pseudo-phase-separation model, which is based on the approximation of regular solutions. The use of this approximation results in a set of relationships between CMC, composition of mixed micelles, surfactant unimer concentration, and interaction parameter, β, which shows the strength of the interactions within the micelles. The analyzed results show that SDS and $C_{10}E_5$ are ideally mixed, while the mixing of SDS with lauryl amidopropyl betain shows a discrepancy from ideal mixing.[212] Although it has been shown by small-angle neutron scattering that the mixing of SDS with $C_{12}E_6$ deviates from the predictions of regular solution theory, the solution is ideal. This can be rationalized in terms of the increase in ion zero excess entropy in mixing, due to the stronger interaction between SDS molecules within the micelles, which results in greater packing constraints and the possibilities of changes in hydration.[213]

As shown in previous studies, the use of only one NMR parameter to elucidate a complex system, such as mixtures of surfactants in an aqueous solution, provides limiting results. The combination of several NMR techniques, such as ^1H chemical-shift changes, spin-lattice and spin–spin relaxation, and especially the 2D NOESY experiments, gives a clearer insight into the microstructure of the mixed micelles. A mixture of a binary surfactant system containing two well-known surfactants, Triton X-100 (*p-tert*-octyl phenyl poly-oxyethylene ether) as the non-ionic surfactant and cetyl trimethyl ammonium bromide as the cationic surfactant, was chosen to examine the dynamic properties of the surfactant molecules and their relative arrangement in the mixed micelles. Resonance peaks of protons on the hydrophobic hydrocarbon chain of cetyl trimethyl ammonium bromide shift to low frequency as the fraction of Triton X-100 increases in the solution. The extent of the shift is highest for the proton resonance of the methylene group nearest to the N atom of the polar head of cetyl trimethyl ammonium bromide. This effect decreases upon going further to the hydrophobic end. The resonance peak of the protons on the trimethyl group is

significantly less influenced by the aromatic ring effect exerted by the Triton X-100 molecules. On the other hand, the resonance peak of the aromatic protons of Triton X-100 shift to high frequency when the fraction of cetyl trimethyl ammonium bromide increases, suggesting that the Triton X-100 molecules are continuously separated by cetyl trimethyl ammonium bromide molecules in the mixed micelles. Spin–spin relaxation measurements show that the Triton X-100 molecules are less closely packed in the mixed micelles than in its self-aggregated ones, but the inverse is observed for the cetyl trimethyl ammonium bromide molecules. This suggests that the mixed micelles are loosened as compared with the Triton X-100 micelles and tightened as compared with the cetyl trimethyl ammonium bromide micelles. The increase in spin–spin relaxation time of the hydrophilic poly-oxyethylene protons is attributed to a change in the conformation of these chains by mixing with cetyl trimethyl ammonium bromide. 2D NOESY experiments of this mixed system are shown in Fig. 5 to give direct information about the interactions among the molecules of the two surfactants inside the mixed micelles. Comparing the inter-proton distances of these Triton X-100–cetyl trimethyl ammonium bromide mixed micelles with those of the self-aggregated Triton X-100 micelles,[66] one can notice that in the mixed system Triton X-100 molecules are separated from each other as if they were in the single molecular state of dilute solution at a concentration below the CMC. However, the fact that the ratio of the spin–spin relaxation time to the spin-lattice relaxation time of the protons of the mixed molecules is much less than unity indicates that these molecules are in the aggregate state. The appearance of the cross-peaks between hydrophilic protons of the two surfactants, the trimethyl protons of cetyl trimethyl ammonium bromide and the protons of the first oxyethylene group next to the phenoxy group of Triton X-100, is direct evidence that the trimethyl groups of cetyl trimethyl ammonium bromide are located between the first oxyethylene groups next to the phenoxy rings of Triton X-100. The appearance of cross-peaks between the hydrophobic protons of the two surfactants, the end methyl protons of both of the surfactants, is strong evidence for the interaction between the two surfactant molecules within the hydrophobic micellar core. It also suggests that the hydrophobic chains of cetyl trimethyl ammonium bromide are bent upon mixed micellization, as in the case of the micellization of sodium *cis*-7-dodecane-1-yl sulfate.[188] The intensities of the cross-peaks between the hydrophilic protons and the remote hydrophobic protons of Triton X-100 gradually decrease with an increase in the fraction of cetyl trimethyl ammonium bromide in the mixed solution, suggesting that the poly-oxyethylene chains gradually extend to leave space for the trimethyl groups of the cetyl trimethyl ammonium bromide attached to the polar head, because they are not involved in the hydrophobic micellar core. This result strongly supports the possible conformational change of the hydrophilic poly-oxyethylene chains of Triton X-100 upon mixed micellization with cetyl trimethyl ammonium bromide deduced from the relaxation measurements.[214] A more complete picture of the mixed micellization

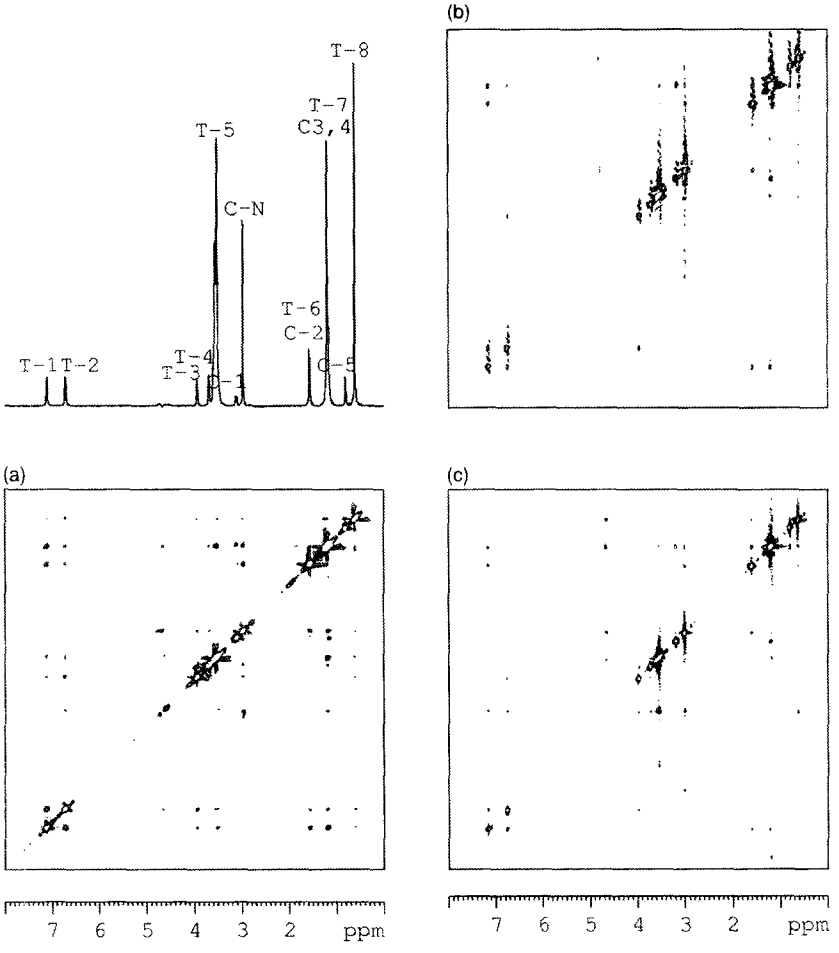

Fig. 5. Contour plots of the 2D NOESY measurements of the Triton X-100 (T) and cetyl trimethyl ammonium bromide (C) mixed aqueous solutions with molar ratios of C/T = 0.5 (a), 1.2 (b), and 1.6 (c), and with a mixing time of 100 ms. T-1 to T-8 correspond to peaks 1–8 in Fig. 3, respectively. C–N is the peak of protons of the trimethyl group attached to the nitrogen atom of cetyl trimethyl ammonium bromide, C-1 is the peak of the α-protons of the hydrophobic chain, C-2 the β-protons, C-3,4 the γ- and the unresolved polymethylene protons, and C-5 the methyl protons of the hydrophobic chain of cetyl trimethyl ammonium bromide. (Reprinted with permission from ref. 214, Copyright 2001 American Chemical Society.)

of Triton X-100 with cetyl trimethyl ammonium bromide will be obtained after obtaining self-diffusion coefficient data of the mixed surfactant system analyzed by the phase separation model to determine the CMC, the mixing parameter β, the composition, and the size of the mixed aggregates. The same approach has been used to study the mixed micellization of Triton X-100 with anionic

surfactant, SDS, in their aqueous solution. Cross-peaks between the hydrophobic protons of SDS and those of Triton X-100 appear in the 2D NOESY map of their mixed solution, suggesting that the hydrophobic chains of the two surfactants are in close proximity, i.e. they are mixed in the hydrophobic micellar core. The effect of the aromatic ring currents of Triton X-100 on the chemical shift of the protons of the methylene groups nearest to the polar heads of SDS molecules shows the near vicinity of these groups and the phenyl rings of Triton X-100. In contrast to the case of the mixed micellization of Triton X-100 with cetyl trimethyl ammonium bromide, the intensities of the cross-peaks between the hydrophilic and hydrophobic protons of Triton X-100 on the 2D NOESY map do not show any remarkable changes with an increase in the fraction of SDS in the mixed solution. This suggests that the hydrophilic chains of Triton X-100 remains coiled in mixing with SDS which has a smaller polar head than cetyl trimethyl ammonium bromide.[215] A similar steric-hindrance effect on the conformational change of the hydrophilic poly-oxyethylene chains of a non-ionic surfactant, Brij-35, with a longer hydrophilic chain than that of Triton X-100, has been observed by mixing with the cationic surfactant, cetyl trimethyl ammonium bromide, while mixing with SDS does not show this effect.[216]

The strong cross-relaxation between the crown heads and the methyl groups in tails of dodecyloxymethyl-18-crown-6 evident in the 2D NOESY spectra suggests that dodecyloxymethyl-18-crown-6 and K^+ chelated molecules form a pseudo-interdigited structure at low temperature.[217] The binding of halothane on SDS micelles has been studied by paramagnetic relaxation of ^{19}F to simulate the interaction of the anesthetic molecules with macromolecular surfaces; a paramagnetic anion, 3-carboxyl-proxyl, was used. It stays mainly in the aqueous phase, due to electrostatic repulsion.[218] NMR self-diffusion coefficient measurements of the mixed micellization of SDS with a sugar-based non-ionic surfactant, dodecylmalono-bis(*N*-methyl glucamide), show that the mixing is ideal and non-cooperative. The composition of the mixed micelles is the same as that in solution.[219] The behavior of atrazine, a compound containing fluorine, in humic micellar solutions differs markedly from that in SDS micellar solutions, in the capacity to absorb solvents and in the effect of these solvents on the ^{19}F chemical shifts of atrazine within the solvent-swollen micelles. Atrazine forms strong cooperative hydrogen bonds when adsorbed within humic hydrophobic domains. Polar, hydrogen bond donor or acceptor, solvents can dissociate atrazine from humic molecules above a critical threshold, but non-polar aprotic solvents seem unable to overcome the strong interactions that bind atrazine to humic molecules.[220] ^1H chemical-shift measurements show that water-soluble anionic dyes, Remazol Red F 3B and Remazol Brillant Yellow GNL, form mixed micelles with different types of surfactants, such as SDS, dodecyl trimethyl ammonium bromide, octyl phenol nonaoxyethylene ether, and dodecyl dimethyl aminopropylsulfonate.[221]

Aqueous micelles affect the rate and equilibria of chemical reactions that occur in the micellar interfacial region. An understanding of the nature of this

region and the forces that come into play therein is of prime importance for a better understanding of micelle-mediated phenomena. Cationic surfactants are suitable for this purpose, because the properties of their self-aggregates can be manipulated by varying the counterion and the length of the hydrophobic chain, and consequently the microstructure of the hydrophilic group. Results of ^1H NMR chemical-shift measurements of both the surfactant and of the mixed compounds confirm that 2,6-diphenyl-4-(2,4,6-triphenyl-1-pyridinio)-1-phenolate and 2,6-dichloro-4-(2,4,6-triphenyl-1-pyridinio)-1-phenolate are located in a less polar environment than hydrophilic 1-methyl-8-oxyquinolinium betaine and sodium 1-methyl-8-oxyquinolinium betaine 5-sulfonate.[222] ^1H chemical-shift changes of dodecyl dimethyl ammonio propanesulfonate micelles show that the micellar rate effects are not due to changes in micellar structure. Non-ionic micelles of the Brij family modestly speed up cyclization of 2-((3-helopropyl)-oxy)-phenoxide ions, but the reaction appears to be in the water with palisade layer of the micelle in conditions such that the distinction between aqueous and micellar pseudo-phases is uncertain.[223] The origin of viscoelasticity in micellar solutions of cetyl trimethyl ammonium bromide and sodium *ortho*-hydroxybenzoate has been followed by the chemical-shift changes of the protons of the benzoate. The chemical-shift changes imply that *ortho*-hydroxybenzoate ions are embedded in the cetyl trimethyl ammonium bromide micelles in an orientation that allows the formation of entangled chains of micelles leading to a gel-like structure, but *meta*-hydroxybenzoate cannot form this structure with cetyl trimethyl ammonium bromide. The signal of cetyl trimethyl ammonium bromide is very broad, while that of water is narrow, showing that the viscoelasticity of the solution is not introduced by the solvent.[224] Analysis of the induced ^1H chemical shift proves that the β-cyclodextrine is located preferentially on the docosane 1,22-bis-(trimethyl ammonium bromide) surfactant chain, with the cationic heads scarcely involved in the complex.[225] The microstructure of sodium cholate–β-cyclodextrin has also been obtained by ^1H chemical-shift measurements.[226] Mixed micelles of sodium cholate and deuterated SDS were studied by ^2H relaxation and self-diffusion measurements. Distributions of the two surfactants in various environments, and interaction parameters, were determined.[227] An NMR self-diffusion study of the interaction between sodium hyaluronate and tetradecane trimethyl ammonium bromide revealed that several hyaluronate chains form a complex with tetradecane trimethyl ammonium bromide. The tetradecane trimethyl ammonium bromide micelles may act as bridging points between and within the sodium hyalurate chains.[228] The phase transition of dodecyl amino oxide–SDS in the presence of perfluoro-octanol from micelle to lamellar and to reverse micelle has been characterized by ^2H NMR.[229] Porphyrins and porphyroids are known to localize in tumor tissues and are therefore of great interest to the medical and pharmaceutical industries. Despite their potential applications in medicine and pharmacy, little is known about the reason for their propensity to accumulate in tumor tissues, or the mechanism of their uptake and delivery into the cell. A ^1H

NMR study of *meso*-tetrakis-(1-methyl pyridinium-4-yl)-porphyrin with SDS and Triton X-100 indicates that it interacts with SDS and exists as monomeric entities in the anionic SDS micelles. No interaction is observed with cetyl trimethyl ammonium bromide and Triton X-100. The intercalation appears to be due to coloumbic rather than hydrophobic interactions.[230] Interactions of water-insoluble mono-*para*-phenyl-substituted tetraphenyl porphyrins with tetradecane trimethyl ammonium bromide, SDS and Triton X-100 have been studied by ^{1}H and ^{13}C NMR spectroscopy in detail.[231]

5.2. Interactions between micelles and biological compounds

Peptide–micelle interactions are often exploited in the chromatographic analysis of complex mixtures, so an accurate knowledge of peptide–micelle association constants is essential for a thorough understanding of the separation mechanism in these techniques. NMR self-diffusion coefficients of the dipeptides leucine enkephalin and D-(Ala)-leucine enkephalin were measured in free solution and in the presence of SDS micelles. The mole fraction of peptide molecules associated with SDS micelles, and the peptide–micelle association constants, K_{eq}, calculated from these data, show that only Phe-Leu associates strongly with the micellar aggregates, with $K_{eq} = 69 \pm 6\,M^{-1}$. Tyr-Gly, Tyr-Ala, Gly-Gly and Gly-Phe exhibit little to no micelle binding. The equilibrium constant of Tyr-Leu is one-quarter that of Phe-Leu. Micelle-induced changes in peptide conformation and peptide hydrophobicity both play important roles in governing peptide–micelle binding.[232] A molecular dynamics simulation study of an adrenocorticotropin hormone by NOE distance restraints showed that the hormone lies on the surface of the SDS micelle. Most of the hydrophobic interactions come from the side-chains of Met-4, Phe-7 and Trp-9. The peptide bonds are either hydrated or involved in intramolecular hydrogen bonding with the SDS hydrophilic head groups. The time correlation functions of the N–H bonds of the peptide, except for the N- and C-termini, are significantly reduced when partitioned in the micelle. *Trans–cis* isomerism at all three proline sites is found in the 11–14 segment of the peptide. The population of *cis*-isomers varies with the environment of the peptide. The presence of dodecyl phosphocholine micelles does not change the *trans–cis* equilibrium in the 11–24 segments from that in water. Intermolecular NOE correlations between the hormone and the micelles are observed only in the 1–10 segments of the peptides, and the hydrophobic side-chains contribute to the intermolecular NOE. The interactions between these peptides and the micelles are via a surface-binding mode, with most of the interactions involving the hydrophobic side-chains.[233,234] Neuropeptides interact with lipid vesicles in a manner similar to a biological membrane, with electrostatic interactions between them providing a mechanism for concentrating the peptide at the surface of the vesicles, followed by hydrophobic interactions between the peptide and the cores of vesicles. 2D

NMR, self-diffusion coefficient measurements and molecular modeling of the SDS micelle and neuropeptide systems show that electrostatic and hydrophobic interactions between the micelle and neuropeptide are completely independent of one another.[235] The structures of peptides (H5 peptide (427–452) and cell-penetrating peptide transportan) bound to SDS micelles have been studied by 1D and 2D ^{1}H NMR.[236–238] Cholinergic anabasine (3,4,5,6-tetrahydro-2,3′-bipyridine), when added to aqueous SDS solution, binds to the SDS micelles and undergoes a change in the position of its ring-chain hydrolysis equilibrium constant. This has been followed by ^{1}H NMR. The ^{1}H signals of anabasine in water show it to exist in two ring-chain tautomeric forms. Each gives rise to a family of clearly separated and easily identifiable signals in rapid equilibrium, the open-chain ammonio ketone and the cyclic iminium ion. The ammonio ketone is generated from the iminium ion on hydrolysis of the imine bond.[239] ^{2}H relaxation of specifically deuterated SDS in bovine serum albumin gels shows that the spin-lattice relaxation rates in the albumin solution and in the gel are similar, but the spin–spin relaxation rate is very high, suggesting slow motions of the SDS molecules bound to large aggregates.[240] ^{1}H spin-lattice relaxation measurements of water in a mixed micelle solution of Triton X-100 and dimyristoyl-phosphatidylcholine confirms that water does not penetrate the hydrophobic core of the mixed micelle, but water does solvate the polar oxyethylene and choline methyl group. ^{13}C chemical-shift, relaxation and linewidth measurements show that the presence of phospholipids in mixed micelles does not affect the microenvironment or motional behavior of Triton X-100 micelles.[241,242] Binary mixtures of alkyl poly-oxyethylene ethers ($C_{10}E_8$ and $C_{12}E_8$) with sodium taurocholate and sodium taurodeoxycholate, 1,2 dimyristoyl-*sn*-glycero-3-phosphocholine having perdeuterated acyl chains, have been studied by chemical-shift, and ^{1}H and ^{2}H relaxation measurements. The following results were obtained: the composition of the mixed micelle changes with the mole fraction of the bile salt; the polarity of the intramicellar interior for sodium taurocholate was more hydrophobic than that of sodium taurodeoxycholate; $C_{12}E_8$ causes a reduced-order parameter and an increase in the conformational freedom of the phospholipid acyl chain; and the fraction of ordered phospholipid chains decreases with increasing detergent/phospholipid molar ratio.[243–245] The hydration of micelles and intermicellar concentration decrease with increasing phospholipid aggregates/bile salt ratio in the micelle, but is independent of the micellar concentration, as deduced from the NMR self-diffusion measurements.[246]

Dodecyl phosphocholine micelles in solution are useful and well characterized as a model membrane system for solution NMR studies. To access the membrane-induced conformation and orientation of cardiotoxins, the interaction of the p-type cardiotoxin II from *Naja oxiana* snake venom with perdeuterated dodecyl phosphocholine was studied by ^{1}H NMR spectroscopy and diffusion measurements.[247] 2D NMR is an efficient tool and has been widely used to study the interaction of dodecyl phosphocholine with peptides and protein.[248–250] 2D

^{1}H NMR experiments show that for neuropeptide Y free in solution and bound to a membrane mimetic, dodecyl phosphocholine, the N-terminal segment (Tyr1–Glu15) is extended like a flexible tail in solution. The peptide is in dimeric form. The dimer interface of neuropeptide Y is similar to the interface of monomer binding to dodecyl phosphocholine micelles. The binding of the monomer to the membrane is the key step preceding receptor binding, thereby pre-orientating the C-terminal tetrapeptide and possibly inducing the bio-active conformation.[248] NOESY spectra of [Ile7] angiotensin III recorded in water at different mixing times do not show any NOEs. This could be due to the intermediate tumbling rate of the peptide in water. In the ROESY spectrum, the τ_c dependence of the intensity of the cross-peaks is relatively small, and has been used for assignment and structural analysis. Two NH–NH NOEs are seen between Tyr3–Ile4 and Ile4–His5 in the dodecyl phosphocholine micellar medium. This observation clearly indicates that the segment of [Ile7] angiotensin III in dodecyl phosphocholine micelles acquires a rigid structure.[250] 2D NOESY of leucine enkephalin shows that it lies on the surface of the dodecyl phosphocholine micelles. The dynorphin A molecules do not appear to have some of their residues inserted into the phosphocholine micelles.[251] Radical-induced relaxation of ^{1}H NMR signals has been used to probe the topological orientation of lipopeptide agonists for the bradykinin B2 receptor with respect to the zwitterionic lipid interface. The radical-induced relaxation and dynamic data indicate that the palmitic acid and N-terminal amino acid residues are embedded in the micelles, while the rest of the polypeptide chain is closely associated with the water–micelle interface.[252] To examine the interaction of human apolipoprotein C-I with a submicellar phospholipid, dihexanoyl glycerol phosphocholine, the ^{1}H NMR spectrum was used. The results were used to establish the capacity of apolipoprotein C-I to assemble individual phospholipid molecules.[253] Many peptide hormones elicit a wide arrary of physiological effects by binding to G-protein-coupled receptors. The conformational difference between pituitary adenylate cyclase activating polypeptide in the specific receptor-bound state and the micelle-bound state is limited to the N-terminal seven residues, as shown by ^{1}H NMR spectroscopy. This observation is consistent with the two-step ligand transportation model, in which the pituitary adenylate cyclase activating polypeptide first binds to the membrane non-specifically and then diffuses two-dimensionally in search of its receptor; a conformational change at the N-terminal region then allows a specific interaction between ligand and receptor.[254] In order to understand the transport of ingested fat and poorly water-soluble drugs through the intestinal mucous layer, the distribution and diffusion of sodium taurocholate–phospholipid micelles with bovine submaxillary mucin have been determined by NMR self-diffusion measurements. It was shown that mucin has a minor effect on the equilibrium distribution of phospholipids and bile salts. However, lipids are readily accommodated by mucus, which can significantly increase the permeability of the mucous layer, particularly for poorly water-soluble drugs.[255] The linear pentadecapeptide gramicidin A has

received attention, due to its ability to form monovalent cation-permeable channels in membranes. 2D NOESY has been used to elucidate the conformation of gramicidin A in a membrane environment, which was provided by SDS micelles. ^{23}Na NMR spectra of gramicidin A in water–trifluoroethyl alcohol-d_3 SDS-d_{25}—aqueous solution show that gramicidin A embedded in SDS micelles does indeed interact with alkali metal ions, and the interactions are competitively blocked by Tl^+ ions, which also competitively block alkali metal ion transport through the channel in lipid layer membranes. Also, gramicidin A in SDS micelles forms a channel with a similar molecular structure to that in lysolecithin micelles and in liposomes.[256,257] The site of monovalent cation binding and hydrogen-exchange sites between amide protons and water molecules in the gramicidin A and Phe-1-gramicidin A channels incorporated into SDS micelles have been studied by 2D NOESY. The cation-binding pocket was found to involve residues 10–15 of the peptide. When incorporated into lipid membranes or SDS micelles, gramicidin A forms right-handed single-stranded helical dimer channels, the monomers being joined at their NH_2 termini. The transport of the cation involves diffusion to the channel entrance, binding with it, transport through it, and then dissociation and diffusion away from the channel.[258] The effects of alanine and glycine substitution for tryptophan on the heterogeneity of gramicidin A analogs in micelles and the relative motion of the indole ring of tryptophans in gramicidin analogs incorporated into SDS micelles have also been studied by ^{1}H relaxations and the NOE effect.[259,260]

5.3. Interactions between micelles and water-soluble polymers

The steadily growing interest in polymer–surfactant systems arises from their wide applications in painting, coating, inks, drug delivery, foodstuffs, cosmetic products, and oil recovery. In this respect, the physical properties of the binary system play an important role in determining the industrial products.

The interaction between the anionic surfactant, SDS, and the neutral polymer, polyethylene oxide, in aqueous solution has been intensively studied by NMR, since Jones reported two discontinuities instead of one in the surface tension curve when SDS was added to a polyethylene oxide solution of fixed concentration.[261] The first discontinuity was attributed to the surfactant beginning to bind with the polymer, defined as CAC, and the second to the beginning of the formation of self-aggregated surfactant micelles when the polymer is completely exhausted, defined as c_2. Intensive studies concerning the structure of the co-aggregate, i.e. the structure of the mixed micelle, have been reported, especially by NMR methods. From the variation of the ^{13}C chemical-shift and relaxation measurements, it has been suggested that the polymer wraps around the self-aggregated surfactant micelles, with some of the ethylene oxide units of the polymer being directly adsorbed on the hydrocarbon–water interface, and most of the remaining units forming loops in solution.[262] Diffusion coefficient

measurements of the polymer show that the individual polymer coils undergo significant expansion upon complexation with the surfactant, and ^{13}C NMR relaxation measurements indicate that the correlation time for local segmental motion of the polymer segments attached to micelles is reduced. However, only a relatively small fraction of the total coil is in direct contact with the micelles at saturation.[263,264] The NMR paramagnetic relaxation behavior of the polymer with different molecular weights gives confirmative results indicating that the polymer is solubilized in the surfactant micelles at concentrations above the CMC of the surfactant. The apparent distribution coefficient of polyethylene oxide in SDS micelles and in the solution has been determined.[265–267] A 2D NOESY experiment on a solution of SDS at a concentration about twice the CMC and 2 gl^{-1} of polyethylene oxide showed that the polymer penetrates into the surfactant micelles.[268] Attention was mostly paid to the interaction of the polymer with the surfactant at concentrations well above the CMC in the studies mentioned above. The behaviors of polyethylene oxide and SDS in dilute surfactant solution (below its CMC) have been studied recently, by, for example, NMR self-diffusion coefficient and relaxation measurements.[269] However, the study of the interaction between SDS and the polymer was not done at a molecular level. All of the studies mentioned above are based on the assumption that SDS starts to interact with polyethylene oxide at the CAC, the first discontinuity, although there is no direct evidence concerning the interaction between the surfactant and the polymer at a molecular level. The turning point on the surface tension curve denotes that the concentration of the free surfactant molecules starts to deviate from the total concentration in the solution, but it does not give any information on interactions between the surfactant and the polymer molecules. What is the structure of the co-aggregate at CAC if it really exists? A comparison of the spin–spin relaxation change of the surfactant protons and the polymer protons with the concentration of the surfactant shows that the turning point of the surfactant occurs at the CAC, while that of the polymer occurs at the CMC (Fig. 6), suggesting that there are no interactions between the surfactant and the polymer at the CAC; the surfactant is probably self-aggregated. A 2D NOESY study (Fig. 7) of the system with various concentrations of the surfactant strongly confirms the relaxation result. There are no cross-relaxation peaks between the protons of the surfactant and the polymer at concentrations between the CAC and CMC, while cross-relaxation peaks between the surfactant remote protons do exist, suggesting the start of self-aggregation of SDS molecules at the CAC. The appearance of strong cross-peaks between the protons of the polymer and the protons of the methylene groups further from the polar head groups of the surfactant support the conclusion that the polymer is solubilized in the interior of the surfactant micelles at a surfactant concentration above its CMC.[270] No sign of a discontinuity is observed at the CAC in the adsorption of SDS at the air–solution interface with increase in the surfactant concentration in the presence of polyethylene oxide, as studied by neutron reflection.[271] Interactions between the end capped by the methoxy group poly-

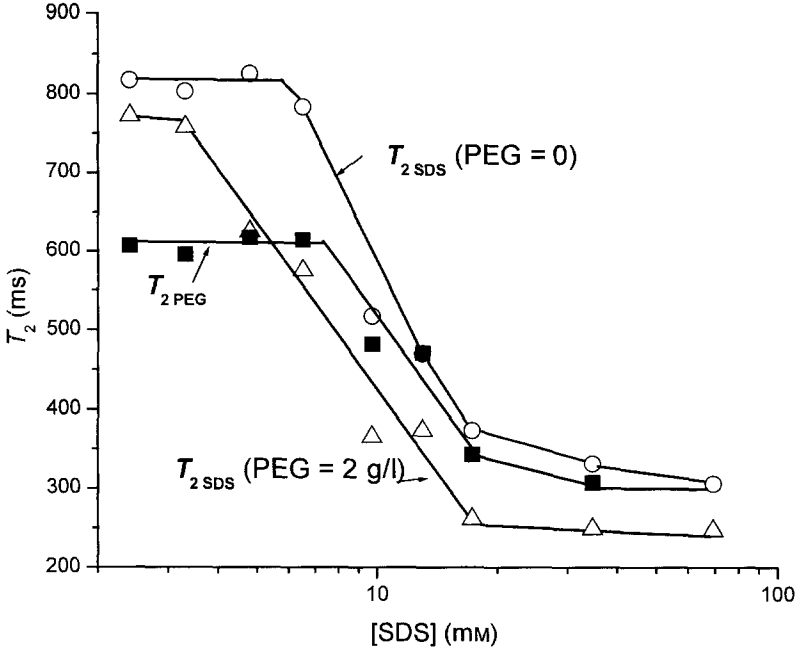

Fig. 6. Spin–spin relaxation time (T_2) dependence of the β-protons of SDS and the protons of PEG on the concentration of SDS without and with the addition of 2 gl^{-1} PEG. (Reprinted with permission from ref. 270, Copyright 2002 Springer-Verlag.)

ethylene oxide and SDS have been studied by self-diffusion, and multi-field ^2H and ^1H relaxation measurements.[272,273] The influence of hydrophobic yet water-soluble polyvinyl methyl ether on the viscoelastic properties of the cetyl trimethyl ammonium bromide–sodium salicylate–water system has been studied by ^1H chemical-shift changes, ^{13}C relaxation measurements, and diffusion ordered spectroscopy.[274,275] The ^{13}C relaxation shows that the drastic reduction of viscosity and the transition from a non-Newtonian to a Newtonian fluid are caused by the breaking down of the long rod-shaped micelles to small and spherical micelles surrounded by the polymer. The association of the micelles with polymer was found to be rather loose. ^1H chemical-shift changes of the salicylate ions showed that they stay embedded in the micelles upon the addition of polyvinyl methyl ether. No difference was found in the dynamics of the polymer in the presence and absence of the surfactant.[274]

The interaction between SDS and a more hydrophobic polymer, polyvinyl pyrrolidone, has been studied by ^{13}C NMR spectroscopy. The results suggest a model similar to the polyethylene oxide–SDS system, in that the polymer molecules are wrapped around the surfactant aggregate.[276] All the carbon atoms of the surfactant except the one closest to the head group undergo ^{13}C chemical-shift changes that are accounted for on the basis of a change in the distribution of

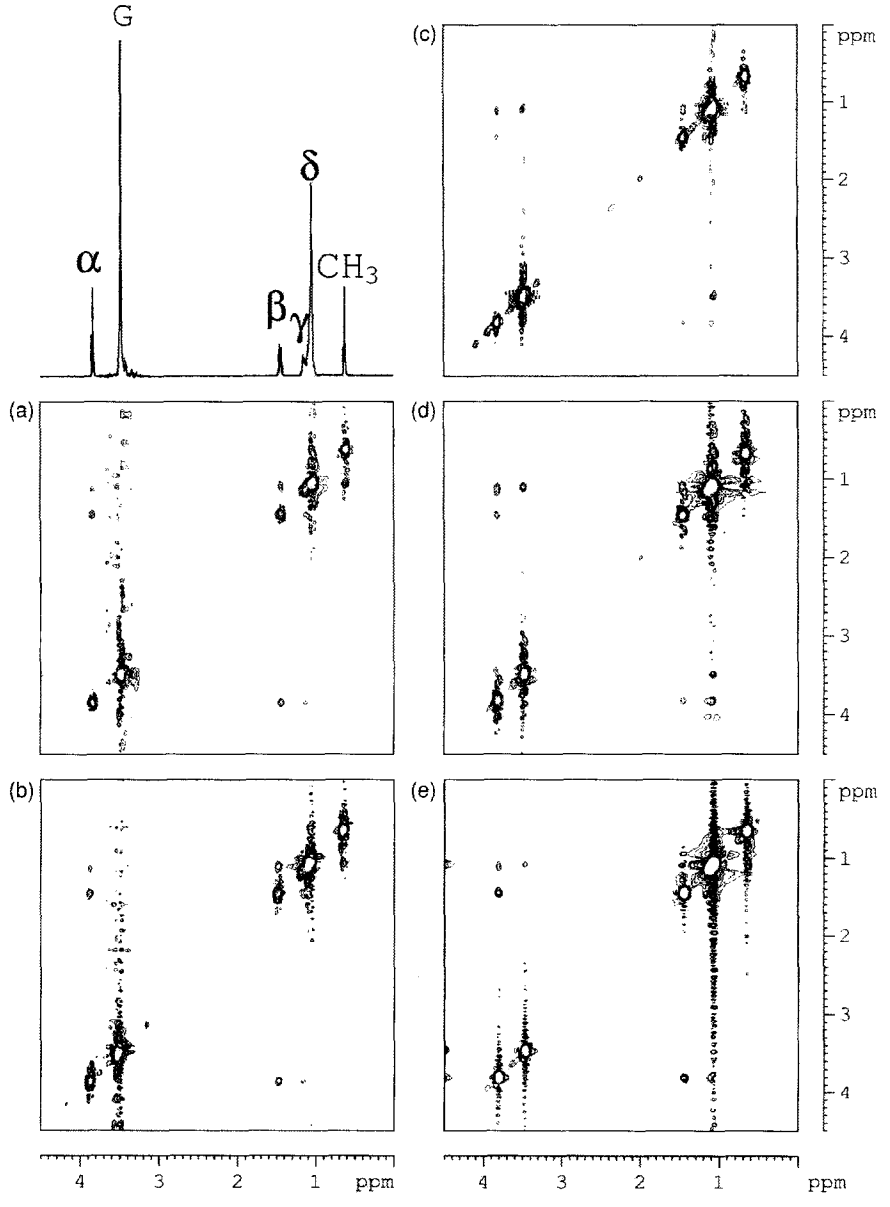

Fig. 7. Contour plots of the 2D NOESY experiments on SDS in PEG ($2\,gl^{-1}$) aqueous solutions at different concentrations of SDS: (a) 3.3 mM; (b) 4.8 mM; (c) 17.3 mM; (d) 34.6 mM; (e) 69.2 mM. (Reprinted with permission from ref. 270, Copyright 2002 Springer-Verlag.)

surfactant between the free and the aggregate states.[277] The interaction between this polymer and lithium heptadodecafluorononate as well as SDS surfactants, deduced from ^{1}H NMR spectra, reveals that the amphiphile in its micellar form links to the polymer chains by hydrophobic interactions with the pyrrolidone functional group of the polymer, causing a significant change in the polyvinyl pyrrolidone structure. A kinetic mechanism has been postulated: (i) at low surfactant concentrations, the surfactant undergoes self-aggregation, and such a kinetic step is not accompanied by conformational changes of the polymer, as shown by ^{1}H NMR spectra; (ii) increasing the surfactant concentration causes interactions between the fluorinated micelles and the polymer to occur. The micelle–polymer interactions involve selected regions of the polymer and thereafter the whole macromolecule. In such a process, the polyvinyl pyrrolidone chains reorganize themselves around the surfactant micelles to give dressed micelles.[278,279]

Polyacrylamide is widely used in ternary oil recovery. The interaction between this polymer and different types of surfactant is therefore of importance in fundamental research. ^{1}H NMR relaxation measurements and a 2D NOESY study of partially hydrolyzed polyacrylamide added to anionic SDS and Triton X-100 aqueous solutions, respectively, showed that there are no interactions between the polymer and either of the anionic and non-ionic surfactants. However, the relaxation measurements suggest a decrease in the CMC of SDS in the presence of polyacrylamide.[280] This is in agreement with the results obtained in a study of the formation of anionic surfactant micelles inside the spherical poly-(*N*-isopropyl-acrylamide) microgels below its CMC, as shown by ^{1}H NMR relaxation.[281] Investigation of the interactions between anionic surfactants and hydrophobically modified polyacrylamides shows that the extent of surfactant binding to hydrophobically modified polyacrylamides, as shown by the change in the ^{1}H chemical shifts and line broadening of the surfactant, is dependent on the degree of hydrophobic substitution, while no evidence for surfactant binding is found in the unmodified polyacrylamide.[282,283] Consequently, the absence of interactions between SDS and polyacrylamide is confirmed. A 2D heteronuclear Overhauser enhancement experiment (2D HOESY) of the polyacrylamide–Triton X-100 aqueous solution (Fig. 8) shows the absence of cross-peaks between the protons of Triton X-100 and those of polyacrylamide. The presence of cross-peaks among the protons of Triton X-100 molecules significantly implies that interaction among the protons of the surfactant molecules is far stronger than that between protons of the polymer and the surfactant. The appearance of cross-correlation peaks between the hydrophobic protons (H-7 and H-8) and the hydrophilic carbon nuclei (h) and vice versa of the same pairs of groups in the 2D HOESY map gives strong evidence for the coiled and folded features of the loosely packed hydrophilic chain of Triton X-100 upon micellization in the presence of the polymer in aqueous solution.[284] The mobility of the counterion Na^+ and the dodecyl sulfate anion determined by the self-diffusion coefficient method reveals that some of the sodium ions are released

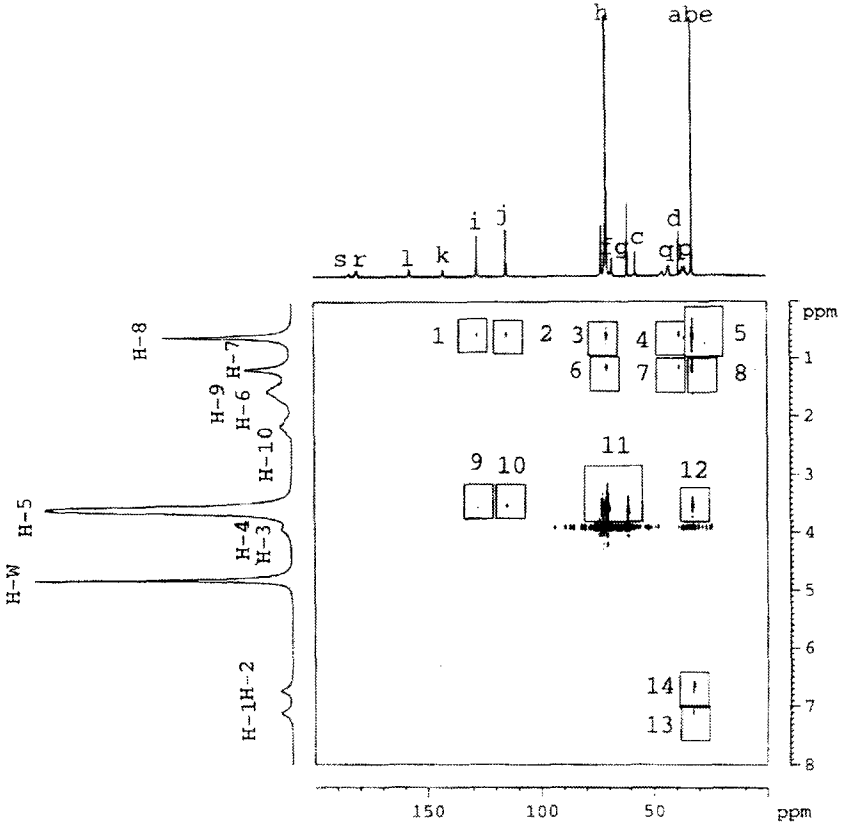

Fig. 8. Contour plot of the 2D ^{13}C–^{1}H heteronuclear Overhauser enhancement (2D HOESY) experiment with Triton X-100 (104 gl^{-1}) in polyacrylamide (40 gl^{-1}) aqueous solution with a mixing time of 800 ms and 512 accumulations. H-1 to H-8 are the peaks of protons corresponding to the peaks 1–8 in Fig. 3, respectively, H-9 and H-10 are the peaks of the methylene and methine protons on the backbone of the polyacrylamide main chain, respectively, and H-W is the peak of water protons. The numbering of the ^{13}C peaks is as follows. For Triton X-100, $(CH_3)_3CCH_2C(CH_3)_2C_6H_4OCH_2CH_2(OC_2H_4)_8OH$: (a) the three end methyl groups; (b) the dimethyl group; (c) the methylene group; (d) the carbon to which the dimethyl groups are attached; (e) the carbon to which the trimethyl groups are attached; (f, g) carbon atoms of the oxyethylene group nearest to the phenoxy ring; (h) carbon atoms of the polyoxyethylene chain; (i, j, k) *meta-*, *ortho-* and *para*-carbon atoms of the phenoxy ring; and (l) the carbon atom of the phenoxy ring to which the polyoxyethylene chain is attached. (p) (q) and (r) are the peaks of the methylene, methane and carboxyl carbon atoms of polyacrylamide, respectively. (Reprinted with permission from ref. 284, Copyright 2001 John Wiley & Sons.)

from the surfactant micelles when polyethylene imine is added to the micellar solution of SDS.[285]

A number of studies relating anionic polymer and cationic surfactants have been performed by ^{1}H chemical-shift, multi-field relaxation differential line broadening, diffusion ordered spectroscopy, and ^{2}H relaxation methods.[286–294]

The tetradecyl trimethyl ammonium bromide molecules in the sodium hyaluronate polyanion gels form relatively small micelle-like aggregates adsorbed on the polyelectrolyte chains. The reorientation of the aggregates in the presence of the polyelectrolyte is not isotropic, but at high polyelectrolyte content it becomes isotropic, as shown by NMR relaxation data.[286] Self-diffusion coefficient measurements indicate the presence of the CAC in solutions of polysaccharide hyaluronate and a cationic surfactant. The CACs are lower than the CMCs, but higher than half of the CMCs of the cationic surfactants dodecyl trimethyl ammonium bromide and decyl trimethyl ammonium bromide, respectively. They increase with an increase in hyaluronate concentration, but the aggregation number of the micelles is unaffected by the presence of hyaluronate.[287] ^{1}H chemical-shift measurements of dodecyl trimethyl ammonium bromide show the hydrophobic effect and the ring current effect of poly-maleic acid co-styrene, poly-maleic acid co-ethylene, polystyrene sulfonate and polyvinyl sulfonate anionic polyelectrolytes on the protons of the bound oppositely charged surfactant. A strong dependence of the binding parameters on the polymer structure is observed, indicating that specific interactions between the surfactant and polymer backbone and the functional groups, as well as conformational changes of the polyanion, play an important role.[288] ^{2}H NMR is a powerful tool for studies of the binding between anionic polyelectrolyte, polystyrene sulfonate, and cationic and mixed cationic–zwitterionic (hexadecyl phosphocholine γ-d_6) surfactants when the deuterated surfactants are available.[289–293] Self-diffusion coefficient and linewidth measurements show that there are micelle-like aggregates of cetyl trimethyl ammonium bromide bound to the anionic chains of the linear biological polysaccharide hyaluronan gel.[294] Self-diffusion measurements of ethyl hydroxyl cellulose non-ionic, cationic and anionic surfactant systems show strong surfactant–polymer interactions leading to the formation of a polymer–surfactant complex. The degree of binding depends on temperature, concentration and the hydrophobicity of the polymer.[295–298] ^{13}C NMR spectroscopy in combination with self-diffusion measurements shows that gelatin interacts with SDS micelles through the electrostatic attraction of cationic residues (lysine, arginine) to the surfactant polar head groups, and through the hydrophobic attraction of the non-polar and aliphatic residues (leucine, isoleucine, valine, etc.) to the exposed hydrocarbon tail of the surfactant. Such interactions lower the micelle diffusion coefficient by almost an order of magnitude.[299] Binding of surfactants (hexadecyl phosphocholine, sodium dodecyl benzene sulfonate, and $C_{12}E_5$), on dispersed polymer particles, such as polystyrene, has been studied by ^{2}H NMR, ^{23}Na relaxation, and self-diffusion coefficient measurements.[300–304] ^{2}H quadrupole splitting of deuterio-labeled hexadecyl phosphocholine on polystyrene particles indicates that the surfactant molecules in their bound state experience rapid anisotropic motional averaging, and that there is a narrow distribution of motional environments, such as would be the case for a monolayer of erect surfactant molecules at the particle surface. When ionic surfactants are blended into the surface mono-

layer, the presence of cationic surfactants causes the ^2H NMR quadrupole splitting to increase, while anionic surfactants cause it to decrease. The results suggest that the choline group of hexadecyl phosphocholine undergoes a conformational change in response to surface charge, similar to that of phosphatidylcholine in a lipid bilayer membrane.[300,301] ^{23}Na NMR relaxation shows the mixed nature of a sodium dodecyl benzene sulfonate–polystyrene dispersion system. The results reveal that the relaxation is caused by local movements and not by dynamics on a timescale associated with the size of the latex particles or the micelles.[302,303] The equilibrium adsorption dynamics of the non-ionic surfactant $C_{12}E_5$ at the surfactant–latex interface has been studied by self-diffusion measurements. A fast adsorption rate was found. The process becomes faster as the concentration of the surfactant is increased.[304] An NMR self-diffusion and relaxation study of binding of SDS and dodecyl trimethyl ammonium bromide with hydrophobically modified ethoxylated urethane showed that, at low surfactant concentrations, the network formation of the hydrophobically modified ethoxylated urethane is enhanced, while at high surfactant concentrations the network is totally disrupted.[305] The self-diffusion coefficient distribution obtained from an inverse Laplace transformation of the pulsed gradient spin echo NMR attenuation function has been obtained as a function of both an associative polymer ($C_{12}E_{200}C_{12}$) and anionic surfactant, SDS concentration. Compared to the parent polymer (polyethylene oxide), the associative polymer exhibits a much wider distribution of self-diffusion coefficients, which narrows with an increase of surfactant concentration. When the surfactant concentration reaches the saturation level for the polymer, the widths of the distributions of the parent homopolymer and associative polymer become identical.[306]

6. POLYMER MICELLES

A ^1H NMR relaxation study of di-block and tri-block copolymers of ethylene oxide and 1,2-butylene oxide aqueous solutions has shown a phase transition from a micelle to a gel in the relaxation time of the ethylene oxide block, consistent with gel formation by close packing of micelles. NOE shows that the blocks of ethylene oxide and 1,2-butylene oxide interpenetrate at the core–fringe boundary.[307] Similar phenomena have been observed for the tri-block copolymer of ethylene oxide and propylene oxide. At the critical micellar temperature, a marked transition in the relaxation times of the hydrophobic propylene oxide block occurs, which is attributed to a change from well-solvated mobile chains below the critical micellar temperature to a more restricted concentrated micelle-core environment above this temperature. However, no transition in the properties of the hydrophilic block of ethylene oxide has been observed. NOE data indicate that in the micelles there is considerable interpenetration of the

ethylene oxide and propylene oxide blocks at the boundary.[308] The behavior of the correlation time for segmental motions in the propylene oxide block indicates an extension of the propylene oxide chains in micelles relative to the monomers. This conformational change is related to the formation of a water-insoluble liquid-like core created by propylene oxide chains in the micelles where the *trans* isomers are favored.[309] Self-diffusion coefficient measurements show that the chain length of the hydrophobic end-capped group of polyethylene oxide greatly influences the onset of aggregation of the polymer.[310] The structure and dynamics of polyethylene oxide end-capped with C_6F_{13} groups have been studied by ^1H and ^{19}F NMR spectroscopy at various temperatures. The observed chemical-shift change is interpreted as resulting from a mixture of aggregated and non-aggregated fluorocarbon end groups. This allows an easy determination of the fraction of free chain ends and thus of the CAC. In this system, a marked increase in the CAC with increasing temperature and a decrease with increasing polymer content are observed.[311] ^1H and ^{13}C NMR experiments have shown that copolymers of polylactic acid and polyethylene glycol with a ratio from 2 : 5 to 15 : 5 form micelles in aqueous solutions. A central core is made from collapsed hydrophobic polylactic acid blocks, and polyethylene glycol blocks form a corona layer extending into the solvent.[312] The behavior of the tri-block copolymer, ethylene $oxide_{100}$–$tetrahydrofuran_{27}$–ethylene $oxide_{100}$, has been studied by NMR self-diffusion coefficient measurements. The apparent radius of gyration of the micelles is fairly independent of the concentration, but large effects are observed on varying the temperature.[313] ^1H NMR analysis indicates that the methoxypolyethylene glycol–poly-ε-caprolactone amphiphilic copolymer nanospheres, which have promising anticancer activity, have a core-shell structure consisting of the hydrophilic outer shell of methoxypolyethylene glycol and the hydrophobic inner core of poly-ε-caprolactone.[314] The amphiphilic graft copolymer polymethyl methacrylate–polyethylene oxide has strong surface activity in $CHCl_3$. It exhibits a stretched conformation in the solution and forms reverse micelles in toluene, and a normal micelle in water, as shown by an NMR study.[315] ^1H NMR shows that the amphiphilic graft copolymer, polystyrene–polyethylene oxide, forms micelles in aqueous solution with the polystyrene backbone as the hydrophobic core and polyethylene oxide as the shell. The stretched single molecules change to spherical reverse micelles as the concentration of the copolymer increases in toluene.[316] ^1H, ^7Li and ^{23}Na NMR spectra and relaxation experiments on sodium and lithium salts of polymethacrylate-block-polyacrylic acid micelles in D_2O indicate a close similarity in the dependence of polyacrylic chain mobility in polyacrylic acid salts and polymethacrylate–polyacrylic acid salts on concentration, and an increase in chain stiffness with dilution. The analogy between the behavior of linear polyacrylic chains and those bound to a rigid micellar core, which cannot be locally diluted, indicates that the collective interchain and intermicellar interactions have an important effect on the local state at the level of individual monomeric units.[317] ^1H single- and double-quantum high-resolution NMR, transverse and

rotating frame relaxation studies of poly-hexyl ethacrylate-block-polyacrylic acid and polydodecyl methacrylate-block-polyacrylic acid micelles in D_2O show that the sidegroups are relatively immobilized to an even higher degree than in poly-2-ethylhexyl acrylate-block-polyacrylic acid micelles under the same conditions. The most immobilized groups are at or near the interface.[318] High-resolution NMR points to the conclusion that polymethyl methacrylate is formed at the micellar core–shell interface when the monomer, methyl methacrylate, is added to a polystyrene-block-polymethacrylic acid micellar solution by γ-irradiation.[319] The micelles formed from poly(solketal methacrylate)-block-poly(2-cinnamnoyl oxyethyl methacrylate)-block-poly(allyl methacrylate) are spherical, with the insoluble poly(2-cinnamnoyl oxyethyl methacrylate)-poly(allyl methacrylate) blocks as the shells and cores, and the poly(solketal methacrylate) block as the coronas.[320] Amphiphilic block copolymers containing poly[(*N*-acyl imineo) ethylene]s and their complexes with lipase form micelle-like aggregates in water.[321] ^{1}H spin-lattice relaxation experiments show that the copolymer sodium 2-(acryl amido)-2-methyl propane sulfonate *N*-dodecyl methacrylamide forms compact micelle-like nanostructures in water–methanol mixed solvent. The hydrophobic microdomains are loosened and the polymer main chains are unfolded with an increase in the methanol content in the mixed solvent.[322] The mobility of the polyethylene oxide segments on the surface of lecithin liposomes has been measured by ^{13}C spin-lattice relaxation. No correlation was found between the behavior and the length of the polyethylene oxide chain.[323]

7. CONCLUSIONS

NMR spectroscopy is a versatile technique for the study of micelles, elucidating the micellization process, the physical properties and structure of micelles, and interactions between micelles and various kinds of substances. Nuclei such as ^{1}H, ^{2}H, ^{13}C, ^{19}F, ^{31}P, ^{7}Li, ^{17}O and ^{23}Na are used in studying micellar systems containing these nuclei. Chemical-shift changes, from which the CMC, aggregation number and counterion binding can be deduced, are easily followed and thereby are widely used. Relaxation experiments provide information about dynamic properties of the surfactant molecules involved in the micelles. Self-diffusion coefficient measurement is an important tool to obtain information about the size and shape of micelles. With the aid of the phase separation model, analysis of the composition of mixed micelles can be achieved. The use of two-dimensional NMR spectroscopy, 2D NOESY, ROESY, and HOESY, is a growing trend in studying the chain packing in micelles as well as interactions between micelles and other molecules. It provides a deeper insight into the relative arrangements of molecules in an associated assembly.

ACKNOWLEDGEMENTS

Financial support by the Fundamental National Key Basic Research Development Program 'Studies of the Extensively Enhanced Petroleum Recovery' (Project Grant G19990225) is gratefully acknowledged. The authors are in debt to Professor G. Z. Cheng of the Wuhan University and Dr L. Zhang of the Technical Institute of Physics and Chemistry for their generous help.

REFERENCES

1. K. L. Mittal and P. Mukerjee, in *Micellization, Solubilization, and Microemulsions*, Vol. 1 (K. L. Mittal, ed.), pp. 1–21, Plenum Press, New York, 1977.
2. K. L. Mittal and B. Lindman, eds, *Surfactants in Solution*, Vol. 2, Plenum Press, New York, 1984.
3. Paul C. Hiemenz, *Principles of Colloid and Surface Chemistry*, 2nd edn, Chapter 8, Marcel Dekker, New York, 1986.
4. D. Myers, *Surfactant Science and Technology*, 2nd edn, Chapters 3 and 4, VCH Publishers, New York, 1992.
5. M. J. Rosen, *Surfactants and Interfacial Phenomena*, Chapter 3, John Wiley & Sons, New York, 1978.
6. J. W. McBain, E. C. V. Cornish and R. C. Bowden, *J. Chem. Soc.*, 1912, **101**, 2042.
7. P. Mukerjee, *Adv. Colloid Interface Sci.*, 1967, **1**, 241.
8. D. Stigter and K. J. Mysels, *J. Phys. Chem.*, 1955, **59**, 45.
9. D. Stigter, *J. Colloid Interface Sci.*, 1974, **47**, 473.
10. D. Stigter, *J. Phys. Chem.*, 1975, **79**, 1008, 1015.
11. G. C. Kresheck, in *Water, a Comprehensive Treatise* (F. Franks, ed.), p. 95, Plenum Press, New York, 1975.
12. P. Mukerjee, J. R. Cardinal and N. R. Desai, in *Micellization, Solubilization, and Microemulsions*, Vol. 1, (K. L. Mittal, ed.), p. 241, Plenum Press, New York, 1977.
13. A. F. Hofmann and D. M. Small, *Annu. Rev. Med.*, 1967, **18**, 333.
14. M. C. Carey and D. M. Small, *Am. J. Med.*, 1970, **49**, 590.
15. D. M. Small, in *The Bile Acids* (P. P. Nair and D. Kritchevsky, eds), Chapter 8, Plenum Press, New York, 1971.
16. J. H. Fendler, *Accounts Chem. Res.*, 1976, **9**, 153.
17. E. H. Cordes and R. B. Dunlap, *Accounts Chem. Res.*, 1969, **2**, 329.
18. E. J. Fendler and J. H. Fendler, *Adv. Phys. Org. Chem.*, 1970, **8**, 271.
19. E. H. Cordes and C. Gitler, *Prog. Bioorganic Chem.*, 1973, **2**, 1.
20. C. A. Bunton, *Prog. Solid State Chem.*, 1973, **8**, 239.
21. I. V. Berezin, K. Martinek and A. K. Yatsimirski, *Russ. Chem. Rev.*, 1973, **42**, 787.
22. V. K. Bansal and D. O. Shah, in *Micellization, Solubilization, and Microemulsions*, Vol. 1, (K. L. Mittal, ed.), p. 87, Plenum Press, New York, 1977.
23. Fredric M. Menger, in *Micelles, Microemulsions, and Monolayers: Science and Technology*, (D. O. Shah, ed.), pp. 53–71, Marcel Dekker, New York, 1998.
24. E. A. G. Aniansson and S. N. Wall, *J. Phys. Chem.*, 1974, **78**, 1024.
25. E. A. G. Aniansson and S. N. Wall, *J. Phys. Chem.*, 1975, **79**, 857.
26. E. A. G. Aniansson, M. A. Imgren and S. N. Wall *et al.*, *J. Phys. Chem.*, 1976, **80**, 905.
27. R. Leung and D. O. Shah, *J. Colloid Interface Sci.*, 1986, **113**, 484.
28. N. Muller, in *Solution Chemistry of Surfactant*, Vol. 1. (K. L. Mittal, ed.), p. 267, Plenum Press, New York, 1979.
29. W. J. Gettings, J. E. Rassing and E. Wyn-Jones, in *Micellization, Solubilization and Microemulsions*, Vol. 1. (K. L. Mittal, ed.), p. 347, Plenum Press, New York, 1977.

30. J. W. McBain, *Trans. Faraday Soc.*, 1913, **9**, 99.
31. Y. Moroi, *Micelles—Theoretical and Applied Aspects*, Chapter 4, Plenum Press, New York, 1992.
32. K. L. Mittal, ed., *Micellization, Solubilization, and Microemulsions*, Vol. 1 and 2, Plenum Press, New York, 1977.
33. K. L. Mittal, *Solution Chemistry of Surfactants*, Vol. 1 and 2, Plenum Press, New York, 1979.
34. J. Pestil, J. Kriz, Z. Tuzar, K. Prochazka, Y. B. Melnichencko, G. D. Wignal, M. R.Talingting, P. Munk and S. E. Webber, *Macromolec. Chem. Phys.*, 2001, **202**, 553.
35. P. Stilbs, *Prog. NMR Spectrosc.*, 1987, **19**, 1.
36. O. Soderman and P. Stilbs, *Prog. NMR Spectrosc.*, 1994, **26**, 445.
37. A. P. Mikhalkin, *Kolloidn. Zh.*, 1994, **56**, 400.
38. P. Stilbs, *Polymer–Surfactant Systems* (Series: Surfactant Science Series) (J. C. T. Kwak, ed.), Marcel Dekker, New York, 1998, **77**, 239.
39. G. Cerichelli, G. Mancini, *Curr. Opin. Colloid Interface Sci.*, 1997, **2**(6), 641–648.
40. P. M. Macdonald, *Colloids Surfaces* A, 1999, **147**, 115.
41. R. Hague, *J. Phys. Chem.*, 1968, **72**, 3056.
42. R. E. Bailey and G. H. Cady, *J. Phys. Chem.*, 1969, **73**, 1612.
43. D. P. Bossev, M. Matsumoto and M. Nakahara, *J. Phys. Chem. B*, 2000, **104**(2), 155.
44. N. Muller, *J. Phys. Chem.*, 1972, **76**, 3012.
45. N. Muller, *Langmuir*, 1994, **10**(7), 2202.
46. J. Zhao and B. M. Fung, *Langmuir*, 1993, **9**(5), 1228.
47. Y. Kameo, S. Takahashi, M. Krieg-Kowald, T. Ohmachi, S. Takagi and H. Inoue, *J. Phys. Chem. B*, 1999, **103**, 9562.
48. L. Okano, O. El. Soud and T. Halsteed, *Colloid Polymer Sci.*, 1997, **275**, 138.
49. B. Rozycka-Rozak, R. Zulka and J. Saraguk, *Z. Naturforsch. C-A J Biosci.*, 2001, **56**, 154.
50. I. Shimizu, H. O. Kabayashi and N. Haltori, *Colloid Polymer Sci.*, 1997, **275**, 293.
51. M. A. Desando, B. McGarvey and L. W. Reeves, *J. Colloid Interface Sci.*, 1996, **181**, 331.
52. K. Esumi, K. Shoji, K. Torigoe, Y. Koide and H. Shosenji, *Colloids Surfaces A*, 2001, **183**, 739.
53. J. A. MacInnis, R. Palepu and D. G. Maragoni, *Can. J. Chem.*, 1999, **77**, 1994.
54. H. Hirata, S. Katayama, H. Okabayashi, H. Furusaka and T. Kavakatsu, *Colloid Polymer Sci.*, 1996, **274**, 245.
55. T. Ngiruwonsanga, K. Quitzch and M. Findeisen, *Tenside Surfactants Detergents*, 2001, **38**, 111.
56. F. M. Menger and C. A. Littau, *J. Am. Chem. Soc.*, 1993, **115**, 10083.
57. J. Ulmius and H. Wennerstrom, *J. Magn. Reson.*, 1977, **28**, 309.
58. U. Olsson, O. Soderman and P. Guering, *J. Phys. Chem.*, 1986, **90**, 5223.
59. T. Drakenberg and B. Lindman, *J. Colloid Interface Sci.*, 1973, **44**, 184.
60. P. Stilbs and B. Lindman, *J. Colloid Interface Sci.*, 1984, **99**, 290.
61. C. Stubenrauch, M. Nyden, C. H. Findenegg and B. Lindman, *J. Phys. Chem.*, 1996, **100**, 17028.
62. F. Nilsson, O. Soderman and I. Johansson, *Langmuir*, 1997, **13**, 3349.
63. M. Scherlund, A. Brodin and M. Malmsten, *Int. J. Pharmaceutics*, 2000, **211**, 37.
64. K. Theander and R. J. Pugh, *J. Colloid Interface Sci.*, 2001, **239**, 209.
65. S. Gouin and X. X. Zhu, *Langmuir*, 1998, **14**, 4025.
66. H. Z. Yuan, Y. R. Du, S. Zhao and J. Y. Yu, *Sci. China A*, 1999, **42**, 319.
67. R. R. Amirov and Z. A. Saprekova, *Kolloidn. Zh.*, 1994, **56**, 160.
68. S. C. Kuebler and P. M. Macdonald, *Langmuir*, 1992, **8**, 397.
69. P. J. B. Edwards, K. J. Jolley, M. H. Smith, S. J. Thomsen and N. Boden, *Langmuir*, 1997, **13**, 2665.
70. R. R. Ernst, G. Bodenhausen and A. Wokaun, *Principles of Nuclear Magnetic Resonance in One and Two Dimensions*, Oxford University Press, New York, 1987.
71. S. Macura and R. R. Ernst, *Mol. Phys.*, 1980, **41**, 95.
72. H. Z. Yuan, G. Z. Cheng, S. Zhao, X. J. Miao, J. Y. Yu, L. F. Shen and Y. R. Du, *Langmuir*, 2000, **16**, 3030.
73. B. O. Persson, T. Drakenberg and B. Lindman, *J. Phys. Chem.*, 1979, **83**, 3011.
74. O. Soderman and P. Guering, *Colloid Polymer Sci.*, 1987, **265**, 76.
75. W. Brown, R. Johnson, P. Stilbs and B. Lindman, *J. Phys. Chem.*, 1983, **87**, 4548.

76. P. G. Nilsson, H. Wennerstrom and B. Lindman, *J. Phys. Chem.*, 1983, **87**, 1377.
77. T. Kato, T. Terao, M. Tsukada and T. Seimiya, *J. Phys. Chem.*, 1993, **97**, 3910.
78. L. Ambrosone, L. Constantino, G. D'Errico and V. Vitgliano, *J. Colloid Interface Sci.*, 1997, **190**, 286.
79. N. Hedin, T. Y. Yu and I. Furo, *Langmuir*, 2000, **16**, 7548.
80. A. Khan, A. Kaplun, Y. Talmon and M. Hellsten, *J. Colloid Interface Sci.*, 1996, **181**, 191.
81. B. Xu, L. Li, A. Yekta, Z. Masoumi, S. Kanagalingam, M. A. Winnik, K. Zhang, P. M. Macdonald and S. Menchen, *Langmuir*, 1997, **13**, 2447.
82. G. Oradd, G. Lindblom, L. B.-A. Johansson and G. Wikander, *J. Phys. Chem.*, 1992, **96**, 5170.
83. O. Annunziata, L. Costantino, G. D'Errico, L. Paduano and V. Vitagliano, *J. Colloid Interface Sci.*, 1999, **216**, 16.
84. G. D'Errico, O. Ortona, L. Paduano and V. Vitagliano, *J. Colloid Interface Sci.*, 2001, **239**, 264.
85. E. Alami and K. Holmberg, *J. Colloid Interface Sci.*, 2001, **239**, 230.
86. F. M. Menger and A. V. Eliseev, *Langmuir*, 1995, **11**, 1855.
87. M. Tornblom, U. Henriksson and M. Ginley, *J. Phys. Chem.*, 1994, **98**, 7041.
88. K. Bijma, E. Rank and J. B. F. N. Engberts, *J. Colloid Interface Sci.*, 1998, **205**, 245.
89. P. G. Nilsson and B. Lindman, *J. Phys. Chem.*, 1983, **87**, 4756.
90. P. G. Nilsson and B. Lindman, *J. Phys. Chem.*, 1984, **88**, 4764.
91. M. Jansson and G. G. Warr, *J. Colloid Interface Sci.*, 1990, **140**, 541.
92. B. Lindstrom, A. Khan, O. Soderman, N. Kamenka and B. Lindman, *J. Phys. Chem.*, 1985, **89**, 5313.
93. N. Hedin, R. Sinikov, I. Furo, U. Henriksson and O. Regev, *J. Phys. Chem. B*, 1999, **103**, 9631.
94. J. Clifford, *Trans Faraday Soc.*, 1965, **61**, 1276.
95. F. Podo, A. Ray and G. Nemethy, *J. Am. Chem. Soc.*, 1973, **95**, 6164.
96. W. Guo, Z. Li, B. M. Fung, E. A. O'Rear and J. H. Harwell, *J. Phys. Chem.*, 1992, **96**, 6738.
97. P. Goon, S. Das, C. J. Clemett, G. J. T. Tiddy and V. V. Kumar, *Langmuir*, 1997, **13**, 5577.
98. I. Berlot, Y. Chevalier, P. Labbe and J. C. Moutet, *Langmuir*, 2001, **17**, 2639.
99. S. Borocci, G. Mancini, C. Cerichelli and L. Luchetti, *Langmuir*, 1999, **15**, 2627.
100. G. Belogi, M. Croce and G. Mancini, *Langmuir*, 1997, **13**, 2903.
101. K. Sugiyama and K. Esumi, *Langmuir*, 1996, **12**, 2613.
102. E. Soderlind and P. Stilbs, *Langmuir*, 1993, **9**, 1678.
103. N. Hattori, A. Yoshino, H. Okabayashi and C. J. O'Connor, *J. Phys. Chem. B*, 1998, **102**, 8965.
104. L. Luchetti and G. Mancini, *Langmuir*, 2000, **16**, 161.
105. M. Shizuma, H. Adachi, M. Kawamura, Y. Takai, T. Takeda and M. Sawada, *J. Chem. Soc. Perkin Trans*, 2001, **2**(4), 592.
106. G. Cherichelli, L. Luchetti and G. Mancini, *Langmuir*, 1997, **13**, 4767.
107. M. Bak, L. K. Rassmussen, T. E. Petersen and N. C. Nielsen, *J. Diary Sci.*, 2001, **84**, 1310.
108. M. Schonhoff, O. Soderman, Z. X. Li and R. K. Thomas, *Bull. Magn. Reson.*, 1998, **20**, 1.
109. D. E. Fremgen, E. S. Smotkin, R. E. Gerald, R. J. Klingler and J. W. Rathke, *J. Supercritical Fluids*, 2001, **19**, 287.
110. J. Zhao and B. M. Fung, *J. Phys. Chem.*, 1993, **97**, 5185.
111. K. Sugiyama, K. Esumi and Y. Koide, *Langmuir*, 1996, **12**, 6006.
112. J. F. Ellena, W. C. Hutton and D. S. Cafiso, *J. Am. Chem. Soc.*, 1985, **107**, 1530.
113. N. C. Maiti, S. Mazumdar and N. Periasamy, *J. Phys. Chem.*, 1995, **99**, 10708.
114. W. Guo, B. M. Fung and E. A. O'Rear, *J. Phys. Chem.*, 1992, **96**, 10068.
115. M. R. Bohmer, L. K. Koopal, R. Janssen, E. L. Lee, R. K. Thomas and A. R. Rennie, *Langmuir*, 1992, **8**, 2228.
116. H. Wennerstrom and J. Ulmius, *J. Magn. Reson.*, 1976, **23**, 431.
117. C. R. Rodriguez, F. V. Chavez, D. J. Pusiol and A. M. F. Neto, *Granular Matter*, 2001, **3**, 53.
118. H. Wennerstrom, B. Lindman, O. Soderman, J. Drakenberg and J. B. Rosenholm, *J. Am. Chem. Soc.*, 1979, **101**, 6860.
119. D. H. Wang, X. L. Xu, N. Y. Deng, G. X. Wang, S. Z. Mao and R. E. Stark, *J. Phys. Chem.*, 1992, **96**, 8187.

120. Z. S. Gao, R. E. Wasylishen and J. C. T. Kwak, *J. Phys. Chem.*, 1990, **94**, 773.
121. P. J. Bratt, D. G. Gillies, A. M. L. Krebber and L. H. Sutcliffe, *Magn. Reson. Chem.*, 1992, **30**, 1000.
122. N. Mahieu, P. Tekeley, J.-C. Boubel, J. M. Cases and D. Canet, *J. Phys. Chem.*, 1993, **97**, 9513.
123. W. Brown, R. Rymden, J. Van Stam, M. Almgren and G. Svensk, *J. Phys. Chem.*, 1989, **93**, 2512.
124. T. Kato, T. Terao and T. Seimiya, *Langmuir*, 1994, **10**, 4468.
125. M. Monduzzi, U. Olsson and O. Soderman, *Langmuir*, 1993, **9**, 2914.
126. O. Soderman, U. Henriksson and U. Olsson, *J. Phys. Chem.*, 1987, **91**, 116.
127. P. Stilbs, H. Walderhaug and B. Lindman, *J. Phys. Chem.*, 1983, **87**, 4762.
128. G. Bodenhausen, G. Wagner, M. Ranee, O. Sorensen, K. Wuretrich and R. Ernst, *J. Magn. Reson.*, 1984, **59**, 542.
129. T. Shikata and Y. Morishima, *Langmuir*, 1997, **13**, 1931.
130. F. Caboi, A. Chittofrati, P. Lazarri and M. Monduzzi, *Colloids Surfaces A*, 1999, **160**, 47.
131. P. D. Profio, R. Gemani, G. Savelli, G. Cerichelli, M. Chiarini, G. Mancini, C. A. Bunton and N. D. Gillitt, *Langmuir*, 1998, **14**, 2662.
132. L. J. Magid, Z. Han, G. G. Warr, M. A. Cassidy, P. D. Batler and W. A. Hamilton, *J. Phys. Chem. B*, 1997, **101**, 7919.
133. S. J. Bachofer and U. Simonis, *Langmuir*, 1996, **12**, 1744.
134. G. Mancini and C. Schiavo, *Langmuir*, 1996, **12**, 3567.
135. K. Bijma and Jan B. F. N. Engberts, *Langmuir*, 1997, **13**, 4843.
136. P. J. Kreke, L. J. Magid and J. C. Gee, *Langmuir*, 1996, **12**, 699.
137. H. Iijima, T. Kato and O. Soderman, *Langmuir*, 2000, **16**, 318.
138. P. Li, M. Jansson and P. Stilbs, *J. Phys. Chem.*, 1989, **93**, 6458.
139. D. P. Bossev, M. Matsumoto and M. Nakahara, *J. Phys. Chem. B*, 1999, **103**, 8251.
140. S. J. Bachofer, U. Simonis and T. A. Nowicki, *J. Phys. Chem.*, 1991, **95**, 480.
141. U. Olsson, O. Soderman and P. Guering, *J. Phys. Chem.*, 1986, **90**, 5223.
142. M. Almgren, P. Stilbs, J. Alsins, P. Liase and N. Kamenka, *J. Phys. Chem.*, 1985, **89**, 2666.
143. P. Stilbs and B. Lindman, *J. Phys. Chem.*, 1981, **85**, 2587.
144. M. Jansson and P. Stilbs, *J. Phys. Chem.*, 1987, **91**, 113.
145. M. Jansson and P. Stilbs, *J. Phys. Chem.*, 1985, **89**, 4868.
146. N. Hedin, I. Furo and P. O. Erikson, *J. Phys. Chem. B*, 2000, **104**, 8544.
147. N. Hedin and I. Furo, *J. Phys. Chem. B*, 1999, **103**, 9640.
148. J. Clifford and B. A. Pethica, *J. Chem. Soc. Faraday Trans*, 1964, **60**, 1483.
149. J. Clifford and B. A. Pethica, *J. Chem. Soc. Faraday Trans*, 1965, **61**, 182.
150. L. M. Corkill, J. F. Goodman and J. Wyer, *Trans Faraday Soc.*, 1969, **65**, 9.
151. C. L. Clemett, *J. Chem. Soc. (A)*, 1970, 2251.
152. T. Walker, *J. Colloid Interface Sci.*, 1973, **45**, 372.
153. B. Halle, T. A. Anderson, S. Forsen and B. Lindman, *J. Am. Chem. Soc.*, 1981, **103**, 500.
154. B. Halle and G. Caristrom, *J. Phys. Chem.*, 1981, **85**, 2142.
155. B. Lindman, M. C. Puyal, N. Kamenka, R. Rymden and P. Stilbs, *J. Phys. Chem.*, 1984, **88**, 5048.
156. D. Canet, N. Mahieu and P. Tekely, *J. Am. Chem. Soc.*, 1982, **114**, 6190.
157. A. Belmajdoub, N. Mahieu, P. Tekely and D. Canet, *J. Phys. Chem.*, 1992, **96**, 1011.
158. P. Palmas, P. Tekely, P. Mutzenhardt and D. Canet, *J. Chem. Phys.*, 1993, **99**, 4775.
159. N. Mahieu, P. Tekely and D. Canet, *J. Phys. Chem.*, 1993, **97**, 2764.
160. R. Raulet, I. Furo, J. Brondeau, B. Diter and D. Canet, *J. Magn. Reson.*, 1998, **133**, 324.
161. S. Krishnakumar and P. J. Somasundaran, *J. Colloid Interface Sci.*, 1994, **162**, 425.
162. A. Yoshino, H. O. Kabayashi, T. Yoshida and K. Kushida, *J. Phys. Chem.*, 1996, **100**, 9592.
163. L. P. Novaki, N. M. Correa, J. J. Silber and O. A. El Seoud, *Langmuir*, 2000, **16**, 5573.
164. Q. Li, T. Li and J. G. Wu, *J. Phys. Chem. B*, 2000, **104**, 9011.
165. L. P. Novaki, P. A. R. Pires and O. A. El Seoud, *Colloid Polymer Sci.*, 2000, **278**, 143.
166. K. Hamada, T. Ikeda, T. Kawai and K. Kon-No, *J. Colloid Interface Sci.*, 2001, **233**, 166.
167. T. H. Fendler, E. J. Fendler, R. T. Medary and V. A. Woods, *J. Am. Chem. Soc.*, 1972, **92**, 7288.
168. M. T. Caudle, R. A. Nieman and V. C. Young, *Inorg. Chem.*, 2001, **40**, 1571.

169. R. Angelico, G. Palazzo, G. Colafemmina, P. A. Cirkel, M. Giustini and A. Ceglie, *J. Phys. Chem. B*, 1998, **102**, 2883.
170. V. E. Yusbmanov and M. Talak, *J. Colloid Interface Sci.*, 1997, **191**, 384.
171. P. Stilbs, *J. Colloid Interface Sci.*, 1982, **87**, 385.
172. G. M. Forland, J. Samseth, M. I. Gjerde, H. Hoiland, A. O. Jensen and K. Mortensen, *J. Colloid Interface Sci.*, 1998, **203**, 328.
173. M. Monduzzi, A. Ceglie, B. Lindman and O. Soderman, *J. Colloid Interface Sci.*, 1990, **136**, 113.
174. C.A. Kennedy, S. N. MacMillan, M. J. McAlduff and D. G. Marangoni, *Colloid Polymer Sci.*, 2001, **279**, 1.
175. J. B. Rosenholm, T. Drakenberg and B. Lindman, *J. Colloid Interface Sci.*, 1978, **63**, 538.
176. O. Soderman, H. Walderhaug and B. Lindman, *J. Phys. Chem.*, 1985, **89**, 1795.
177. B. E. Hawrylak and D. G. Marangoni, *Can. J. Chem.*, 1999, **77**, 1241.
178. R. E. Wasylishen, J. T. C. Kwak, E. Verpoorte and J. B. MacDonald, *Can. J. Chem.*, 1991, **69**, 822.
179. M. Tornblom and U. Henriksson, *J. Phys. Chem. B*, 1997, **101**, 6028.
180. J. C. Eriksson, *Acta Chem. Scand.*, 1963, **17**, 1963.
181. J. C. Eriksson and G. Gillberg, *Acta Chem. Scand.*, 1966, **20**, 2019.
182. J. E. Gordon, J. C. Robertson and R. L. Thorne, *J. Phys. Chem.*, 1970, **74**, 957.
183. K. Ganesh, P. Miltra and D. Balasubramanlan, *J. Phys. Chem.*, 1982, **86**, 4291.
184. A. B. Mandal, V. Wang, K. Brown and R. E. Verrall, *J. Colloid Interface Sci.*, 1993, **161**, 292.
185. G. Cerichelli and G. Mancini, *Langmuir*, 2000, **16**, 182.
186. V. Suratka and S. Mahapatra, *J. Colloid Interface Sci.*, 2000, **225**, 32.
187. C. A. Bunton and M. J. Minch, *J. Phys. Chem.*, 1974, **78**, 1490.
188. E. Kolehmainen, *Magn. Reson. Chem.*, 1988, **26**, 760.
189. G. J. Duns, L. N. Reeves and D. W. Yang, *J. Colloid Interface Sci.*, 1995, **173**, 261.
190. Z. S. Gao, R. E. Wasylishen and J. T. C. Kwak, *J. Phys. Chem.*, 1989, **93**, 2190.
191. Z. S. Gao, R. E. Wasylishen and J. T. C. Kwak, *J. Chem. Soc. Faraday Trans*, 1991, **87**, 947.
192. D. G. Marangoni, A. P. Rodenhiser, J. M. Thomas and J. T. C. Kwak, *Langmuir*, 1993, **9**, 438.
193. J. A. Zoltewicz and L. B. Bloom, *J. Phys. Chem.*, 1992, **96**, 5156.
194. L. E. Almeida, J. E. Borissevitch, V. E. Yushmanov and M. Tabak, *J. Colloid Interface Sci.*, 1998, **203**, 456.
195. Z. S. Gao, R. E. Wasylishen and J. C. T. Kwak, *Macromolecules*, 1989, **22**, 2544.
196. J. K. McCulloch, D. Fornasiero, J. M. Perera, B. S. Murray, G. W. Stevens and F. Griaser, *J. Colloid Interface Sci.*, 1993, **157**, 180.
197. D. G. Barett and S. H. Gellman, *J. Am. Chem. Soc.*, 1993, **115**, 9343.
198. R. Auzely-Velty, C. Pean, F. Djeddaini-Pilard, T. Zemb and B. Perly, *Langmuir*, 2001, **17**, 504.
199. J. Kriz, B. Masar and D. Doskocilova, *Macromolecules*, 1997, **30**, 4391.
200. Z. Yang, E. Pousia, F. Heatly, C. Price, C. Booth, V. Castelletto and I. W. Hamley, *Langmuir*, 2001, **17**, 2106.
201. S. Das, R. G. Bhirud, N. Nayyar, K. S. Narayan and V. V. Kumar, *J. Phys. Chem.*, 1992, **96**, 7454.
202. N. Nayyar, S. Das, R. G. Bhirud, K. S. Narayan, A. P. Singh and V. V. Kumar, *J. Colloid Interface Sci.*, 1993, **160**, 496.
203. R. M. Clapperton, R. H. Ottewill and B. Ingram, *Langmuir*, 1994, **10**, 51.
204. D. P. Bossev, M. Matsumoto, T. Sato, H. Watanabe and M. Nakahara, *J. Phys. Chem. B*, 1999, **103**, 8259.
205. O. Soderman, K. L. Herrington, E. W. Kaler and D. D. Miller, *Langmuir*, 1997, **13**, 5531.
206. O. Regev and A. Khan, *J. Colloid Interface Sci.*, 1996, **182**, 95.
207. W. Guo, E. K. Guzman, S. D. Heavin, Z. Li, B. M. Fung and S. D. Christian, *Langmuir*, 1992, **8**, 2368.
208. P. G. Nilsson and B. Lindman, *J. Phys. Chem.*, 1984, **88**, 5391.
209. P. Guering, P. G. Nilsson and B. Lindman, *J. Colloid Interface Sci.*, 1985, **105**, 41.
210. T. R. Desai and S. G. Dixit, *J. Colloid Interface Sci.*, 1996, **177**, 471.
211. R. R. Amirov and Z. A. Sparikova, *Colloid J.*, 1999, **61**, 432.

212. A. M. Misselyn-Bauduin, A. Thibaut, J. Grandjean, G. Broze and R. Jerome, *Langmuir*, 2000, **16**, 4430.
213. J. Penfold, E. Staples, L. Thompson, I. Tucker, J. Hines, R. K. Thomas, J. R. Lu and N. Warren, *J. Phys. Chem. B*, 1999, **103**, 5204.
214. H. Z. Yuan, S. Zhao, G. Z. Cheng, L. Zhang, X. J. Miao, J. Y. Yu, L. F. Shen and Y. R. Du, *J. Phys. Chem.*, 2001, **105**, 4611.
215. T. Z. Wang, S. Z. Mao, X. J. Miao, S. Zhao, J. Y. Yu and Y. R. Du, *J. Colloid Interface Sci.*, 2001, **241**, 465.
216. H. C. Gao, S. Zhao, S. Z. Mao, H. Z. Yuan, J. Y. Yu, L. F. Shen and Y. R. Du, *J. Colloid Interface Sci.*, 2002, **249**, 200.
217. S. Ozeki and H. Seki, *J. Phys. Chem.*, 1992, **96**, 10074.
218. A. Yoshino, K. Murate, T. Yoshida, H. Okabayashi, P. R. Krishna, H. Kamaya and I. Ueda, *J. Colloid Interface Sci.*, 1994, **166**, 375.
219. P. C. Griffith, P. Stilbs, K. Paulsen, A. M. Howe and A. R. Pitt, *J. Phys. Chem. B*, 1997, **101**, 915.
220. Y. Y. Chien and W. F. Bleam, *Langmuir*, 1997, **13**, 5283.
221. L. A. Guo, I. Arnaud, M. Petit-Ramel, R. Gauthier, C. Monnet, P. Le Perchec and Y. Chevalier, *J. Colloid Interface Sci.*, 1994, **163**, 334.
222. E. B. Tada, L. P. Novaki and O. A. El Seoud, *Langmuir*, 2001, **17**, 652.
223. G. Cerichelli, L. Luchetti, G. Mancini, G. Savelli and C. A. Bunton, *Langmuir*, 1996, **12**, 2348.
224. C. Manohar, U. R. K. Rao, B. S. Valaulikar and R. M. Iyer, *J. Chem. Soc. Chem. Commun.*, 1986, **5**, 379.
225. G. Gonzalez-Gaitano, A. Guerrero-Martinez, F. Ortega and G. Tardajos, *Langmuir*, 2001, **17**, 1392.
226. G. Gonzalez-Gaitano, A. Compositizo, S. Sachez-Martin and G. Tardajos, *Langmuir*, 1997, **13**, 2235.
227. O. Soderman, K. Wiedmer and M. L. Riekkola, *J. Dispersion Sci. Technol.*, 2000, **21**, 209.
228. M. Bjoiling, A. Herslof-Bjoiling and P. Stilbs, *Macromolecules*, 1995, **28**, 6970.
229. S. Zourab, I. Al-Kashef and I. Kayali, *J. Dispersion Sci. Technol.*, 2001, **22**, 111.
230. K. M. Kadish, B. G. Maiya and C. Araullo-Mc Adams, *J. Phys. Chem.*, 1991, **95**, 427.
231. M. Vermathen, E. A. Louie, A. B. Chedosh, S. Ried and U. Simonis, *Langmuir*, 2000, **16**, 210.
232. K. R. Deaton, E. A. Feyen, H. J. Nkulabi and K. F. Morris, *Magn. Reson. Chem.*, 2001, **39**, 276.
233. T. Wymore and T. C. Wong, *J. Biomolec. Struct. Dynamics*, 2000, **18**, 461.
234. X. F. Gao and T. C. Wong, *Biopolymers*, 2001, **58**, 20.
235. T. L. Whitehead, L. M. Jones and R. P. Hicks, *Biopolymers*, 2001, **58**, 593.
236. K. Shindo, H. Takahashi, K. Shinozaki, K. Kami, K. Anzai, S. Lee, H. Aoyagi, Y. Kirino and I. Shimada, *Biochim. Biophys. Acta Protein Struct. Molec. Enzymol.*, 2001, **1545**, 153.
237. M. Lindberg, J. Jarvet, U. Langel and A. Graslund, *Biochemistry*, 2001, **40**, 3141.
238. M. Lindberg and A. Graslund, *FEBS Lett.*, 2001, **479**, 39.
239. J. A. Zoltewicz and L. B. Bloom, *J. Phys. Chem.*, 1992, **96**, 2007.
240. A. Valstar, M. Vasilescu, C. Vigouroux, P. Stilbs and M. Almgren, *Langmuir*, 2001, **17**, 3208.
241. A. A. Rebeiro and E. A. Dennis, *Biochemistry*, 1975, **14**, 3746.
242. A. A. Rebeiro and E. A. Dennis, *J. Phys. Chem.*, 1976, **80**, 1746.
243. K. Suzuki, T. Hasegava, Y. Takamura, K. Takahashi, H. Asano and M. Ueno, *Langmuir*, 1996, **12**, 5536.
244. D. Otten, M. F. Brown and K. Beyer, *J. Phys. Chem. B*, 2000, **104**, 12119.
245. S. S. Funari, B. Nuscher, B. Rapp and K. Beyer, *Proc. Natl. Acad. Sci. USA*, 2001, **98**, 8938.
246. C. Y. Li and T. S. Wiedmann, *J. Phys. Chem.*, 1996, **100**, 18464.
247. P. V. Dubovskii, D. V. Dementieva, E. V. Bocharov, Y. N. Utkin and A. S. Arseniev, *J. Mol. Biol.*, 2001, **305**, 137.
248. R. Bader, A. Bettio, A. G. Beck-Sickinger and O. Zerbe, *J. Mol. Biol.*, 2001, **305**, 307.
249. X. F. Gao and T. C. Wong, *Biopolymers*, 2001, **58**, 643.
250. A. B. Patel, S. Srivastava and R. S. Phadke, *Magn. Reson. Chem.*, 1999, **37**, 279.
251. D. A. Kallick, M. R. Tessmer, C. R. Watts and C. Y. Li, *J. Magn. Reson. Ser. B*, 1995, **109**, 60.

252. C. Giragossian, E. Nardi, C. Savery, M. Pellegrini, S. Meini and C. A. Maggi, *Biopolymers*, 2001, **58**, 511.
253. B. W. Ateliffe, C. A. McRaild, P. R. Gooley and G. J. Howlett, *Eur. J. Biochem.*, 2001, **268**, 2838.
254. H. Inooka, T. Ohtaki, O. Kitahara, T. Ikegami, S. Endo, C. Kitada, K. Ogi, H. Onda, M. Fugino and M. Shirakawa, *Nature Struct. Biol.*, 2001, **8**, 161.
255. T. S. Wiedmann, C. Deye and D. Kallick, *Pharmaceutical Res.*, 2001, **18**, 45.
256. F. Vladimir, B. F. Bystrov, A. S. Arseniev, I. L. Barsukov and A. L. Lomize, *Bull. Magn. Reson.*, 1986, **8**, 84.
257. A. S. Arseniev, T. L. Barsukov and V. F. Bystrov, in *Chemistry of Peptides and Proteins*, Vol. 3 (W. Voelter, E. Bayer, Y. A. Ovchinnikov and V. T. Ivanov, eds), p. 127. Walter de Gruyter & Co., Berlin, New York, 1986.
258. J. F. Hinton, *J. Magn. Reson. Ser. B*, 1996, **112**, 26.
259. J. F. Hinton, A. M. Washburn-McCain, A. Snow and J. Douglas, *J. Magn. Reson.*, 1997, **124**, 132.
260. J. F. Hinton and A. M. Washburn-McCain, *J. Magn. Reson.*, 1997, **125**, 259.
261. M. N. Jones, *J. Colloid Interface Sci.*, 1967, **23**, 36.
262. B. Cabane, *J. Phys. Chem.*, 1977, **81**, 1639.
263. K. Chari, B. Antalek and J. Minter, *Phys. Rev. Lett.*, 1995, **74**, 3624.
264. K. Chari, B. Antalek, M. Lin and S. Sinka, *J. Chem. Phys.*, 1994, **100**, 5294.
265. Z. S. Gao, R. E. Wasylishen and J. C. T. Kwak, *J. Phys. Chem.*, 1991, **95**, 462.
266. Z. S. Gao, R. E. Wasylishen and J. C. T. Kwak, *J. Colloid Interface Sci.*, 1990, **137**, 137.
267. Z. Gao and J. C. T. Kwak, in *Surfactants in Solution*, Vol. 11 (K. L. Mittal and D. O. Shah, eds), p. 261, Plenum Press, New York, 1991.
268. M. I. Gjerde, W. Nerdal and H. Hoiland, *J. Colloid Interface Sci.*, 1996, **183**, 285.
269. M. I. Gjerde, W. Nerdal and H. Hoiland, *J. Colloid Interface Sci.*, 1998, **197**, 191.
270. H. Z. Yuan, L. Luo, L. Zhang, S. Zhao, S. Z. Mao, J. Y. Yu, L. F. Shen and Y. R. Du, *Colloid Polymer Sci.*, 2002, **280**, 479.
271. D. J. Cooke, C. C. Dong, J. R. Lu, R. K. Thomas, E. A. Simister and J. Penfold, *J. Phys. Chem. B*, 1998, **102**, 4912.
272. S. Abrahmsen-Alami and P. Stilbs, *J. Phys. Chem.*, 1994, **98**, 6359.
273. G. Baskar and A. Mandal, *Chem. Phys. Lett.*, 1997, **266**, 443.
274. T. C. Wong, C. S. Liu, C. D. Poon and D. Kwoh, *Langmuir*, 1992, **8**, 460.
275. K. F. Morris, C. S. Johnson, Jr. and T. C. Wong, *J. Phys. Chem.*, 1994, **98**, 603.
276. K. Chari and W. C. Lenhart, *J. Colloid Interface Sci.*, 1990, **137**, 204.
277. K. Chari, *J. Colloid Interface Sci.*, 1992, **151**, 294.
278. B. Sesta, A. L. Segre, A. D'Aprano and N. Proietti, *J. Phys. Chem. B*, 1997, **101**, 198.
279. B. Sesta, A. D'Aprano, A. L. Segre and N. Proietti, *Langmuir*, 1997, **13**, 6612.
280. H. Z. Yuan, S. Zhao, J. Y. Yu, L. F. Shen and Y. R. Du, *Colloid Polymer Sci.*, 1999, **277**, 1026.
281. Y. B. Gao, S. C. F. Au-Yeung, S. Q. Zhou and C. Wu, *J. Macromolec. Sci. Phys. B*, 1997, **36**, 417.
282. J. J. Effing, I. J. McLennan, N. M. van Os and J. C. T. Kwak, *J. Phys. Chem.*, 1994, **98**, 12397.
283. J. J. Effing, I. J. McLennan and J. C. T. Kwak, *J. Phys. Chem.*, 1994, **98**, 2499.
284. H. Z. Yuan, X. J. Miao, S. Zhao, L. F. Shen, J. Y. Yu and Y. R. Du, *Magn. Reson. Chem.*, 2001, **39**, 33.
285. M. A. Winnik, S. M. Bystryak, C. Chassenieux, V. Strashko, P. M. Mcdonald and J. Siddiqui, *Langmuir*, 2000, **16**, 4495.
286. T. C. Wong, K. Thalberg, B. Lindman and H. Gracz, *J. Phys. Chem.*, 1991, **95**, 8850.
287. K. Thalberg, J. van Stam, C. Lindblad, M. Almgren and B. Lindman, *J. Phys. Chem.*, 1991, **95**, 8975.
288. Z. S. Gao, R. E. Wasylishen and J. C. T. Kwak, *J. Colloid Interface Sci.*, 1988, **126**, 371.
289. P. M. Macdonald, D. Staring and Y. Yue, *Langmuir*, 1993, **9**, 381.
290. P. M. Macdonald and Y. Yue, *Langmuir*, 1993, **9**, 1206.
291. D. J. Senchyschyn, M. A. Carbone and P. M. Macdonald, *Langmuir*, 1996, **12**, 253.
292. P. M. Macdonald and A. Jang, *Langmuir*, 1997, **13**, 2259.
293. K. J. Crowell and P. M. Macdonald Jr., *J. Phys. Chem. B*, 1997, **101**, 1105.

294. K. Thalberg and B. Lindman, *Langmuir*, 1991, **7**, 277.
295. K. W. Zhang, M. Jonstromer and B. Lindman, *J. Phys. Chem.*, 1994, **98**, 2459.
296. H. Walderhaug, B. Nystrom, F. K. Hansen and B. Lindman, *J. Phys. Chem.*, 1995, **99**, 4672.
297. K. Thuresson, O. Soderman, P. Hasson and G. Wang, *J. Phys. Chem.*, 1996, **100**, 4909.
298. H. Walderhaug, A. L. Kjfniksen and B. Nystrom, *J. Phys. Chem. B*, 1997, **101**, 8892.
299. D. D. Miller, W. Lenhart, B. J. Antalek, A. J. Williams and J. M. Hewitt, *Langmuir*, 1994, **10**, 68.
300. P. M. Macdonald, Y. Yue and J. R. Rydall, *Langmuir*, 1992, **8**, 164.
301. Y. Yue, J. R. Rydall and P. M. Macdonald, *Langmuir*, 1992, **8**, 390.
302. J. P. H. Zwetsloot, J. G. Hollander and J. C. Leyte, *J. Colloid Interface Sci.*, 1996, **178**, 233.
303. J. P. H. Zwetsloot and J. C. Leyte, *J. Colloid Interface Sci.*, 1996, **181**, 351.
304. M. Schonhoff and O. Soderman, *J. Phys. Chem. B*, 1997, **101**, 8237.
305. K. Zhang, B. Xu, M. A. Winnik and P. M. Macdonald, *J. Phys. Chem.*, 1996, **100**, 9834.
306. K. Persson, P. Griffiths and P. Stilbs, *Polymer*, 1996, **37**, 253.
307. J. Godward, F. Heatley, S. Smith, S. Tandekaew, Y. W. Yang and C. Booth, *J. Chem. Soc. Faraday Trans*, 1995, **91**, 3461.
308. J. Godward, F. Heatley and C. Booth, *J. Chem. Soc. Faraday Trans*, 1995, **91**, 1491.
309. F. Cau and S. Lacelle, *Macromolecules*, 1996, **29**, 170.
310. S. Abrahmsen-Alami and P. Stilbs, *J. Colloid Interface Sci.*, 1997, **189**, 137.
311. J. Preuschen, J. Rottstegge and H. W. Spiess, *Colloids Surfaces* A, 1999, **158**, 89.
312. C. R. Heald, S. Stolnik, C. De Matteis, M. C. Garnett, L. Illum, S. S. Davis and F. A. M. Leermarkers, *Colloids Surfaces A*, 2001, **179**, 79.
313. P. Holmqvist, S. Nilsson and F. Tiberg, *Colloid Polymer Sci.*, 1997, **275**, 467.
314. S. Y. Kim and Y. M. Lee, *Biomaterials*, 2001, **22**, 1697.
315. Z. S. Xu, C. F. Yi, S. Y. Cheng, L. X. Feng and C. Wu, *Acta Polymer. Sin.*, 2000, 701.
316. Y. C. Chen, C. F. Yi, Z. S. Xu and S. Y. Cheng, *Acta Physico-chim. Sin.*, 2001, **17**, 471.
317. J. Kriz, B. Masar, J. Dybal and D. Doskocilova, *Macromolecules*, 1997, **30**, 3302.
318. J. Kriz, J. Brus, J. Plestil, D. Kurkova, B. Masar, J. Dybal, C. Zune and R. Jerome, *Macromolecules*, 2000, **33**, 4108.
319. J. Plestil, H. Pospisil, P. Kadlec, Z. Tuzar, J. Kriz and V. I. Gordeliy, *Polymer*, 2001, **42**, 2941.
320. F. T. Liu and J. G. Liu, *Macromolecules*, 2001, **34**, 1302.
321. K. Naka, T. Nakamura, A. Ohki and S. Maeda, *Polymer J.*, 1995, **27**, 1071.
322. A. Hashidzume, I. Tomatsu and Y. Morishima, *Kobunshi Ronbunshu*, 2001, **58**, 195.
323. N. Morone, Y. Okamura and J. Sunamoto, *J. Bioactive Compatible Polymers*, 2001, **16**, 194.

Index

Note – Page numbers in *italic* type refer to figures and tables.